Lehrstuhl für Aerodynamik und Strömungsmechanik
Technische Universität München

Aerodynamic Design Optimisation for Utility Helicopter Drag Reduction

Moritz Grawunder

Vollständiger Abdruck der von der Fakultät für Maschinenwesen der Technischen Universität München zur Erlangung des akademischen Grades eines

Doktor-Ingenieurs

genehmigten Dissertation.

Vorsitzender: Prof. Dr.-Ing. Hans-Jakob Kaltenbach

Prüfer der Dissertation:

1. apl. Prof. Dr.-Ing. Christian W. M. Breitsamter
2. Prof. Dr.-Ing. Manfred Hajek

Die Dissertation wurde am 09.11.2016 bei der Technischen Universität München eingereicht und durch die Fakultät für Maschinenwesen am 24.02.2017 angenommen.

Childhood.
School.
Studies.
Life.
To those I had the privilege to learn from.

Abstract

This work focuses on improving the aerodynamic design of Twin-Engine-Light (TEL) class utility helicopter. The main objective for this optimisation is to increase TEL-class helicopter's dynamic productivity for achieving high level goals, such as reduced fuel consumption and emissions. Preliminary studies showed, that a viable approach for achieving efficiency gains is reducing the helicopter's parasite drag. The fuselage, the skid-landing-gear and the rotor-head are the main sources of parasite drag for TEL-class utility helicopter. Thus, the potential for aerodynamic design optimisation with respect to these components is investigated.
For the aerodynamic design optimisation, a clear step-wise approach is chosen. The reference configuration is investigated first. The viability of the subsequent design optimisations is assessed based on this reference. The reference configuration is a current production type TEL-class helicopter. It features a blunt fuselage aft-body, a skid-landing-gear and a five-bladed bearingless rotor-head. The aerodynamic characteristics of the reference configuration and its modifications are evaluated by extensive wind-tunnel experiments and complementary numerical flow simulations.
The conducted experiments include forces and moments, surface pressures and wake velocity measurements. The numerical flow simulations are based on the Unsteady Reynolds Averaged Navier Stokes (URANS) equation model in combination with the Reynold's Stress turbulence Model (RSM).
The reference configuration's main parasite drag sources were confirmed to be the form drag of the fuselage (23%), the skid-landing-gear (21%) and the rotor head (26%). Thus, in order to achieve a more efficient design, aerodynamic fairings for the skid-landing-gear and passive flow control devices at the rear fuselage's upsweep are considered. The optimisation task is to reduce the helicopter's parasite drag without significantly increasing its downforce.
On aggregate a drag benefit of 22% is achieved with those design modifications. The increase in downforce is confined to a equivalent weight penalty in cruise of less than 80 kg. The achieved drag reduction can reduce the required power in cruise by up to 11%, which also translates into a fuel flow reduction potential of similar magnitude. Flight tests on Airbus Helicopter's Bluecopter Demonstrator confirmed this fuel flow reduction potential for the developed modifications.

Zusammenfassung

Diese Arbeit beschäftigt sich mit der Verbesserung der aerodynamischen Auslegung von leichten, zweimotorigen Transporthubschraubern. Die Zielsetzung dabei ist, die dynamische Produktivität zu steigern um übergeordnete Anforderungen nach Verbrauchs- und Emissionseinsparungen zu erfüllen. Voruntersuchungen haben gezeigt, dass ein aussichtsreicher Ansatz zur Effizienzsteigerung die Reduktion des parasitären Widerstands bietet. Die primären Widerstandsquellen leichter Transporthubschrauber stellen der Rumpf, das Landewerk und der Rotorkopf dar. Daher ist das Ziel dieser Arbeit, den aerodynamische Entwurf dieser Komponenten zu verbessern.
Die aerodynamische Optimierung folgt einem klaren, schrittweisen Ansatz. Zunächst wird die Referenzkonfiguration untersucht. Anhand dieser Daten wird dann die Tauglichkeit der Entwurfsverbesserungen bewertet. Die Referenzkonfiguration stellt eine aktuelle Serienmaschine eines leichten Transporthubschraubers dar, welcher eine stumpfe Hecksektion, ein Kufenlandewerk und einen lagerlosen 5-Blatt-Rotorkopf besitzt. Die aerodynamischen Eigenschaften der Referenzkonfiguration und der eingebrachten Veränderungen werden mit Hilfe umfangreicher Windkanalmessungen und ergänzenden Strömungssimulationen bewertet.
Die durchgeführten Versuche beinhalten die Messung von Kräften und Momenten, Oberflächendrücken und Geschwindigkeitsfelder im Nachlauf. Die Strömungsimulationen basieren auf den instationären Reynolds-gemittelten Navier-Stokes- Gleichungen in Verbindung mit einem Reynoldsspannungsmodell zur Turbulenzmodellierung.
Die Hauptwiderstandsanteile der Referenzkonfiguration wurden ermittelt zu 23% am Rumpf, zu 21% am Landewerk und zu 26% am Rotorkopf. In Folge dessen, werden aerodynamische Verkleidungen für das Landewerk und passive strömungsbeeinflussende Maßnahmen am Rumpf zur Effizienzsteigerung in Betracht gezogen. Die Optimierungsaufgabe lautet dabei den Widerstand zu reduzieren, ohne den Abtrieb substanziell zu erhöhen.
In Summe konnte der Widerstand durch diese Maßnahmen um 22% reduziert werden. Das äquivalente Gewichtshandikap im Reiseflug infolge des erhöhten Abtriebs ließ sich dabei auf unter 80 kg beschränken. Die erzielte Widerstandsreduktion setzt sich im Reiseflug in einen um 11% reduzierten Leistungsbedarf um. Dementsprechend ist eine Steigerung der Treibstoffeffizienz gleicher Größenordnung zu erwarten. Flugversuche mit dem Bluecopter Demonstrator seitens Airbus Helicopters bestätigten dieses Potential zur Verbrauchsminderung.

Contents

List of Figures

List of Tables

Nomenclature

Symbols

Symbol	Unit	Description
A_{ref}	m^2	reference area
a	-	quadratic pre-factor for parabolic least-square-fit
b_f	m	fuselage width
b_f	m	skid-landing-gear width
C_D	-	drag coefficient
C_L	-	lift coefficient
C_l	-	rolling moment coefficient
C_m	-	pitching moment coefficient
C_n	-	yawing moment coefficient
c_p	-	pressure coefficient
C_Y	-	side force coefficient
D_{rh}	m	rotor head diameter
D/q	m^2	equivalent flat plate area
F_x, F_y, F_z	N	aerodynamic forces (aerodynamic coordinate system)
h_{total}	m	total vehicle height
h_f	m	fuselage height
h_m	m	model height
l_{edge}	m	maximum size of the surface mesh elements
l_{ref}	m	reference length
l_{total}	m	total vehicle length
l_f	m	fuselage lenght
l_m	m	model length
l_r	m	rear tapering length
$M_{x'}$, $M_{y'}$, $M_{z'}$	Nm	aerodynamic moments (model-fixed coordinate system)
Ma	-	Mach number
p_∞	Pa	ambient pressure
P_i	W	induced power requirements
P_o	W	profile power requirements
P_p	W	parasite power requirements
P_{TOT}	W	total power requirements
P_{TR}	W	tail rotor power requirements
Re	-	Reynolds number
T_∞	K	ambient temperature
Tu_{tot}	-	magnitude turbulence intensity

$Tu_X,\ Tu_Y,\ Tu_Z$	-	turbulence intensity in test section coordinates
U_∞	m/s	freestream velocity
$u,\ v,\ w$	m/s	time-averaged velocity components in aerodynamic coordinate system
$X,\ Y,\ Z$	m	test section coordinates
$x,\ y,\ z$	m	aerodynamic coordinates
$x',\ y',\ z'$	m	model-fixed coordinates
y^+	-	non-dimensional wall distance
α	deg	angle of attack
β	deg	angle of sideslip
δ_{99}	m	boundary-layer height
Δz_{bow}	m	eccentricity bow
Δz_{stern}	m	eccentricity stern
Θ	deg	blade pitch angle
Θ_0	deg	collective blade pitch angle
Θ_S	deg	lateral cyclic blade pitch angle
Θ_C	deg	longitudinal cyclic blade pitch angle
μ	-	advance ratio
μ_t/μ	-	eddy viscosity ratio
ν	m^2/s	kinematic viscosity
ρ	kg/m^3	freestream density
Ψ	deg	azimuth angle
ψ	-	humidity
χ	deg	wake skew angle
ω_x	1/s	axial vorticity

Subscripts

Symbol	**Description**
b	back flow
exp	value obtained by experiment
f	fuselage coordinate center
i	incoming flow
m	model coordinate center
max	maximum value
min	minimum value
r	rear fuselage coordinate center
ref	reference configuration value
sim	value obtained by flow simulation
∞	freestream condition

Superscripts

Symbol	Description
T	transposed
LS	skid-landing-gear domain
-	arithmetic mean

Abbreveations

Acronym	Description
ACARE	Advisory Council for Aviation Research and Innovation in Europe
AL	attachment line
AoA	angle of attack
AoS	angle of sideslip
C	characteristic streamline
CAD	computer aided design
CCD	charged-coupled-device
CFRP	carbon reinforced polymer
CNC	computerised numerical control
CSV	corner separation vortex
CV	cavity vortex
EARSM	Explicit Algebraic Reynolds Stress Model
EV	exhaust vortex
F_A	attachment focus
F_S	separation focus
FR	flow region
FVM	finite-volume-method
HEMS	Helicopter-Emergency-Medical-Services
LoI	line of inflection
LV	landing-gear vortex
MTOW	Maximum Take-Off Weight
MV	mast fairing vortex
N_A	attachment nodus
Nd:YAG	neodym-doped yttrium aluminium garnet
N_S	separation nodus
OPEC	Organization of the Petroleum Exporting Countries
POM	polyoxymethylene
RSM	Reynolds stress model
RZ	recirculation zone
SAR	Search and Rescue
SL	separation line
S_S	separation saddle point

SV	separation vortex
TEL	Twin-Engine-Light
TEM	Twin-Engine-Medium
TUM-AER	Technische Universität München, Chair of Aerodynamics and Fluid Mechanics
(U)RANS	(Unsteady) Reynolds Averaged Navier Stokes
UV	upsweep vortex
VGV	vortex generator vortex
VTOL	Vertical Take-Off and Landing
W/T	wind tunnel
WR	wake region
WTA	wind tunnel A
2D2C	two-dimensional two-component
2D3C	two-dimensional three-component

1 Introduction

The aeronautical industry faces the same challenges as any other industry today. The main challenges are global competition, technological progress, recruitment of skilled work force and securing investment funding. An important factor to be able to compete on the market is the reduction of costs for the customer while maintaining, or even increasing, the quality and performance of products. In the aeronautical industry, this essential business quest can be achieved by technological progress and to some extent by improved logistic processes. Achieving these goals requires, especially in high-tech industries, highly specialised work force and after all significant research and development budgets. Thus, the key challenge of global competitiveness is linked to all the other main challenges.
A typical indicator for the quality of air transport solutions is dynamic productivity. Dynamic productivity is defined by

$$\frac{payload \cdot range \cdot speed}{costs}. \tag{1.1}$$

Two important technological challenges are associated to this parameter. The first challenge is improving performance. The second challenge is reducing the operational costs. For aircraft the aerodynamic performance of the vehicle is essential for reducing costs, while increasing the payload range and speed. Other parameters which can improve the aircraft's dynamic productivity are for example the empty weight, the lifecycle costs and the engine efficiency. During the recent decades the fuel prizes have become more and more volatile; see Fig. 1.1. Thus, the operational costs associated to an aircraft's fuel consumption are exposed to the risk of unpredictable market behaviour. Therefore, improving the aerodynamic efficiency is impacting also considerably on the denominator of the dynamic productivities equation; see Eq. 1.1.

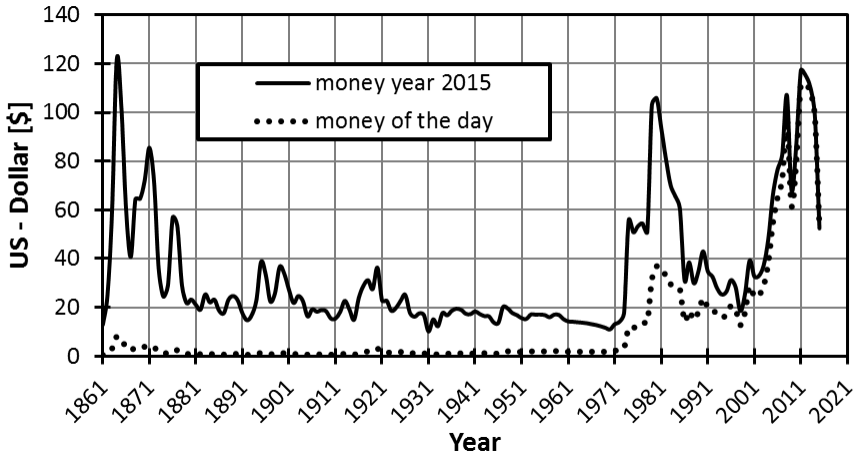

Figure 1.1: *Crued oil prices expressed in USD of the day and USD deflated for 2015 value [50]*

Beside these essential requirements other aspects become relevant as well. That is the social and ecological impact a company and its products evokes. The motivation for this development are declining natural resources, society's increasing awareness for the environment, increased legal standards and competition in the industry. According to the Advisory Council for Aviation Research and Innovation in Europe's (ACARE) vision *Flightpath 2050* the challenges associated to this developement in the aeronautical industry are to

- reduce CO_2 emissions by 75%
- reduce NO_x emissions by 90%
- reduce perceived aircraft noise by 65%
- reduce the environmental impact of the products life-cycle.

However, these aspects are not only relevant for the social and ecological impact. In fact, the basic business quests are well in line with these requirements. In this work, improving helicopter's dynamic productivity is the main objective in order to obtain a competitive design for the next generation of helicopter. In the following sections, the motivation for the chosen optimisation is given, the state of research is documented and the contribution of this work is summarised.

1.1 Motivation

Fixed wing aircraft are generally more fuel efficient, provide longer range at higher speed and lower noise levels than rotorcraft. Nevertheless, rotorcraft still provide important services to the society; see also Grawunder et al. [17]. First, rotorcraft feature Vertical Take-Off and Landing (VTOL) capabilities. Thus, they can operate in remote areas with minimal infrastructure or in airspace which is not accessible by other aircraft. Second, rotorcraft can provide excellent economy of time for specific missions, e.g. search and rescue (SAR) missions. Finally, rotorcraft are providing superior dynamic productivity compared against other modes of transportation for certain scenarios, e.g. crew exchange on oil platforms or inspection of offshore wind farms.
In order to reduce the environmental impact and costs of these services, it is necessary to reduce emissions and increase range, speed and fuel efficiency of rotorcraft. The described rotorcraft missions are generally performed by utility helicopters. Therefore, it is desirable raising the efficiency of this helicopter class. A substantial market share of the global helicopter fleet is associated to twin-engine-light (TEL) class utility helicopter. TEL utility helicopter typically feature two jet engine at a maximum takeoff weight (MTOW) of up to 4 tons. Based on the recorded flight hours for the global helicopter fleet from the year 2000, TEL class utility helicopter perform approximately 10% of the global helicopter fleet's flight hours. The TEL class helicopter are employed for helicopter-emergency-medical-services (HEMS), SAR missions, law enforcement, offshore supply (oil & gas, wind farms) and executive transport. Hence, raising the efficiency of the TEL-class will impact considerably on the fleets operational costs and its environmental footprint.
In order to identify viable approaches for increasing the efficiency of a helicopter, the breakdown of the total power requirements in cruise is instructive. Cruising, or fast forward level flight, is the prominent flight condition for all the stated TEL class missions. Stroub and Rabbott [39] showed that for a single-rotor design the total power requirements P_{TOT} for a helicopter in fast-forward level-flight are associated to the induced power P_i, the profile power P_o, the parasite power P_p and the tail rotor power P_{TR}; see Eq. 1.2.

$$P_{TOT} = P_i + P_o + P_p + P_{TR} \tag{1.2}$$

Stroub and Rabbott [39] identified the total power fraction for each of these contribution for helicopters featuring 1.4 and 4.5 metric tons MTOW in level-flight at 185 km/h; see Tab. 1.1.

MTOW	P_i	P_o	P_p	P_{TR}
1.4 metric tons	11%	29%	55%	5%
4.5 metric tons	21%	33%	41%	5%

Table 1.1: *Power breakdown in percentage of the total power required for helicopters with 1.4 and 4.5 metric tons MTOW in level flight at 185 km/h, taken from Stroub and Rabbott [39].*

Based on the data provided by Stroub and Rabbott it becomes clear that the biggest single source for the power requirements in cruise within the TEL-class is the parasite power with about 50%. The parasite power is defined as the power which is required to overcome the losses due to the parasite drag. This form of drag is defined as the force opposed to the direction of flight F_x, which is generated at the non-lifting components of an aircraft. Thus, reducing parasite drag is a viable approach for increasing TEL-class utility helicopter's efficiency and dynamic productivity.

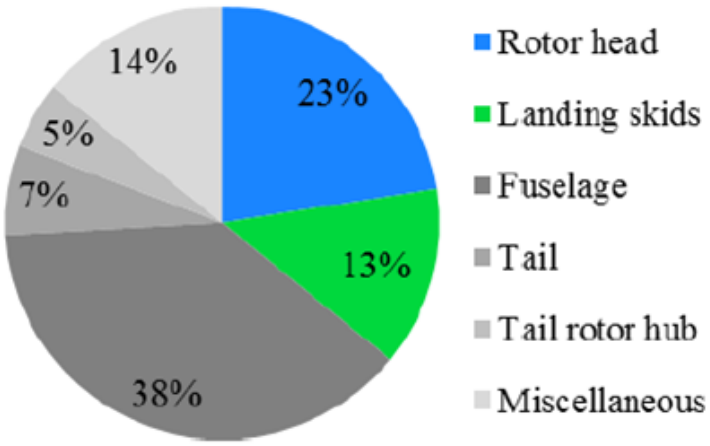

Figure 1.2: *Parasite drag breakdown for a TEL-class utility helicopter after Wagner [44].*

In order to assess the biggest contributors to the total parasite drag, the literature is revised for the parasite drag breakdown of a TEL-class helicopter. Wagner [44] presents data for a TEL-class helicopter dated from the 1970's; see Fig. 1.2. This analysis reveals that the three biggest contributors to the total parasite drag are the rotor head, the skid-landing-gear and the fuselage. Those components account for 74% of the total parasite drag.

$$P_p = F_x \cdot U_\infty = 1/2 \cdot \rho \cdot A_{ref} \cdot C_D \cdot U_\infty^3 \tag{1.3}$$

Eq. 1.3 presents the relationship between the parasite drag and the required power for overcoming this drag. Eq. 1.3 reveals a linear dependancy between a

reduction in parasite drag and a reduction of parasite power. This shows, that any percental reduction in parasite drag weighted with a factor of 0.5 transfers into the amount of achieved power reduction. Assuming that the fuel flow is also linearly dependant of the required power, the same statement is true for the fuel flow reduction. Thus, for TEL-class utility helicopter a 10 % reduction of parasite drag would result in a 5 % reduction of fuel flow in fast-forward level-flight.
In summary it becomes clear, that optimising aerodynamically the rotor head, the fuselage and the skid-landing-gear for minimal drag is a viable approach in order to achieve efficiency gains. Furthermore, this also impacts positively on the other design objectives range, speed, noise and costs. However, the aerodynamic down force of the optimised components should not increase significantly at the same time. Otherwise, compensating the additional downforce by the rotor's vertical thrust could deteriorate the achieved efficiency gains. In consequence the optimisation task for the presented work is reducing the parasite drag of the fuselage and the skid-landing-gear without significantly increasing the down force of these components. For this purpose modifications to the stated components are developed and their potential for increasing the aircrafts efficiency is evaluated through extensive wind tunnel (W/T) experiments and numerical simulations based on the Reynolds Averaged Navier Stokes (RANS) equation model. The rotor head is excluded from the optimisation task for the presented work. Nevertheless, a full-fairing for the rotor head and an optimised mast-fairing has been studied in the course of the ADHeRo[1] project; see Breitsamter et. al. [10]. The reference configuration for the optimisation represents a current production-type TEL-class utility helicopter, which features a bearingless main rotor system and a skid-landing-gear; see chapter 2. This helicopter defines the benchmark for this helicopter class and, therefore, is the best candidate for identifying further optimisation potential.

[1] Aerodynamic Design Optimisation of a Helicopter Fuselage including a Rotating Rotor Head (www.ADHeRo.de)

1.2 State of Research

The analysis of helicopter's parasite drag and the aerodynamic effects associated to it has seen two time periods of increased research and development efforts. The first time period has been the seventies and early eighties. The motivation at this time has been the oil crises of 1973 and 1979 caused by, respectively, the Organization of the Petroleum Exporting Countries (OPEC) embargo and the Iranian revolution; see Fig. 1.1. These crises hit the helicopter industry of the day with its comparatively fuel inefficient products particularly hard.

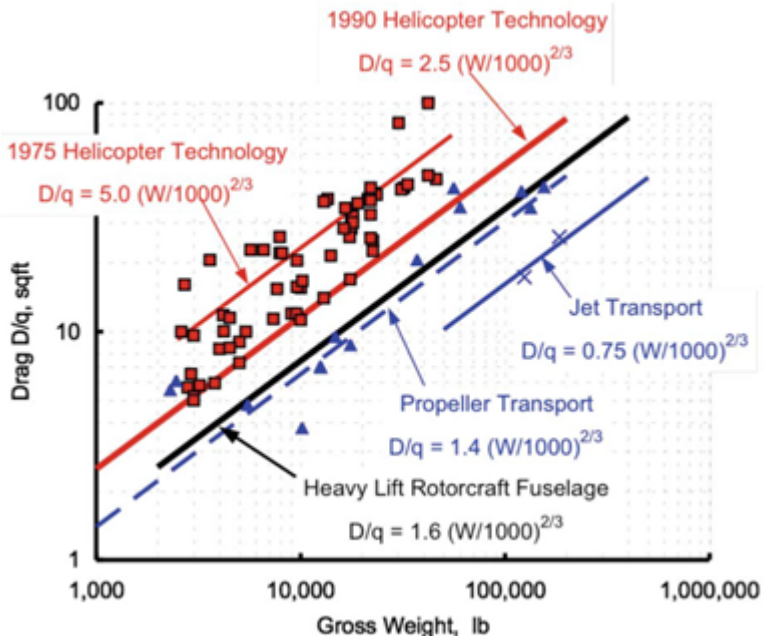

Figure 1.3: *Helicopter's parasite drag expressed in equivalent flat plate area (D/q) in dependence of the total gross weight for various machines [34].*

The effect of this first period of helicopter aerodynamic design optimisation becomes clear in Fig. 1.3. As can be seen, the drag area in dependance of the gross weight is cut in half between the global helicopter fleet from the year 1975 compared against 1990. Important work on transport helicopter drag analysis in this period has been contributed by various authors. The main objectives of their optimisation studies were an improved aerodynamic shape of the fuselage nose, the canopy/ramp corner, the fuselage cross-section, aft-body contraction and camber shape. Furthermore, the application of passive flow control devices and modifications for the skid-landing-gear have been considered. In addition, the importance of parasite drag reduction is also investigated from a system point of view.
Keys and Wiesner [21] published one of the most comprehensive drag analyses for utility helicopter. They consider important aspects for an optimum fuselage design of a utility helicopter, such as the shape of the nose section, the canopy corners, the cross section and the aft-body. Venegoni [40] presents an analysis of different fuselage shapes with respect to the nose and aft-body geometry. Polz [31] investigates different aft-body geometries. He considers a spherical aft-body,

a shortened and an extended aft-body. Seddon [36] investigates the application of passive flow control devices at ramp-type rear fuselage geometries. He consideres strakes, deflectors and rounded ramp edges. Wagner [44] presents a review of the parasite drag prediction by different means; e.g. flight test, full-scale and small-scale wind tunnel tests. He points out, that small-scale wind tunnel tests are an effective means for studying the global forces acting on the non-rotating parts, but that reference data is required - ideally in the form of flight test data. Williams [47] summarises the origin of parasite drag sources and provides design guidelines for reducing helicopter's parasite drag level. Duhan [13] proposes an approach for determining how much weight and how much money it is worth to spend on drag reduction efforts. Whereas, Gormont [16] discusses the tradeoff to be made when designing low drag helicopter. Thus, how to balance increased range, speed, payload and productivity against increased development, operating and maintenance costs.

After the early eighties it became silent for a while with respect to the research and development efforts spend on the parasite drag reduction of utility helicopter. The reason for this is associated to the development of the oil prices during the late eighties and the nineties. In this period, almost the price level prior to the seventies oil crises is achieved when the inflation corrected values are considered; see Fig. 1.1. In the early years of the twenty-first century, the oil prices again began sky rocketing and consequently more effort is spent on further reducing utility helicopter's parasite drag during this period. Additionally, an increased societal awareness about polluting the environment triggered the implementation of new regulations, which made fuel efficiency even more important for competing on the global market.

During the last 15 years, the same drag reduction concepts are followed as during the seventies and early eighties. However, the tools, techniques and available materials have meanwhile progressed considerably. Especially, the available computer resources of the day allow expensive numerical analyses. In consequence most of the aerodynamic optimisations are performed by a combined approach of simulations, experiments and ultimately flight test. In addition to the passive flow control devices, also active flow control is considered in the recent investigation in order to reduce the utility helicopter's parasite drag. Furthermore, the available computer power allows for automatic design optimization.

A large effort has been made during the last decade to investigate detailed utility helicopter fuselages and their appendages by both experiment and simulation. The work focussing on idealised geometries, like the ROBIN [15] configuration, are not presented here.

In Europe, the GOAHEAD platform, based on the NH90 heavy transport helicopter, has been an important test base during the last decade. This configuration features the characteristic ramp-type rear fuselage geometry for this type of helicopter. Thus, it is suitable to test the numerical schemes for their ability to predict the flow separation occurring at the ramp as well as means to mitigate this separation. Several authors have contributed to the analysis of this configuration and also proposed drag reducing modifications.

Boelens et al. [6] consolidate the results of the blind-test activity for the GOAHEAD program. They showed that common RANS solver employed in the European Union are capable of predicting most of the phenomena well. This includes the breakdown of aerodynamic forces, the surface pressure distribution and the main and tail rotor wake for different flow conditions. Khmer [23] investigates means to reduce drag associated to the rotor head and fuselage aerodynamic interference for the GOAHEAD configuration. Renaud et al. [33] provide a detailed drag breakdown of the GOAHEAD fuselage and hub based on numerical simulation. Boniface [7] developed a simulation strategy for investigating the impact of vortex generator on the GOAHEAD ramp flow. The sponson shape and position are optimised by Wentrup [45] through automatic design optimisation.
Active flow control is also considered for parasite drag reduction. Le Pape et al. [30] present results for ONERA's generic fuselage ASF2. For this generic utility helicopter geometry they obtained active flow control on a wind tunnel model by steady blowing, unsteady blowing, and zero-net-mass-flux blowing. In a previous study by Lienard et al. [28] the effect of active flow control on the ASF2 are investigated also numerically and the results are validated by experimental data.
Khier [22] investigates the impact of the skid-landing-gear on the flow field and aerodynamic forces of a TEL-class utility helicopter dated from the seventies. He compares simulation data against wind tunnel data. However, both the wind tunnel model and numerical model feature a model support attached to the ventral side of the fuselage. Vogel et al. [42] showed that this significantly impacts on the aft-body flow topology and, thus, affects the validity of the results for the actual helicopter. For this reason Vogel et. al. introduced a new tailboom model support, which is also used for the results presented in this work.
Batrakov et al. [3],[4] investigate the Kasan Ansat's (TEL-class utility helicopter) fuselage drag and suggest improved aft-body shapes for reduced parasite drag. They perform both wind tunnel experiments and numerical simulations for this purpose. Vogel [43] investigates the aerodynamic characteristics of a production type TEL-class and twin-engine-medium class utility helicopter by numerical simulation and experiments. The model includes the fuselage, tailboom, empennage and rotor head.

1.3 Contribution of this work

The performed aerodynamic analyses in this work are based on the experiments conducted during the course of the ADHeRo project. This includes aerodynamic forces and moments, surface pressure and wake velocity fields measurements for a variety of TEL-class utility helicopter model configurations. In total more than 50 wind tunnel model configurations are tested during more than 240 single measurement runs. Thus, a detailed data base about the aerodynamic characteristics of current production type as well as optimised low drag TEL-class utility helicopter is provided. For the experiments, a new wind tunnel model is designed, which features a high level of geometric details. In order to obtain viable results, the model scale is selected as large as possible. This is achieved through a newly developed design methodology, which assesses the impact of the selected model scale on all relevant requirements and limitations of the experimental setup. This includes both structural as well as aerodynamic considerations.
In addition to the experiments, selected configurations are investigated by RANS simulations in order to gain further insight into local flow phenomena. For this work a selection of five configurations are investigated by unsteady RANS simulations and six additional preliminary designs are assessed through steady RANS simulations.
Based on the combined experimental and numerical data sets a detailed understanding of the aerodynamic phenomena associated to the generation of parasite drag at TEL-class utility helicopter is obtained. Furthermore, specific design optimisations are introduced to mitigate the identified drag sources.
In order to assess the benefits of the optimised components, the baseline configuration is analysed first. In a second step, the gained knowledge about the drag sources of the reference configuration is employed for finding improved solution for the affected components. Finally, the selected optimisations are compared against the reference configuration and the associated benefits are discussed. In this work, the considered design optimisations include aerodynamic fairings for the skid-landing-gear and the application of passive flow control devices at the fuselage's aft-body.
In *Chapter 2 Model Design Process*, the reference configuration is presented and necessary design simplifications for the wind tunnel model are discussed. Furthermore, the chosen model segmentation is presented for achieving a high modularity in order to easily implement design modifications. The selected model support and its functionality is also outlined in this chapter. Based on these inputs, the design loop for achieving the maximum feasible model scale is presented. At the end of chapter 2, the final model design is detailed and a parametric definition of the model geometry is introduced.
Chapter 3 Experiments summarises all information about the experimental method. This includes the characteristics of the employed wind tunnel, the selected test conditions, and the specification for the applied measurements techniques.

The applied numerical method for the unsteady simulations is described in *Chapter 4 Numerical Method*. The setup for the steady simulations is outlined in the analysis chapter. The description of the numerical method includes the selected configurations, the description of the meshing strategy, the chosen meshing parameter, the specification of the flow solver, and the investigated test condition. The chapter is concluded by a validation study of the obtained numerical data against the corresponding experimental data.
The performed analyses of this work are divided into two chapters. The analysis of the baseline configuration is presented in *Chapter 5 Baseline Model*. The investigated design modifications are analysed in *Chapter 6 Design Modifications.* This chapter sub-divides into the section committed to the application of faired skid-landing-gear designs and the application of passive flow control devices. The analyses always commence with description of the considered sub-configurations and the selection of investigated design modifications where applicable. Then, the global aerodynamic forces are analysed with a special focus on the configurations drag and lift. In a next step, the observed global characteristics are connected to the local pressure distribution at the fuselage's aft-body. Finally, the observed effects are linked to the near-surface and wake-flow topology.
The manuscript concludes by a summary of the obtained insight into the aerodynamic phenomena as well as the achieved improvements, and an outlook on further optimisation potential is provided; see *Chapter 7 Conclusion and Outlook*.

2 Model Design Process

The real helicopter, which is to be reproduced through the ADHeRo W/T model, represents a characteristic state-of-the-art TEL-class utility helicopter; see Fig. 2.1. Its maximum take-off weight (MTOW) is about 3 metric tons. Utility helicopters are typically distinguished from other types of helicopters by a blunt rear fuselage geometry, in order to provide a rear loading capability. Thus, the investigated helicopter features a steep rear fuselage upsweep and a significant lateral tapering. Furthermore, the helicopter is characterised by the conventional skid-landing-gear made from circular tubes, a new five-bladed bearingless main-rotor (not depicted in Fig. 2.1) and the empennage including the horizontal stabilisers and the vertical fin with an integrated shrouded tail-rotor (Fenestron). This configuration represents the reference for all the proposed optimisations.

Figure 2.1: *Twin Engine Light Utility Helicopter - Production Model Type*

The derived design of the ADHeRo W/T model is primarily driven by the requirement of precise parasite drag force prediction. In order to achieve this, three aspects are essential. First of all, the relevant components of the actual helicopter geometry have to be reproduced precisely. Second, the aerodynamic interference of the model support and the model itself needs to be minimal. Third, in order to encounter as little low Reynolds number effects as possible, the model scale needs to be as large as possible. Based on these objectives, a clear step-wise approach has been developed for the design:

1. Define necessary design modifications, in order to obtain a feasible model for the W/T experiments without significantly affecting the validity of the experiments.
2. Specify the model segmentation, such that a functional model is obtained, which also allows for modifications through a high modularity.
3. Select the type of wind tunnel installation, such that the aerodynamic interference of the model support with the model is minimal.

4. Derive the W/T model scale, in order to obtain the maximum feasible model size.

This chapter structures accordingly and is concluded by a section about the final baseline model design.

2.1 Design Simplifications

In chapter 1 it was shown, that for TEL-class utility helicopter the main contributor to parasite drag are the fuselage, the skid-landing-gear and the rotor-head. Consequently, the ADHeRo W/T model is designed such that the aerodynamic characteristics of these components can be assessed as precisely as possible. The complexity of the model is adapted in order to obtain a feasible model for the experiments. The following simplifications are made:

- The primary air inlets and ejectors are closed with aerodynamic fairings.
- The tail boom is truncated in front of the empennage.
- Excrescences, such as antennas, rivets, etc. are not included.
- The series 4-bladed rotor is replaced by a newly designed 5-bladed rotor, which represents the state-of-the-art of current rotor design [5].
- The blades are truncated at the radially first aerodynamic-effective section of the blade. Thus, only the blade cuffs, the lead-lag damper and the flexbeams are retained.

By sealing the air inlets and the ejectors the engine mass flow is not modelled. The empennage, including the vertical stabiliser and the Fenestron, is neglected to be able to design the model at the largest possible scale; see section 2.4. The larger the final model scale is, the higher the Reynolds number becomes for the fuselage, the skid-landing-gear and the rotor-head. Thus, low Reynolds number effects are mitigated. This is essential for a as precise as possible prediction of their aerodynamic characteristics. For this purpose, it has to be accepted that the stability of the reference configuration and the investigated modifications cannot be evaluated by the performed experiments. The ability to investigate the aerodynamic interference of the fuselage, skid-landing-gear and rotor head wake with the empennage is also excluded because of this simplification. Most of the excrescences are neglected, since their effect on the flow cannot be adequately modelled within the desired model scale range of 1:5.5 to 1:4. Larger geometrical details of the fuselage are retained; i.e. the curved windows, attachment surfaces for additional equipment and the cavities housing the cross beams in the under body, the sliding-door joints and the contours of the ejectors. Truncating the blades and only retaining the structural components of the rotor head and the blade cuffs is a common simplification of experimental and also numerical helicopter drag analysis. Especially, when focussing on cruising flight conditions; i.e. fast-forward

level flight. Leishman [26] shows that this is an acceptable simplification for cruising flight, because for advance ratios $\mu \geq 0.25$ the aerodynamic interference of the rotor with the airframe becomes minimal. Only if μ exceeds 0.4, the increasing disturbances of the flow through the rotor plane by the fuselage can lead to substantial aerodynamic interference; see pp. 661 and 662 in [26]. The flight conditions investigated in this work correspond to $\mu \approx 0.35$. In this scenario, the rotor downwash sheds into the wake at an skew angle χ which is typically smaller than 4 *deg*; see Fig. 3.28, p. 160 in [26]. Since the empennage is neglected, the interference of the rotor wake with the airframe is confined to the upper deck for the investigated configuration. The experimental investigations of Le Pape et. al. [27] and the numerical investigations of Renaud et. al. [32] and d'Alascio et. el [1] show that even this interference is minimal. Hence, only retaining the rotor head has no substantial impact on the validity of the performed optimisation.

2.2 Model Segmentation

The geometrical basis for the design of the ADHeRo wind tunnel model in its baseline configuration is shown in Fig. 2.2. The fuselage is supposed to be composed of different replaceable shells. The associated segments of the computer aided design (CAD) loft are distinguished by different colours in Fig. 2.2a. The geometrical input for the model rotor head design is shown in Fig. 2.2b. It can be seen that even with the necessary simplifications, see section 2.1, a high level of geometrical detail is retained.

a)

b)

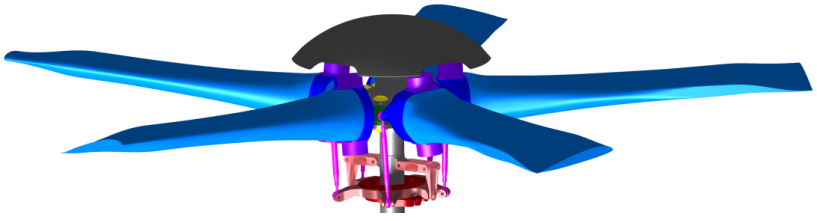

Figure 2.2: *Segmentation of the ADHeRo wind tunnel model in its baseline configuration. a) Fuselage and skid-landing-gear, b) rotor head. (For a improved visualisation, the scale of figure b) is increased compared against figure a).*

The baseline model is composed of (stated colours in accordance to Fig. 2.2a)

- the cabin front (orange), including the cockpit and the fuselage middle segment with curved windows (blue) and sliding-door joints (red) and the front part of the engine cowling
- the fuselage's ventral side (purple)
- the backdoor (bright green)
- the rear engine cowling (blue) with the closed ejectors (beige)
- the mast fairing (yellow)
- the tailboom junction (turquoise)
- the remaining tailboom segment up to the horizontal stabilizers (brown)
- the skid-landing-gear (dark green) consisting of the cross-beams, the steps, the skids and the fuselage attachments
- the rotor head including the rotor mast, the swash plate, the scissors, the control rods, the hub cap and the blade cuffs featuring the lead-lag dampers and the flexbeams.

This segmentation is selected such that the planned optimisations can be investigated without rebuilding a large portion of the outer shell. The design of the model rotor head also needs to provide the full kinematic complexity of the full-scale design. This includes the rotor head rotation at the same advance ratio and the collective and cyclic pitch motion of the blade cuffs as for the real helicopter.

2.3 Wind Tunnel Installation

There are different types of model-supports for positioning helicopter models inside a wind-tunnel test-section; e.g. the top, side, bottom, Prandtl-type and tailboom support. For the prediction of the models aerodynamic characteristics, most of these supports limit the accuracy by aerodynamic interference with the model flow. Vogel et. al. demonstrate this limitation for the analysis of the flow around an isolated fuselage [42]. They show that bottom and top supports significantly interfere with the model flow and substantially affect the aerodynamic loads and the flow topology. Therefore, they designed a new, fully faired, tailboom support for the application in wind tunnel A (WTA) at the Technische Universität München, Chair of Aerodynamics and Fluid Mechanics (TUM-AER); see section 3.3. For the experiments conducted throughout the course of the ADHeRo project, the model support developed by Vogel et. al. was used.; see Fig. 2.3

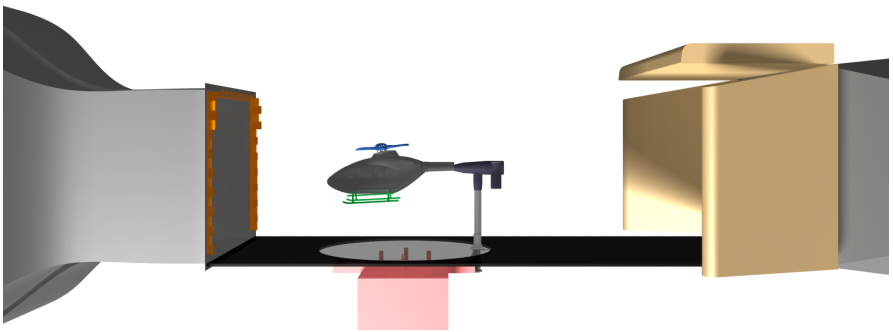

Figure 2.3: *Employed experimental setup for the ADHeRo experiments.*

For most experiments, various combinations of angle of attack α and angle of sideslip β are relevant. However, it is import to maintain optimal freestream conditions for all model attitudes. With the tailboom support by Vogel et. al., the model attitude is changed by rolling and yawing the model, thus, keeping the model in the test section centre; see section 3.3. This minimises wall effects and optimal freestream conditions are maintained.

2.4 Model Scale

The scale of the wind tunnel model needs to be as large as possible in order to avoid low Reynolds number effects. This is important for achieving good agreement between experimental data and the desired flight conditions of the real helicopter. Furthermore, the larger the model scale becomes, the more geometrical details become feasible to be modelled. For this purpose, a dedicated design loop is developed in order to find the maximum feasible model scale. The feasibility of the model scale is evaluated by controlling several quantitative parameter, which

are associated to the selected wind tunnel setup; see section 2.3. For this setup, the following parameters have to be assessed and compared against viable limits:

- the maximum wind tunnel blockage for the desired range of angle of attack AoA and angle of sideslip AoS
- the inertial and aerodynamic loads on the external wind tunnel balance
- the maximum elastostatic deformation of the tailboom support based on inertial and aerodynamic loads
- the required actuation torque for rolling the model
- the power needed for rotor head actuation.

The logic for the employed iterative design loop is presented in Fig. 2.4. The desired model range is in between 1:5.5 to 1:4. A critical parameter is the ratio of the models frontal area, including the support, with respect to the wind tunnel nozzle cross section; i.e. wind tunnel blockage. It is not feasible to exceed a 10 % blockage. This limit is only applicable for bodies similar to a utility helicopter at maximum angle of attack and angle of sideslip. The limit is based on a maximum allowed blockage effect for the employed experimental setup of 0.5% according to the method of Mercker and Wiedemann; see pp. 6/23 - 6/28 in [14]. The combined inertial and aerodynamic model loads are not allowed to exceed the limit loads of the external wind tunnel balance.

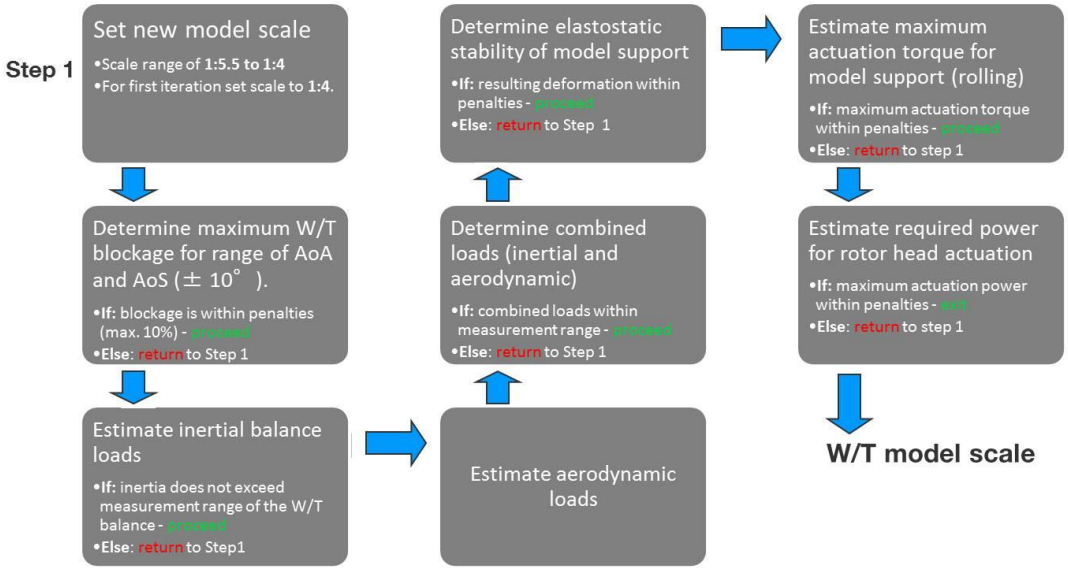

Figure 2.4: *Design loop for finding the maximum W/T model scale.*

The inertial loads were estimated based on the known tailboom support weight and an approximation of the model weight. The model weight is approximated by scaling weights of previous helicopter models accordingly to the surface or the volume of the new model dimensions. The aerodynamic loads on the model are estimated based on the aerodynamic coefficients recorded by Vogel et. al. [41] for a Twin-Engine-Medium (TEM) class utility helicopter. The elastostatic stability of the support was investigated by estimating the maximum deflection

of the model nose based on beam bending theory. The required actuation torque for rolling the model is determined by approximating the mass moment of inertia and the aerodynamic torque acting on the rolling actuation. The mass moment of inertia are assessed by abstracting the complex model geometry to basic bodies; e.g. cylinder shells. The choice of these basic bodies is such that a conservative estimation of mass moments of inertia is derived. The mass of each component is based on the performed approximation of the models weight. The required power for maintaining the rotor head rotation is estimated by assessing the drag of the blade cuffs. This assumes that the power required to actuate the kinematics of the rotor head is comparatively small. The drag at the blade cuffs is estimated by the drag generated at cylinders of similar dimension rotating around their transverse axis. This design loop could be successfully terminated for the final model scale of 1:5.

2.5 Model Design

Based on the preliminary steps of the design process the actual 1:5 scaled baseline CAD model is obtained; see Fig. 2.5. The model consists of the internal load bearing structure (frame and tailboom sting) and the geometrical components. According to the segmentation defined in section 2.2, the fuselage is composed of 7 different components. The skid-landing-gear is attached directly to the fuselage's ventral side. The rotor head is attached to the frame. Alternatively, the skid-landing-gear and the rotor head can be attached to the internal six-component strain-gauge balance through special mounts, see section 3.3.

Figure 2.5: *CAD baseline model design.*

In accordance to the CAD model the actual wind tunnel model is manufactured. The fuselage components, the skid-landing-gear and the tailboom-model support are depicted in Fig. 2.6. The fuselage shells are made from carbon reinforced polymer (CFRP). A precise representation of the CAD geometry is assured by laminating the shells into high-density polyurethane foam negative moulds, which

are machined by computerised numerical control (CNC) milling. The window elements and the tailboom junction, on the other hand, are directly machined by CNC milling from polyoxymethylene (POM). The mast fairing is CNC milled from a high-density polyurethane foam.

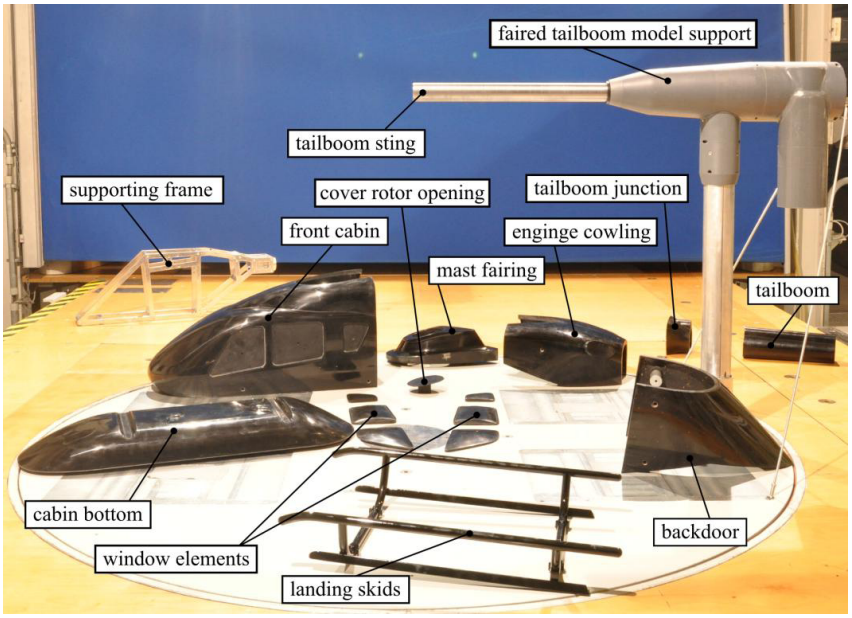

Figure 2.6: *Fuselage components, internal frame and the model support arranged in the test section of WTA*

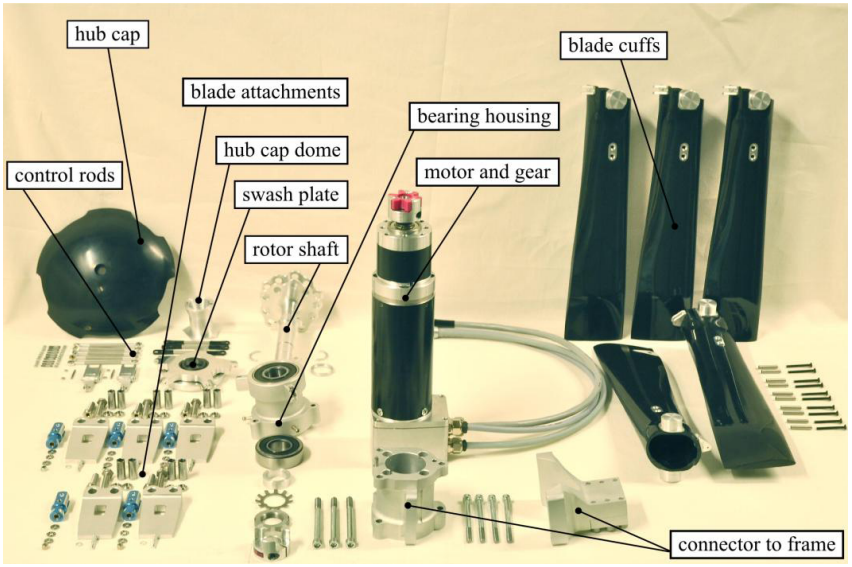

Figure 2.7: *Rotor head components, motor and gear.*

The landing-gear's skids and cross-beams are made of cylindrical brass tubes. The step, the skid's hemispherical end-caps and the fuselage attachment elements are CNC milled out of aluminium alloy. The supporting frame consist of two side plates, which are connected by multiple cross-bars and the connector to the tailboom sting. The side plates are laser-cut out of sheets of aluminium alloy, whereas the cross-bars and the connector are CNC milled out of aluminium alloy. The rotor head components are depicted in Fig. 2.7. The CAD-model geometry is precisely reproduced for all components exposed to the flow. The model rotor head also provides collective and cyclic pitch control of the blade cuffs with the fully functional swash blade. Most of the components are CNC milled from aluminium alloy. The blade cuffs are made from CFRP laminated into negative moulds, which are CNC milled out of an aluminium alloy. The hub cap is lathe machined from POM.
The assembled baseline model attached to the tailboom support is shown in Fig. 2.8. The entire model has a polished black surface. For the CFRP components, this is achieved by a black gel-coat, whereas the high-density polyurethane foam components are painted with a black two-component paint. The POM components remain uncoated, since they are made out of black-dyed material.

Figure 2.8: *Complete baseline model installed on the tailboom model support in the test section of WTA.*

The main dimensions of the reference geometry and the simplified model geometry are presented in Fig. 2.9. Based on the definition introduced by Vogel [43], the actual values of the model dimensions and geometrical parameter are presented in Tab. 2.1 in there non-dimensional form.

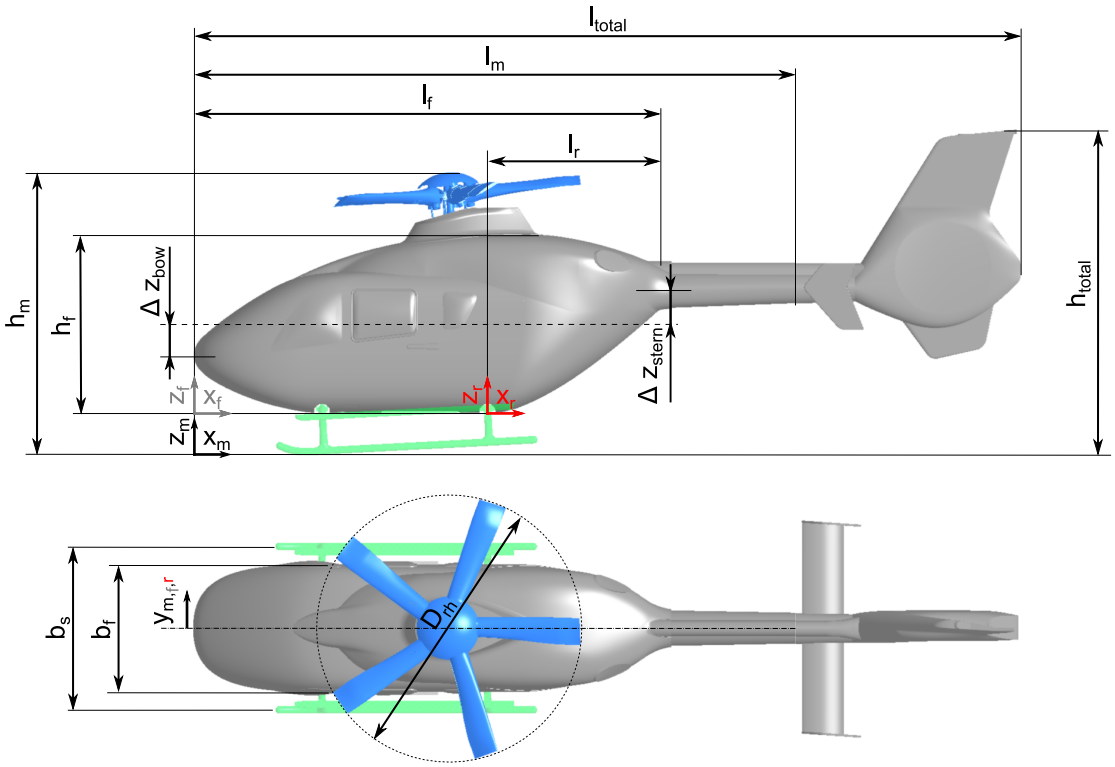

Figure 2.9: *The model dimensions and coordinate systems.*

Reference parameter		
Reference area	A_{ref}	(confid.)
Reference length	l_{ref}	$\sqrt{A_{ref}}$
Dimensions		
Total length	l_{total}/l_{ref}	5.5
Total height	h_{total}/l_{ref}	2.15
Fuselage length	l_f/l_{ref}	3.11
Fuselage width	b_f/l_{ref}	0.84
Fuselage height	h_f/l_{ref}	1.18
Model length	l_m/l_{ref}	3.99
Model height	h_m/l_{ref}	1.87
Skid-landing-gear width	b_f/l_{ref}	1.08
Rear tapering length	l_r/l_{ref}	1.15
Rotor head diameter	D_{rh}/l_{ref}	1.74
Shape Parameter		
Eccentricity bow	$\Delta z_{bow}/l_{ref}$	0.21
Eccentricity stern	$\Delta z_{stern}/l_{ref}$	0.22

Table 2.1: *Parametric definition of the ADHeRo model's reference parameter, dimensions and shape parameter.*

3 Experiments

In this chapter, the employed experimental methodology for this work is detailed. This includes the description of the wind tunnel facility and its freestream characteristics; see *section 3.1 Wind tunnel*. The test conditions at which the experiments are performed are described in *section 3.2 Test Conditions*. This includes both the freestream conditions and the trim condition for the experiments including the rotating rotor head. Finally, the applied measurement techniques are presented. In *section 3.3 Aerodynamic Force and Moment Measurements* the setup for measurements with the external and internal balance is presented and the performed post-processing for obtaining the force and moment coefficients is outlined. The approach for recording the surface pressure data is presented in *section 3.4 Surface Pressure Measurements*. This includes the specifications of the employed pressure sensors, the distribution of the pressure probing locations and the associated post-processing of the acquired data. In the last *section 3.5 Wake Velocity Measurements* the Particle Image Velocimetry system for recording velocity fields in the model's wake is detailed.

3.1 Wind Tunnel

All experiments are conducted in the wind-tunnel A (WTA) at TUM-AER. This wind-tunnel is of closed-return type, and can be operated in open or closed test-section mode. Breitsamter performed a detailed certification of the wind tunnel's characteristics [8]. For the ADHeRo project, the WTA is always operated in the open mode, thus, only the freestream characteristics for this operational mode are provided. The location within WTA's test section is defined by the test sections coordinate system (X, Y, Z). Its longitudinal axis X is normal to the nozzle exit plane and points towards the collector. The origin of the test sections coordinate system is located 1.5 m from the centre of the nozzle exit plane into the test section along the X-axis. Its vertical axis Z is pointing upwards and the lateral axis Y is normal to X and Z, such that a right-hand coordinate system is obtained; see Fig. 3.1.

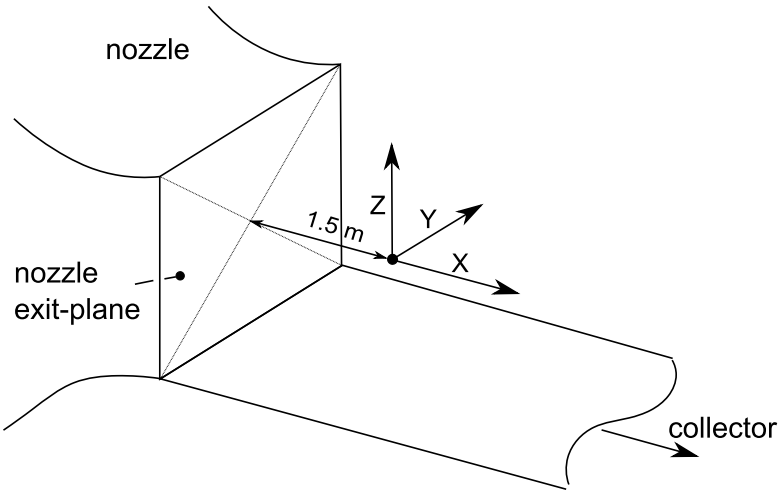

Figure 3.1: *Test section coordinate system for WTA.*

At $X = 0\ m$ and $Y, Z = 0\ m$, Tu_{tot} is always lower than 0.5% for the entire range of free- stream velocities $U_\infty \leq 65\ m/s$. For freestream velocities in excess of $20\ m/s$, the turbulence intensities in all three directions in space (Tu_X, Tu_Y, Tu_Z) also never exceed this limit. At $X = 0\ m$, $Tu_X, Tu_Y, Tu_Z < 0.5\%$ is maintained within the core flow region ($-0.90\ m < Y < 0.90\ m$ and $-0.85\ m < Z < 0.60\ m$). The variation of the static pressure along the X-axis $(Y, Z = 0)$ is lower than 0.5% of the dynamic pressure at the nozzle exit q_∞. The dynamic pressure q_∞ is assessed by recording the pressure difference between the settling chamber and the nozzle exit; i.e. the nozzle method. For $U_\infty > 20\ m/s$, the temporal deviation of the freestream velocity ΔU_∞ is confined to $\pm 0.67\%$ of U_∞. The spatial deviation of the freestream velocity within the freestream core region is confined to $\Delta U_\infty \leq \pm 1\%$ of U_∞. The deviation of the flow angle in the XZ-plane and the XY-plane, respectively, $\Delta\alpha$ and $\Delta\beta$ are lower than $\pm 0.2\ deg$. With the employed tailboom support, the ADHeRo model is always maintained inside the core flow region; see Fig. 3.2. Thus, optimal freestream conditions are assured for the experiments in WTA.

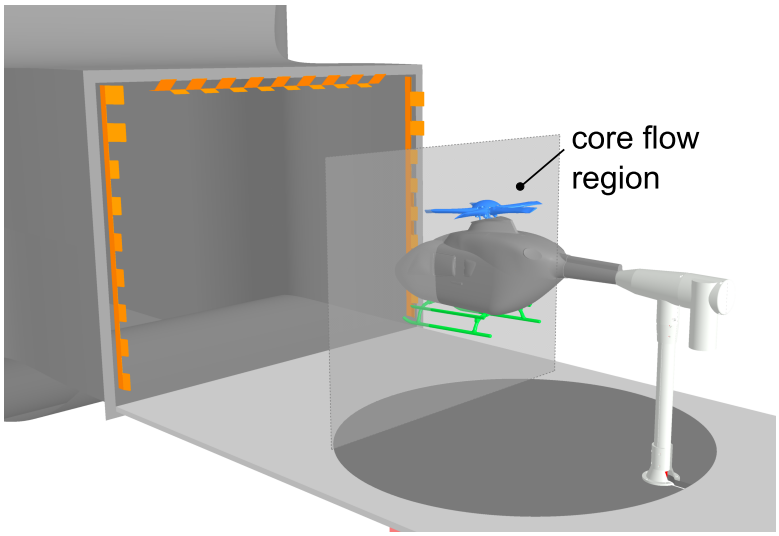

Figure 3.2: *CAD model of the ADHeRo setup and the test-section of WTA with its core flow region.*

3.2 Test conditions

The test conditions for the performed experiments are characterised by the freestream conditions and the performed sweeps over angles of attack and angles of sideslip; i.e. polars. In total, seven freestream conditions and four different polars are considered. The different freestream conditions are characterised by varying freestream velocities. This variation is necessary in order to investigate if substantial Reynolds number effects occur and which freestream velocity is sufficient to minimise those effects, see section 5.1. Based on this analysis, the standard freestream velocity is defined to be 40 m/s. For each experiment, the wind tunnel's power is set such that the test condition's nominal freestream velocity is achieved. This tuning depends both on the ambient conditions and the model's blockage. The model's blockage changes with angle of attack and angle of sideslip. Since the performed optimisation focuses on forward level flight, the wind tunnel power is always set for $\alpha, \beta = 0\ deg$. The mean ambient conditions for the performed experiments at the standard test condition 'd' are $p_\infty = 9.62 \cdot 10^4\ Pa$, $T_\infty = 290\ K$ and $\varphi = 50\%$. This corresponds to mean freestream values for the density of $\rho_\infty = 1.15\ kg/m^3$ and the kinematic viscosity of $\nu_\infty = 1.56 \cdot 10^{-5}\ m^2/s$. Tab. 3.1 summarises the considered test conditions. For the standard test condition 'd', the variations over all measurements in consequence of changes in ambient conditions and the model's blockage are stated as well.

Condition	U_∞ $[m/s]$	Ma_∞ $[-]$	Re_∞ $[mio.]$
a	25	0.07	0.59
b	30	0.09	0.71
c	35	0.10	0.83
d	$40^{\pm 1}$	$0.12^{\pm 0.004}$	$0.95^{\pm 0.07}$
e	45	0.13	1.07
f	50	0.15	1.19
g	55	0.16	1.31

Table 3.1: *Freestream conditions for the ADHeRo experiments. Variations over all experiments are stated for the standard test condition 'd'.*

The different polars employed during the ADHeRo experiments are presented in Tab. 3.2. Polars of different resolution in α and β are considered. The largest polar, featuring 121 polar points, is the mixed α and β polar $A1B1$. All the other polars are subsets of this polar. Thus, it is possible to compare the results of matching fuselage attitudes against each other even when different polars are employed. Polar A1B1 is the standard polar for forces and moments measurements. However, smaller polars are also considered for the forces and moments measurements in order to identify isolated effects or for preliminary studies. The polar A2B2 is always used for the steady and unsteady surface pressure measurements. This confines the number of polar points to 25. The wake velocity measurements are conducted for the single polar point A0B0.

Polar	α $[deg]$	β $[deg]$	$\Delta\alpha$ $[deg]$	$\Delta\beta$ $[deg]$
A0B0	0	0	-	-
A1B1	$[-10; +10]$	$[-10; +10]$	2	2
A2B2	$[-10; +10]$	$[-10; +10]$	5	5
A2B0	$[-10; +10]$	0	5	-

Table 3.2: *Polars over angle of attack and angle of sideslip for the ADHeRo experiments.*

The trim condition for the rotating rotor head is derived from the real helicopter in fast-forward level flight at 0 *deg* angle of attack and angle of sideslip. The rotational speed of the model rotor head is set such that the advance ratio $\mu \approx 0.35$ at this flight condition of the real helicopter is preserved for the given wind tunnel freestream velocity. The trim condition with respect to collective and cyclic pitch is defined according to Eq. 3.1.

$$\Theta(\Psi) = \Theta_0 + \Theta_C \cdot cos(\Psi) + \Theta_S \cdot sin(\Psi) \tag{3.1}$$

The individual blade angle Θ is defined in dependence of the azimuth angle Ψ, the collective pitch angle Θ_0, the lateral cyclic pitch angle Θ_C and the longitudinal

cyclic pitch angle Θ_S. The azimuth angle $\Psi = 0$ *deg* refers to the state when the considered blade's axis is parallel to the fuselage's longitudinal axis pointing towards the tail.

3.3 Aerodynamic Force and Moment Measurements

Two different type of balances are employed to perform the aerodynamic force and moment measurements; an external under-floor and an internal balance. The external balance records the forces and moments acting on the entire W/T model installed on the faired tailboom support; see Fig. 3.3. Hence, providing the global aerodynamic loads. Fairing the tailboom support decouples the support itself from any aerodynamic loads. Thus, the dynamic calibration of the force and moment measurement with the external balance becomes obsolete. Furthermore, the support of the model through the tailboom reduces the aerodynamic interference of the support with the model to a minimum; see Vogel et al. [42]. This leads to a substantially less complex and more accurate experimental setup.

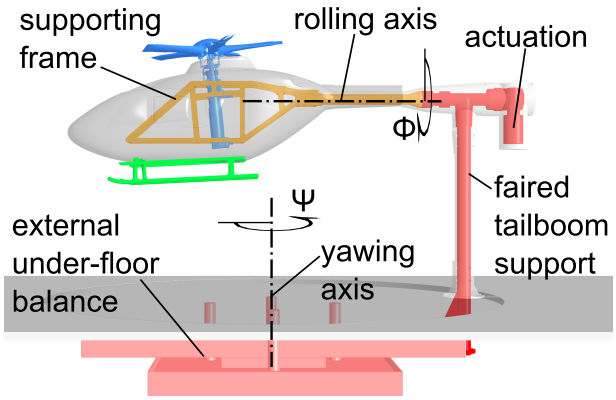

Figure 3.3: *Employed tailboom support for positioning the model and the external (under-floor) wind-tunnel balance.*

The variation of the model's angle of attack and angle of sideslip is transformed to a combination of roll (Φ) and yaw (Ψ) angles. The supports rolling and yawing axis are indicated in Fig. 3.3. The resulting model attitude during experiments with only $\alpha \neq 0$ *deg* and both $\alpha, \beta \neq 0$ *deg* is exemplified in Fig. 3.4 a) and b), respectively. The recorded force and moment polars are then transferred back to a representation of the model's attitude based on the angle of attack and angle of sideslip.

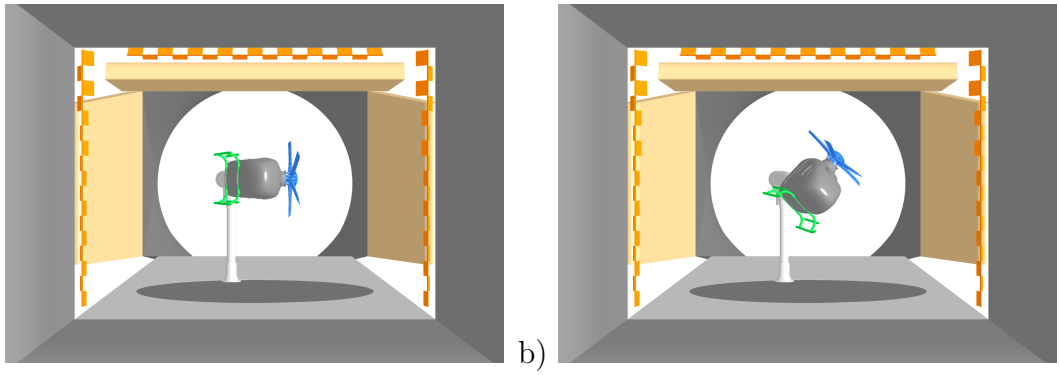

a) b)

Figure 3.4: *Positioning of the ADHeRo wind-tunnel model with the tailboom-support for a) $\alpha \neq 0deg, \beta = 0$ deg and b) $\alpha, \beta \neq 0$ deg. View: Downstream through the W/T nozzle.*

The internal balance is mounted inside the W/T model, such that only the loads acting on the W/T model's skid-landing-gear or the rotor head are recorded; see Fig. 3.5 a) and b). With this installation the loads on those components can be distinguished from interference effects. This would not be possible by only assessing the load increments between different configurations with and without the specific component.

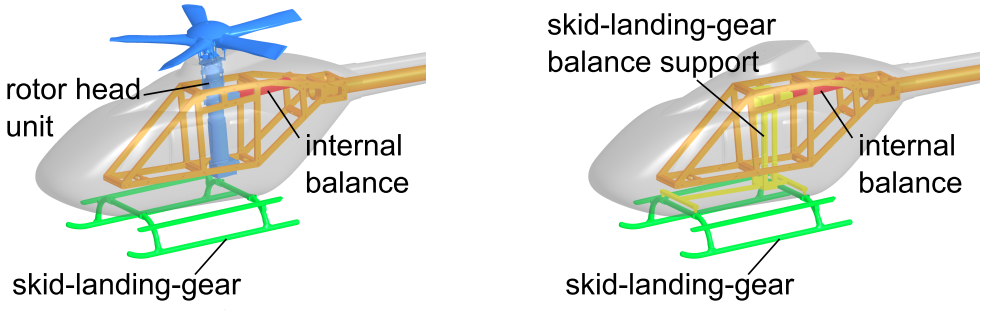

a) b)

Figure 3.5: *Application of the internal balance for seperately recording the loads acting on a) the rotor head and b) the skid-landing-gear.*

Both balances are six-component strain-gauge balances, which record the forces and moments in all three-directions in space. The forces recorded with both the balances are transferred to a common coordinate system aligned with the inflow; i.e. the aerodynamic coordinate system $(\vec{x}, \vec{y}, \vec{z})$. The moments are transferred to the model-fixed coordinate system $(\vec{x'}, \vec{y'}, \vec{z'})$. The origin of both coordinate systems is the location of the generic centre of gravity. This is obtained by transferring the relative location of the real helicopter's centre of gravity to the scaled model; see Fig. 3.6.

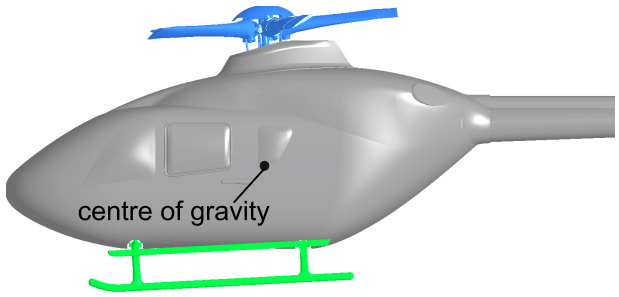

Figure 3.6: *Location of the generic centre of gravity for the ADHeRo W/T model.*

The model-fixed coordinate system is aligned with the model's main axis; i.e. the longitudinal axis, the lateral and the vertical axis. $\vec{x'}$ is parallel to the longitudinal axis pointing towards the bow, $\vec{z'}$ is parallel to the vertical axis pointing toward the fuselage bottom and $\vec{y'}$ is normal to both $\vec{x'}$ and $\vec{z'}$; see. Fig. 3.7 a). Thus, $(\vec{x'}, \vec{y'}, \vec{z'})$ defines a right-hand coordinate system. The x-axis of the aerodynamic coordinate system $(\vec{x}, \vec{y}, \vec{z})$ is always aligned parallel with the freestream direction. The z-axis lies within the model's symmetry plane and is normal to the x-axis, such that it is parallel to the models vertical axis for $\alpha, \beta = 0\ deg$. The y-axis is normal to $\vec{x}$ and $\vec{z}$, such that a right-hand coordinate system is obtained; see Fig. 3.7 b).

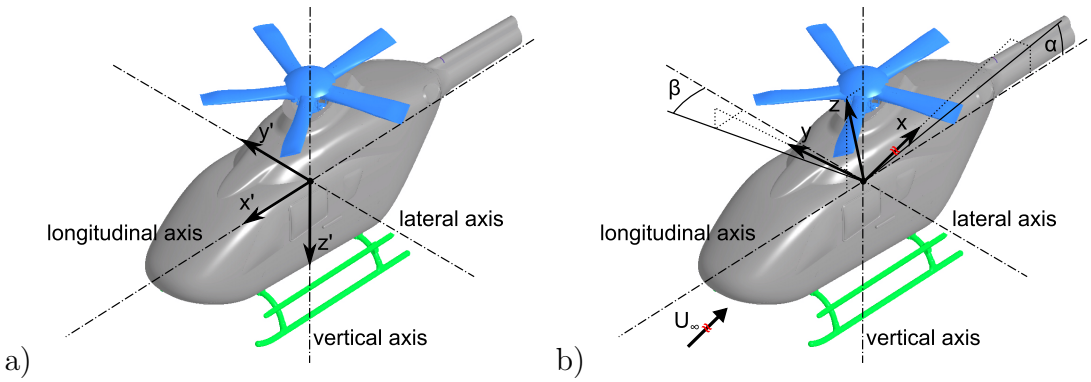

Figure 3.7: *Employed coordinate systems for the ADHeRo W/T model. a) model-fixed $(\vec{x'}, \vec{y'}, \vec{z'})$, b) aerodynamic $(\vec{x}, \vec{y}, \vec{z})$.*

The aerodynamic forces and moments vector with respect to the aerodynamic and model-fixed coordinate system are $(F_x\ F_y\ F_z)^T$ and $(M_{x'}\ M_{y'}\ M_{z'})^T$, respectively. In order to differentiate between the inertial and aerodynamic loads a static balance calibration is necessary. The static calibration is achieved by recording only the inertial model loads for the desired polar in a pre-run with the W/T inoperative. If the investigated configuration includes the rotor head, the rotor head remains fixed at $\theta = 0\ deg$. The inertial loads polar is then subtracted from the combined inertial and aerodynamic loads polar recorded at the desired free-stream conditions. This yields the aerodynamic loads $(F_x\ F_y\ F_z)^T$ and $(M_{x'}\ M_{y'}\ M_{z'})^T$. Only the temporal mean values are considered for the analysis. For this purpose the arithmetic mean of the forces $(\bar{F}_x\ \bar{F}_y\ \bar{F}_z)^T$ and moments $(\bar{M}_{x'}\ \bar{M}_{y'}\ \bar{M}_{z'})^T$ is assessed over the measurement time of 15 s. The aerodynamic coefficients are calculated based on these temporal mean values; see Eq. 3.2 - 3.7. Note that

in contradiction to the conventional definition of the aerodynamic coefficients the reference area A_{ref} is kept constant for all configurations. This methodology is desirable since it allows to directly compare the coefficients of different configurations without first assessing their variation in frontal area. A_{ref} is always identical to the frontal area of the baseline configuration, see section 2.5. The accuracy of the recorded force and moment coefficients is ±2.5% based on random error calculations.

$$C_D = \frac{\bar{F}_x}{\frac{1}{2} \cdot \rho_\infty \cdot U_\infty^2 \cdot A_{ref}} \tag{3.2}$$

$$C_Y = \frac{\bar{F}_y}{\frac{1}{2} \cdot \rho_\infty \cdot U_\infty^2 \cdot A_{ref}} \tag{3.3}$$

$$C_L = \frac{\bar{F}_z}{\frac{1}{2} \cdot \rho_\infty \cdot U_\infty^2 \cdot A_{ref}} \tag{3.4}$$

$$C_l = \frac{\bar{M}_{x'}}{\frac{1}{2} \cdot \rho_\infty \cdot U_\infty^2 \cdot A_{ref}^{\frac{3}{2}}} \tag{3.5}$$

$$C_m = \frac{\bar{M}_{y'}}{\frac{1}{2} \cdot \rho_\infty \cdot U_\infty^2 \cdot A_{ref}^{\frac{3}{2}}} \tag{3.6}$$

$$C_n = \frac{\bar{M}_{z'}}{\frac{1}{2} \cdot \rho_\infty \cdot U_\infty^2 \cdot A_{ref}^{\frac{3}{2}}} \tag{3.7}$$

3.4 Surface Pressure Measurements

For the surface pressure measurements, 218 pressure tabs are installed at the fuselage of the W/T model. Most of the pressure tabs are clustered in the aft-body region; see Fig. 3.8. In this region the pressure tabs are distributed over the intersections of 12 horizontal and 17 vertical sections. The horizontal sections are equidistantly distributed along the models vertical axis. They are identified by numbers ranging from 1 to 12, whereof 1 is closest to the dorsal side and 12 is closest to the ventral side of the fuselage. The vertical sections are slices at azimuth angles
Psi ranging from 0 deg to ±90 deg. They are identified by roman alphabet upper cases A to Q. The pressure tab locations in the aft-body region are, thus, labeled by a combination of the associated vertical section's upper case and the horizontal section's number; e.g. D6. Section I corresponds to the intersection of the rear fuselage with its symmetry plane. The other sections are obtained by intersecting planes at azimuth angles of $\pm 6, 11, 18, 25, 35, 50, 70$ and 90 deg to the symmetry plane. The axis of rotation is the intersection of the symmetry plane with the plane parallel to y_r and z_r through the onset of the rear fuselage upsweep; see section 2.5. Section A and Q, respectively, corresponds to $\theta = -90$ deg and $+90$ deg. The

intermediate sections are labeled in alphabetical order in the counter-clockwise direction with respect to θ. However, not all intersections of horizontal and vertical sections in the aft-body region are equipped with a pressure tab; see Fig. 3.8. Furthermore, three additional sections S, X and Y are equipped with 23, and two times 12 pressure tabs, respectively. Section S represents the intersection of the front fuselage with its symmetry plane. The pressure tabs located on section S are distinguished by alpha-numerical labels $S1$ to $S23$. Starting at the rear end of section S on the mast fairing with $S1$, continuing along S to the front until the bow ($S13$) and back along the fuselage's ventral side up to $S23$, see Fig. 3.8. Sections X and Y are representing, respectively, the port-side and starboard-side of the intersection of the fuselage and the horizontal plane through the bow of the fuselage. The pressure tabs on sections X and Y are also distinguished by alpha-numerical labels ranging bow to stern from $X1$ to $X12$ and $Y1$ to $Y12$, respectively.

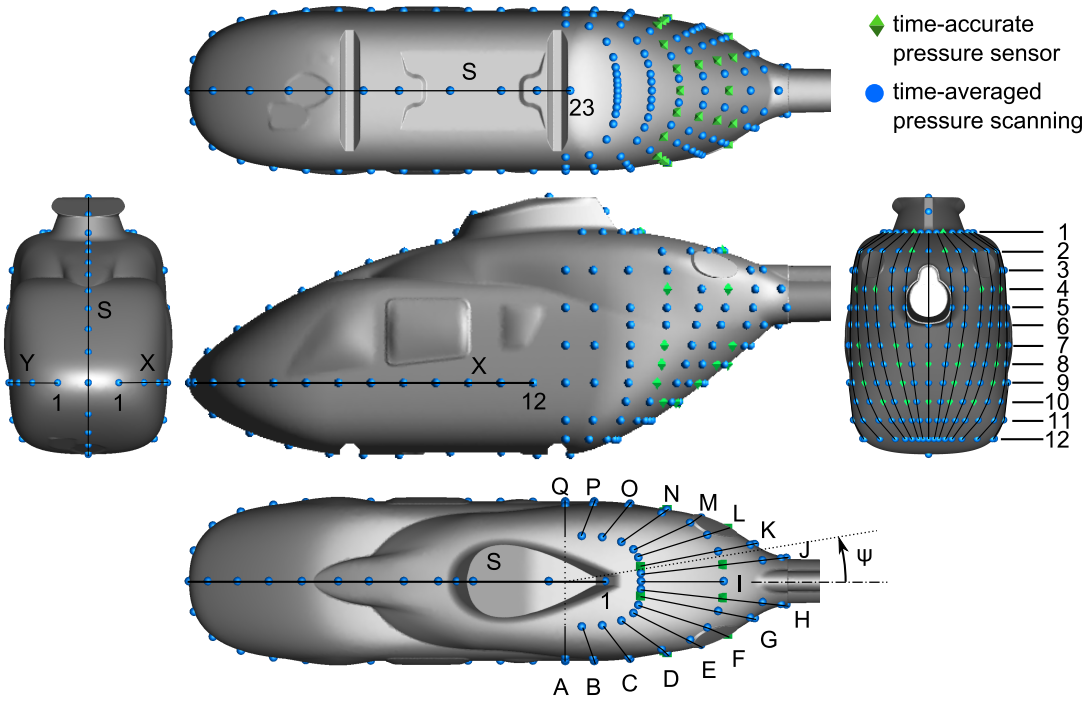

Figure 3.8: *Time-accurate pressure sensor and time-averaged pressure scanning locations and nomenclature for the ADHeRo W/T model.*

Out of the 218 pressure tabs, 26 are equipped with time-accurate pressure sensors. In Fig. 3.8 the positions of the pressure tabs equipped with time-accurate sensors are indicated by green tetrahedrons. The employed sensors are *HCL 0025 P*'s by the First Sensor AG. This sensor features a measurement range between 0 and 2500 Pa. At a static input pressure, the best straight-line-fit is within $\pm 0.05\%$ of the full scale pressure (2500 Pa). This corresponds to an accuracy for the temporal mean pressure of ± 1.25 Pa, which is equal to $c_p = \pm 1.3 \cdot 10^{-3}$.
The remaining 192 pressure tabs are employed for time-averaged surface pressure measurements. The time-averaged surface pressures are measured with the Scanivalve Cooperation's electronic pressure scanning modules of the type ZOC33/64PX-2.5psid. Each of these modules features 64 input channels, resulting in a total

number of 3 ZOC modules for the performed experiments. The ZOC modules are installed directly inside the fuselage. This circumvents restrictions associated to the space inside the tailboom support, since only the power supply, the high pressure line for the pneumatic control valves, the reference pressure line and the data cable need to fit through the support. The pressure is sampled at 48 kHz, but only the time averaged values are considered. The pressure at each input is time-averaged over the measurement time of 15 s. The accuracy corresponds to $\pm 0.1\%$ of the full-scale pressure (17 kPa) or $c_p = \pm 17.6 \cdot 10^{-3}$.
The time-averaged surface pressure $\bar{p}$ are post-processed to obtain the time-averaged, non-dimensional, pressure coefficient c_p; see Eq. 3.8.

$$c_p = \frac{\bar{p} - p_\infty}{\frac{1}{2} \cdot \rho_\infty \cdot U_\infty^2}. \tag{3.8}$$

The large number of pressure scanning locations in the aft-body region allows to calculate c_p contour plots in that region. For this purpose a Kriging function is applied to transform the scattered pressure information into a contour plot. The Kriging function is solved, by incorporating the eight closest data points, at each node of a (i,j)-structured surface mesh (100,000 cells). The mesh matches the surface which is confined by sections A to Q and 1 to 12; see Fig. 3.9.

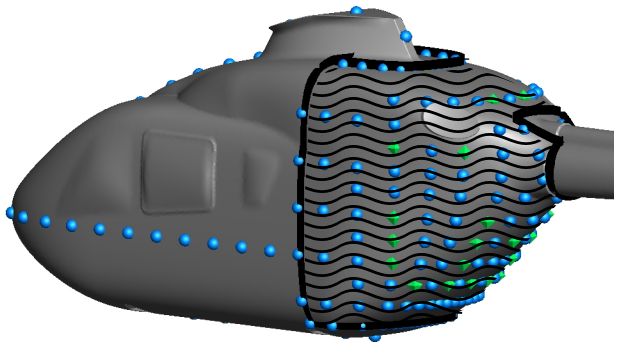

Figure 3.9: *Aft-body region with the region of the kriging mesh displayed (hatching).*

3.5 Wake Velocity Measurements

The velocity field in the wake of the model is investigated by Stereo-Particle-Image-Velocimetry (Stereo-PIV). Through this approach it is possible to obtain the time-averaged velocity fields in a large wake flow area.The wake velocity measurements are performed at 0 *deg* angle of attack and angle of sideslip at test condition 'd'; see section 3.2.
Particle-Image-Velocimetry (PIV) is an optical, non-intrusive measurement technique to detect the velocity components within a plane of a flow field seeded with particles. For the performed experiments vaporised Bis(2-ethylhexyl)-sebacat was employed as seeding. Since these seeding particles feature diameters of only some micrometers ($1 - 2\ \mu m$), it is assumed that they ideally follow the flow. The technique is based on tracking the positions of these particles at two instances in time in quick succession. Their positions are tracked by illuminating the measurement plane with a laser sheet and capturing the light scattered back from the particles on camera. This allows assessing the displacement vectors by applying correlation functions on subsets of the particle images at the two recorded events. In consequence, velocity vectors can be computed by dividing the displacements by the known time lag between the two events. PIV-setups with only one camera installed can provide two-dimensional velocity vectors within the measuring plane (2D2C). PIV can be augmented to Stereo-PIV by capturing the particle images with a second camera from a different perspective. Then, by exploiting the principles of stereogrametry, it is possible to also assess the velocity components normal to the measurement plane. Thus, it is feasible to asses the local three-dimensional velocity vector at each location within the two-dimensional measurement plane; i.e. 2D3C.
The laser's power output limits the maximum sufficiently illuminated area of the measurement plane. Current lasers are limited to some 10 mJ power output at repetition frequencies in the order of several kHz. Higher power outputs can only be obtained at lower repetition frequencies in the order of 10 Hz. However, measurement planes with an area in the order of 1 m^2 necessitate power outputs in excess of 100 mJ. This limitation did not allow time-accurate measurements at relevant sample frequencies for the presented experiments.

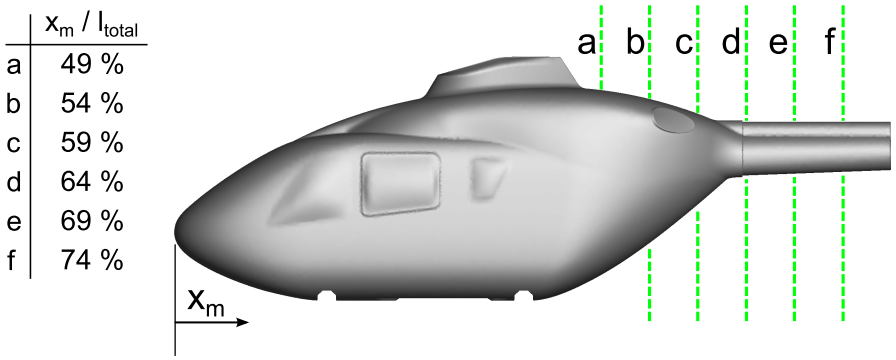

Figure 3.10: *Position of the measurement planes for Stereo-PIV relative to the fuselage's total length (including the empennage).*

The Stereo-PIV measurements are performed in 6 planes normal to the freestream direction in the wake of the model; see Fig. 3.10. The first plane 'a' is located at $x_m/l_{total} = 49\%$. The remaining five consecutive planes downstream ('b'-'f') are equidistantly distributed along the models longitudinal axis at increments of 5% x_m/l_{total}.

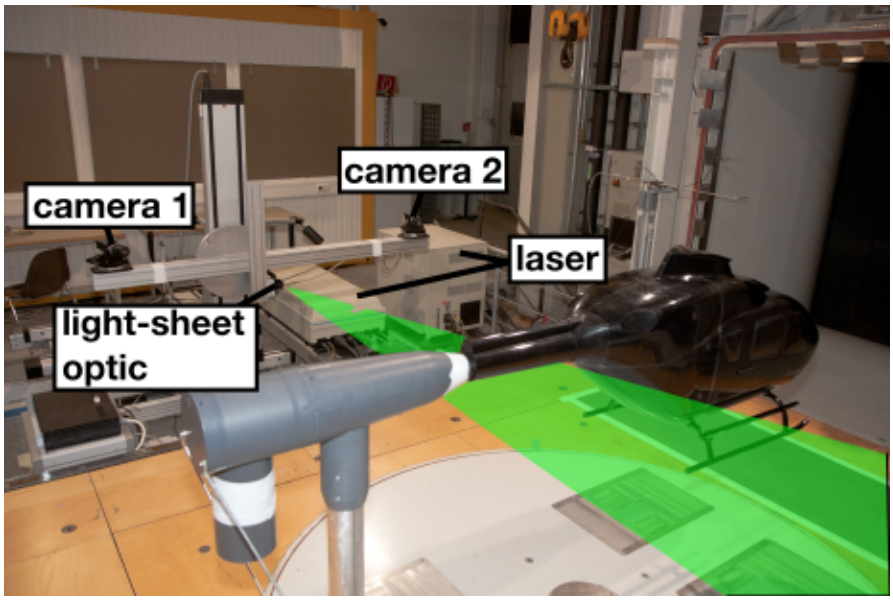

Figure 3.11: *General equipment arrangement for the employed Stereo-PIV setup.*

Two different Stereo-PIV setups are employed for the ADHeRo project. The general equipment arrangement is presented in Fig. 3.11. *Setup 1* employs a conventional Stereo-PIV system. This setup includes two charge-coupled-device (CCD) cameras with a pixel resolution of 1600 x 1200 and optics featuring a focal length of 135 mm and a relative aperture of 2.8. The laser of *setup 1* is a frequency doubled, double oscillator neodymium-doped yttrium aluminium garnet (Nd:YAG) laser with a pulse energy of 200 mJ at a repetition frequency of 10 Hz and a wave length of 532 nm. With *setup 1*, 130 data samples are recorded for each measurement position. For *setup 2*, a state-of-the-art Stereo-PIV system is used. This system has not been available from the beginning of the project. Therefore, not for all tested configurations data acquired with this system are available. The new Stereo-PIV system features two CMOS cameras with a pixel resolution of 2560 x 2160. The laser of *setup 2* is as well a frequency doubled, double oscillator Nd:YAG laser, but features a pulse energy of 320 mJ at a repetition frequency of 15 Hz. The emitted laser beam also has a wave length of 532 nm. With *setup 2* at each measurement location 400 data samples are recorded at a sample rate of 15 Hz. The obtained time-averaged velocity vectors are denoted as $(u\ v\ w)^T$ with respect to the aerodynamic coordinate system $(x\ y\ z)^T$; see Fig. 3.7. The employed PIV-systems record the average velocities at an accuracy of $\pm 2\%$ with respect to the freestream velocity's magnitude.

4 Numerical Method

This chapter presents the method of the numerical simulations presented in this work. First, the generation of the computational mesh is outlined. This also includes the analysis of the required mesh density. In section 4.2, the used commercial flow solver and the applied solver settings are described. Furthermore, the applied initial and boundary conditions as well as the fluid properties are detailed. In the last section of this chapter, the obtained numerical results are validated against the corresponding experimental data. The validation study includes the global forces, the surface pressure distribution and the velocity field in the model's wake.
Fig. 4.1 presents all configurations investigated numerically. The first configuration F0M0 represents the isolated fuselage of the reference configuration. Note that the horizontal part of the tailboom model support is retained for all the configurations considered for the numerical simulations. However, the forces acting on this component are not included in the numerically assessed aerodynamic forces and moments. The configuration F0M0L0 includes the reference fuselage and the reference skid-landing-gear. Both for F0M0 and F0M0L0, the open cavities housing the skid-landing-gear's central cross-beam elements are retained. For configuration F1M0, the open cavities and attachment surfaces at the fuselage's ventral side are smoothed. F1M0L1 combines F1M0's fuselage with the retrofittable faired skid-landing-gear. The last configuration investigated numerically is F1M0L1 fitted with the passive flow control device combination S2LVG2X20.

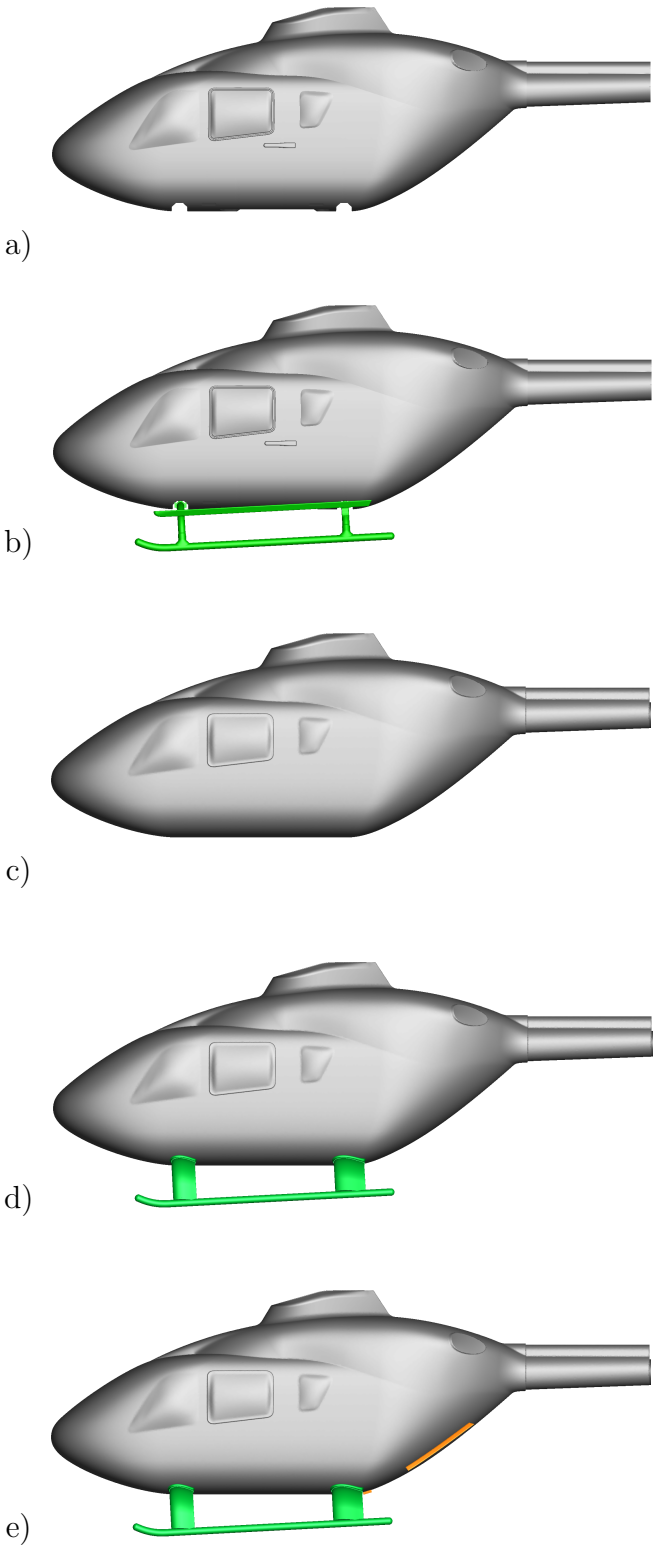

Figure 4.1: *Lateral side views (CAD rendering) of the different model configurations considered for the numerical simulations. a) F0M0, b) F0M0L0, c) F1M0, d) F1M0L1 and e) F1M0L1S2LVG2X20.*

4.1 Computational Mesh

The meshing of the investigated configurations for this work is performed with ANSYS ICEM CFD. Vogel [43] showed that for TEL-class utility helicopter type of fuselage geometries the mesh topology (structured/unstructured) does not influence the simulation results. Therefore, only unstructured meshes are generated in order to confine the necessary effort for adapting the mesh to the geometric modifications.

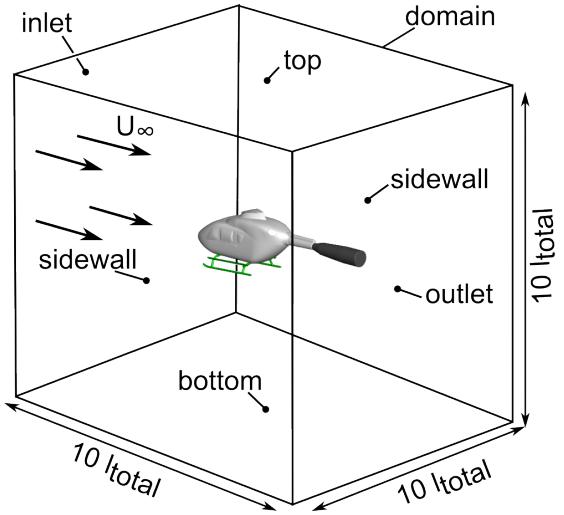

Figure 4.2: *Schematic representation of the computational domain for configuration F0M0L0.*

The computational domain features in all three directions in space the outer dimension of $10 \cdot l_{total}$; for the definition of l_{total} see section 2.5. The model is positioned in the center of the domain. The wind tunnel is not modelled for the simulations, but the horizontal part of the tailboom model support is retained; see Fig. 4.2.
The meshing process incorporates two steps. The surface mesh is calculated first with the Octree algorithm; see Shepard and Georges [37] as well as Yerry and Shepard [48]. Based on this surface mesh, the prism layers and the tetrahedral volume mesh is generated with Delaunay's algorithm [12].
For resolving the flow around the model and in its wake more precisely, the volume mesh is refined by the definition of density regions. For this purpose two levels of density regions are interleaved around the fuselage model. The first level density region DR1 encloses the entire model; see Fig. 4.3. This density region is defined in order to control the maximum element size in the vicinity of the model. The second level density regions DR2-1 and DR2-2 are then used in order to refine, respectively, the fuselage's and mast fairing's as well as the skid-landing-gear's wake flow more precisely.

Vogel showed [43] that for his configuration GR a total number of $7.8 \cdot 10^6$ nodes is sufficient for achieving grid independent results with respect to the global aerodynamic forces and moments, the surface pressure distribution and the flow field

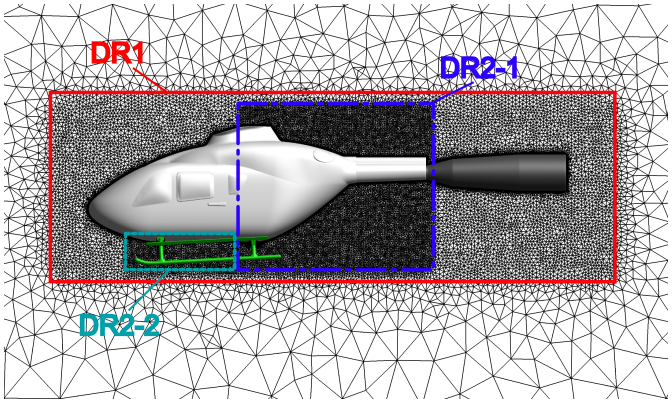

Figure 4.3: *Location of the density regions DR1, DR2-1 and DR2-2 exemplified for configuration F0M0L0.*

in the model's wake. Configuration GR corresponds to the reference configuration without the rotor head; see section 2.5. Vogel resolved the boundary layer region with 25 prism layers in the direction normal to the wall. The height of the first prism layer is defined such that the non-dimensional wall distance y^+ is always $y^+ < 2$ and the expansion factor for the prism layers is set to 1.3. The maximum size of the surface elements edge l_{edge} is equal to 0.015 l_{edge}/l_{ref} for the computational meshes of Vogel's simulations. Based on the guidelines provided by Vogel [43] comparable meshing parameters are applied for the computational meshes of the simulations presented in this work. Since the mesh is refined additionally compared against the parameter recommended by Vogel, a grid independency study is not required for the presented results.

Configuration	Total	Surface	Prism	Volume
F0M0	25.8	0.5	15.3	10.0
F0M0L0	31.2	0.7	18.6	11.9
F1M0	19.8	0.4	11.9	7.5
F1M0L1	28.1	0.6	18.2	9.3
F1M0L1S2LVG2X20	42.4	1.0	28.3	13.1

Table 4.1: *Number of elements in millions for all configurations investigated by numerical simulation.*

The computational meshes used for this work feature 25 prism layers at the skid-landing-gear and 30 prism layers at the fuselage for all investigated configurations. The expansion factor of the prism layer is reduced to 1.2 and the height of the first element at the wall is defined such that $y^+ \leq 1$. The surface elements maximum edge length is confined to 0.011 l_{edge}/l_{ref}. In consequence, the total number of nodes for the reference configuration without the rotor head and the empennage amounts to $11.5 \cdot 10^6$. In Tab. 4.1 the corresponding number of elements is presented for all investigated configurations.

4.2 Solver

The numerical simulations presented in this work are performed with the commercial finite-volume-method (FVM) solver ANSYS CFX 14.5. The numerical solution is obtained by solving the incompressible unsteady Reynolds averaged Navier-Stokes (URANS) equations on the three-dimensional unstructured meshes described in section 4.1. Applying the incompressible formulation is justified, since the Mach number Ma never exceeds $Ma = 0.2$ for the investigated configurations. The RANS formulation is closed through a turbulence approximation based on Launder's [25] Reynolds stress model (RSM); i.e. BSL-RSM. The RSM model determines the individual Reynolds stresses based on their transport equations and the turbulence energy dissipation rate ϵ. The calculated Reynolds stresses are employed for closing the momentum equation of the RANS formulation. For the BSL-RSM model Menter's baseline-ω-equation [29] is used in order to blend between the k-ϵ-model in the outer part of the boundary layer with Wilcox' k-ω-equation [46] near the wall. Wall functions are not necessary for the performed simulations since the wall distance of the first computational grid point is small enough ($y^+ \leq 1$) to capture the velocity gradient appropriately. The advantage of the BSL-RSM model is that it accounts for anisotropic turbulence, which improves the accuracy of predicting separated flows under the influence of stress-driven secondary flows compared against two-equation turbulence models. The price for this increase in accuracy is the computational cost in terms of CPU time and memory requirements for solving the six additional Reynolds stresses differential equations. The discretization of the described numerical model in space and time is performed, respectively, with the high resolution scheme [2] and the implicit second order backward Euler method.
In order to be able to compute the solution based on the described numerical method, initial and boundary conditions need to be defined. The boundary conditions are defined at the inlet, top, bottom, sidewall, outlet and on the model itself as follows:

- the inflow with a constant velocity, turbulence intensity and eddy viscosity ratio at the inlet,
- the outflow with zero pressure gradient at the outlet
- no-slip walls at the surface of the model and
- free-slip walls at the sidewalls, the top and the bottom of the domain.

The velocity vector $(u, v, w)^T$ at the inlet is defined in accordance to the standard test condition 'd' at $\alpha, \beta = 0\ deg$ with $u = U_\infty = 40\ m/s$ and $v, w = 0\ m/s$; see also section 3.2. The medium is dry air ($\varphi = 0\%$) at ambient conditions of $p_\infty = 10.13 \cdot 10^4\ Pa$ and $T_\infty = 298\ K$. This corresponds to $\rho_\infty = 1.15\ kg/m^3$, $\nu_\infty = 1.55 \cdot 10^{-5}\ m^2/s$, $Re_\infty = 0.95 \cdot 10^6$ and $Ma_\infty = 0.12$.
Furthermore, the turbulence intensity Tu_{tot} is set to 0.8% and the eddy viscosity ratio μ_t/μ is defined to be 51 at the inflow. With those settings, the turbulence decay up to the stagnation point of the model is tailored in such a way that the wind tunnel's turbulence intensity of $T_{tot} = 0.3\%$ upstream of the model is

matched.
All numerical results presented in this work are based on averaged data obtained by URANS simulations. In order to obtain the unsteady results, a steady RANS simulation is performed first. This steady simulation is initialised by imposing the boundary conditions at the inlet onto the entire domain. The steady simulation is solved for a pseudo time step equivalent to an increment of the rotor-heads azimuth angle Ψ of about 6 *deg*. The steady simulation is stopped after 200 time steps and the obtained solution is employed to initialise the consecutive unsteady simulation. The unsteady simulations are performed for two different time steps. First, the time step is set to a value equivalent to an increment of the rotor-heads azimuth angle Ψ of 3 *deg*. With this setting 480 time steps are calculated, which would correspond to the time required for four rotor-head revolutions. Finally, the time step is reduced to the equivalent value of a 1 *deg* rotor head azimuth increment for another 1080 time steps. The averaged data presented in this work are obtained by averaging over the final 720 time steps, which correspond to the time required for two rotor head revolutions.

4.3 Validation

In this section, the obtained numerical data are validated against the corresponding experimental data. The validation study is performed for the global aerodynamic forces, the surface pressure distribution and the flow field in the wake of configuration F0M0, F0M0L0, F1M0, F1M0L1 and F1M0L1S2LVG2X20. The comparison of the numerical data against the experimental data with respect to the surface pressure distribution and the flow field in the model's wake is presented in the analysis chapters 5 and 6. This comparison is summarised at the end of this section.

Configuration	$C_{D,sim}$	$C_{D,exp}$	$\frac{\Delta C_D}{\lvert C_{D,ref}\rvert}$	$C_{L,sim}$	$C_{L,exp}$	$\frac{\Delta C_L}{\lvert C_{L,exp}\rvert}$
F0M0	0.1188	0.0918	7%	-0.0635	-0.0836	24%
F0M0L0	0.2104	0.1837	7%	0.0313	-0.0064	588%
F1M0	0.0982	0.0807	4%	-0.1171	-0.1071	-9%
F1M0L1	0.1251	0.1022	6%	-0.0943	-0.1086	13%
F1M0L1S2LVG2X20	0.1232	0.0961	7%	-0.0867	-0.1099	21%

Table 4.2: *Numerically predicted drag and lift coefficients ($C_{D,sim}$, $C_{L,sim}$) compared against the values obtained by wind tunnel experiments ($C_{D,exp}$, $C_{L,exp}$) for configurations F0M0, F0M0L0, F1M0, F1M0L1 and F1M0L1S2LVG2X20.*

For validation of the numerical simulation data with respect to the aerodynamic forces the prediction of the drag and lift force coefficients is compared to the experimental data. The side force coefficient is excluded from this analysis, since the configurations are symmetric with respect to the (x_m, z_m) plane.

In Tab. 4.2 the deviation ΔC_D of the numerically predicted drag coefficient $C_{D,sim}$ of the individual sub-configurations is compared to the corresponding value recorded by the wind tunnel experiments $C_{D,exp}$. The results are presented in percentage of the reference configuration's drag coefficient $C_{D,ref}$; see section 5.2.
The comparison of the numerical simulation to the experiments with respect to the drag coefficients reveals a good agreement for all considered sub-configurations. The relative deviation $\Delta C_D/C_{D,ref}$ remains well below 10%. For all 5 configurations, the simulation over predicts the drag level by 4% up to 7% $\Delta C_D/C_{D,ref}$. The deviation is apparently mainly associated to the prediction of the fuselage's drag. This becomes apparent as the relative deviation does not change significantly by adding L0 or L1 to F0M0 or F1M0, respectively.

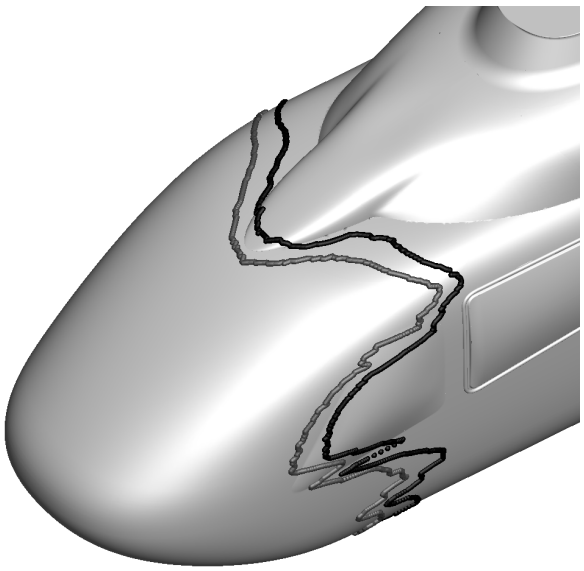

Figure 4.4: *Three-dimensional reconstruction of the location of transition onset (gray) and transition end (black) on F0M0's CAD geometry; Grawunder et. al. [20].*

Grawunder et al. [20] showed that for F0M0 about 25% of the fuselage's surface is exposed to a laminar boundary layer; see Fig. 4.4. However, the performed numerical simulations are based on the assumption of fully turbulent boundary layers. Thus, the contribution of the wall-shear to the total fuselage drag is over predicted by simulation. This could explain the observed $\Delta C_D/C_{D,ref}$ since the shear forces contribute about 30% to the total drag force in the presented simulations.
Furthermore, Tab. 4.2 presents both the lift coefficients obtained by numerical simulation $C_{L,sim}$ and by wind tunnel experiments $C_{L,exp}$ for configurations F0M0, F0M0L0, F1M0, F1M0L1 and F1M0L1S2LVG2X20.
Comparing F0M0's $C_{L,sim}$ and $C_{L,exp}$ reveals a under-prediction of the down force generated at the fuselage by the simulation. The observed relative deviation $\Delta C_L/C_{L,exp} = (C_{L,sim} - C_{L,exp})/C_{L,exp}$ is 24% for F0M0. F0M0L0's C_L is not predicted well by the numerical simulation. Nevertheless, F0M0L0's drag level is still predicted as accurate as for the other configuration's. F1M0's relative devia-

tion with respect to the lift coefficient is $\Delta C_L = -9\%$. This represents the best agreement of a configuration's lift coefficient obtained by simulation and experiment for the results presented in this work. In contrast to the other configurations, the simulation over-predicts the down-force generated at F1M0. For F1M0L1 and F1M0L1S2LVG2X20, the simulation under-predicts the generated downforce by 13% and 21%, respectively.
The near-surface pressure distribution obtained by numerical simulation and experiments do agree well for configuration F0M0; see Fig. 5.8. However, the simulation under predicts the pressure level at the rear fuselage's symmetry plane by about $\Delta c_p = 0.1$. Nevertheless, the characteristic of the surface pressure distribution and even the absolute c_p values are predicted well for $y_r/(b_f/2) \neq 0$. Only at Z11 the deviation observed at $y_r/(b_f/2) = 0$ prevails for $y_r/(b_f/2) \neq 0$.
F0M0L0's experimental and simulation surface pressure data do not reveal a as good agreement as for the other configurations; see Fig. 5.9. The simulation under predicts the pressure level for most of F0M0L0's rear fuselage region, because the primary separation location at the fuselage's lateral side is not captured well. The characteristics of c_p as a function of $y_r/(b_f/2)$ and x_r/l_r are still in good agreement. For configurations F1M0, F1M0L1 and F1M0L1S2LVG2X20 the experimental and numerical surface pressure data are qualitatively and quantitatively in excellent agreement; see Fig. 6.18, Fig. 6.20 and Fig. 6.48
F0M0's, F1M0's, F1M0L1's and F1M0L1S2LVG2X20's experimental and numerical wake velocity u/U_∞ fields are in excellent agreement with respect to the absolute values and the extension of the wake regions. For F0M0L0's u/U_∞ in the wake the experiment and simulation data are in good agreement with respect to the absolute values and the extension of the wake region. However, the near wake region's extension in the vertical and lateral direction is over predicted due to the deviation with respect to the primary separation location observed for F0M0L0. Further downstream, F0M0L0's absolute values of u/U_∞ are in better agreement between the experiment and the simulation. Nevertheless, the lateral extension of the wake region close to the tailboom is under predicted by simulation.

5 Baseline Model Aerodynamic Characteristics

In order to assess the potential benefits of the design modifications, the baseline configuration is analysed first. Based on the data obtained for the baseline model, the reference for the performed optimisations is defined. The geometry corresponds to a state-of-the-art TEL-class utility helicopter featuring a new five-bladed rotor head with a MTOW of about 3 metric tons, see chapter 2. The reference geometry is simplified in order to adapt the model for the wind tunnel experiments; see section 2.1. This results in the baseline model presented in Fig. 5.1.

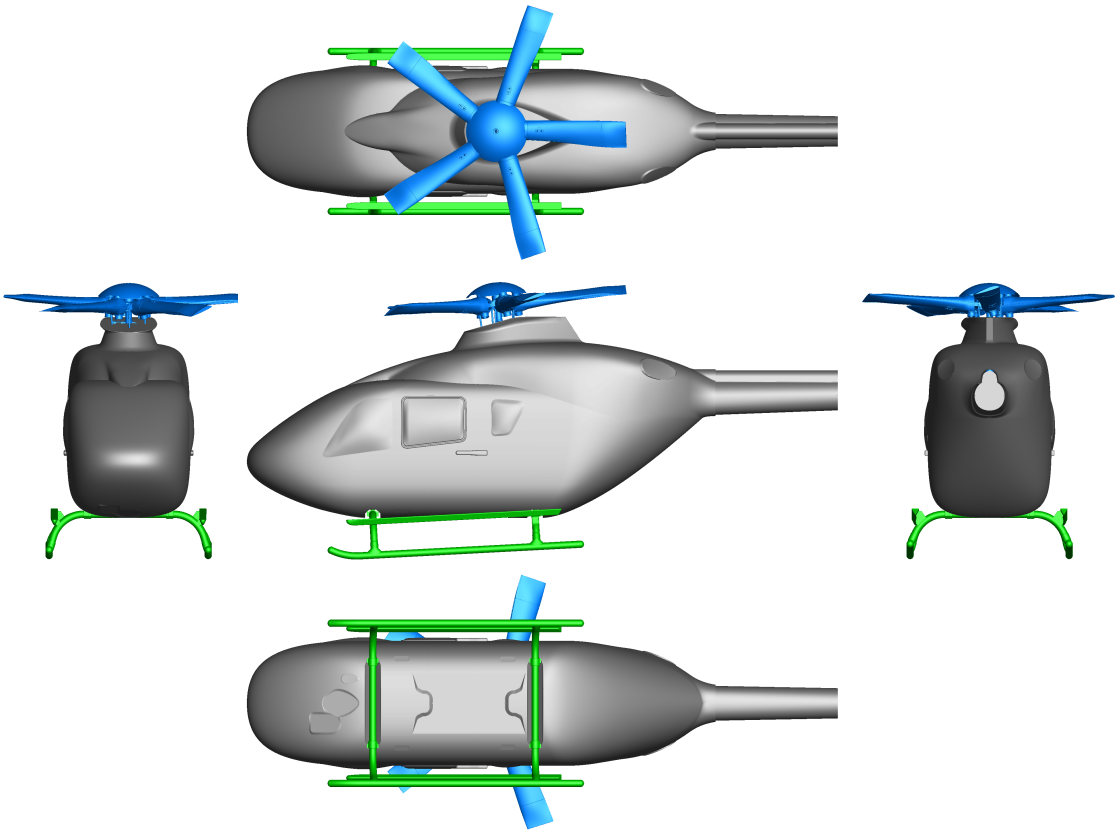

Figure 5.1: *Front and rear view as well dorsal, lateral and ventral side view (CAD rendering) of the complete baseline model F0M0L0R0.*

For the baseline campaign 4 different configurations are investigated. This includes the complete baseline model and its sub-configurations. The complete baseline model features the baseline version of the fuselage F0, the mast-fairing M0, the skid-landing-gear L0 and the rotor head R0. The most basic sub-configuration of the baseline model only includes the fuselage and the mast-fairing F0M0. Furthermore, two configurations of intermediate complexity are considered. Those configurations are obtained by adding either the skid-landing-gear or the rotor head to the basic model; i.e. F0M0L0 and F0M0R0.

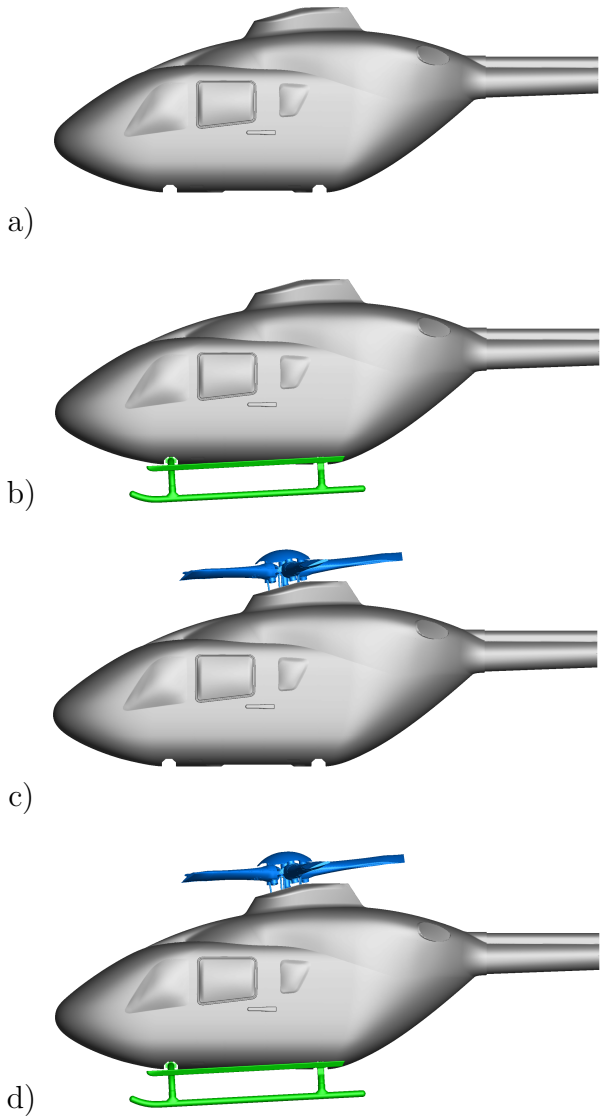

Figure 5.2: *Lateral side views (CAD rendering) of the different model configurations considered for the baseline campaign. a) F0M0, b) F0M0L0, c) F0M0R0 and d) F0M0L0R0.*

By comparing the baseline model and its sub-configuration with each other a detailed analysis of the global and local aerodynamic characteristics can be performed, which also assesses the impact of the components interference effects. The results of this analysis are presented in the following sections.
First of all, the influence of the freestream Reynolds number on the global aerodynamic characteristics is presented in section *5.1 Reynolds Number Study*. Based on this study the standard test condition for all further investigations is defined. In section *5.2 Aerodynamic Forces and Moments* the impact of F0M0L0R0's components on the global aerodynamic loads for sweeps over angle of attack and sideslip is analysed. This leads to the selection of the most relevant fuselage attitude, for which the reference configuration's drag and lift decomposition is investigated in detail. This analysis is complemented in section *5.3 Surface Pressure* by investigating the local pressure distribution at F0M0's, F0M0L0's and F0M0L0R0's rear fuselage. Finally, the most relevant sub-configurations are selected for the detailed analysis of the near-surface and wake flow topology; presented in section *5.4 Flow Topology*.

5.1 Reynolds Number Study

In this section the influence of the freestream Reynolds number Re_∞ on the global aerodynamic loads is discussed. The freestream conditions of the real helicopter in fast-forward level-flight at an altitude of 1000 m above mean sea level (MSL) according to the international standard atmosphere (ISA) are characterised by $Re_\infty = 8.2097 \cdot 10^6$ and $Ma_\infty = 0.208$. Both Re_∞ and Ma_∞ cannot be matched with the available experimental setup due to the reduced model scale of 1:5 and the limited freestream velocity of the wind tunnel ($U_\infty \leq 65\ m/s$). Even higher Mach numbers have to be expected locally. The highest Mach number of the real helicopter is observed at the blade tips of the main rotor on the advancing blades. Since the blades are not considered in the experiments, the highest Mach number is observed at the tip of the truncated blade stubs. At this location a Mach number of 0.356 is obtained for the real helicopter in fast-forward level-flight. Thus, only negligible compressibility effects occur on the components considered for this analysis. Consequently, the influence of the freestream Mach number is not further investigated.
The difference of the experimental and real freestream Reynolds number is not negligible though. At the standard test condition 'd' $Re_\infty = 9.5 \cdot 10^5$. Hence, in the experiments Re_∞ is almost one order of magnitude lower compared to the real helicopter in fast-cruising level-flight. Therefore, the influence of the Reynolds number on the global aerodynamic loads is investigated. For this purpose, aerodynamic forces and moment measurements are performed for a variation of U_∞ between 25 m/s and 55 m/s at a 5 m/s increment according to test conditions 'a'-'f'; see section 3.2. The configurations considered for this analysis are the isolated fuselage (F0M0), the fuselage with the skid-landing-gear (F0M0L0) and the fuselage with the skid-landing-gear and the rotor head fixed at 0 deg azimuth angle (F0M0L0R0 $\Psi = 0\ deg$).

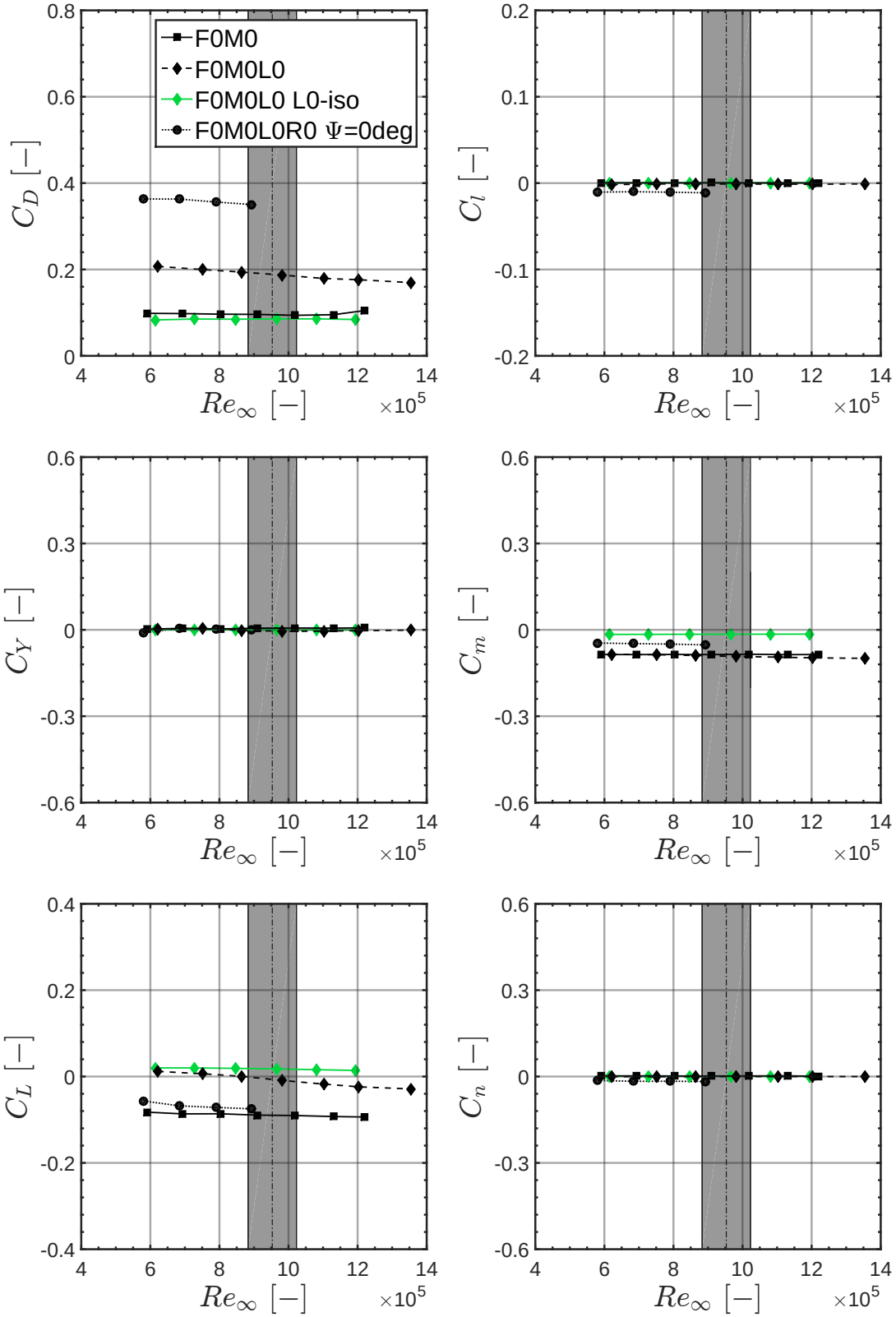

Figure 5.3: *C_D, C_Y, C_L, C_m, C_l and C_n as a function of Re_∞ for configuration F0M0, F0M0L0, F0M0L0 L0-iso and F0M0L0R0 with the rotor head fixed at $\Psi = 0$ deg. The Reynolds number variation corresponds to test conditions 'a'-'f' (F0M0, F0M0L0, F0M0L0 L0-iso) and 'a'-'d' (F0M0L0R0 $\Psi = 0$ deg); see section 3.2. The dashed-dotted line indicates the mean Re_∞ and the grey shaded region represents the variation of Re_∞ for test condition 'd'. $\alpha, \beta = 0$ deg.*

Furthermore, the aerodynamic loads acting on the skid-landing-gear L0 alone on configuration F0M0L0 are recorded with the internal strain-gauge balance. This yields configuration F0M0L0 L0-iso. The resulting Reynolds number variation is about $6 \cdot 10^5 \leq Re_\infty \leq 1.3 \cdot 10^6$. For the configuration including the rotor head (F0M0L0R0 $\Psi = 0\ deg$) only test conditions 'a'-'d' are feasible ($Re_\infty \leq 9 \cdot 10^5$). For all those measurements, α and β are fixed at 0 deg.
Fig. 5.3 presents the global force and moment coefficients as a function of Re_∞ for configuration F0M0, F0M0L0, F0M0L0 L0-iso and F0M0L0R0 with $\Psi = 0\ deg$. The vertical dashed dotted line indicates the mean Reynolds number for test condition 'd' and the region shaded in grey corresponds to the range of Re_∞ observed for test condition 'd', see section 3.2.
The aerodynamic coefficients C_D and C_L reveal a notable dependency of Re_∞ for F0M0L0R0 $\Psi = 0\ deg$. The origin of this dependency can be identified by comparing the characteristics of C_D and C_L for the sub-configurations F0M0 and F0M0L0. For the isolated fuselage (F0M0), C_D and C_L are almost independent of Re_∞. When the skid-landing-gear is added to the model (F0M0L0) C_D and C_L exhibit a notable dependency of Re_∞. However, the skid-anding-gear itself (F0M0L0 L0-iso) does not feature any dependency of Re_∞ within the investigated Reynolds number range. This shows that the aerodynamic interference between the skid-landing-gear and the fuselage is responsible for the Reynolds dependency observed for F0M0L0. Furthermore, C_D and C_L as a function of Re_∞ reveal the same trend for the configuration F0M0L0 and F0M0L0R0 $\Psi = 0\ deg$. Thus, the rotor head does not introduce additional Reynolds effects to the global aerodynamic model loads within the considered Reynolds number range. The aerodynamic coefficients C_Y, C_l, C_m and C_n do not reveal any significant Reynolds dependencies.
Due to the observed Reynolds number characteristics for the aerodynamic interference of the skid-landing-gear and the fuselage, the standard test condition was selected such that the highest possible Re_∞ could be achieved. The limiting factor for operating the wind tunnel model at high Re_∞ are the structural loads acting on the rotating rotor head and the required power for the rotor head actuation. The performed pre-tests revealed, that an operation of the rotating rotor head is not feasible for $U_\infty > 40\ m/s$. Thus, test condition 'd' is selected as the standard test condition for the present work. For details regarding the ambient conditions associated to test condition 'd' see section 3.2.

5.2 Aerodynamic Forces and Moments

In order to assess the global aerodynamic characteristics of the baseline configuration, aerodynamic force and moment measurements are performed for the configurations F0M0, F0M0L0, F0M0R0 and F0M0L0R0; see beginning of chapter 5. The measurements are performed for the polar *A1B1* which corresponds to a combined sweep over angles of attack and angles of sideslip in the range of $-10\ deg \leq \alpha, \beta \leq 10\ deg$ at 2 *deg* increments. This range of α and β corresponds to the forward-flight domain of the helicopter. However, fast-forward level-flight is confined to $-2\ deg \leq \alpha \leq 0\ deg$ and $-2\ deg \leq \beta \leq 2\ deg$. This flight condition is in the focus here, since fast-forward level flight is dominant in typical TEL-class utility helicopter's mission profiles.The tests are performed at the standard test conditions 'd'; see section 3.2. Furthermore, the component loads acting on the skid-landing-gear L0 and the rotor head R0 are recorded by internal strain-gauge balance measurements on F0M0L0 and F0M0L0R0, respectively. Those measurements are also performed for the test condition 'd', but only at $\alpha, \beta = 0\ deg$.
In Fig. 5.4, the force and moment coefficients for F0M0, F0M0L0, F0M0R0 and F0M0L0R0 are presented for $\beta = 0\ deg$ and $-10\ deg \leq \alpha \leq 10\ deg$. The component loads of L0 and R0 are superimposed on the global loads at $\alpha, \beta = 0\ deg$ of F0M0 and F0M0L0, respectively. This yields the entries F0M0+L0 and F0M0L0+R0 in the polar plots. Thus, it is possible to analyse if the observed variation in the global model loads by adding a component is associated to the component itself or a combination of the component load and its aerodynamic interference.
F0M0's C_D as a function of α features a negative slope $\partial C_D/\partial\alpha$ over almost the entire range of $-10\ deg \leq \alpha \leq 10\ deg$. Performing a parabolic least-square-fit for F0M0's C_D over α returns a minimal drag coefficient $C_{D,min} = 0.074$ at $\alpha = \alpha_{min} = 9.3\ deg$ and the quadratic pre-factor $a = 2.099 \cdot 10^{-4}$ according to Eq. 5.1. The result is depicted in Fig. 5.4 as grey solid line.

$$C_D(\alpha) = a \cdot (\alpha - \alpha_{min})^2 + C_{D,min} \tag{5.1}$$

The observed characteristic can be explained with the fuselage asymmetric shape with respect to the longitudinal model axis (x_m). This asymmetry leads to a stronger curvature of the rear fuselage upsweep compared to the rear-engine cowling. According to Keys [21], the minimum in the parabolic drag polar is associated to α_0 where $C_L = 0$ for cambered fuselage sections. F0M0's C_L becomes zero at $\alpha = 7\ deg$. Considering the fact that no data points for $\alpha > 10\ deg$ are available for interpolation, the parabolic least-square-fit for $\alpha_{min} = 9.3\ deg$ might not be precise. The 'chord line' of the fuselage can be defined as the connection through the bow and the centre of the contraction at the stern. For F0 this results in an angle of the chord line against the model's longitudinal axis x_m of $\approx -8\ deg$. This correlates well with F0M0's α_0.

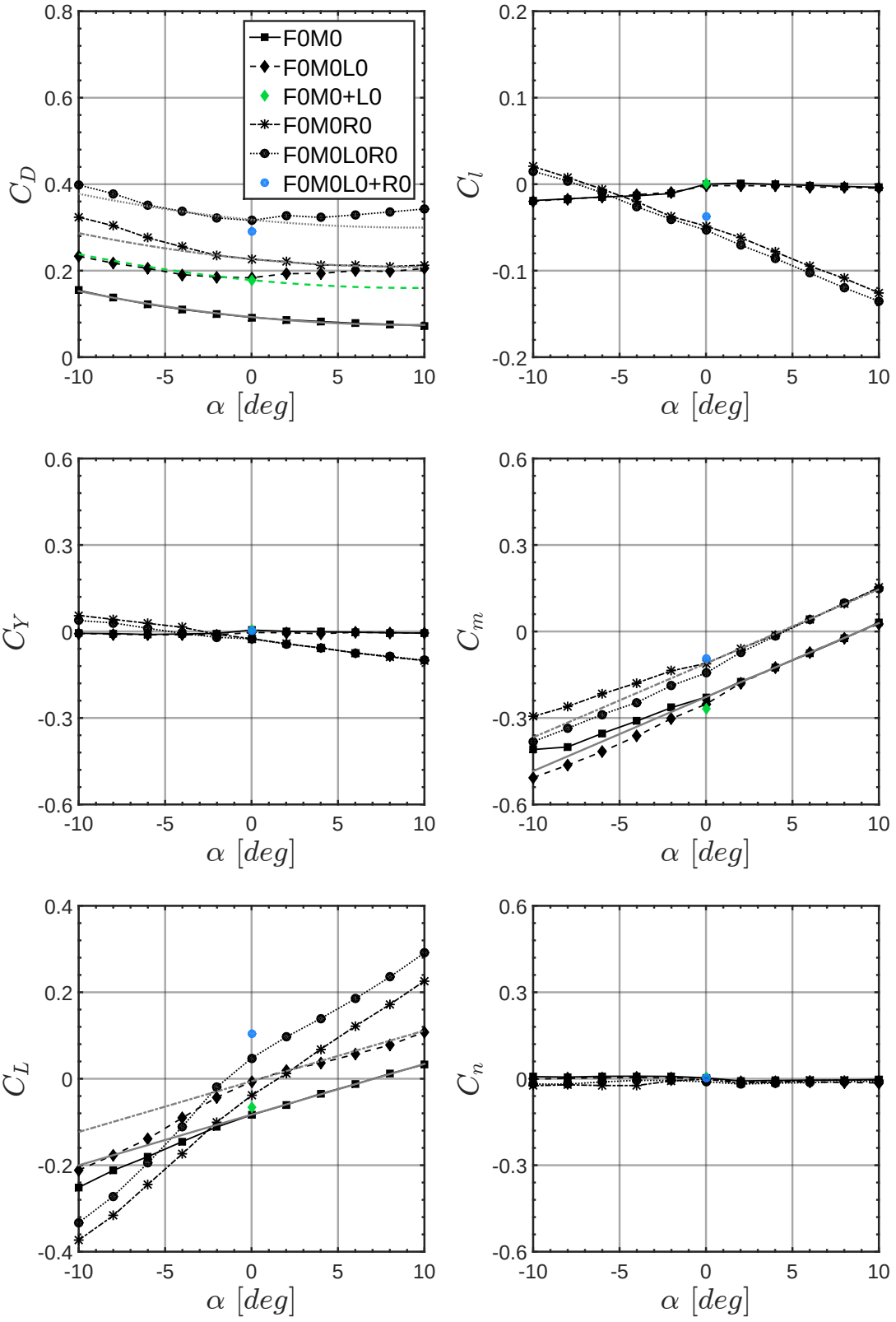

Figure 5.4: *Aerodynamic force and moment coefficients in dependency of* -10 *deg* $\leq \alpha \leq$ 10 *deg for configuration F0M0, F0M0+L0, F0M0L0, F0M0L0+R0 and F0M0L0R0.* $Re_\infty \approx 0.95 \cdot 10^6$, $\beta = 0$ *deg.*

F0M0's C_L characteristic as a function of α at $\beta = 0\ deg$ features a constant $\partial C_L/\partial\alpha = 0.69$ in the range of $-2\ deg \leq \alpha \leq 10\ deg$; see linear least-square-fit $C_L(\alpha)$ depicted as grey solid line in Fig. 5.4. For $-10\ deg \leq \alpha \leq -2\ deg$, the lift curve slope is also constant, but $\partial C_L/\partial\alpha = 1.0$. This indicates that the flow topology changes at $\alpha \approx -2\ deg$. For utility helicopters featuring blunt, ramp-type aft-body sections, Seddon [35] describes three different flow topologies. The vortex flow, the eddy flow and streamlined flow topology. He claims that depending on the rear fuselage upsweep angle Φ and the angle of attack one of those three flow topologies is observed. Based on the eccentricity at the stern $\Delta z_{stern}/l_{ref}$ and the rear tapering length l_r/l_{ref} of the investigated fuselage, the upsweep angle is approximated to $\Phi = 35\ deg$; see section 2.5. According to Seddon, this results in the eddy flow topology in the range of $-2\ deg \lesssim \alpha \lesssim 8\ deg$ for the given Φ. This could explain the observed change in $\partial C_L/\partial\alpha$ at $\alpha \approx -2\ deg$. However, the sudden change in C_D when switching from the vortex to the eddy flow topology as described by Seddon is not observed for F0M0.

The reason for this deviation is associated to the smooth contour change at the longitudinal and lateral tapering implemented at F0M0's rear fuselage upsweep instead of a typical ramp-type geometry. Studying F0M0's flow topology for $\alpha, \beta = 0\ deg$ confirms this effect. In section 5.4 it is shown, that a substantial separation occurs at the beginning of F0M0's rear fuselage upsweep. This is also observed for ramp-type geometries in the eddy-flow regime. However, for F0M0 still a three-dimensional free surface separation occurs at which partially an upsweep vortex is formed. Thus, the transition from the vortex to the eddy flow topology occurs via a hybrid vortex and eddy flow topology at F0M0's rear fuselage.

Investigating F0M0's C_m as a function of α at $\beta = 0\ deg$ shows, that the fuselage is inherently unstable with the empennage not installed ($\partial C_m/\partial\alpha > 0$). For F0M0, also a change in its C_m characteristic is observed at $\alpha \approx -2\ deg$. For $-2\ deg \leq \alpha \leq 10\ deg$ the derivative $\partial C_m/\partial\alpha$ is equal $1.45 \approx const.$. For $-10\ deg \leq \alpha \leq -2\ deg$, F0M0's C_m becomes more stern-balanced compared to the linear regression of C_m for $-2\ deg \leq \alpha \leq 10\ deg$. This is in agreement with the increased $\partial C_L/\partial\alpha$ in this region of α. Generating a larger down force at the rear fuselage upsweep for the given CG-location results in a larger C_m as observed.

F0M0's C_l as a function of α is neutral for $-2\ deg \leq \alpha \leq 10\ deg$. However, for $-10\ deg \leq \alpha < 0\ deg$ F0M0's C_l is negative. This is remarkable, since the model is symmetric with respect to the x_m, z_m plane except some minor asymmetries associated to the external equipment attachment surfaces at the fuselage ventral side towards the bow; see Fig. 5.1.

Adding the skid-landing-gear to F0M0 in order to obtain F0M0L0 changes the characteristic of C_D over α considerably. Especially, for $\alpha \geq 0\ deg$ this becomes evident through a positive $\partial C_D/\partial\alpha$. However, for $-10\ deg \leq \alpha \leq -2\ deg$ F0M0L0's drag characteristic is similar to the one observed for F0M0. In fact, adding L0's C_D at $\alpha, \beta = 0\ deg$ to $C_{D,min}$ of F0M0's least-square parabolic fit $C_D(\alpha)$ yields a good agreement with the characteristic of F0M0L0's C_D between $-10\ deg \leq \alpha \leq -2\ deg$; see green-dashed line in Fig. 5.4. Thus, the skid-landing-gear apparently causes no aerodynamic interference on F0M0 affecting C_D for this range of α. For $-2\ deg \leq \alpha \leq 10\ deg$, the skid-landing-gear causes a considerable amount of aerodynamic interference on F0M0. In section 5.4 it

is shown for $\alpha, \beta = 0\ deg$, that L0 perturbs the flow along the fuselages ventral side, which leads to a more substantial separation at the fuselage's rear upsweep. This effect becomes more and more pronounced as α is increased in the range of $-2\ deg \leq \alpha \leq 10\ deg$.
F0M0L0's C_L as a function of α for $\beta = 0\ deg$ in the range of $-10\ deg \leq \alpha \leq 10\ deg$ reveals two different characteristics. For $0\ deg \leq \alpha \leq 10\ deg$, F0M0L0's C_L features a constant offset of $\Delta C_L \approx 0.08$ compared to F0M0's linearly increasing C_L. However, the lift generated at the skid-landing gear alone at $\alpha, \beta = 0\ deg$ does only account for about 22% of the observed offset; see F0M0+L0. Thus, the skid-landing-gear's aerodynamic interference on F0M0 also impacts on the fuselage's lift. Decreasing α between $-10\ deg \leq \alpha \leq -2\ deg$ at $\beta = 0\ deg$ continuously reduces L0's impact on lift. In the range of $-10\ deg \leq \alpha \leq -2\ deg$ L0's interference on F0M0 with respect to drag vanishes. Nevertheless, F0M0L0's C_L is still larger in this α - range compared to F0M0. It is unlikely that this increase in C_L is associated to the skid-landing-gear itself, because it would also experience a negative angle of attack at its steps and skid in this α - range. Thus, even though L0's aerodynamic interference on F0M0 with respect to drag vanishes its aerodynamic interference with respect to lift prevails for $-10\ deg \leq \alpha \leq -2\ deg$ at $\beta = 0\ deg$.
The influence of both the observed changes in F0M0L0's C_D and C_L are superimposed on F0M0L0's C_m characteristic. For $2\ deg \leq \alpha \leq 10\ deg$, adding L0 to F0M0 does not affect C_m at all. Thus, the increase in C_D and the increase in C_L counter balance each other in their effect on C_m for this range of α. Only for $-10\ deg \leq \alpha \leq 2\ deg$, F0M0L0's C_m is decreased compared to F0M0. For F0M0L0's C_l, the same characteristic as described for F0M0 is observed.
Adding the rotor-head R0 to F0M0 results in configuration F0M0R0. For $-2\ deg \leq \alpha \leq 10\ deg$, F0M0R0's C_D characteristic is similar to the one observed for F0M0. Adding the difference in C_D between F0M0 and F0M0R0 at $\alpha, \beta =\ deg$ to $C_{D,min}$ of F0M0's least-square parabolic fit $C_D(\alpha)$ yields a good agreement with the characteristic of F0M0R0's C_D between $-2\ deg \leq \alpha \leq 10\ deg$; see grey dash-dotted line in Fig. 5.4. However, the difference in C_D between F0M0 and F0M0R0 is larger than R0's C_D. The additional increase in C_D is probably associated to M0. When R0 is installed M0 is not closed anymore in order to provide the necessary space for R0's mechanical control and shaft. Additional aerodynamic interference of R0 with F0 cannot be observed at the rear fuselage though; see section 5.3. Thus, opening the mast fairing cavity is responsible for R0's interference on F0M0. The constant offset in F0M0R0's C_D in the range of $-2\ deg \leq \alpha \leq 10\ deg$ indicates that this interference is indepent of α in this α - range. However, decreasing α in the range of $-10\ deg \leq \alpha \leq -2\ deg$ causes an additional increase in F0M0R0's C_D compared to F0M0. This could be associated to a more pronounced interaction of the incoming flow with the mast-fairing cavity at negative angles of attack.
F0M0 and F0M0R0's have the same C_L at $\alpha \approx -2\ deg$. For larger angle of attack ($-2\ deg \leq \alpha \leq 10\ deg$), F0M0R0's $\partial C_L/\partial\alpha$ features a constant increase by $\partial C_L/\partial\alpha = 0.87$ compared to F0M0. For smaller angle of attack ($-10\ deg \leq \alpha \leq -2\ deg$), F0M0R0's lift curve slope even increases by $\partial C_L/\partial\alpha = 0.96$ compared to F0M0.

F0M0R0's C_m characteristic is only changed by a constant offset of $\Delta C_m \approx 0.12$ compared to F0M0. This offset is related to the additional drag generated at M0 and R0 in the presence of the rotor-head. The increase in C_L associated to R0 has only a minimal influence on C_m due to the short lever arm between the rotor axis and the CG-location. In consequence the configuration becomes more stern-balance by adding the rotor-head.
R0 changes F0M0R0'S C_Y characteristic compared to F0M0. Without the rotor-head installed the side force coefficient C_Y is nearly zero, because no significant asymmetries with respect to the fuselage symmetry plane are present. With R0 installed C_Y as a function of α features a negative $\partial C_Y/\partial\alpha = -0.4$ for $-10\ deg \leq \alpha \leq 10\ deg$ at $\beta = 0\ deg$. C_Y becomes zero at the same α were the difference between F0M0's and F0M0R0's C_L vanishes. Thus, the angle of zero lift for the rotor head is identical to the angle of zero side force. This shows that the side-force is associated to the generation of lift at the rotor-head in consequence of a tilted thrust vector under the influence of collective and cyclic pitch control. As a result of the side force generated at the rotor-head F0M0R0's rolling moment coefficient C_l features a negative slope throughout $-10\ deg \leq \alpha \leq 10\ deg$.
Adding the rotor-head R0 to F0M0L0 yields configuration F0M0L0R0. The characteristic of F0M0L0R0's C_D as a function of α is compared to the parabolic least-square-fit for F0M0's C_D. For this purpose, $C_{D,min}$ of F0M0's parabolic least-square-fit is increased by the difference in C_D between F0M0L0R0 and F0M0 at $\alpha, \beta = 0\ deg$; see grey dotted line in Fig. 5.4. Through this comparison it becomes clear that the characteristic of F0M0L0R0's C_D over α can be divided into two regions. One region in which R0 and one region in which L0 causes the deviation from F0M0's C_D characteristic, respectively, $-10\ deg \leq \alpha \leq -2\ deg$ and $-2\ deg\alpha \leq 10\ deg$. Comparing C_D of F0M0L0+R0 with F0M0L0R0's C_D at $\alpha, \beta = 0$ shows that the drag increase is mainly associated to R0's component drag.
Generally it can be concluded, that F0M0L0R0's force and moment coefficients can be obtained by superimposing the increment between F0M0L0 and F0M0 onto F0M0R0. Thus, no aerodynamic interference between R0 and L0 is impacting on the characteristics of the complete configuration F0M0L0R0 for $-10\ deg \leq \alpha \leq 10\ deg$ at $\beta = 0\ deg$.
In Fig. 5.5, the force and moment coefficients for F0M0, F0M0L0, F0M0R0 and F0M0L0R0 are presented for $-10\ deg \leq \beta \leq 10\ deg$ at $\alpha = 0\ deg$. Performing a parabolic least-square-fit for F0M0's C_D as a function of $-10\ deg \leq \beta \leq 10\ deg$ at $\alpha = 0\ deg$ returns a minimal drag coefficient $C_{D,min} = 0.0911$ at $\beta = \beta_{min} = 0.1\ deg$ and the quadratic pre-factor $a = 3.61 \cdot 10^{-4}$ according to Eq. 5.2. The result for F0M0's $C_D(\beta)$ is depicted in Fig. 5.5 as grey solid line.

$$C_D(\beta) = a \cdot (\beta - \beta_{min})^2 + C_{D,min} \tag{5.2}$$

Thus, F0M0's C_D shows that the minor asymmetries at the fuselage's ventral side do not impact on F0M0's drag characteristic as a function of β for $\alpha = 0\ deg$.

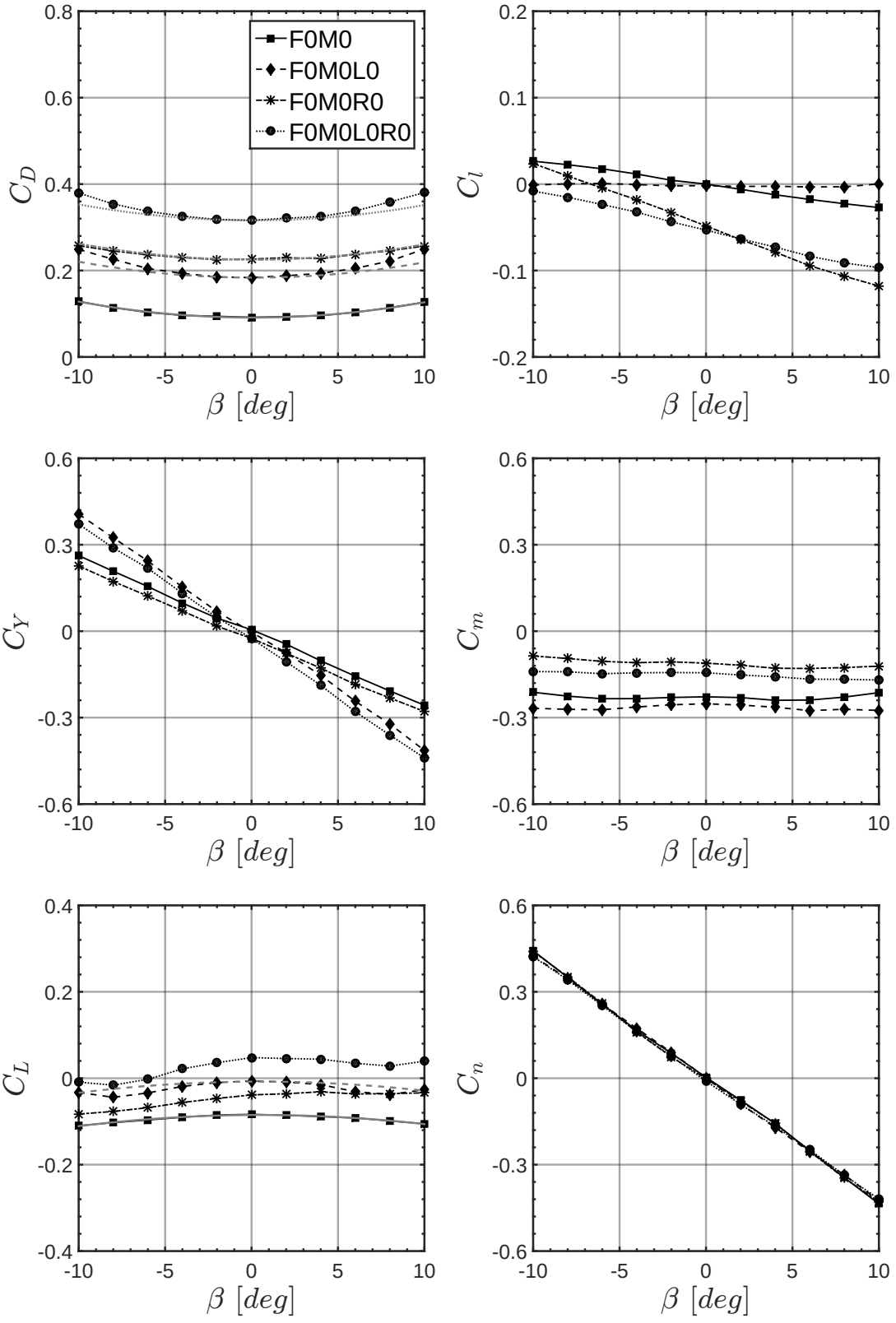

Figure 5.5: *Aerodynamic force and moment coefficients in dependency of* -10 *deg* $\leq \beta \leq$ 10 *deg for configuration F0M0, F0M0L0, F0M0R0 and F0M0L0R0.* $Re_\infty \approx 0.95 \cdot 10^6$, $\alpha = 0$ *deg.*

F0M0's C_Y characteristic as a function of β is also symmetric with respect to $\beta = 0\ deg$, featuring $C_Y > 0$ for $-10\ deg \leq \beta < 0\ deg$ and $C_Y < 0$ for $0\ deg < \beta \leq 10\ deg$. Throughout the investigated β - range F0M0's C_Y varies at a constant $\partial C_Y/\partial\beta = -1.49$.

$$C_L(\beta) = a \cdot (\beta - \beta_{max})^2 + C_{L,max} \tag{5.3}$$

F0M0's C_L in dependence of $-10\ deg \leq \beta \leq 10\ deg$ can also be described with a parabolic least-square-fit. The curvature of this parabola is inverted compared to the one obtained for F0M0's C_D. Hence, the formulation for $C_L(\beta)$ is adapted as described in Eq. 5.3. The obtained parameter for the parabola are the parabolic pre-factor $a = -2.34 \cdot 10^{-4}$ and the maximum lift coefficient $C_{L,max}$ at $\beta = \beta_{max} = 0.1\ deg$. $C_L(\beta)$ is depicted in Fig. 5.5 as grey solid line. Thus, as F0M0's drag increases for $|\beta| > 0\ deg$ more downforce is generated at the fuselage.
F0M0's C_l reveals an almost linear dependency of $-10\ deg \leq \beta \leq 10\ deg$ at $\partial C_l/\partial\beta = -0.15$, which is also symmetric with respect to $\beta = 0\ deg$.
Since both F0M0's C_D and C_L as a function of β are symmetric with respect to $\beta = 0\ deg$ this behaviour is also observed for C_m. For F0M0's C_m almost no dependency of β is observed, which could be explained with the similar but opposing trends for the parabolic characteristic of F0M0's C_D and C_L. F0M0 is nose-heavy over the entire investigated β - range at $\alpha = 0\ deg$.
Furthermore, F0M0 is unstable in yaw for $-10\ deg \leq \beta \leq 10\ deg$ since the empennage is neglected on the wind tunnel model. This becomes clear in F0M0's C_n characteristic as a function of β by a negative C_n gradient of $\partial C_n/\partial\beta = -2.52$. For F0M0L0, F0M0R0 and F0M0L0R0 almost identical trends of C_n are observed. Thus, the skid-landing-gear L0 and the rotor-head R0 do not contribute to F0M0L0R0's yaw instability for $-10\ deg \leq \beta \leq 10\ deg$ at $\alpha = 0\ deg$.
F0M0L0's C_D characteristic for $-10\ deg \leq \beta \leq 10\ deg$ at $\alpha = 0\ deg$ features a similar trend as observed for F0M0's C_D. Adding the difference in drag between F0M0 and F0M0L0 at $\alpha, \beta = 0\ deg$ to F0M0's $C_D(\beta)$ (grey dashed line) reveals that the drag increase for $|\beta| > 0\ deg$ is amplified through the presence of L0. However, it is obvious that within the domain of fast-forward level flight ($-2\ deg \leq \beta \leq 2\ deg$) the deviation of F0M0L0's from F0M0's C_D characteristic is minimal.
Adding L0 to F0M0 does not affect the general characteristic of C_Y; only $\partial C_Y/\partial\beta$ is decreased from -1.49 to -2.35.
F0M0L0's C_L increases significantly compared to F0M0's C_L over the entire β - range. For $-6\ deg \leq \beta \leq 6\ deg$ also a parabolic trend is observed, but with an increased curvature compared to F0M0. However, as for C_D the deviation of F0M0L0's from F0M0's C_L characteristic is minimal within the fast-forward level flight domain; see F0M0's $C_L(\beta)$ shifted by the difference in C_L between F0M0 and F0M0L0 at $\alpha, \beta = 0\ deg$ (dashed grey line). For β below $-6\ deg$ and in excess of $6\ deg$, the characteristic deviates from F0M0's $C_L(\beta)$ shifted by the difference in C_L between F0M0 and F0M0L0 at $\alpha, \beta = 0\ deg$. This could be related to a premature flow-separation at the rear fuselage upsweep in consequence of the skid-landing-gear's presence under the influence of sideslip.
C_m decreases in consequence of F0M0L0's increased C_D and C_L compared to F0M0's. Thus, F0M0L0 becomes slightly more nose-heavy in comparison to F0M0.

C_m's dependency of β remains minimal for F0M0L0.
F0M0R0's C_D characteristic is in good to excellent agreement with F0M0's parabolic least-square-fit $C_D(\beta)$ when adding the difference in drag between F0M0 and F0M0L0 at $\alpha, \beta = 0\ deg$ to F0M0's $C_D(\beta)$; see grey dash-dotted line in Fig. 5.5. Thus, R0's C_D and its aerodynamic interference with F0M0 is apparently independent of $-10\ deg \leq \beta \leq 10\ deg$ at $\alpha = 0\ deg$.
For F0M0R0's C_Y as a function of $-10\ deg \leq \beta \leq 10\ deg$ at $\alpha = 0deg$, the presence of R0 shifts F0M0's characteristic by a constant margin of $\Delta C_Y = -0.03$. This offset is probably associated to the collective and cyclic pitch input for the truncated blade cuffs, which deflects the resultant force vector slightly towards starboard.
The effect of the collective and cyclic pitch input also becomes evident in F0M0R0's C_L characteristic over β at $\alpha = 0\ deg$. This leads to a linear increase of the lift generated at the rotor head for $-10\ deg \leq \beta \leq 10\ deg$. The reason for this behaviour can be related to the fixed collective and cyclic trim condition, which is derived for fast-forward level flight at $\alpha, \beta = 0\ deg$; see section 3.2. Thus, for $\beta < 0\ deg$ the angle of attack on the advancing side is reduced and vice versa for $\beta > 0\ deg$. In consequence F0M0R0's C_L almost gradually increases as β is increased. Nevertheless, the deviation from C_L at $\alpha, \beta = 0\ deg$ is minimal within the range of fast-forward level flight.
Furthermore, R0's negative C_Y at $\beta = 0\ deg$ and its form drag significantly changes F0M0R0's C_l characteristic compared to F0M0's. Firstly, R0's negative C_Y at $\beta = 0\ deg$ leads to a negative C_l at this incidence due to the force application point above the CG location (positive lever arm). Secondly, R0's form drag decreases F0M0R0's $\partial C_l/\partial\beta$ compared to F0M0's by 0.25 to $\partial C_l/\partial\beta = -0.4$.
F0M0R0's C_m is significantly increased compared to the on of F0M0. The reason for this increase is associated to the additional rotor-head drag. Due to the short lever arm between the rotor axis and the CG-location the lift generated at the rotor head only has a minor impact on C_m. Consequently, the asymmetric characteristic of F0M0R0's C_L only marginally transfers into a β - dependency of C_m. However, the increase in C_D associated to R0 translates into an increase in C_m and F0M0R0 becomes more stern-balanced compared to F0M0.
As for the investigated α-range at $\beta = 0\ deg$ it can be concluded that F0M0L0R0's force and moment coefficients can be obtained by superimposing the increment between F0M0L0 and F0M0 onto F0M0R0 for the investigated β-range at $\alpha = 0\ deg$. Thus, no aerodynamic interference between R0 and L0 is impacting on the characteristics of the complete configuration F0M0L0R0 for $10\ deg \leq \beta \leq 10\ deg$ at $\alpha = 0\ deg$.
Fast-forward level flight is the most relevant flight condition within the mission envelopes of TEL-class utility helicopter for achieving fuel flow reduction by aerodynamic optimisation. For this flight condition, parasite drag contributes significantly to the power-requirements as reported by Stroub and Rabbott [39]; see also chapter 1. Thus, the focus of this work is the aerodynamic optimisation of a TEL-class utility helicopter through parasite drag reduction. From the aerodynamic analysis of the baseline's force and moment characteristics in dependency of α and β it becomes clear, that the aerodynamic characteristics of the investigated helicopter do not deviate considerably from the conditions at $\alpha, \beta = 0\ deg$ within the fast-forward level flight domain ($-2\ deg \leq \alpha, \beta \leq 2\ deg$). Thus, the

performed aerodynamic optimisation focuses on reducing the drag without significantly increasing the down-force at $\alpha, \beta = 0$ *deg*.

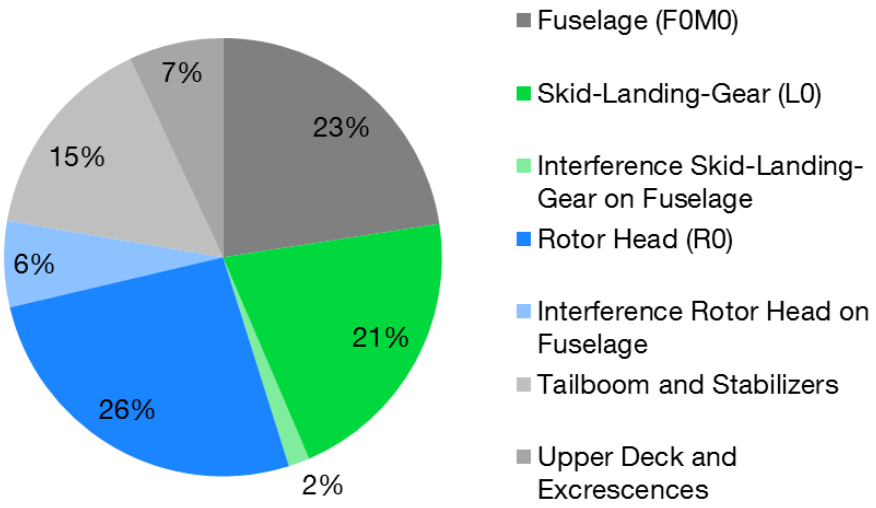

Figure 5.6: *Drag Decomposition for the reference configuration. The drag contribution of the components not included on the ADHeRo W/T model are based on corporate data of Airbus Helicopters Deutschland.* $Re_\infty \approx 0.95 \cdot 10^6$, $\alpha, \beta = 0$ *deg*.

In Fig. 5.6, the drag decomposition of the reference configuration is depicted. The data for the component drag of the fuselage, the skid-landing-gear and the rotor-head as well as the aerodynamic interference of the skid-landing-gear and the rotor-head on the fuselage at $\alpha, \beta = 0$ *deg* can be assessed with the available experimental database. However, in order to assess the complete parasite drag decomposition of the reference geometry, also the contribution of the tailboom, the stabilisers, the flow through the upper deck and excrescences needs to be assessed. This is not possible with the ADHeRo W/T model. Therefore, Airbus Helicopters Deutschland provided corporate data for the contribution of those components to the parasite drag. The author acknowledges the fact that any modification to the fuselage, the skid-landing-gear or the rotor-head could also interfere on the aerodynamic characteristics of those additional components. However, this is beyond the scope of the presented work and, therefore, this simplification is employed to estimate the entire parasite drag decomposition for the reference as well as for the optimised configurations.
Fig. 5.6 reveals, that the components included on the ADHeRo W/T model represent 78% of the reference's configuration total parasite drag. The fuselage itself already contributes 23% to the total parasite drag. Another 23% of the total parasite drag are associated to the skid-landing-gear. The majority of the skid-landing-gear's contribution is linked to its form drag (21%). Further 2% of the total parasite drag are caused by the skid-landing-gear's aerodynamic interference on the fuselage. In section 5.3 and 5.4 it is shown, that this additional fuselage drag is associated to an increased extension of the flow separation at the fuselage's rear upsweep in the presence of the skid-landing-gear. The biggest drag increment is generated at the rotor-head, which causes 32% of the total parasite drag. This contribution splits into 26% generated through the rotor-head's form drag and 6%

occurs due to its aerodynamic interference with the fuselage. However, comparing the surface pressure distribution of F0M0L0 with F0M0L0R0 did not reveal any significant differences by adding the rotor head to F0M0L0; see section 5.3. The surface pressure data do not allow to investigate the influence of the mast-fairing cavity, housing the rotor-shaft and mechanical control elements (i.e the swash-plate and the scissors), on the local pressure distribution. In the experiments, this cavity is closed when the rotor head is not installed. Thus, the impact of the rotor-heads aerodynamic interference on the fuselage drag could be associated to the mast-fairings cavity. Nevertheless, more evidence needs to be acquired in order to confirm this hypothesis. The tailboom and stabilisers contribute 15% and the flow through the upper deck and excrescences contribute 7% to the total parasite drag.

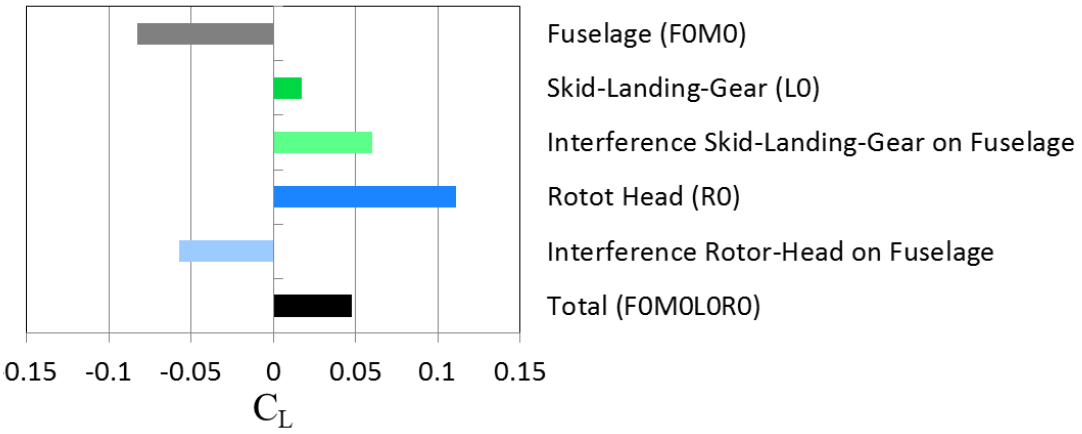

Figure 5.7: *Lift Decomposition for the baseline configuration F0M0L0R0.* $Re_\infty \approx 0.95 \cdot 10^6$*,* $\alpha, \beta = 0$ *deg.*

In Fig. 5.7, the lift decomposition for the baseline configuration F0M0L0R0 is depicted for test condition 'd' at $\alpha, \beta = 0$ *deg*. As for the drag decomposition it is distinguished between the direct contribution of the components F0M0, L0 and R0 and L0's and R0's interference on the fuselage and mast fairing F0M0.
F0M0 alone generates down-force, since the flow is not fully separated at the rear fuselage's upsweep; see section 5.3 and 5.4. The skid-landing-gear adds lift to the configuration. However, this contribution is comparably small. More relevant is the impact of L0's aerodynamic interference on the fuselage. In consequence of the skid-landing-gear wake, the flow past the fuselage's ventral side is disturbed - causing a more substantial flow separation at the rear fuselage's upsweep; see section 5.3 and 5.4. The additional lift generated both at the skid-landing-gear and through its aerodynamic interference on the fuselage almost fully balances out F0M0's down force. Another considerable contribution to the lift results from the vertical thrust of the rotor head. The blade cuffs were optimised for low drag by Kneisch et al. [24]. In consequence, they feature a drop-like shape, which generates lift under the influence of collective and cyclic pitch inputs on the rotating rotor-head in fast-forward level flight's trim state. This lift is partially deteriorated under the influence of the rotor heads aerodynamic interference on the fuselage. As discussed above, there is no notable difference between F0M0L0's and F0M0L0R0's surface pressure distribution. Therefore, it is assumed that

opening the mast fairing cavity when the rotor-head is installed also causes the aerodynamic interference on F0M0 with respect to downforce.

5.3 Surface Pressure

In Fig. 5.8, F0M0's c_p contours in the rear fuselage region are shown for $\alpha, \beta = 0\ deg$ (top left). Furthermore, c_p is depicted as a function of $y_r/(b_f/2)$ and x_r/l_r for the selected horizontal slices $Z5, Z7, Z9, Z11$ and the vertical slice Y0, respectively. Fig. 5.8 presents both the results obtained by experiment and numerical simulation at the test condition 'd'. The markups showing the flow characteristics in Fig. 5.8 are derived from the topological analysis of F0M0's near-surface and wake flow, which is based on simulation data; see section 5.4. The surface pressure data obtained by experiment and simulation are generally in good agreement. However, some differences are notable. Comparing the experimental and simulation data for the pressure distribution along Y0 reveals that the simulation under predicts the pressure level at the rear fuselage's symmetry plane by about $\Delta c_p \approx 0.1$. Nevertheless, the characteristic is predicted well by the simulation. Comparing the data along the horizontal slices Z5, Z7 and Z9 shows that even the absolute c_p values are well predicted for $y_r/(b_f/2) \neq 0$. Only at Z11 the deviation observed at $y_r/(b_f/2) = 0$ prevails for $y_r/(b_f/2) \neq 0$.
For F0M0, a significant suction peak is observed at the beginning of both the fuselage's vertical upsweep and lateral tapering; see Fig. 5.8. Vogel [43] shows that those suction peaks are associated to a significant change in the local surface curvature. In section 5.4, the near-surface and wake flow topology is discussed for the baseline configuration F0M0. By this analysis it is shown that downstream of those suction peaks the flow separates from the surface.
At the fuselage's lateral sides the separation occurs along the primary separation line SL2. SL2 emerges from a free-surface separation. In consequence, two regions have to be distinguished on SL2. The region along which vortex formation occurs in consequence of the free surface separation (SL2a) and where no vortex formation occurs (SL2b). At the beginning of the fuselage's vertical upsweep the separation occurs along the separation line SL3, which originates from the separation saddle S_{S3}. The effect of the large scale separation originating from separation lines SL2 and SL3 on F0M0's rear fuselage pressure distribution is discernible as plateaus in c_p as a function of $y_r/(b_f/2)$. At slices Z7, Z9 and Z11 the pressure plateau covers the regions between $y_r/(b_f/2) = \pm 0.78$, $y_r/(b_f/2) = \pm 0.75$ and $y_r/(b_f/2) = \pm 0.64$, respectively.
At Z11, the pressure plateau is associated to the separation from SL3. In this region the vortex formation along SL2a is still effective and the flow remains attached between SL2a and SL3. At Z9, the vortex formation has broke down. This occurs since the separation region associated to SL3 disturbs the vortex formation as it approaches the primary separation line SL2. Nevertheless, the flow in between SL2b and SL3 is still attached. Thus, the pressure plateau at Z9 is associated to SL3. Between the vertical position of Z9 and Z7 SL3 reaches SL2b and separates from the surface. Therefore, the pressure plateau at Z7 is defined by the separation from SL2b.

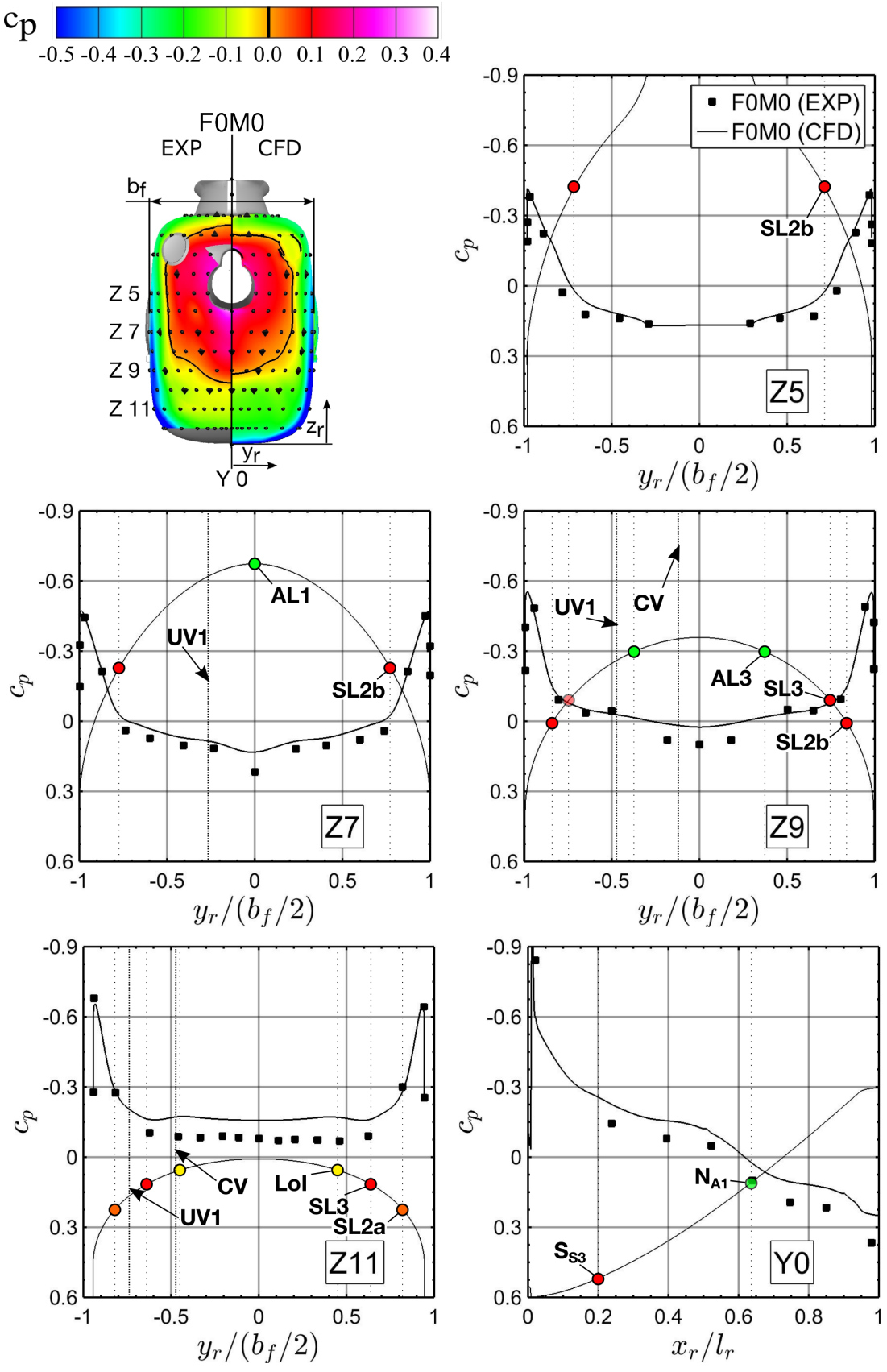

Figure 5.8: *c_p distribution at the rear fuselage for F0M0 (top left) and the associated slices Z5, Z7, Z9,Z11 and Y0. $Re_\infty \approx 0.95 \cdot 10^6$, $\alpha, \beta = 0$ deg.*

The vortex which is formed at the free-surface separation from SL2a is the upsweep vortex UV1. Since the flow around the fuselage is symmetric with respect to the model' symmetry plane UV1 appears on either side of the fuselage. Those upsweep vortices are counter-rotating. As long as they remain in close proximity to the surface, the upsweep vortices induce additional lateral velocities near the fuselage surface. Vogel [43] showed that this effect leads to local pressure minima at the surface near the vortices' trajectories. However, Vogel did not consider the open cavities at the fuselage's ventral side housing the skid-landing-gears central cross-beams. This leads to a more pronounced flow separation at the beginning of the fuselage's rear upsweep; i.e. SL3. As discussed above this confines the vortex formation along SL2 and the vortex strength of UV1 is reduced compared to the case considered by Vogel. Nevertheless, local pressure minima can be observed for F0M0's c_p as a function of $y_r/(b_f/2)$ along Z11 at $y_r/(b_f/2) = \pm 0.5$. However, for the fuselage including the cavities these minima are associated to an additional vortex pair caused by presence of the cavities; i.e. the cavity vortex CV.
In between the upsweep vortices, i.e. close to the models symmetry plane Y0, the counter-rotation of the vortices induce a velocity component in direction of the models positive vertical axis z_r. Thus, the flow past the fuselages bottom is re-energised with high momentum fluid from further away from the wall. In consequence, the flow reattaches at the attachment nodus N_{A1} after initial separation at S_{S3}. This effect also explains why a considerably amount of downforce is generated on F0M0; see section 5.2. Between those two points a recirculation zone (RZ) is formed within the large scale separation bounded by SL2b and SL3. RZ extends from $y_r/(b_f/2) = 0.2$ up to $y_r/(b_f/2) = 0.68$ causing a pressure plateau in this region; see slice Y0 in Fig. 5.8.
In Fig. 5.9, F0M0's dataset presented in Fig. 5.8 is compared to the corresponding dataset for F0M0L0. The markups showing the flow characteristics in Fig. 5.9 are associated to the topological analysis of F0M0L0's near-surface and wake flow; see section 5.4. Comparing the experimental and simulation data for F0M0L0 does not reveal a as good agreement as observed for F0M0. The simulation under predicts the pressure level for most of F0M0L0's rear fuselage region. The difference in c_p in those regions is in the range between -0.1 up to -0.2. Studying the deviation in detail reveals that the simulation predicts the primary separation location (SL5) at the fuselage's lateral side slightly more upstream compared to the experiment; see e.g. slice Z7. This effect impacts considerably on the obtained pressure level, since the primary separation is located in the region of the highest streamwise pressure gradient. Nevertheless, the characteristic of c_p as a function of $y_r/(b_f/2)$ and x_r/l_r is still predicted well.
Analyzing F0M0L0's c_p as a function of $y_r/(b_f/2)$ reveals that the size of the separated flow region increases considerably compared to F0M0. As mentioned above the primary separation is now associated to the separation line SL5, which originates from S_{S5}. This becomes evident as the pressure plateau's along Z7, Z9 and Z11 span almost over the entire fuselage's beam covering the regions between $y_r/(b_f/2) = \pm 0.85$, $y_r/(b_f/2) = \pm 0.92$ and $y_r/(b_f/2) = \pm 0.91$, respectively.

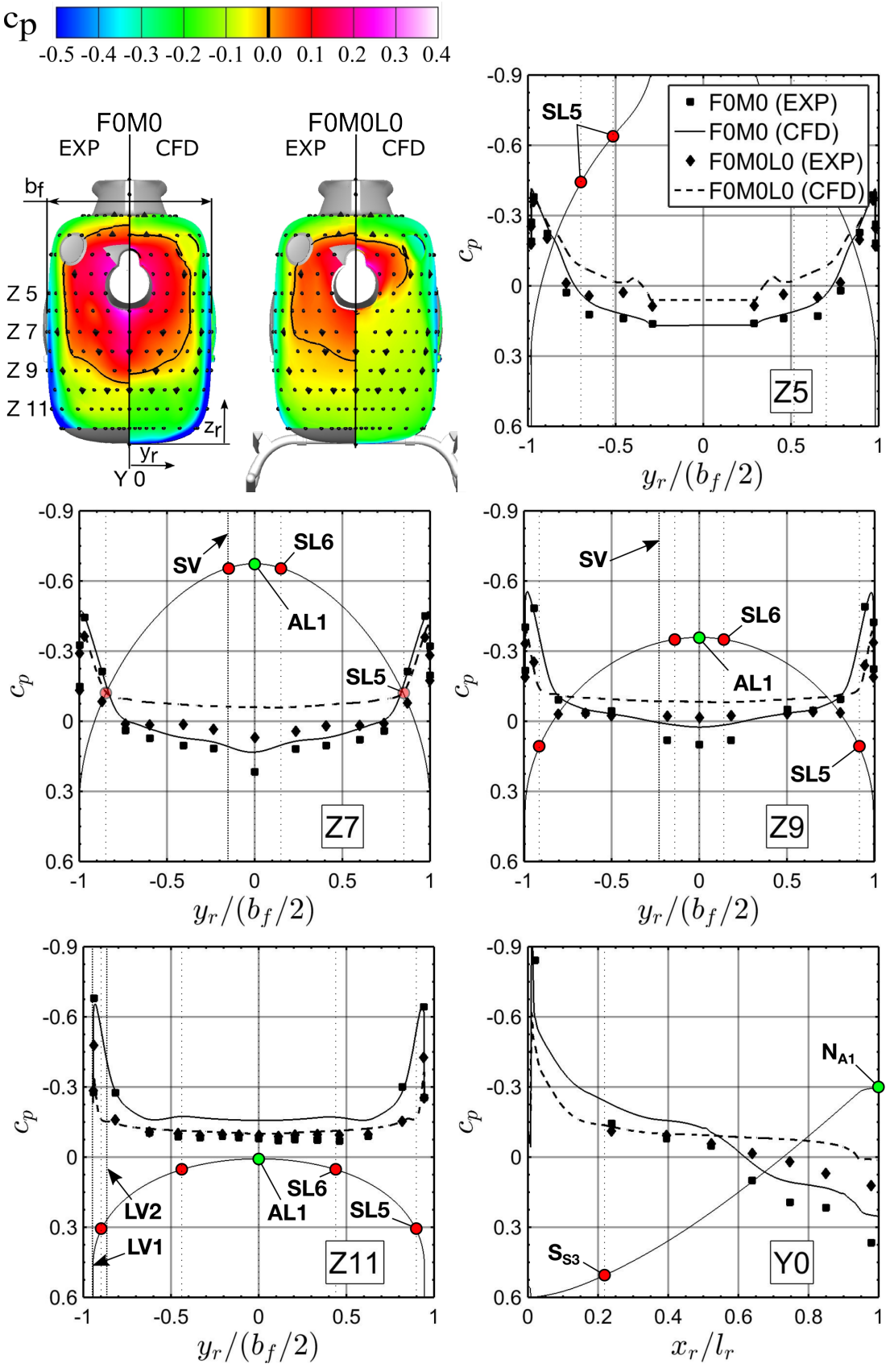

Figure 5.9: *c_p distribution at the rear fuselage for F0M0 and F0M0L0 (top left) and the associated slices Z5, Z7, Z9,Z11 and Y0. $Re_\infty \approx 0.95 \cdot 10^6$, $\alpha, \beta = 0$ deg.*

The lateral extension of F0M0L0's rear fuselage flow separation at Z7, Z9 and Z11 thereby increases compared to F0M0 by about 9%, 23% and 42%, respectively. Thus, also explaining the observed skid-landing-gears impact on the fuselage's drag; see section 5.2. The source of the more pronounced flow separation is the aerodynamic interference of the skid-landing-gear with the flow around the fuselage's ventral side. In consequence lower momentum fluid reaches the rear fuselage's upsweep and the flow cannot withstand the positive pressure gradient as long as for F0M0. The separation at the beginning of F0M0L0's rear fuselage vertical upsweep occurs at SL3 and SL4, which originate from S_{S3} and S_{S4}, respectively.
The increased size of the separation zone also attenuates the acceleration of the flow around the beginning of both the fuselage's vertical upsweep and lateral tapering. Thus, the suction peaks observed for F0M0 in these regions are attenuated in the presence of the skid-landing-gear.
Furthermore, the formation of the upsweep vortex along the free-surface separation observed for F0M0 is not observed on F0M0L0. This fact is associated to the more substantial flow perturbation in the presence of the skid-landing-gear, which suppresses the free-surface separation. In consequence, the flow also does not reattach on F0M0L0 as early as on F0M0. Nevertheless, a closed recirculation zone (RZ) is observed at F0M0L0's rear fuselage upsweep near the model's symmetry plane. Along Y0 this recirculation zone covers the region of $0.23 \leq x_r/l_r \leq 1$; i.e. between S_{S3} and N_{A1}. The increased extension of the recirculation zone also reduces the deflection of the flow along the model's positive vertical axis. This explains why the skid-landing-gear's aerodynamic interference was observed to reduce the fuselage's downforce; see section 5.2.
Instead of the upsweep vortices two different vortex systems emerge from F0M0L0's rear fuselage upsweep. These are the two pairs of landing-gear vortex LV1 and LV2 and the separation vortex SV. LV1 and LV2 are counter-rotating and are caused by the interaction of the flow with the skid-landing-gear's outer cross-beams and steps on either side of the fuselage. The separation vortex forms as higher momentum fluid enters the rear fuselage's upsweep along the dorsal side due to the lack of upward directed momentum entering from the ventral side. The dorsal flow rolls up within the separated flow regime to form the SV between SL5 and SL6. SV's sense of rotation is opposite to the one observed for F0M0's UV1. The vortices LV1, LV2 and SV were found to have no significant local impact on F0M0L0's rear fuselage pressure distribution.
In Fig. 5.10, F0M0L0's dataset presented in Fig. 5.9 is compared to the corresponding dataset for F0M0L0R0. Fig. 5.10 presents only the results obtained by experiment at the test condition 'd'.
By comparing the pressure distribution of F0M0L0 and F0M0R0 it becomes clear that adding the rotor head does not significantly affect the pressure field in the rear fuselage region. From section 5.2 the contribution of the rotor head itself and through aerodynamic interference on the fuselage to the drag and lift decomposition is known.

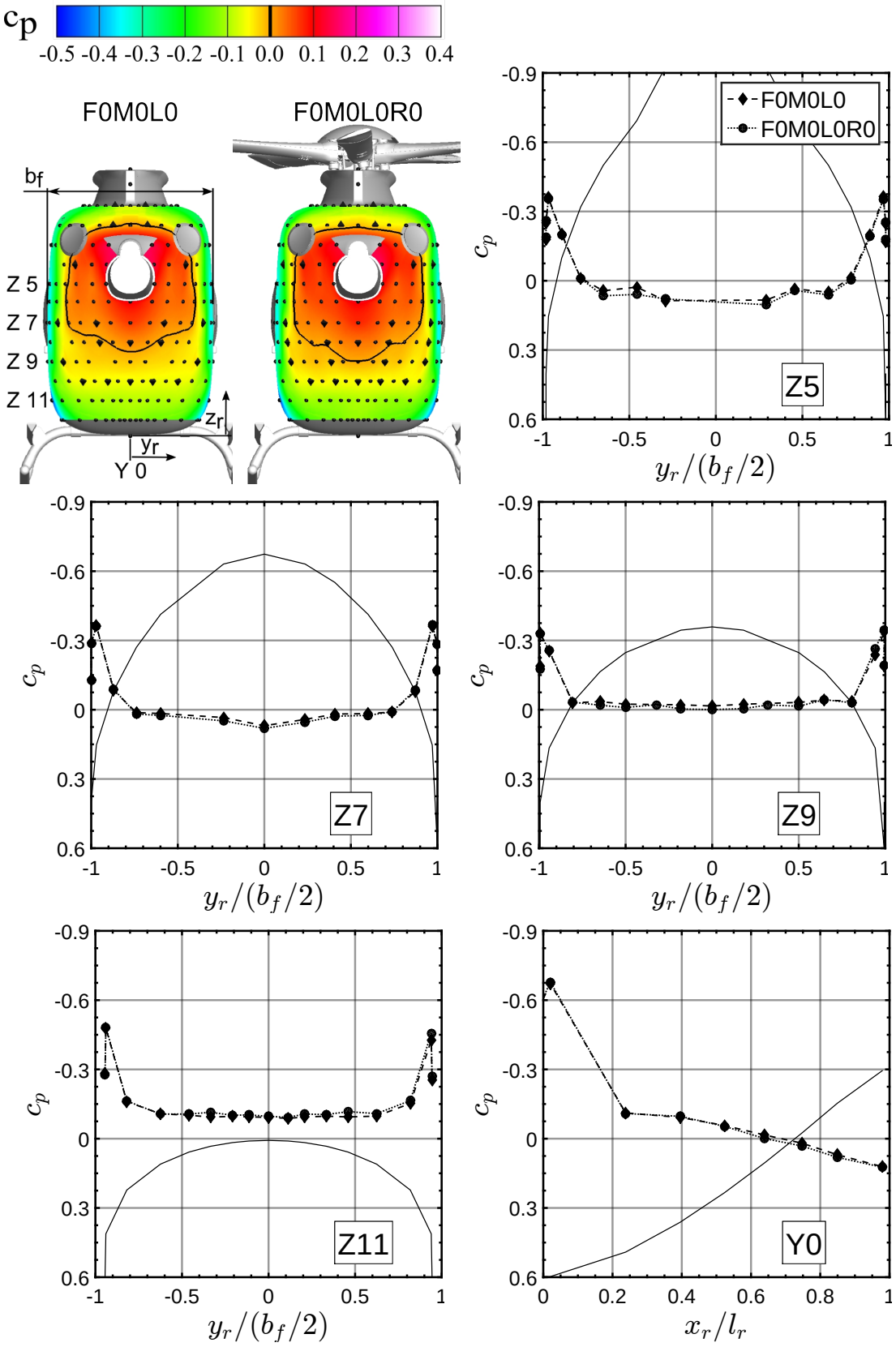

Figure 5.10: *c_p distribution at the rear fuselage for F0M0 and F0M0L0R0 (top left) and the associated slices Z5, Z7, Z9,Z11 and Y0. $Re_\infty \approx 0.95 \cdot 10^6$, $\alpha, \beta = 0$ deg.*

This analysis shows, that the rotor head itself generates a significant amount of lift, but its aerodynamic interference with the fuselage adds downforce to the total lift characteristic of the baseline configuration F0M0L0R0. Furthermore, the aerodynamic interference of the rotor head on the fuselage adds additional drag to the configuration. This appears contradictory to the observed surface pressure field in the rear part of fuselage. However, adding the rotor head to F0M0L0 also requires to remove the cover of the mast fairing cavity, which houses the rotor-shaft and control elements; see section 5.2. The associated distortion of the flow around the mast fairing might attenuate the lift and increases the drag generated at the mast fairing. This could resolve the observed contradiction, since the local pressure distribution at the open or closed mast fairing cannot be assessed with the available surface pressure data.

5.4 Flow Topology

In this section, the flow topologies of the baseline model's sub-configurations F0M0 and F0M0L0 are analysed. This includes both the near-surface flow topology and the flow topology in the wake of these configurations. F0M0's and F0M0L0's near-surface topology is analysed first and relevant flow regions are identified; see section 5.4.1. In a second step, the resulting wake flow topologies of F0M0 and F0M0L0 are analysed in order to identify vortex structures and their trajectories, recirculation zones and the envelope of the wake regions. These results are presented in section 5.4.2.

5.4.1 Near-Surface Flow Topology

The presented analysis of the near-surface flow topology is based on skin-friction-lines, which are assessed by URANS simulations. Based on these near-surface skin-friction patterns, the flow topology is analysed with respect to the classifications given by Chapman [11]. Chapman's analysis is based on identifying two-dimensional characteristic points within the near-surface flow topology. Generally, one has to distinguish between nodus (N) focus (F) and saddle (S) points. Nodi and foci are further categorised as attachment or separation type; e.g. N_A or N_S. Saddle points are always of separation type; i.e. S_S. For a closed topological near-surface field, the weighted sum of all nodi N and saddle points S needs to be equal to 2 around a three-dimensional body. Foci F are treated as nodi. Thus, all characteristic points of the near-surface field need to comply with Eq. 5.4.

$$\sum N - \sum S = 2 \tag{5.4}$$

The most simple closed near-surface flow topology around a spheroid is shown in Fig. 5.11. Since the flow remains fully attached, the only two characteristic points in this field are the attachment nodus and separation nodus at the body's nose and tail, respectively.

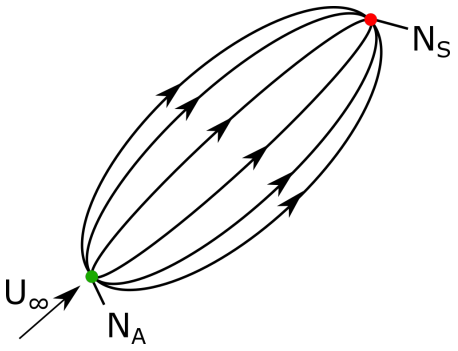

Figure 5.11: *Generic near-surface flow field around a spheroid.*

Furthermore, specific streamlines are high-lighted in this analysis. It is distinguished between attachment lines (AL), separation lines (SL) and characteristic streamlines (C). Attachment lines define the centre line for regions of diverging streamlines, whereas separation lines constitute the asymptotic line within regions of converging streamlines. The characteristic streamline is further categorised as incoming or back flow type. The reason for this is that the a pair of incoming characteristic streamlines C_i and back flow characteristic streamlines C_b define the two streamlines colliding in a separation saddle S_S. Based on the characteristic streamlines, the near-surface flow topology is sub-divided into different flow regions (FR). The nomenclature for describing the near-surface flow topology is summarised in Tab. 5.1.

Symbol	Description
AL	Attachment Line
C	Characteristic Streamline
N_A	Attachment Nodus
N_S	Separation Nodus
F_A	Attachment Focus
F_S	Separation Focus
S_S	Separation Saddle Point
SL	Separation Line

Table 5.1: *Summary of the nomenclature employed for the analysis of the near-surface flow topology.*

In Fig. 5.12 a) and b), a schematic representation of the near-surface flow topology is depicted for configuration F0M0. This topology is derived from calculated skin-friction-lines based on numerical simulations for test condition 'd' at $\alpha, \beta = 0\ deg$. In Fig. 5.12 a), the flow around the fuselage F0 is decomposed into relevant flow regions, whereas Fig. 5.12 b) depicts the identified structure of the near-surface flow topology. The flow topology at F0M0's fuselage can be divided into four main flow regions (FR). The flow around F0M0's fuselage is symmetric with respect to the model's symmetry plane. Thus, each flow region is observed on each side of the model's symmetry plane. The flow region FR1 covers the upper part of the fuselage; i.e. the engine cowling. FR1 further divides into the sub-regions FR1a and FR1b. FR1a covers the engine cowling area close to the models symmetry plane. In the lateral direction, FR1a is limited by the symmetry plane and the characteristic streamline of the back flow $C5_b$. $C5_b$ connects the attachment nodus at the fuselage nose N_{A0} and the separation saddle point S_{S5}; see Fig. 5.12 b). At the downstream end FR1a is limited by the end of the engine cowling at the junction to the tailboom. The flow topology at the tailboom is not considered in this analysis. Thus, the topology is closed at the downstream end by the fictional separation nodus N_{S0}. At the end of this section it is shown that the topology can be closed consistent with the topological rule after Chapman [11] by adding this fictional separation nodus.

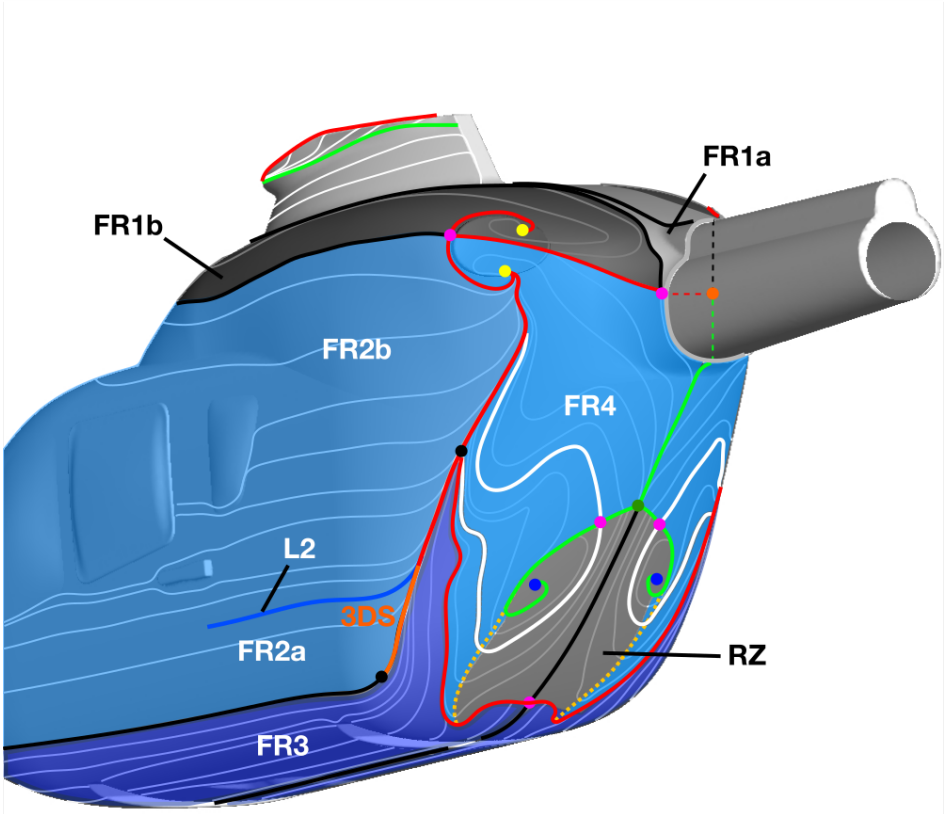

a)

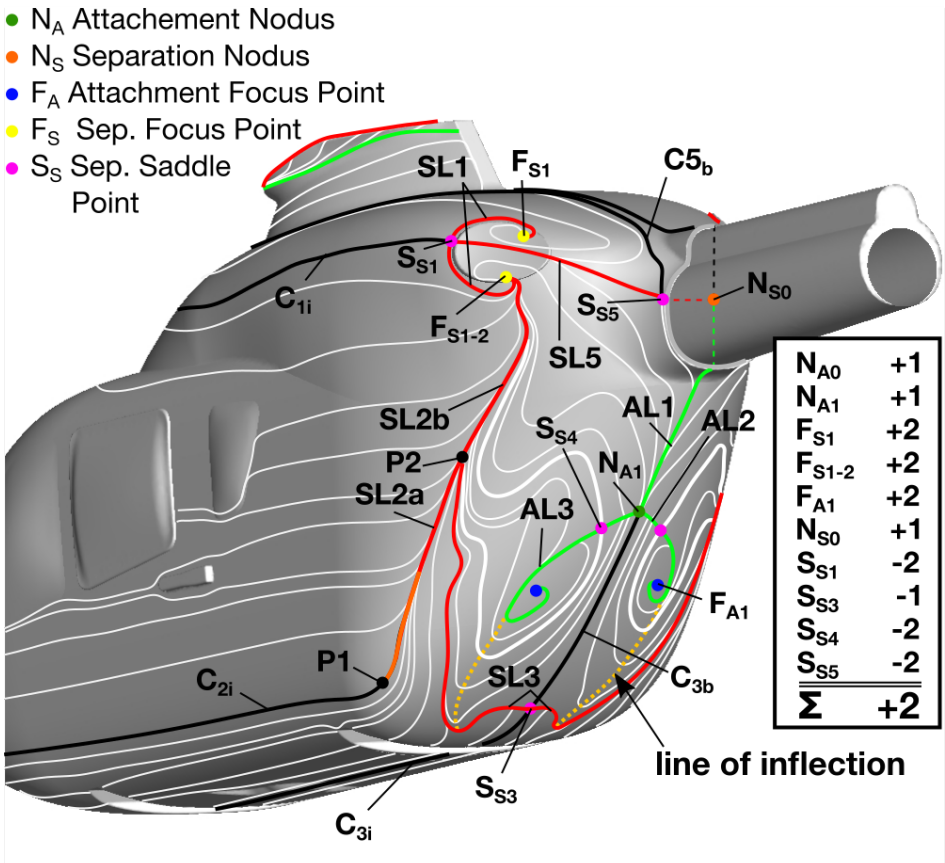

b)

Figure 5.12: *Schematic representation of the near-surface flow topology for F0M0; a) flow regions, b) flow topology.* $Re_\infty \approx 0.95 \cdot 10^6$, $\alpha, \beta = 0$ *deg.*

FR1b is located adjacent to FR1a's outboard limit $C5_b$ and extends up to the characteristic streamline of the incoming flow $C1_i$ in the lateral direction. $C1_i$ connects N_{A0} and S_{S1}. The downstream end of FR1b's longitudinal extension constitutes the separation line SL5, which originates from S_{S5}. SL5 interacts with $C1_i$ at S_{S1} and, thus, closes the boundaries of FR1b. From S_{S1} the separation line SL1 originates. The inboard section of SL1 is embedded in FR1b. It ends in the separation focus F_{S1}. F_{S1} is the origin of one of the two exhaust vortices trajectory; see section 5.4.2.
At the fuselage's side, the flow region FR2 is identified. In the vertical direction FR2 is limited by the dorsal bounding streamline $C1_i$ and the ventral bounding streamline $C2_i$. $C2_i$ connects N_{A0} with the separation nodus F_{S1-2}, which is the origin of the second exhaust vortex trajectory. On the characteristic streamline of the incoming flow $C2_i$ the point P1 is located, which marks the beginning of converging skin-friction-lines along $C2_i$. Downstream from this point a three-dimensional free surface separation occurs. Thus, the section of $C2_i$ between P1 and F_{S1-2} constitutes SL2.
At F_{S1-2}, both SL2 and the outboard section of SL1 separate from the surface. Hence, SL2 and the outboard section of SL1 define the downstream limit of FR2. SL2 is further divided into SL2a and SL2b. The distinction indicates the regions where the detaching shear-layer is fed into the primary upsweep vortex (SL2a) and where not (SL2b); see section 5.4.2. The boundary between those two regions in the vertical directions is defined by the incoming skin-friction line L2, which converges towards SL2 at the interface between SL2a and SL2b.
At the fuselage's ventral side, the flow region FR3 is located. In the lateral direction FR3 is bounded by the characteristic streamlines of the incoming flow C_{2i} and C_{3i}. C_{3i} is congruent with the model's symmetry plane and connects N_{A0} with S_{S3}. The downstream end of FR3 constitute SL3. SL3 originates at S_{S3} and terminates in P2, which is located on C_{2i} in the domain of SL2b. At P2, SL3 separates from the surface by encountering SL2b.
The near-surface flow topology is completed by the flow region FR4. FR4 is limited laterally by SL2b and the attachment line AL1 and the characteristic streamline of the back flow C_{3b}. AL1 and $C3_b$ are both located at the model's symmetry plane. $C3_b$ connects the reattachment point N_{A1} with the downstream side of S_{S3}. AL1 originates at N_{A1} and connects N_{A1} with the fictional separation nodus N_{S0}. The downstream end of FR4 is defined by SL5 and the outboard section of SL1. Furthermore, FR4 encompasses the recirculation zone (RZ). In consequence of the flow reattachment downstream of S_{S3} at N_{A1}, a vortex is formed inside RZ. This recirculation vortex reattaches to the surface at the attachment foci F_{A1}; see section 5.4.2. The region within FR4 affected by RZ is limited laterally by the line of inflection (LoI) and the attachment lines AL2 and AL3. AL2 originates from N_{A1}, whereas AL3 originates from F_{A1}. Both AL2 and AL3 end in S_{S4} whereof they define the characteristic streamline of the back flow and incoming flow, respectively.
The box on the right of Fig. 5.12 b) summarises all identified characteristic points of the near-surface flow topology and their contribution to the topological rule for skin-friction lines on a three-dimensional body; see Eq. 5.4. As can be seen N_{S0} consistently closes the topological rule for F0M0 by returning a sum of 2.

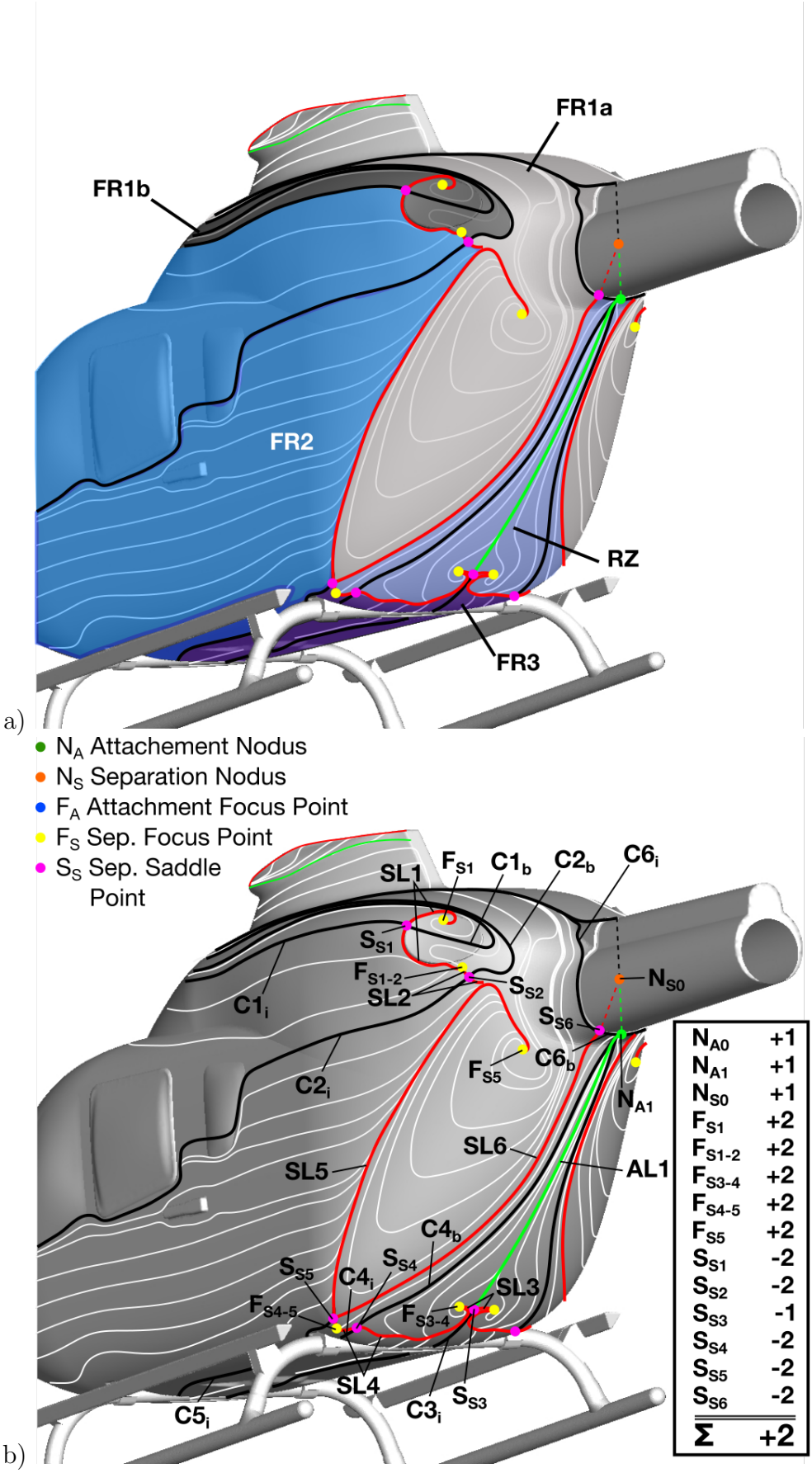

Figure 5.13: *Schematic representation of the near-surface flow topology for F0M0L0; a) flow regions, b) flow topology.* $Re_\infty \approx 0.95 \cdot 10^6$, $\alpha, \beta = 0$ *deg.*

In Fig. 5.13 a) and b), the schematic representation of F0M0L0's near-surface flow topology is depicted. The flow topology at F0M0L0's fuselage is divided into three main flow regions; i.e. FR1, FR2 and FR3. Furthermore, a recirculation zone is identified at the fuselage's rear upsweep near the model's symmetry plane. The flow around F0M0L0's fuselage is also symmetric with respect to the model's symmetry plane.
FR1 covers the engine cowling and a portion of the rear fuselage. It divides into the sub-regions FR1a and FR1b. FR1a covers the engine cowling area close to the model's symmetry plane and extends into the fuselage's rear upsweep region. At the engine cowling, FR1a is limited in the lateral direction by the symmetry plane and the characteristic streamline of the back flow $C2_b$. $C2_b$ connects the attachment nodus at the fuselage nose N_{A0} and the separation saddle point S_{S2}; see Fig. 5.13 b). Between S_{S2} and the model's symmetry plane the flow within FR1a enters the fuselage's rear upsweep region. There FR1a is limited laterally by the outboard section of SL5 and SL6 and the inboard section of SL2. SL6 originates at S_{S6}. S_{S6} appears upon the interaction of the associated characteristic streamline $C6_i$ and $C6_b$. $C6_i$ and $C6_b$ originate at N_{A0} and N_{A1}, respectively. SL6 also constitutes the characteristic streamline of the back flow of S_{S5}, which is the origin of SL5. The characteristic streamline of the incoming flow for S_{S5} constitutes $C5_i$, which originates at N_{A0}. The inboard and outboard section of SL5 separate from the surface at F_{S4-5} and F_{S5}, respectively. The boundary of SL1a is closed by the inboard section of SL2. SL2 originates from S_{S2} in consequence of the interaction of $C2_i$ and $C2_b$. The inboard section of SL2 separates from the surface as it encounters the outboard section of SL5. Thus, closing the boundary of SL1a. The outboard section of SL2 ends in F_{S1-2}. Between $C6_i$ and the model's symmetry plane at the engine cowling the flow within FR1a exits the region considered for this analysis. The associated gap in the topological field is closed by adding the fictional separation nodus N_{S0}.
FR1b is located adjacent to FR1a at the fuselage's engine cowling. FR1b's boundaries are defined by $C2_b$, $C1_i$ and the outboard sections of SL1 and SL2. The characteristic streamline of the incoming flow $C1_i$ connects N_{A0} with the upstream side of S_{S1}. Within FR1b the characteristic streamline of the back flow $C1_b$ is located, which connects N_{A0} and the downstream side of S_{S1}. At S_{S1} SL1 originates. SL1's and SL2's outboard sections both end in in F_{S1-2}, which completes the boundary of FR1b. The inboard section of SL1 terminates in F_{S1} within FR1b. In analogy to F0M0, F0M0L0's exhaust vortex trajectories originate at F_{S1} and F_{S1-2}.
FR2 is located at the fuselage's lateral side. Since no free-surface separation occurs at F0M0L0's lateral tapering FR2 is not further divided. In the vertical direction, FR2 is limited by its dorsal and ventral bounding streamlines defined by $C1_i$ and $C5_i$, respectively. FR2's downstream end constitute SL2 and the outboard sections of SL1 and SL5. Furthermore, FR2 encompasses $C2_i$.
The fuselage's ventral side covers FR3. In the lateral direction, FR3 is limited by the model's symmetry plane and $C5_i$. FR3's downstream limit is defined by the separation lines SL3, SL4 and the inboard section of SL5. SL3 originates from S_{S3}, which appears in consequence of the interaction of $C3_i$ and AL1. AL1 connects N_{A1} and the downstream side of S_{S3}. SL4 emerges from S_{S4}. S_{S4} is generated where $C4_i$ and $C4_b$ encounter each other. The trajectory of $C4_i$ is not presented in Fig. 5.13 b), because the interaction of the flow past the fuselage's ventral side and

the open cavities in conjunction with the skid-landing-gear's central cross-beam and attachment elements is not detailed in this analysis. SL3 and the inboard section of SL4 separate from the surface in F_{S3-4}, whereas the outboard section of SL4 and the inboard section of SL5 separate from the surface at F_{S4-5}.
Downstream of S_{S3} the flow reattaches at the attachment nodus N_{A1}. In consequence the recirculation zone (RZ) is formed. RZ's lateral boundaries are defined by AL1 and SL6. AL1 coincides with the model's symmetry plane. The upstream end of RZ is defined by SL3, SL4 and the inboard section of SL5. Within RZ $C4_b$ is located. Comparing F0M0's and F0M0L0's near-surface topologies reveals the impact of L0 on the flow around F0M0's rear fuselage. There are three main differences between the two topologies. On F0M0 a free-surface separation is observed, which leads to the formation of the upsweep vortex UV1; see section 5.4.2. For F0M0L0, this vortex system is not observed, because L0 perturbs the flow around the fuselage's ventral side. This leads to a more pronounced flow separation on F0M0L0, which spans over the entire upsweep region. Furthermore, in consequence of this perturbation, the primary separation line is shifted further upstream on F0M0L0 compared to F0M0. Finally, the flow coming along the fuselage dorsal side enters the upsweep region on F0M0L0. This leads to the formation of the separation vortex SV, which is not observed without the skid-landing-gear installed; see section 5.4.2.

5.4.2 Wake Flow Topology

In Fig. 5.14, the vortex formation at F0M0's rear fuselage is depicted for $\alpha, \beta = 0\ deg$ at test condition 'd' based on the URANS simulation. In the top left corner, contours of the non-dimensional axial vorticity $\omega_x \cdot l_{ref}/U_\infty$ are depicted for slices at constant x_m; superimposed on the near-surface flow topology. Furthermore, contours of $\omega_x \cdot l_{ref}/U_\infty$ are depicted as a function of $y_r/(b_f/2)$ and x_r/l_r for the selected horizontal slices $Z5, Z7, Z9, Z11$. Thus, a direct comparison to the surface pressure data also presented for these slices is possible.
At each side of the rear fuselage's upsweep a vortex is formed. This vortex is called the primary counter-rotating upsweep vortex UV1. UV1's vortex roll-up begins as the shear-layer starts to separate along the three-dimensional separation at SL2a. UV1 is identified after the initial roll-up as two regions of $\omega_x \cdot l_{ref}/U_\infty = \pm 12$ at slice Z11. Due to the flow separation along SL3 and the formation of the recirculation zone the vortex roll-up is confined to the fuselage's lower lateral sides (SL2b); see section 5.4.1. In consequence, UV1's trajectory quickly deviates from the rear fuselage contour and UV1 is shed into the wake. Thus, at slice Z9 the vortex core of UV1 is not in close proximity to the surface anymore and no local pressure minima are observed; see 5.3. The formation of UV1 induces an additional upward directed velocity field close to the models symmetry plane. This leads to the observed flow reattachment at N_{A1}. At Z7, UV1 is also evident but the vortex core is shifted even further away from the surface.
Besides UV1 another vortex pair is present in F0M0's wake. This vortex is formed by the interaction of the flow past the fuselage's ventral side with the rear cavity for housing the skid-landing-gear's central cross beam. This interaction is not detailed here, but the progression of the associated cavity vortex CV is discussed. At Z11, CV's trajectory already starts to deviate from the rear fuselage's contour. It is located at either side of the recirculation zone RZ close to the bounding line of inflection LoI; see section 5.4.1. In consequence of CV's induced velocities, local pressure minima are observed in c_p as a function of $y_r/(b_f/2)$ at Z11; see section 5.3. Further downstream CV's trajectory propagates through F0M0's wake just below the vertical position of slice Z9. Nevertheless, Z9 cuts through the upper portion of CV and, thus, it is still discernible at this slice location.
In Fig. 5.15 a), the main flow features observed in F0M0's near wake are summarised by a schematic representation. Besides the vortex systems which are generated at the rear fuselage's upsweep two more vortex systems are generated at F0M0. These vortex systems are the two pairs of counter-rotating exhaust vortices (EV) and the counter-rotating mast fairing vortex (MV). The EV are generated on both the closed exhaust pipes in consequence of the fixed surface separation. The fixed surface separation starts at SL1 originating from S_{S1}. The MV originate from the outer lip of the mast fairing's dorsal side in consequence of a fixed surface separation as well.
In Fig. 5.15 a), the extension of the recirculation zone (RZ) is presented. The structures within RZ are detailed in Fig. 5.15 b). In consequence of UV1's induced velocities, the separated flow is pushed back towards the surface. This leads to the reattachment at N_{A1} and the formation of the closed RZ. Within RZ the recirculation vortex is generated, which reattaches within RZ at F_{A1}.

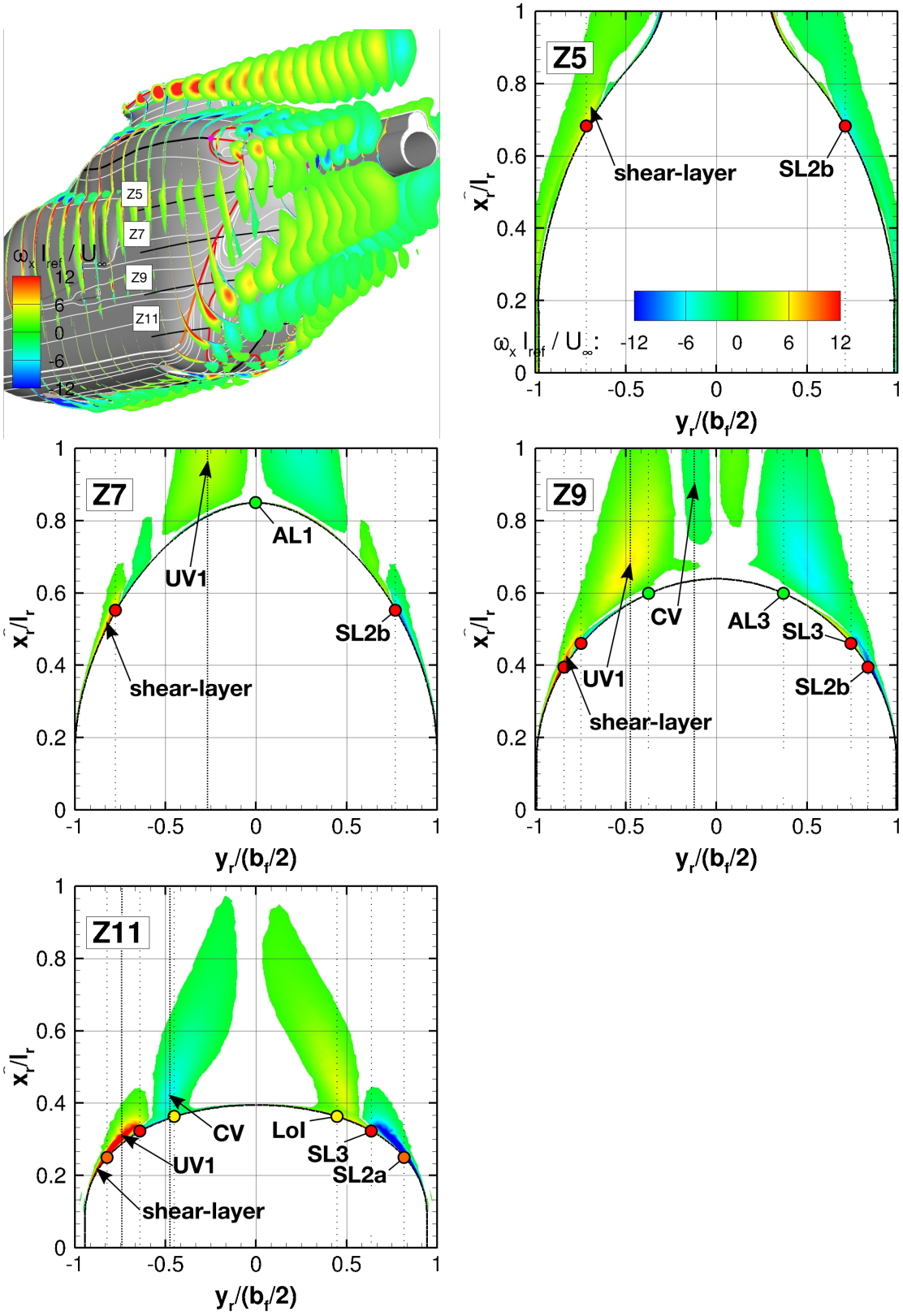

Figure 5.14: *Contours of $\omega_x l_{ref}/U_\infty$ in F0M0's wake at slices of constant x (isometric view) and constant z (2D view) at Z5, Z7, Z9 and Z11. $Re_\infty \approx 0.95{\cdot}10^6$, $\alpha, \beta = 0$ deg.*

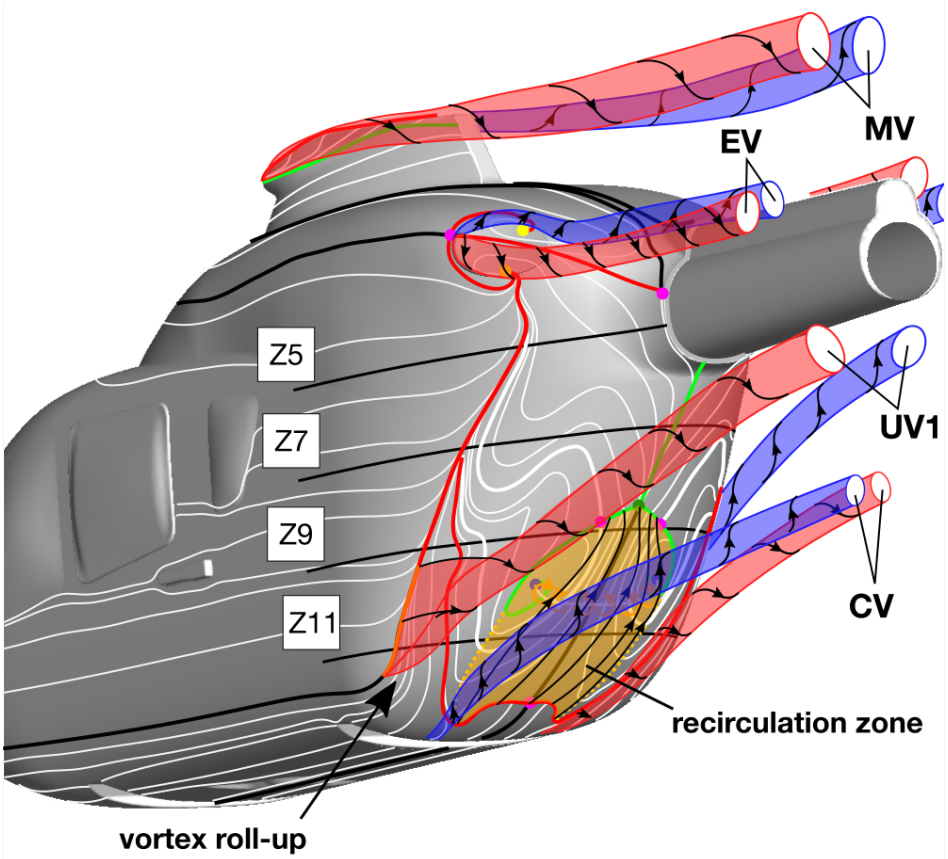

a)

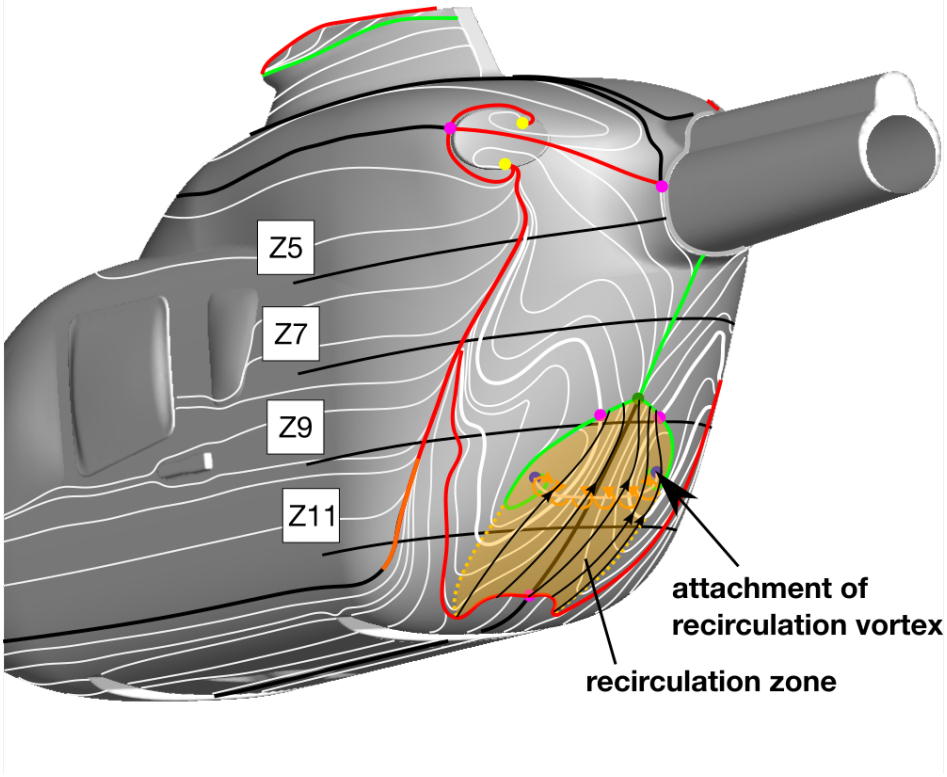

b)

Figure 5.15: *Schematic representation of F0M0's vortex systems and recirculation zone (RZ); a) overview and b) detailed view of the structures within RZ.* $Re_\infty \approx 0.95 \cdot 10^6$, $\alpha, \beta = 0$ *deg.*

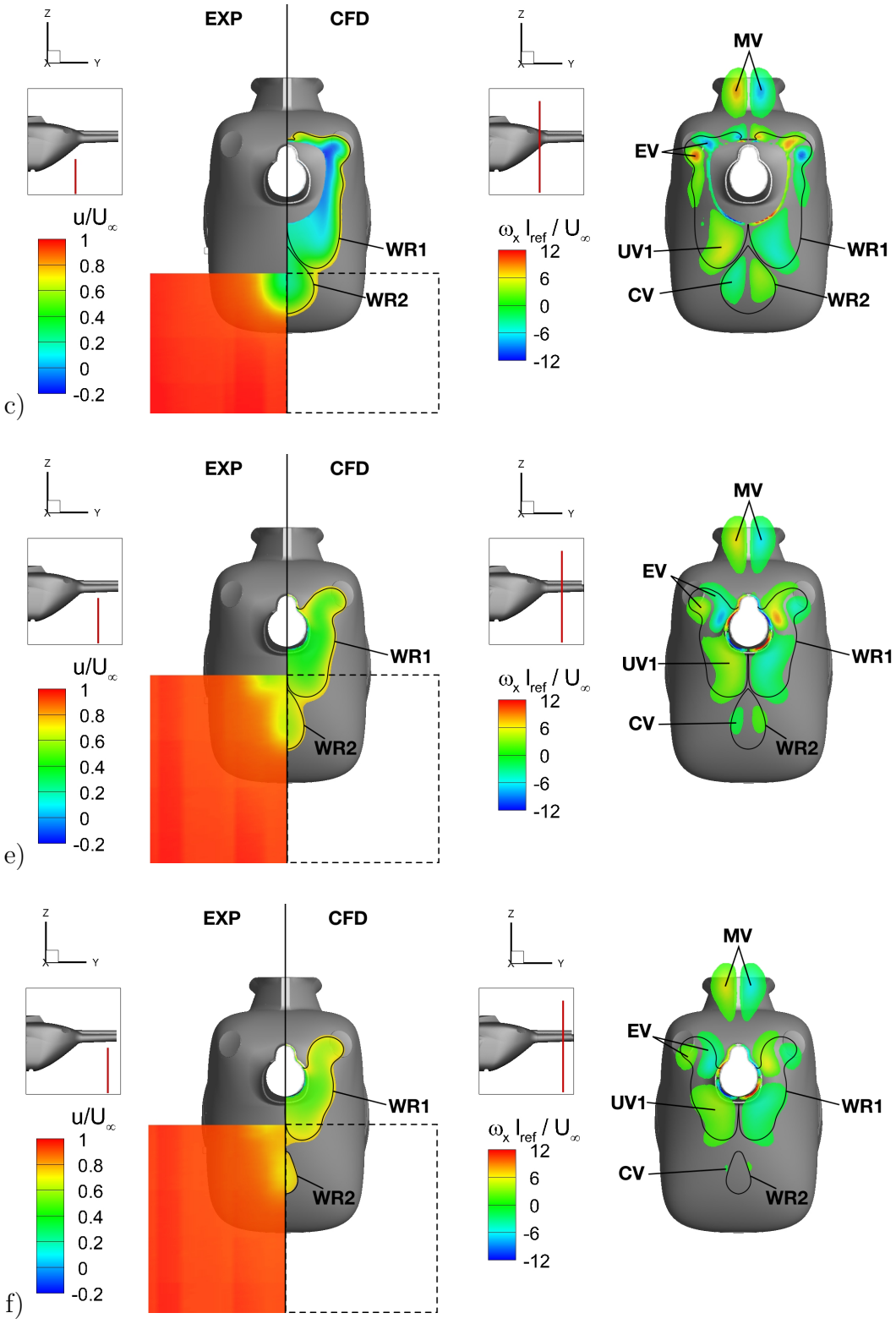

Figure 5.16: *Contours of u/U_∞ (Exp/CFD) and $\omega_x l_{ref}/U_\infty$ (CFD) in F0M0's wake at slice locations 'c','e' and 'f',$Re_\infty \approx 0.95 \cdot 10^6$, $\alpha, \beta = 0$ deg. Wake region boundaries correspond to $u/U_\infty = 0.8$.*

In section 5.2, it is argued that F0M0's wake flow topology switches from the vortex type to the eddy type via a hybrid vortex and eddy flow topology. The observed wake flow topology for F0M0 actually supports this hypothesis, since both the large scale separation and the formation of upsweep vortices are observed.
In Fig. 5.16, contours of the non-dimensional axial velocity u/U_∞ and $\omega_x \cdot l_{ref}/U_\infty$ are shown along the wake slice locations 'c','e' and 'f' for test condition 'd', $\alpha, \beta = 0$ *deg*. For u/U_∞ the experimental results obtained by PIV are compared to the CFD data. Non-dimensional axial vorticity distributions are only presented based on the CFD data. The identified wake regions are defined by iso-lines of $u/U_\infty = 0.8$.
The comparison of F0M0's PIV data against the CFD data does reveal a good to excellent agreement for u/U_∞ with respect to the absolute values and the extension of the wake region (WR). In particular two wake regions can be distinguished; i.e. WR1 and WR2. WR1 extends to the side and the top of the fuselage's aft-body. This wake region is associated to the separation along SL1, SL2 and SL5. WR2 is located close to the models symmetry plane and below the fuselage's aft-body and tailboom. WR2 is associated to the recirculation zone RZ and the formation of the cavity vortex CV. At slice 'c' WR1 and WR2 are still adjacent to each other. As the wake progresses downstream, WR1 and WR2 further deviate from each other. Finally, at slice 'f', WR1 and WR2 are completely separated.

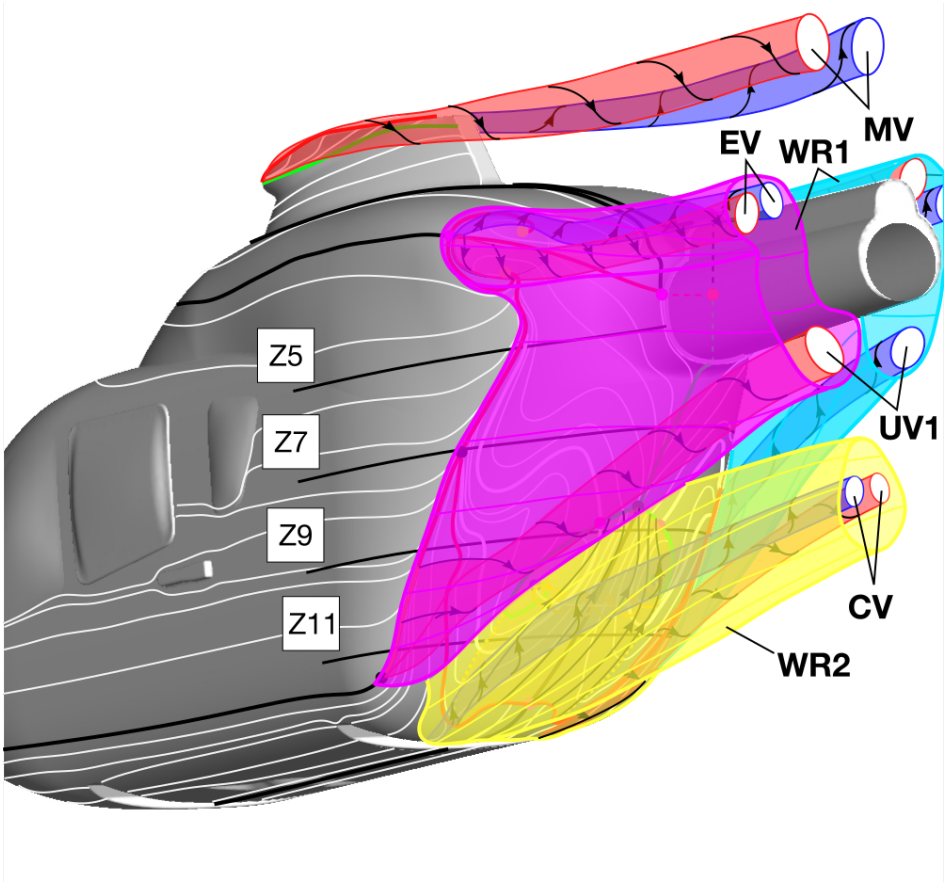

Figure 5.17: *Schematic representation of F0M0's wake including the vortex systems and the envelope of the wake regions.* $Re_\infty \approx 0.95 \cdot 10^6$„ $\alpha, \beta = 0$ *deg.*

By superimposing the extension of the wake regions onto the contour plots of $\omega_x \cdot l_{ref}/U_\infty$ it becomes clear, that WR1 defines the envelope for the observed vortex systems UV1 and EV within the wake. WR1 can be observed throughout the wake up to the tailboom's downstream end. WR2 encloses the cavity vortex CV. Fig. 5.17 summarises the identified wake topology for F0M0 as a schematic three-dimensional representation. This includes the vortex systems and the identified envelope of the two wake regions WR1 and WR2.

In Fig. 5.18, the vortex formation at F0M0L's rear fuselage is presented in the same way as for F0M0 in Fig. 5.14. At Z11, the two vortices LV1 and LV2 generated along the skid-landing-gear's outer cross-beams and step are discernible on either side of the fuselage near SL5. Both LV1 and LV2 do not remain in close proximity of the wall further downstream. Thus, there are not registered at the other slices of constant z.
In between SL5 and SL6, the separation vortex SV is formed. It appears as the flow entering the rear fuselage upsweep region along the fuselage dorsal side rolls up as it encounters the recirculation zone and the flow along the fuselage's lateral side. At Z5, the onset of SV's formation becomes evident as two regions of $\omega_x \cdot l_{ref}/U_\infty = \pm 12$ near SL5. At Z5, two instances of the primary separation line SL5 are observed, because SL5 is curled back before separating from the surface at F_{S5}; see section 5.4.1. At Z7, SV's vortex core is not in close proximity to the surface anymore. It is located just downstream of the recirculation zone RZ between SL6 and AL1 at Z11. At Z9, SV is also located in this region.
In Fig. 5.19 a), the main flow features observed in F0M0L0's near wake are summarised by a schematic representation. Besides the vortex systems LV1, LV2 and SV two more vortex systems are generated at F0M0L0. In analogy to F0M0's wake these vortex systems are the two pairs of counter-rotating exhaust vortices (EV) and the counter-rotating mast fairing vortex (MV). EV are generated in consequence of the fixed surface separation at SL1. MV originate from the outer lip of the mast fairing top as observed for F0M0.
In Fig. 5.19 b), the schematic representation of the recirculation zone's extension is presented alone. In contrast to F0M0 the recirculation zone extends over the entire rear fuselage's upsweep longitudinal extension. Furthermore, it extends further down in the vertical direction. Thus, the size of the recirculation zone significantly increases by the presence of the skid-landing-gear. A concentrated recirculation vortex is not observed for F0M0L0.
In Fig. 5.20, F0M0L0's contours of the non-dimensional axial velocity u/U_∞ and $\omega_x \cdot l_{ref}/U_\infty$ are shown along the wake slice locations 'c','e' and 'f' in analogy to Fig. 5.16. The comparison of F0M0L0's PIV data with the CFD data does reveal a good agreement for u/U_∞ with respect to the absolute values and the extension of the wake region (WR). However, some differences are notable. First of all, the extension in the vertical and lateral direction of the region of reduced u/U_∞ appears to be over predicted by the URANS simulation at slice 'c'; see Fig. 5.20 top left. In section 5.3, it is discussed that the numerical simulations predict the primary separation at SL5 slightly more upstream compared to the experiments.

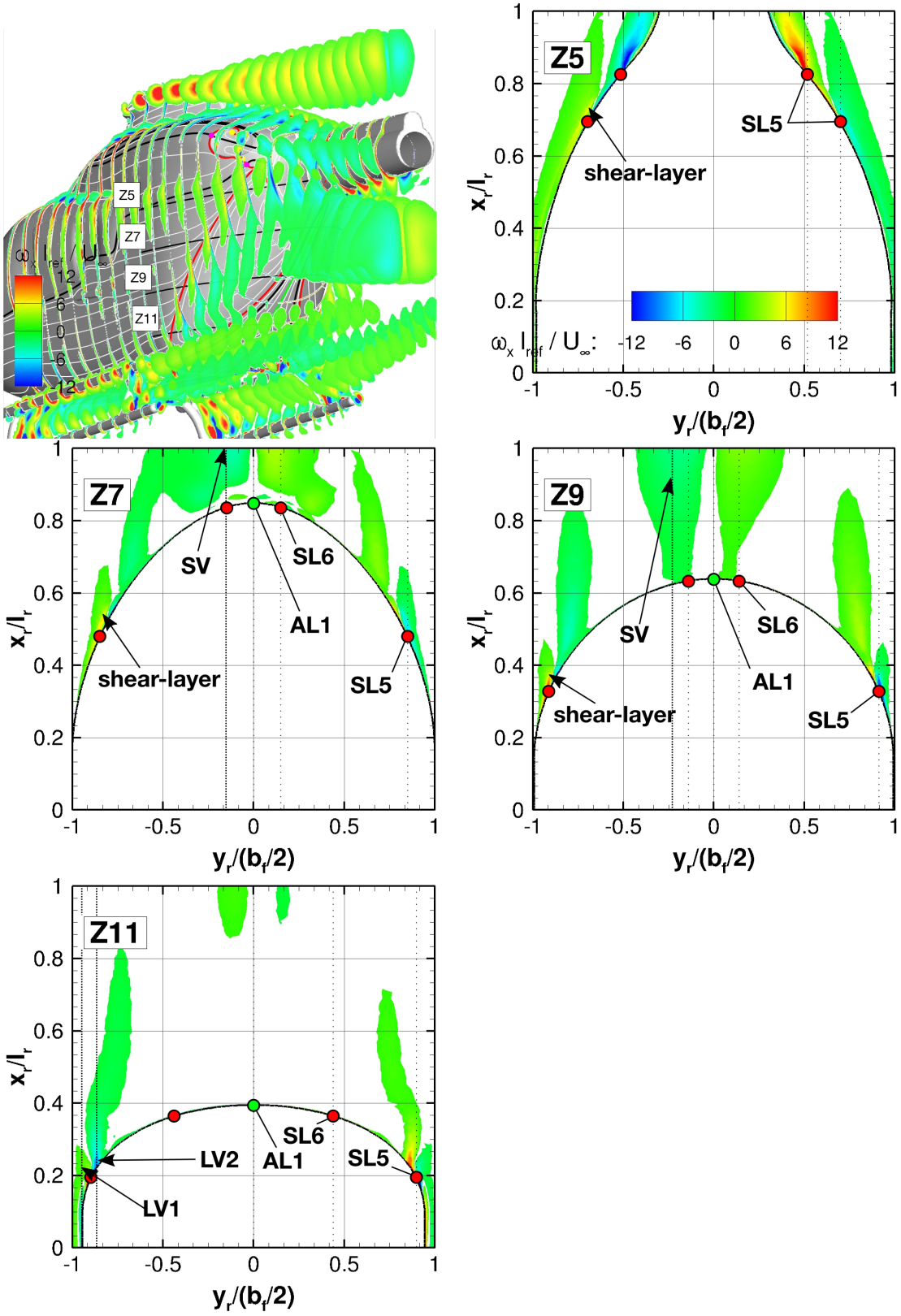

Figure 5.18: *Contours of $\omega_x l_{ref}/U_\infty$ in F0M0L0's wake at slices of constant x (isometric view) and constant z (2D view) at Z5, Z7, Z9 and Z11. $Re_\infty \approx 0.95{\cdot}10^6$, $\alpha, \beta = 0$ deg.*

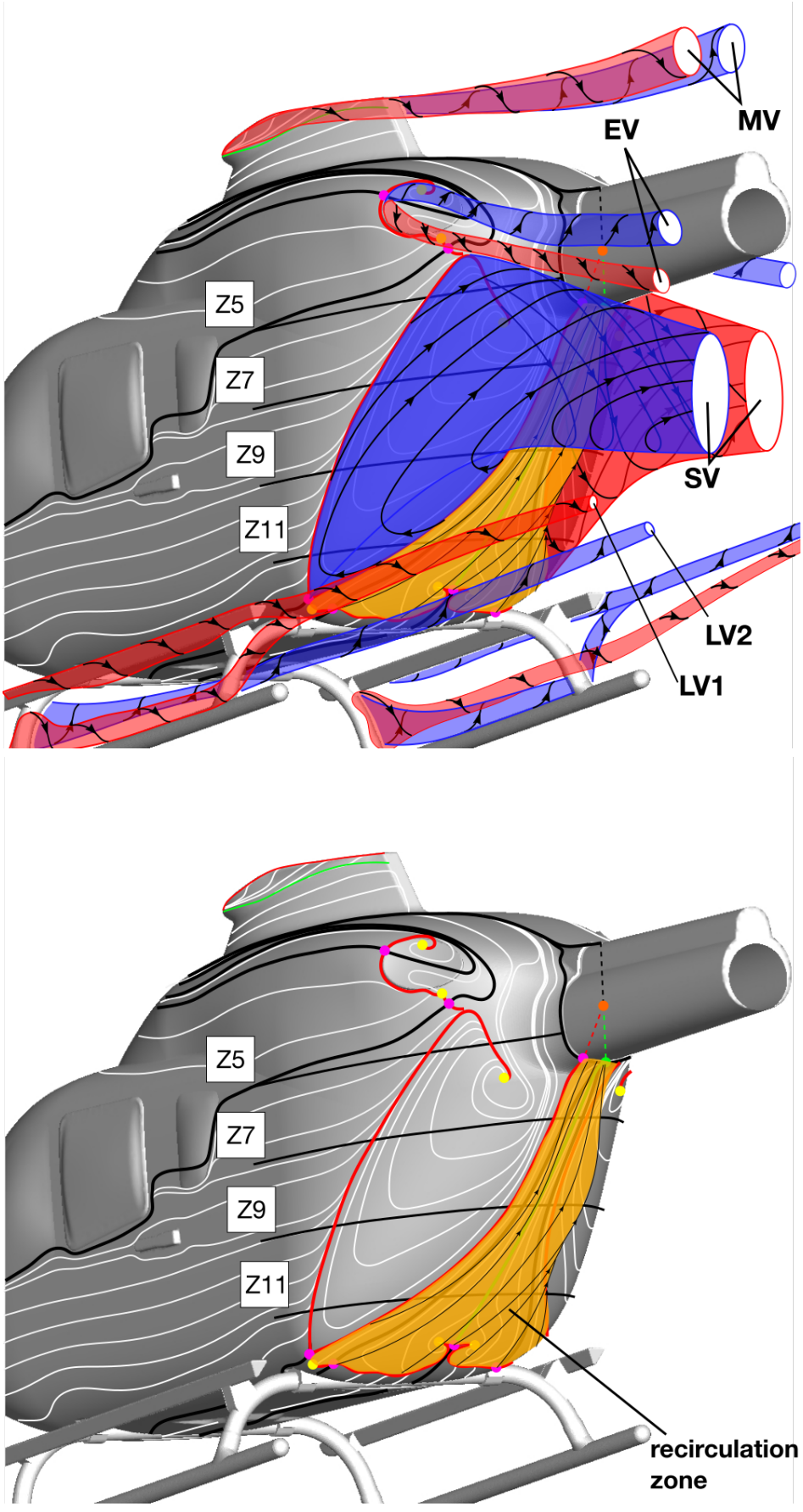

Figure 5.19: *Schematic representation of F0M0L0's vortex systems and recirculation zone (RZ); a) overview and b) detailed view of RZ's extension.* $Re_\infty \approx 0.95 \cdot 10^6$, $\alpha, \beta = 0$ *deg.*

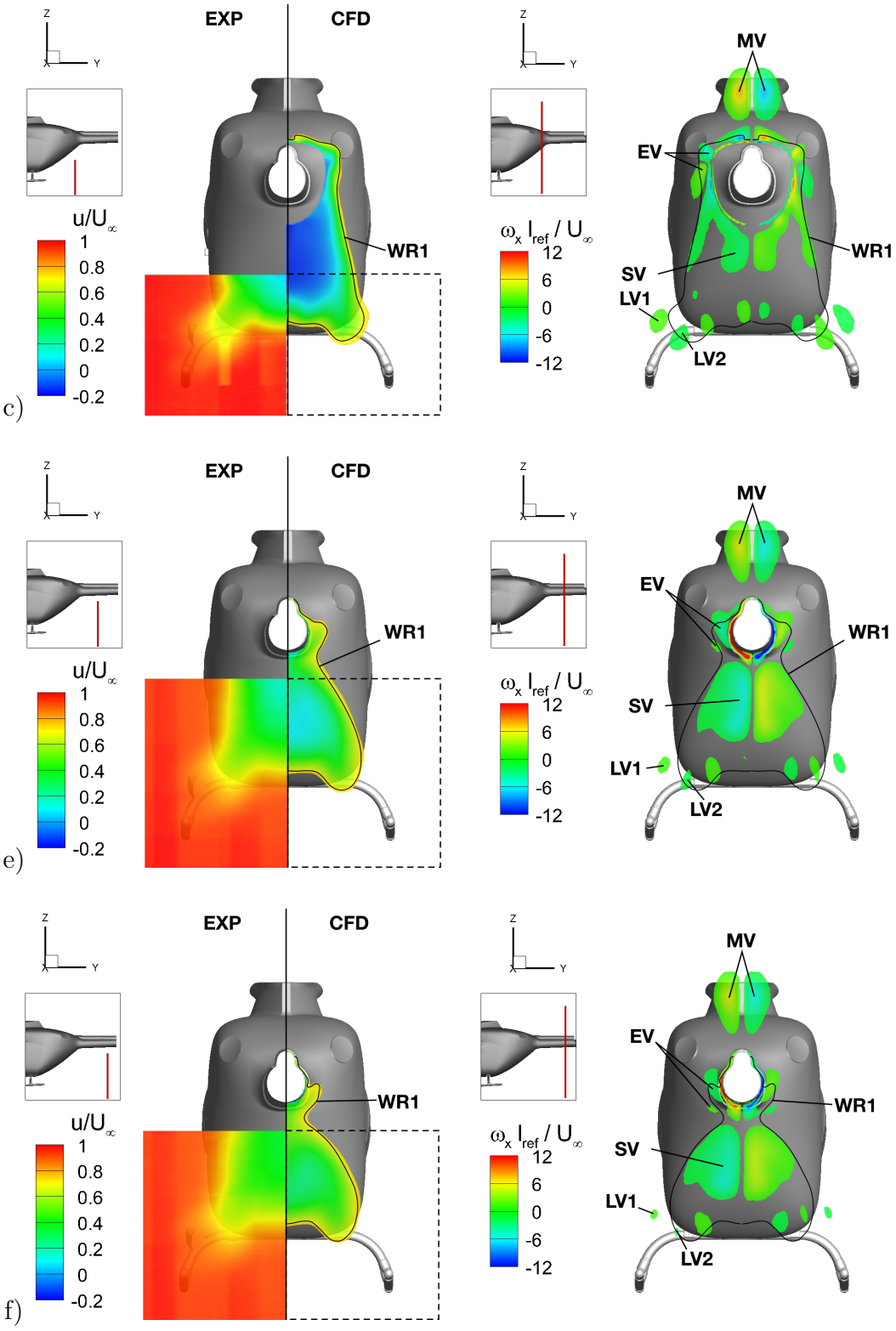

Figure 5.20: *Contours of u/U_∞ (Exp/CFD) and $\omega_x l_{ref}/U_\infty$ (CFD) in F0M0L0's wake at slice locations 'c','e' and 'f' ,$Re_\infty \approx 0.95 \cdot 10^6$, $\alpha, \beta = 0$ deg. Wake region boundaries correspond to $u/U_\infty = 0.8$.*

In consequence, also the extension of the region where $u/U_\infty \leq 0.8$ is over-predicted. At the other slices further downstream, the absolute values of u/U_∞ are in better agreement between experiment and simulation. However, at slices 'e' and 'f', the lateral extension of the wake region close to the tailboom is under predicted by the simulation.
In contrast to F0M0, only one instead of two wake regions can be observed for F0M0L0; i.e. WR1. This wake region is associated to the separation along SL1, SL2, SL3, SL4 and SL5 and the separation at the skid-landing-gear. By superimposing the extension of WR1 onto the contour plots of $\omega_x \cdot l_{ref}/U_\infty$ it becomes clear that WR1 inhibits the vortex system SV and LV2; see Fig 5.20 right column. For the exhaust vortex EV this is not always the case. The inboard vortex of the counter-rotating EV remains within WR1 in F0M0L0's wake. However, EV's outboard vortex is only confined within WR1 at slice 'c'. Further downstream it leaves the enveloped defined by $u/U_\infty = 0.8$. This is probably associated to the diminishing intensity of EV's outboard vortex along its trajectory through the wake. In consequence, the deceleration of the axial velocity associated to this vortex reduces as well. Thus, downstream of slice 'c' EV's outboard section is not confined within the WR1 envelope anymore. The same effect is also observed for LV1. However, LV1 remains outside the wake envelope along its formation at the landing-gear's skid and as it propagates through the wake; see Fig. 5.21.

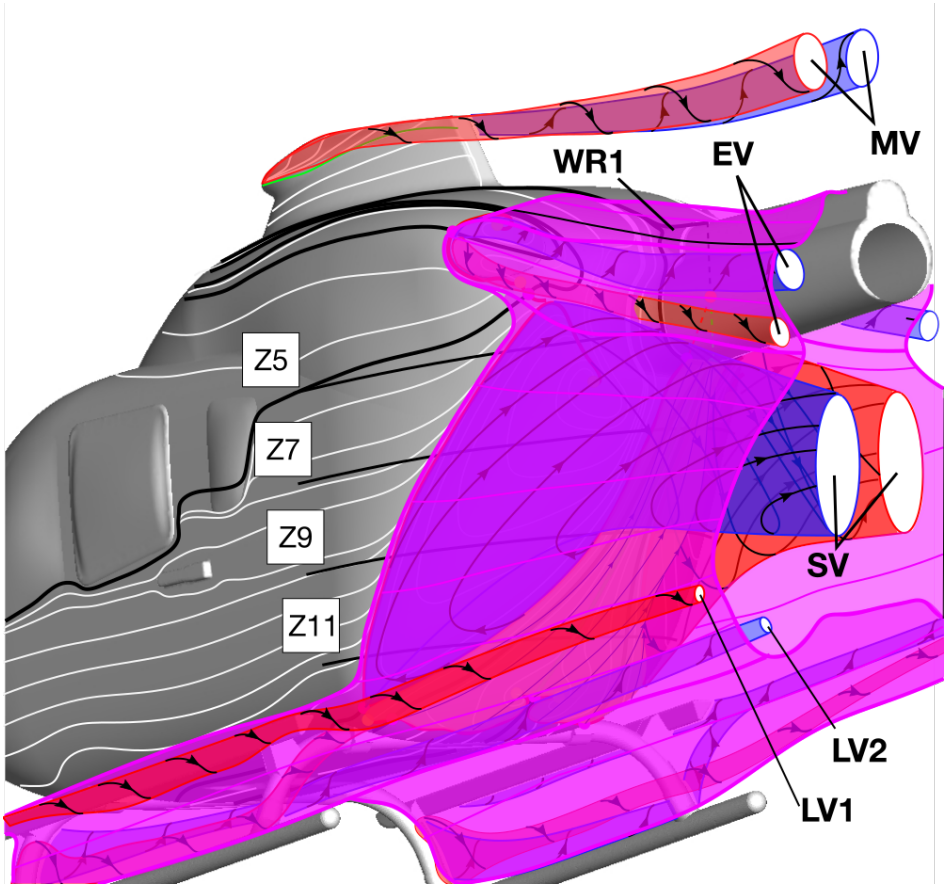

Figure 5.21: *Schematic representation of F0M0L0's wake including the vortex systems and the envelope of the wake region WR1.* $Re_\infty \approx 0.95 \cdot 10^6$, $\alpha, \beta = 0$ *deg.*

6 Design Modifications on Drag Reduction

In this chapter, the developed aerodynamic design optimisations based on the gained knowledge about the reference configuration's global and local aerodynamic characteristics are presented. This includes both the skid-landing-gear's design modifications and the applied means of passive flow control at the rear fuselage. First, the aerodynamic characteristics of the skid-landing-gear modifications are analysed. Afterwards, the impact of the passive flow control devices are assessed. For both analysis sections, the same structure as in the baseline model's analysis is employed. Thus, the global aerodynamic characteristics are investigated first. In a second step, the local pressure distribution is analysed. Finally, the impact of the modifications on the near-surface and wake flow topology is presented.

6.1 Optimised Skid-Landing-Gear Designs

The detailed drag analysis of the reference configuration has shown, that the skid-landing-gear is generating 23% of the total parasite drag; see Fig. 5.6. Modifying the landing-gear's design, therefore, can contribute significantly to reducing the fuel-flow in fast-forward level flight. There are several options for the design of the landing-gear. For single-engine-light (SEL) and TEL - class helicopter the standard solution is a skid-landing-gear design. Other design variants include fixed wheeled-landing-gears and retractable wheeled-landing-gears. In Fig. 6.1, the components of the reference configuration's skid-landing-gear L0 and details of the fuselage's bottom are presented. The skid-landing-gear consists of the skids, the outer and central cross-beam elements, the steps and the blunt fuselage attachment elements. The central cross-beams are embedded in open cavities on the fuselage's ventral side. Furthermore, the fuselage's ventral side of the reference configuration provides attachment surfaces for external equipment.

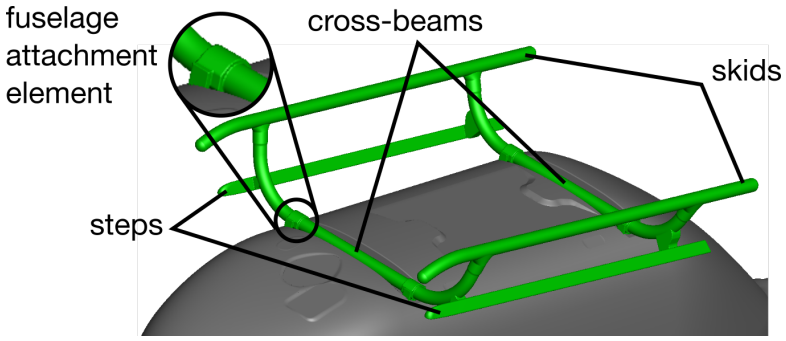

Figure 6.1: *Components of the reference configuration's skid-landing-gear L0.*

In 2013, Grawunder et. al. [18] discussed the advantages and disadvantages of the different landing-gear design solutions. The largest landing-gear drag contribution is observed for fixed wheeled-landing-gears. According to Keys [21], fixed wheeled-landing-gears exceed the drag level of skid-landing-gears by about 60%. Installing retractable wheeled-landing-gears, however, can provide advantages in comparison to skid-landing-gears. Keys [21] shows, that at cruising-speeds in excess of $75m/s$ the advantages in drag-coefficient begin to compensate the cost- and weight-penalties. However, this remains only valid as long as the fuselage's frontal area has not to be increased in order to provide the necessary installation space. This would not be possible for helicopter within the SEL and TEL class, since the fuselage volume for those helicopter classes is very limited. In consequence, the best way for achieving efficiency gains associated to the skid-landing-gear in these classes is to employ drop-like shaped instead of circular tubes or by fairing the tubes with aerodynamically optimised panels. Examples for this approach in the SEL and TEL class can be found, respectively, on the EC120, R44, MD600 and on the executive transport version of the EC145 T1.
For this work, two different faired skid-landing-gear variants are considered. The faired skid-landing-gear L1 is designed such that the fairing panels can be retrofitted

to the standard skid-landing-gear L0. The retrofittable fairing solution was designed at TUM-AER. It is based on an initial design provided by Airbus Helicopters Deutschland GmbH, and has then been further improved; see section 6.1.1. The second faired skid-landing-gear L2 is a more progressive design. Realising this design would also require substantial structural modification, both to the design of the skid-landing-gear as well as the airframe's structure. The design of L2 has been developed by Airbus Helicopters Deutschland GmbH.
Furthermore, the fuselage alone contributes as much to the reference configuration's total parasite drag as the skid-landing-gear. Thus, the design of the baseline's fuselage is revised in the course of the landing-gear's modification as well. In particular, the fuselage's ventral side is smoothed by fairing the attachment surfaces for external equipment and the cavities for housing the skid-landing-gear's central cross-beam elements.

6.1.1 Shape modifications

In Fig. 6.2, the fuselage's ventral side of the baseline fuselage F0 is depicted together with the fuselage modification F1. In order to obtain a smoothed fuselage ventral side, the design is simplified in several ways. Generally all fuselage openings have been removed, such that the sheer hull geometry is obtained.

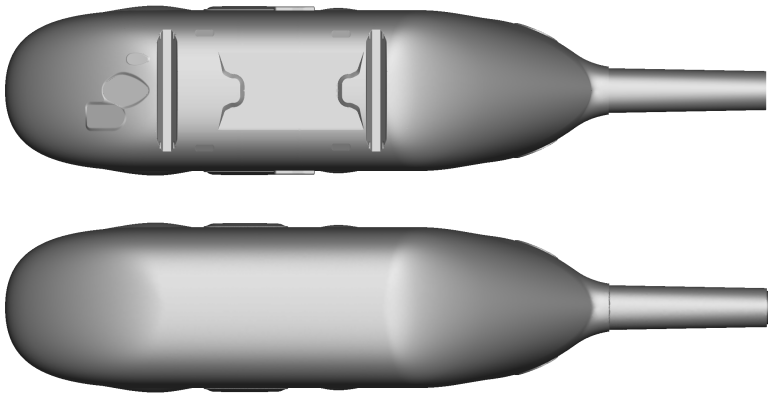

Figure 6.2: *Ventral side views (CAD rendering) of the fuselages a) F0 and b) F1.*

The openings which are removed include

- the cavities housing the skid-landing-gear's attachment elements and the central cross-beams.
- the attachment surface for external equipment at the fuselage's ventral side in between the cross-beams; i.e. sling-load-hook attachment.
- the attachment surfaces for external equipment towards the bow; i.e. a forward looking infrared camera or a spot-light.

The consequence for the helicopter operational capability in missions requiring the stated external equipment needs to be addressed separately. It is not scope of this work.
For the faired skid-landing-gear L1, the design of the panels for fairing the outer cross-beams has been received by Airbus Helicopters Deutschland GmbH. The panels feature an airfoil cross-section which is positioned such the thickness maximum along the chord is congruent with the circular cross-beam center. Thus, the entire panel can be obtained by extruding the airfoil cross-section along the cross-beam's centerline. The employed airfoil is the DU-06-W200 developed by the Technical University Delft. It is a thick airfoil originally designed for wind-turbine applications. The DU-06-W200 features a maximum thickness to chord ratio of 19.8% and a maximum chamber to chord ratio of 0.5% at 31% and 84% chord, respectively. The twist distribution starts at approximately 0 *deg* relative to the fuselage longitudinal axis and the cross-beams centerline at the skids. Towards the junction with the fuselage the twist is linearly increased to its maximum value. In order to avoid a negative impact on the helicopter's pitching stability, the rear cross-beam fairing features an increased chord compared with the front fairing.
Based on this input by Airbus Helicopters Deutschland GmbH, in total six different fairings were designed for the attachment elements. The construction of these fairings has been performed by Spagl [38]. Generally, those fairings can be grouped into two categories in accordance to the shape of the attachment element fairings. Those categories are denoted L1-a and L1-b.
The attachment element fairings of category L1-a are obtained by extruding the outer cross-beam's fairing beyond the attachment elements towards the fuselage's symmetry plane. In order to guarantee the necessary clearance to the attachment elements, the profile is scaled with respect to chord. Without modifying the profile, this would also result in a significant increase in the profile's chord length. This is circumvent by truncating the profile at the trailing edge. The disadvantage of this design is a comparatively large frontal area.

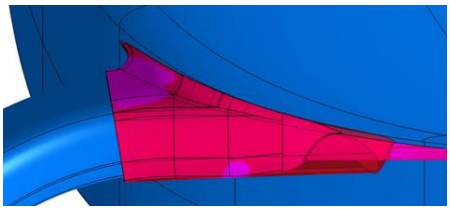

Figure 6.3: *Comparison of attachment fairings frontal area for skid-landing-gear L1 of type a (translucent red) and b (magenta) [38], frontal view of starboard fairings.*

In contrast the attachment element fairings for L1-b are designed, such that the frontal area is reduced by incorporating a as compact shape as possible; see Fig. 6.3. The design still obeys the required clearance for the structural components. In order to obtain the compact shape, the panel features complex surface curvature transitions. Spagl [38] still ensured sheer panel shapes by performing dedicated curvature analysis.

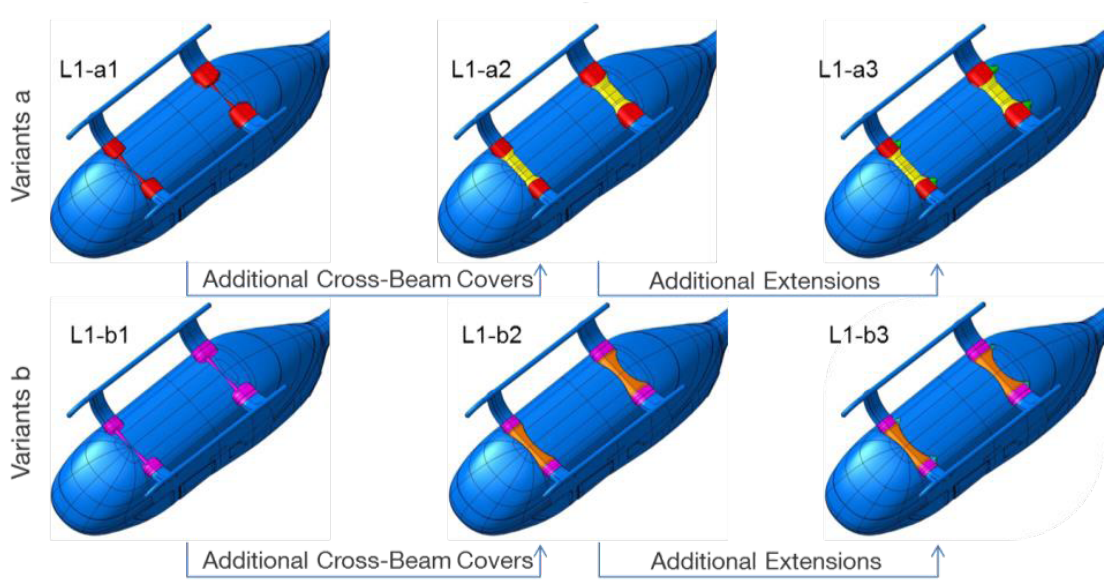

Figure 6.4: *Considered central cross-beam covers and attachment fairings for the retrofittable skid-landing-gear modification L1-a and L1-b [38].*

Fig. 6.4 presents an overview of the six different retrofittable fairing geometries considered for the preliminary design analysis. L1-a1 and L1-b1 only incorporate the two different attachment element fairings of category a and b. The central cross-beam elements are not covered. The cavity housing the central cross-beams is closed such that only the portion of the central cross beams extending outside of the sheer hull geometry are exposed to the flow. For L1-a2 and L1-b2 additional covers are added for fully fairing also the central cross-beams with streamlined panels. The shape of those panels in category b is also optimised for minimal frontal area, whilst maintaining a smooth transition to the hull geometry.

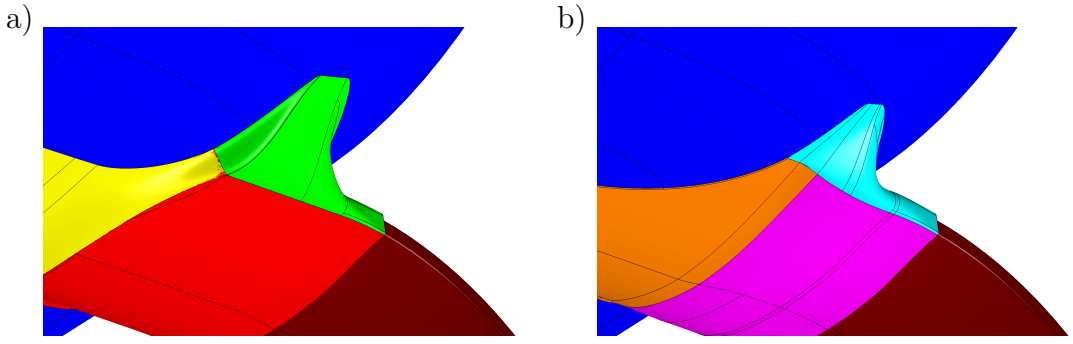

Figure 6.5: *Detailed view of the additional extensions in the wake of the attachment element fairings, a) L1-a3, b) L1-b3 [38], rear view of starboard elements.*

Finally L1-a3 and L1-b3 feature additional extensions in the wake of the attachment elements fairings. Fig. 6.5 depicts a more detailed view of those extensions. They are intended to mitigate flow separation at the attachment element fairings blunt trailing edge.

In order to select the final shape modification L1 for further analysis, numerical simulations are performed by solving the incompressible Navier Stokes equations through the application of the Reynolds Averaged Navier Stokes (RANS) equation model. For this preliminary numerical analysis, the numerical effort is confined by performing steady state simulations only. The turbulence model for the employed RANS formulation is the Explicit Algebraic Reynolds Stress Model (EARSM). The applied EARSM equations are based on Launder et al. [25]. All the simulations are performed with the commercial solver ANSYS CFX. The spatial discretisation is performed with the High Resolution Scheme, which blends between first and second-order accuracy. The second-order accurate temporal discretization is realised by applying the implicit Backward - Euler - Method. The time-step for the steady state simulations is determined with the local timescale option of ANSYS CFX. Details on the solver theory are presented in the CFX - Solver Theory Guide [2]. The necessary boundary conditions for the simulations are

- the inflow condition at constant velocity profile with a turbulence intensity of 5% at the inlet,
- the outflow condition with zero pressure gradient at the outlet
- no-slip walls at the surface of the model and
- free-slip walls at the sidewalls, the top and the bottom of the domain.

The initialisation is performed by setting the inlet conditions in the entire computational domain. The freestream condition corresponds to test condition 'd'; see section 4.2. All the preliminary simulations are performed for $\alpha, \beta = 0\ deg.$
In Fig. 6.6, the variants a1, a2, a3, b1, b2 and b3 of the faired skid-landing-gear together with the smoothed cabin F1 are compared with the baseline configuration F0M0L0 with respect to C_D. This comparison reveals that F1M0L1-b1 and F1M0L1-b3 feature the lowest drag level of all considered L1 variants. Configurations L1-a3 and L1-b3 can compete with L1-b1 in terms of drag reduction, but are geometrically more complex. This potentially leads to higher manufacturing costs and higher weight penalties when retrofitted to a machine.
Fig. 6.7 presents the predicted C_L through preliminary numerical simulations for configurations F0M0L0 and F1M0L1 with variants a1, a2, a3, b1, b2 and b3. The baseline configuration F0M0L0 is neutral with respect to C_L.
The preliminary aerodynamic investigation through numerical simulations shows that the highest downforce is generated for design variant b2, whereas the lowest downforce is produced by design variant a1. The generation of downforce is undesirable, since it could deteriorate efficiency gains by requiring additional rotor thrust to compensate for it. However, the impact of the parasite drag on the overall efficiency is more significant. Therefore, design variant b1 is selected for a detailed aerodynamic analysis. The equivalent weight penalty through aerodynamic downforce in cruise is less than 20 kg for the real helicopter.

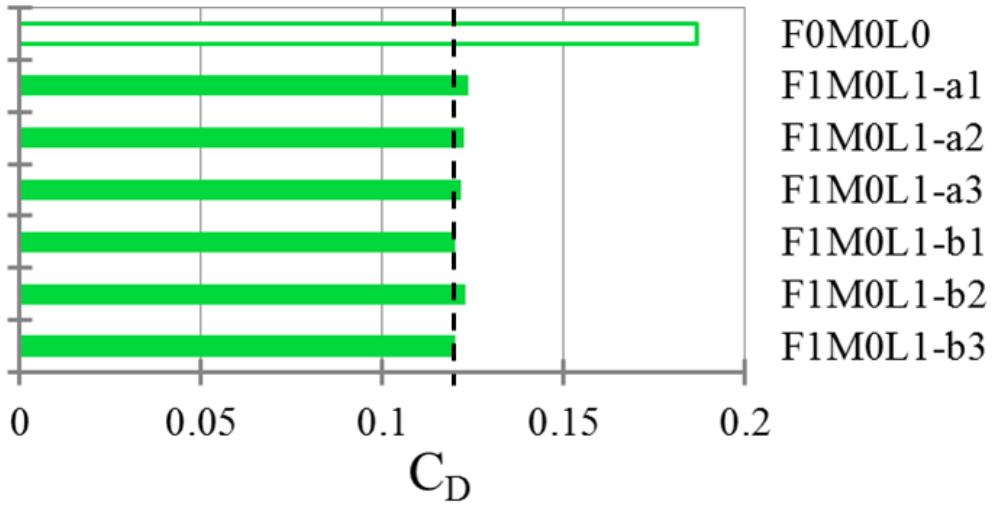

Figure 6.6: *Comparison of F0M0L0 against F1M0L1 variants a1, a2, a3, b1, b2 and b3 with respect to C_D. Numerical simulation (RANS-EARSM). $Re_\infty \approx 0.95 \cdot 10^6$, $\alpha, \beta = 0$ deg.*

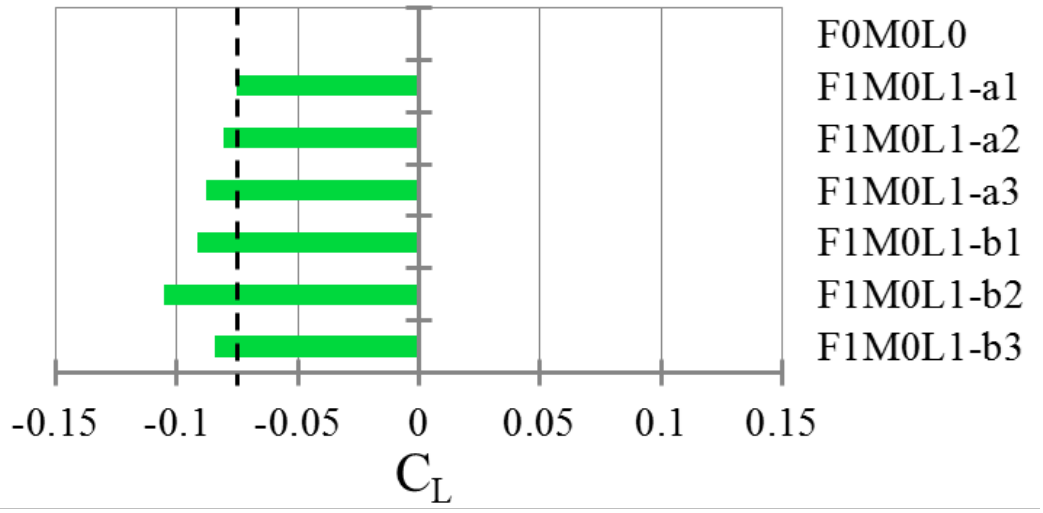

Figure 6.7: *Comparison of F0M0L0 against F1M0L1 variants a1, a2, a3, b1, b2 and b3 with respect to C_D. Numerical simulation (RANS-EARSM). $Re_\infty \approx 0.95 \cdot 10^6$, $\alpha, \beta = 0$ deg.*

Fig. 6.8 presents the final configuration L1 selected for the detailed aerodynamic analysis.

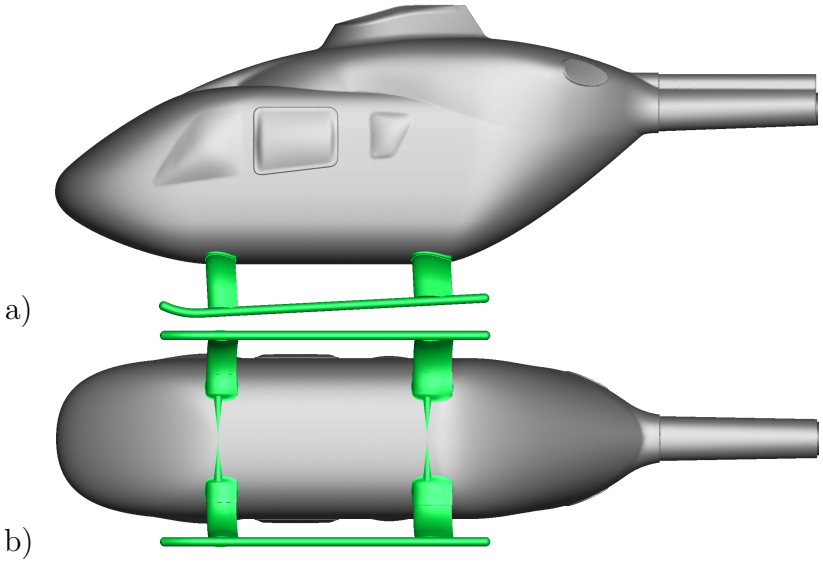

Figure 6.8: *Faired skid-landing gear variant L2 installed on F1M0 (CAD rendering), a) lateral view, b) ventral view*

The preliminary design analysis for the progressive design variant L2 of the faired skid-landing-gear has been performed by Airbus Helicopters Deutschland GmbH. Only the best candidate with respect to minimal drag and minimal downforce out of this parameter analysis (chord and twist variation) is investigated in detail; see Fig. 6.9.
The prerequisite for this design variant is that the fuselage attachment elements and the central cross-beam elements can be displaced vertically into the fuselage. In consequence, those elements become immersed inside the fuselage hull geometry and no additional external aerodynamic fairings are necessary. This minimises the aerodynamic interference of the skid-landing-gear and the fuselage. Furthermore, the junction of the outer cross-beam fairings to the fuselage can be designed primarily with respect to aerodynamic efficiency with only limited geometric constraints.
Fig. 6.10 depicts the obtained junction geometry with its smooth filleted transition between the two adjacent parts. In order to provide the necessary installation space inside the fuselage, substantial modifications to the airframe become necessary. Wether those changes are feasible or not is not considered here.

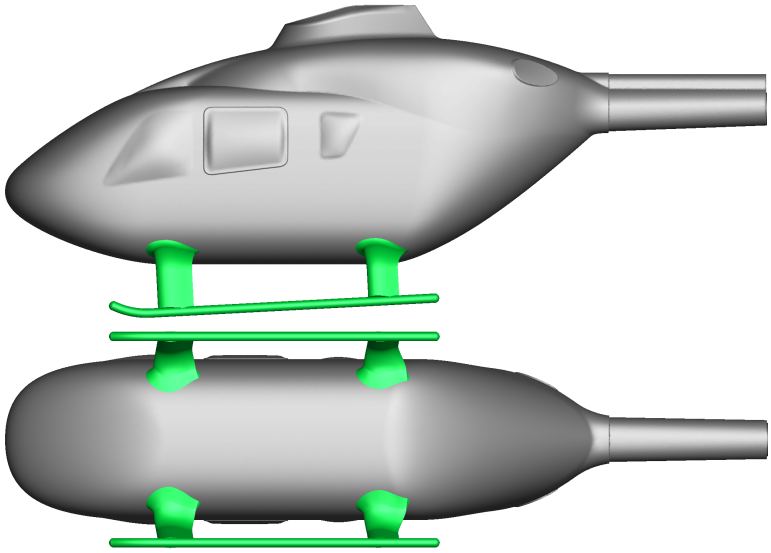

Figure 6.9: *Faired skid-landing gear variant L2 installed on F1M0 (CAD rendering), a) lateral view, b) ventral view*

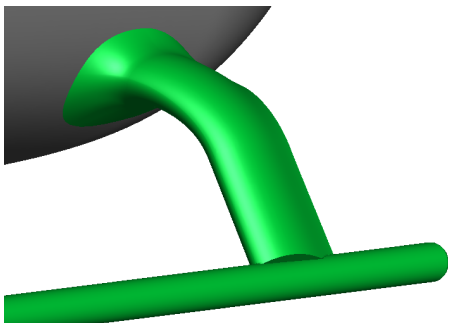

Figure 6.10: *Detailed view of the junction between the skid-landing-gear fairing and the fuselage for design variant L2 (CAD rendering).*

In analogy to the baseline campaign, incremental configurations are tested in order to determine the impact of each component. The configurations considered for the skid-landing-gear modification campaign are

- the isolated fuselage with smoothed ventral side and the baseline mast fairing F1M0.
- the final skid-landing-gear variant L1 installed on F1M0.
- the skid-landing-gear variant L2 installed on F1M0.
- the final skid-landing-gear variant L1 and the rotor head R0 installed on F1M0.
- the skid-landing-gear variant L2 and the rotor head R0 installed on F1M0.

The configurations are named accordingly F1M0, F1M0L1, F1M0L2, F1M0L1R0 and F1M0L2R0; see Fig. 6.11.

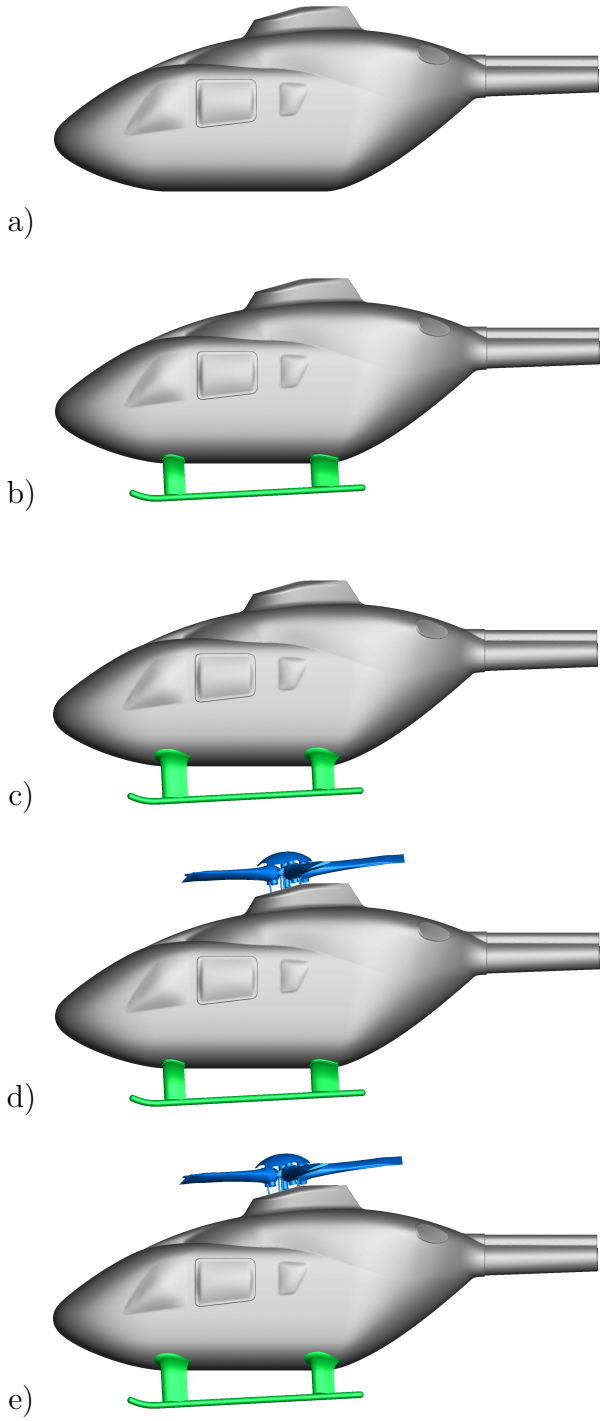

Figure 6.11: *Lateral views (CAD rendering) of the different model configurations considered for the skid-landing-gear modification campaign. a) F1M0, b) F1M0L1, c) F1M0L2, d) F1M0L1R0 and e) F1M0L2R0.*

6.1.2 Aerodynamic Forces

For assessing the aerodynamic improvements through the skid-landing-gear (L1, L2) and the fuselage ventral side (F1) modifications their impact on the global aerodynamic characteristics is investigated first. In Fig. 6.12 and 6.13, the contribution of each component to the total parasite drag is depicted and compared to the reference configuration at $\alpha, \beta = 0\ deg$. For this purpose, all component drag coefficients C_D are set in relation to the global drag coefficient of the reference configuration $C_{D,ref}$. Thus, any change in the metric $C_D/C_{D,ref}$ allows to directly deduce the achieved reduction of the total parasite drag. As outlined in chapter 1, the parasite drag of TEL-class helicopter contributes to about 50% to the total power requirements in fast-forward level flight. This means that any change in $C_D/C_{D,ref}$ weighted by a factor of 0.5 approximately corresponds to the achievable fuel flow reduction in fast-forward level flight. Unfortunately, the component $C_D/C_{D,ref}$ due to aerodynamic interference of the faired skid-landing-gears and the fuselage cannot be assessed. This limitation is associated to the junction between the skid-landing-gear fairings and the fuselage, which provides a smooth surface transition. Hence, traction between the faired skid-landing-gear and the fuselage cannot be avoided on the W/T model. In consequence, internal strain-gauge balance measurements are not feasible for the faired skid-landing-gears and distinguishing between the landing-gears form and interference drag is not possible. Therefore, both these contributions to the total parasite drag of L1 and L2 are presented as aggregates, respectively, in Fig. 6.12 and 6.13.

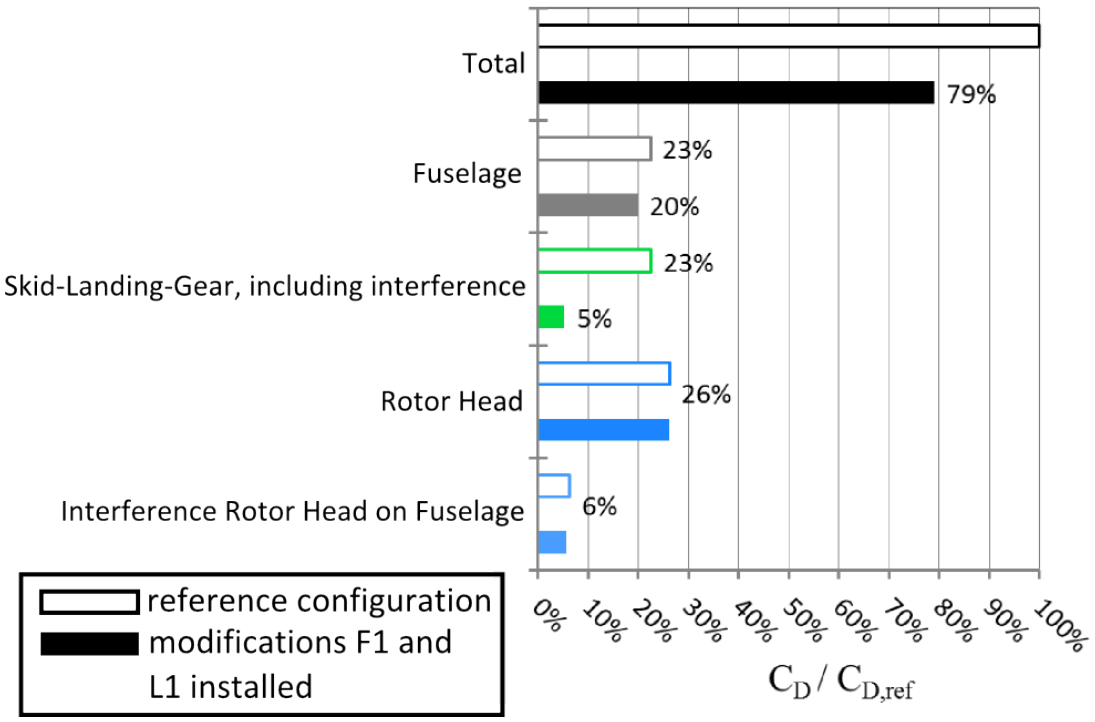

Figure 6.12: *Drag decomposition relative to the reference configuration's total parasite drag with and without modifications L1 and F1 installed.* $Re_\infty \approx 0.95{\cdot}10^6$, $\alpha, \beta = 0\ deg$.

In Fig. 6.12, $C_D/C_{D,ref}$ of the reference configuration is compared with the configuration featuring the skid-landing-gear L1 and fuselage F1. This comparison reveals that the total parasite drag can be reduced by 21% with the retrofittable skid-landing-gear fairing L1 and the fuselage with smoothed ventral side F1 installed on the reference configuration. The majority of this drag reduction is associated to the skid-landing-gear. Through the retrofittable fairing L1 the skid-landing-gear's drag is reduced to 5% of $C_{D,ref}$. Thus, the retrofittable fairing L1 yields 18% total parasite drag reduction. The remaining drag benefits are achieved by smoothing the fuselage's ventral side. F1M0's $C_D/C_{D,ref}$ is reduced by 3% relative to the reference fuselage F0M0. The remaining components do not contribute additional drag reductions.
Based on the made assumptions, the total drag reduction achieved with the modifications L1 and F1 of 21% could lead to a reduction of the total power requirements in fast-forward level flight of about 10%. Thus, also the fuel flow could be reduced by this order of magnitude with those modifications.

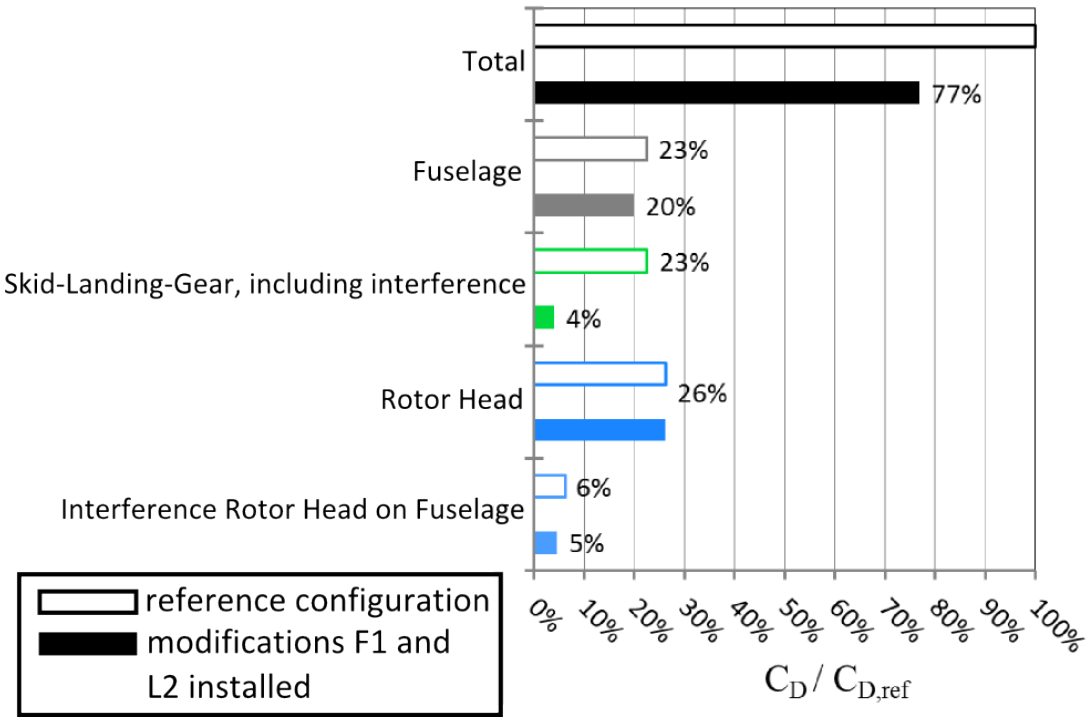

Figure 6.13: *Drag decomposition relative to the reference configuration's total parasite drag with and without modifications L2 and F1 installed.* $Re_\infty \approx 0.95 \cdot 10^6$, $\alpha, \beta = 0$ *deg.*

Fig. 6.13 depicts the components $C_D/C_{D,ref}$ of the reference configuration in comparison to the configuration featuring skid-landing-gear L2 and fuselage F1. With the progressive design variant of the faired skid-landing-gear L2 in combination with the fuselage with smoothed ventral side F1 a total drag reduction of 23% is achieved. As for the configuration modified with L1 and F1 the fuselage F1M0 contributes 3% to the total drag reduction. The majority of the achieved drag benefit is associated to the faired skid-landing-gear L2. It reduces the drag contribution of the skid-landing-gear by 19% to 4% of $C_D/C_{D,ref}$. Thus, skid-

landing-gear L2 reduces the drag by another 1% of $C_D/C_{D,ref}$ compared to L1. With L2 installed another 1% of $C_D/C_{D,ref}$ drag reduction is associated to aerodynamic interference of the rotor head with the fuselage.
In Fig. 6.14 and 6.15, the resulting drag decomposition of the reference configuration fitted with F1 and, respectively, L1 and L2 is depicted. The data for the component drag of the fuselage, the skid-landing-gear (including aerodynamic interference with F1M0) and the rotor-head as well as the aerodynamic interference of the rotor-head on F1M0 at $\alpha, \beta = 0deg$ can be assessed with the available experimental database. In order to assess the complete parasite drag decomposition of the reference geometry fitted with F1 and L1 or L2, the contribution of the tailboom, the stabilisers, the flow through the upper deck and excrescences is assessed based on the corporate data provided by Airbus Helicopters Deutschland; see section 5.2.
For the reference configuration fitted with F1 and L1 the fuselage accounts for 25% of the configuration's total parasite drag; see Fig. 6.14. For the reference configuration the fuselage only contributed 23% to the reference total parasite drag. Thus, the relevance of the fuselage for further drag reduction has increased by a small margin. The skid-landing-gear drag contribution, including interference, still amounts to 7%. The rotor-head including interference effects is responsible for the largest single contribution (40%) to the total parasite drag of the reference configuration fitted with F1 and L1. Hence, the fuel flow reduction potential by reducing the rotor-head drag for such a more streamlined design is significant. The tailboom and stabilisers and the upper deck and excrescences add, respectively, another 19% and 9% to the total parasite drag. On the reference configuration those components only added 22% to the total parasite drag.

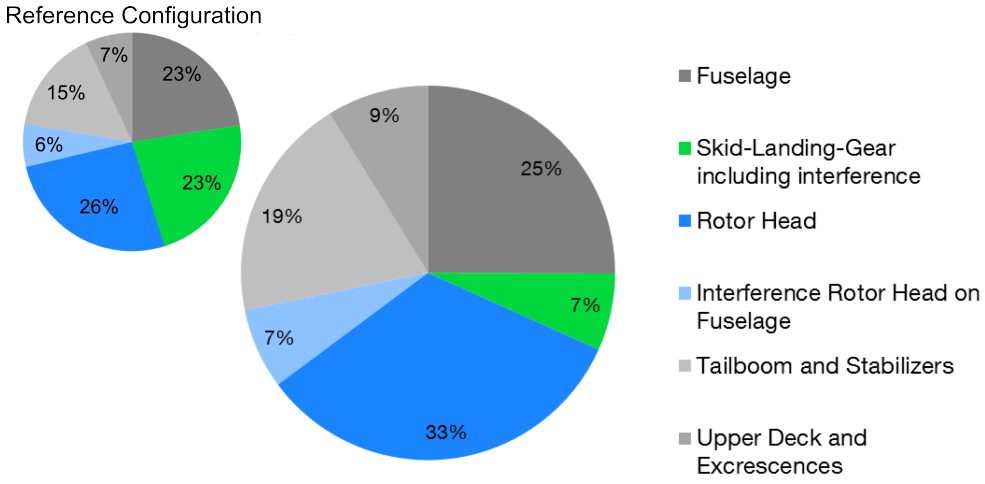

Figure 6.14: *Drag Decomposition for F1M0L1R0. The drag contribution of the components not included on the ADHeRo W/T model are based on corporate data of Airbus Helicopters Deutschland.* $Re_\infty \approx 0.95 \cdot 10^6$, $\alpha, \beta = 0$ *deg.*

For the reference configuration fitted with F1 and L2 the fuselage accounts for 26% of the configuration's total parasite drag; see Fig. 6.15. The skid-landing-gear's drag contribution, including interference, is further reduced compared to the reference configuration fitted with F1 and L1. With F1 and L2 installed the skid-landing-gear contributes 5% to the configurations total parasite drag. The rotor-head including interference effects is also responsible for the largest single contribution on the reference configuration with F1 and L2 installed. The rotor-head contributes 40% to the total parasite drag. The tailboom and stabilisers and the upper deck and excrescences add, respectively, another 20% and 9% to the total parasite drag.

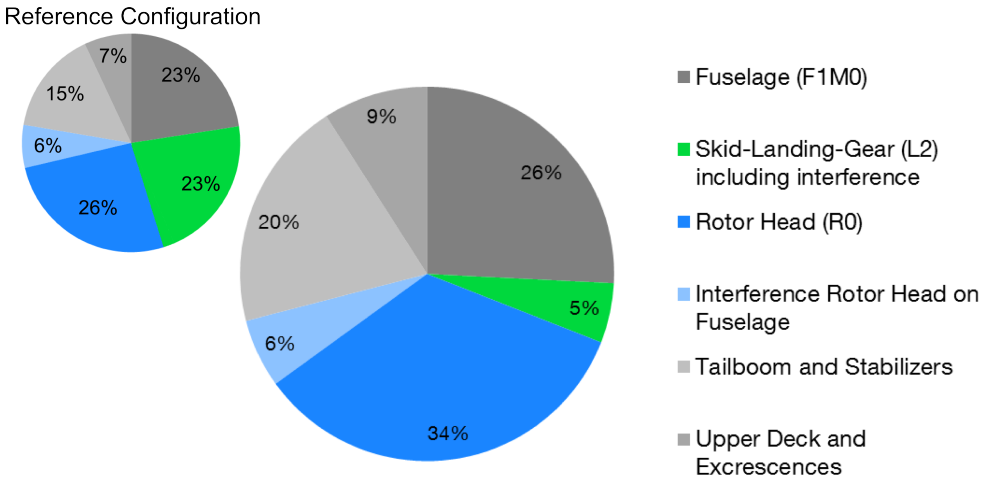

Figure 6.15: *Drag Decomposition for F1M0L2R0. The drag contribution of the components not included on the ADHeRo W/T model are based on corporate data of Airbus Helicopters Deutschland.* $Re_\infty \approx 0.95 \cdot 10^6$, $\alpha, \beta = 0$ *deg.*

In Fig. 6.16 and 6.17, the lift decomposition of the baseline configuration is compared to the same configuration fitted with F1 and, respectively, L1 and L2. The data for the component's lift of the fuselage, the skid-landing-gear (including aerodynamic interference with F1M0) and the rotor-head as well as the aerodynamic interference of the rotor-head with the fuselage is assessed at $\alpha, \beta = 0$ *deg*. The contribution to the configurations total lift of the tailboom, the stabilisers, the flow through the upper deck and excrescences is not assessed.
The fuselage with the smoothed ventral side increases the downforce generated at the isolated fuselage; see Fig. 6.16. This decreases the fuselage's C_L from -0.083 (F0M0) to -0.107 (F1M0). Streamlining the fuselage's ventral side decreases the drag of the isolated fuselage by attenuating the separation at the fuselage's rear upsweep; see section 6.1.3. In consequence, the flow is better deflected along the models positive vertical axis x_m and the downforce increases. Thus, the effect of delayed separation through the fuselage's smoothed ventral side is not only observed in drag, but in lift as well.

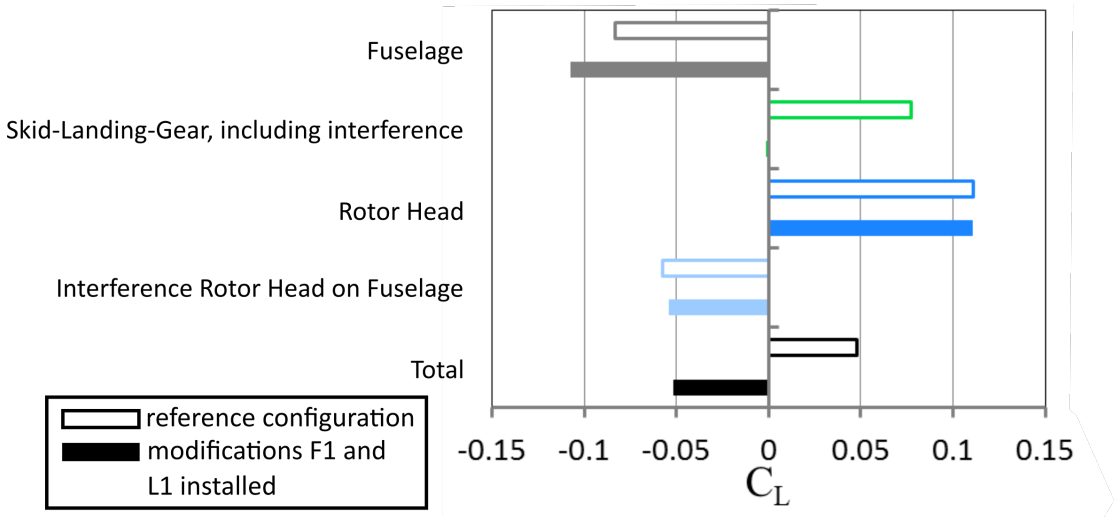

Figure 6.16: *Comparison of F1M0L1R0's lift decomposition against F0M0L0R0's.* $Re_\infty \approx 0.95 \cdot 10^6$, $\alpha, \beta = 0$ *deg.*

The baseline skid-landing-gear increases the configuration's C_L. In section 6.1.3, it is shown that this increase in C_L is associated to the skid-landing-gear's aerodynamic interference with the fuselage. This interference leads to a more pronounced separation at the rear fuselage's upsweep. Thus, the upward deflection of the flow around the upsweep decreases substantially and the generated downforce is significantly reduced. For the faired skid-landing-gear L1, this effect is not observed. The skid-landing-gear L1 including its aerodynamic interference with the fuselage is basically neutral with respect to lift. Between configurations F0M0L0R0 and F1M0L1R0 a minor deviation between the rotor-head's contribution to lift is observed. In consequence of the discussed changes in the lift decomposition, the total lift of configuration F1M0L1R0 deviates considerably from F0M0L0R0. Instead of a net lift equivalent to $C_L = 0.05$ for F0M0L0R0 a net downforce equivalent to $C_L = -0.05$ is obtained for F1M0L1R0 . The equivalent weight penalty through aerodynamic downforce in cruise is less than 80 kg for the real helicopter.
The faired skid-landing-gear L2 actually adds lift to the modified configuration including F1 and L2; see Fig. 6.17. Compared to the baseline skid-landing-gear the magnitude is smaller though. The reason for this is that the faired skid-landing-gear L2 is minimising aerodynamic interference with the fuselage even further than the faired skid-landing-gear L1. On the other hand, the fairings of the landing-gears are designed to generate lift through the applied twist variation; see section 6.1.1. Furthermore, the attachment to the fuselage could be designed to avoid generating any downforce. For the configuration fitted with F1 and L2, the same effect regarding the interference of the rotor head with the fuselage in terms of lift is observed as for the configuration fitted with F1 and L1. However, the downforce resulting from the interference of the rotor-head with the fuselage is further reduced with L2. On aggregate, this results in a downforce for the configuration F1M0L2R0 which is considerably reduced compared to F1M0L1R0. This difference in generated down force, equal to 30 kg in cruise, could provide reasoning to consider L2 for future machines.

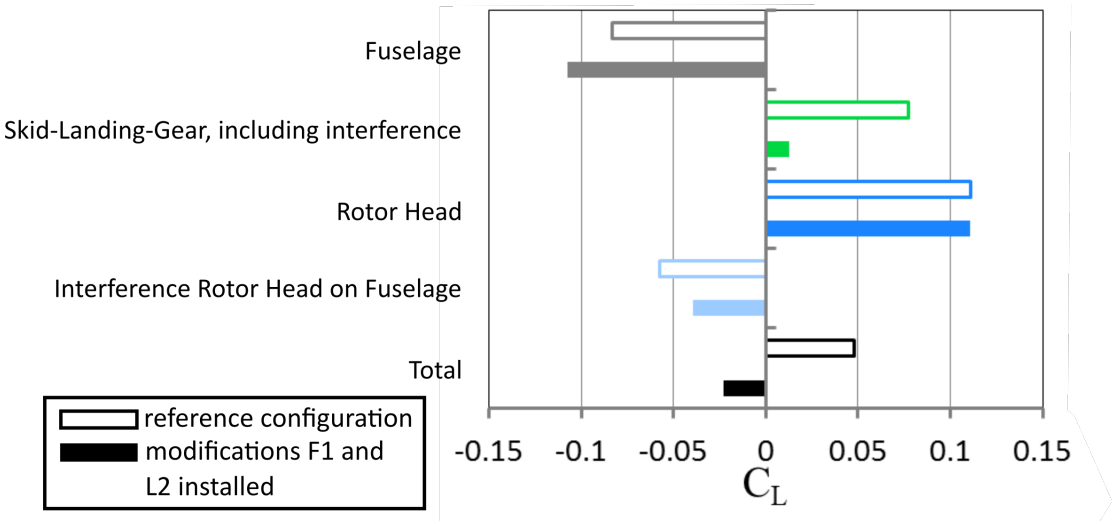

Figure 6.17: *Comparison of F1M0L2R0's lift decomposition against F0M0L0R0's.* $Re_\infty \approx 0.95 \cdot 10^6$, $\alpha, \beta = 0$ *deg.*

However this design is more challenging to be implemented due to the required structural changes, which could also impose additional weight penalties. For this reason only the faired skid-landing-gear L1 is considered for further aerodynamic analysis in this work.

6.1.3 Surface Pressure

In Fig. 6.18, F0M0's and F1M0's c_p contours in the rear fuselage's region, based both on experimental and numerical data, are depicted for $Re_\infty \approx 0.95 \cdot 10^6$ at $\alpha, \beta = 0\ deg$ (top left). Furthermore, c_p is depicted as a function of $y_r/(b_f/2)$ and x_r/l_r for selected horizontal slices $Z5, Z7, Z9, Z11$ and the vertical slice Y0, respectively. The markups showing the flow characteristics in Fig. 6.18 are derived from the topological analysis of F1M0's near-surface and wake flow, which is based on simulation data; see section 6.1.4. The surface pressure data obtained by experiment and simulation are qualitatively and quantitatively in good to excellent agreement for F1M0.
Smoothing the fuselage's ventral side has a significant impact on the rear fuselage flow topology; see section 6.1.4. The source of the observed drag reduction for F1M0 compared to F0M0 is associated to the delay of the flow separation observed at the rear fuselage's upsweep. Furthermore, closing the cavities for housing the skid-landing-gear's cross-beams on F0M0 eliminates the pressure drag associated to the flow entering these cavities and no cavity vortices (CV) are generated. The impact of delaying the separation at the rear fuselage's upsweep on the surface pressure distribution can be assessed qualitatively by comparing the contour plots for c_p; see top left image in Fig. 6.18. Especially, at the ventral side of the rear fuselage's upsweep the pressure recovery is improved by smoothing the fuselage's ventral side. Furthermore, a significant part of the flow past the rear fuselage's upsweep reattaches after the initial separation to the upsweep's surface; see section 6.1.4. This leads to increased c_p levels near the model's symmetry plane, thus, reducing the drag of F1M0 compared to F0M0.
For F0M0, significant suction peaks have been observed at the beginning of both the fuselage's vertical upsweep and lateral tapering; see section 5.3. Those peaks are also observed for F1M0 but the peaks magnitudes are different. The suction peak's magnitude along Y0 at the ventral side of the vertical fuselage's upsweep reduces by $\Delta c_p = 0.14$. Furthermore, its location is shifted downstream by $x_r/l_r = 0.03$. This difference is associated to the omitted cavities for housing the skid-landing-gear's cross-beams on F1M0. In consequence, the flow past the fuselage's ventral side does not impinge on the trailing edge of the rear cavity and the local suction peak reduces. By alleviating the flow perturbations along the smoothed fuselage's ventral side, higher momentum fluid reaches the rear fuselage's upsweep within flow region FR3. Thus, the near-surface flow withstand the adverse pressure gradient at the vertical upsweep longer and the flow separation is delayed. This also impacts on the location of the primary free surface separation at the fuselage's lateral side along separation lines SL3a and SL3b, which corresponds to F0M0's SL2a and SL2b; see section 5.4. SL3a and SL3b are shifted further downstream by a small margin. Thus, the flow is accelerated more around the lateral tapering and the suction peak increases in magnitude. This effect is more prominent at the lateral tapering's ventral side. Consequently, the suction peak's magnitude observed in slices Z11 and Z9 increases more, compared to F0M0, than those at slices Z7 and Z5. The suction peak observed at Z11 increases by $\Delta c_p = 0.14$. At Z5, the increase in the suction peak's magnitude compared to F0M0 is almost negligible.

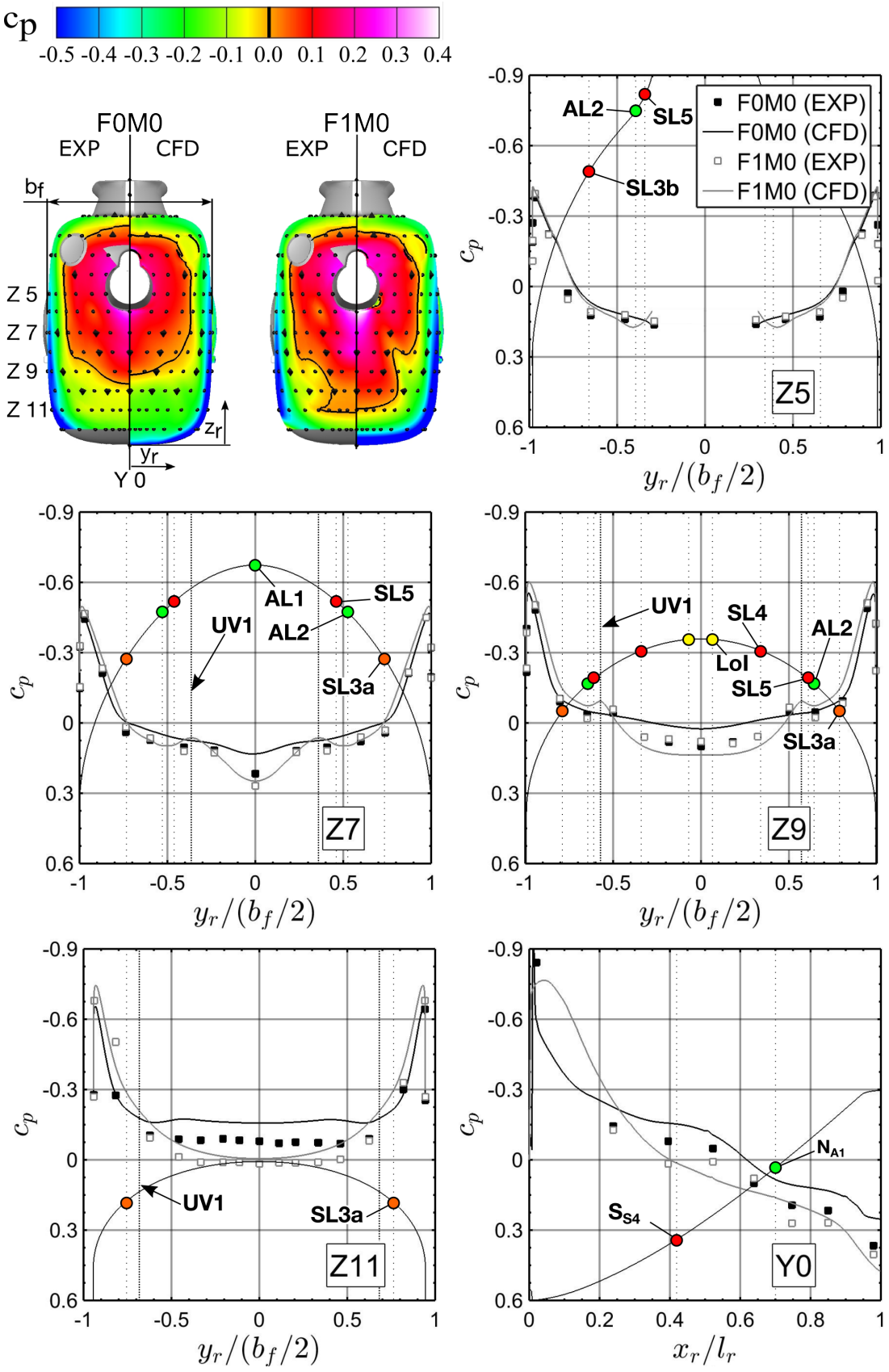

Figure 6.18: *c_p distribution at the rear fuselage for F0M0 and F1M0 (top left) and the associated slices Z5, Z7, Z9,Z11 and Y0. $Re_\infty \approx 0.95 \cdot 10^6$, $\alpha, \beta = 0$ deg.*

The separation at the lateral tapering along SL3a and SL3b correlates well with the decrease in pressure recovery in the lateral direction. This means that the flow can initially withstand the adverse pressure gradient downstream of the suction peak. In this region, the shear-layer begins to develop, which then eventually begins to roll-up into the primary counter-rotating upsweep vortex UV1 after separating at SL3a.
For the baseline fuselage F0M0, local minima in c_p associated to the formation of CV have been identified; see section 5.3. Those minima cannot be observed for F1M0, because the cavities at the fuselage's ventral side are closed. However, the formation of the primary upsweep vortex UV1 is intensified. In consequence, local pressure minima are observed for F1M0's c_p as a function of $y_r/(b_f/2)$ along Z9 and Z7, respectively, at $y_r/(b_f/2) = \pm 0.58$ and $y_r/(b_f/2) = \pm 0.38$. At Z11 no local minima are observed near the location of UV1's vortex core location. At this position the vortex just began to roll-up and, therefore, doesn't yet significantly impact on the surface pressure in this region. At Z5, no impact of UV1 on the c_p distribution is observed either. However, in this case the vortex is already well developed but its trajectory is not in close proximity to the wall anymore; see section 6.1.4. Thus, its influence on the surface pressure is not observable as local c_p minima.
In consequence of the smoothed fuselage's ventral side, the extension of the secondary separation (FR4) reduces for F1M0 compared to F0M0. This becomes evident in c_p as a function of $y_r/(b_f/2)$ at slices Z7, Z9 and Z11. For F0M0, a substantial pressure plateau associated to the secondary separation (SL3) is observed at Z11 in between $y_r/(b_f/2) \leq \pm 0.64$. This pressure plateau is eliminated on F1M0 since the secondary separation is not present at Z11. At Z9 the secondary separation on F1M0 causes a pressure plateau between $y_r/(b_f/2) \leq \pm 0.34$, which is associated to separation line SL4. On F0M0 the corresponding pressure plateau, in between SL3, extends to $y_r/(b_f/2) \leq \pm 0.74$. Hence, by smoothing F1M0's ventral side the extension of the pressure plateau at Z9 is reduced by 64% compared to F0M0. This leads to a pressure increase of $\Delta c_p = 0.15$ within F1M0's secondary separation at Z11. At Z7 the pressure plateau on F0M0 is defined by the primary separation line SL2b, since SL3 has converged to SL2b and separated from the surface at P2. For F1M0, the vortex formation along SL3a is still effective at Z7. Thus, the flow in between the primary and secondary separation remains attached. In consequence, higher pressure levels are observed on F1M0 in between SL3a and SL5 compared to F0M0. In between SL5, no pressure plateau is observed for F1M0, since the flow reattaches along AL1 in consequence of UV1's induced velocity field. This leads to the local pressure maximum at $y_r/(b_f/2) = 0$ along Z7.
The effect of delayed separation and increase in vortex intensity on F1M0 shifts the recirculation zone (RZ) further downstream and reduces its longitudinal extension compared to F0M0; see section 6.1.4. F1M0's RZ is located along Y0 in the range of $0.42 < x_r/l_r < 0.7$. For F0M0 the recirculation zone extends to $0.2 < x_r/l_r < 0.68$. For c_p as a function of x_r/l_r at Y0 this effect becomes evident by an increased pressure level compared to F0M0 of about $\Delta c_p = 0.1$ after the initial suction peak.

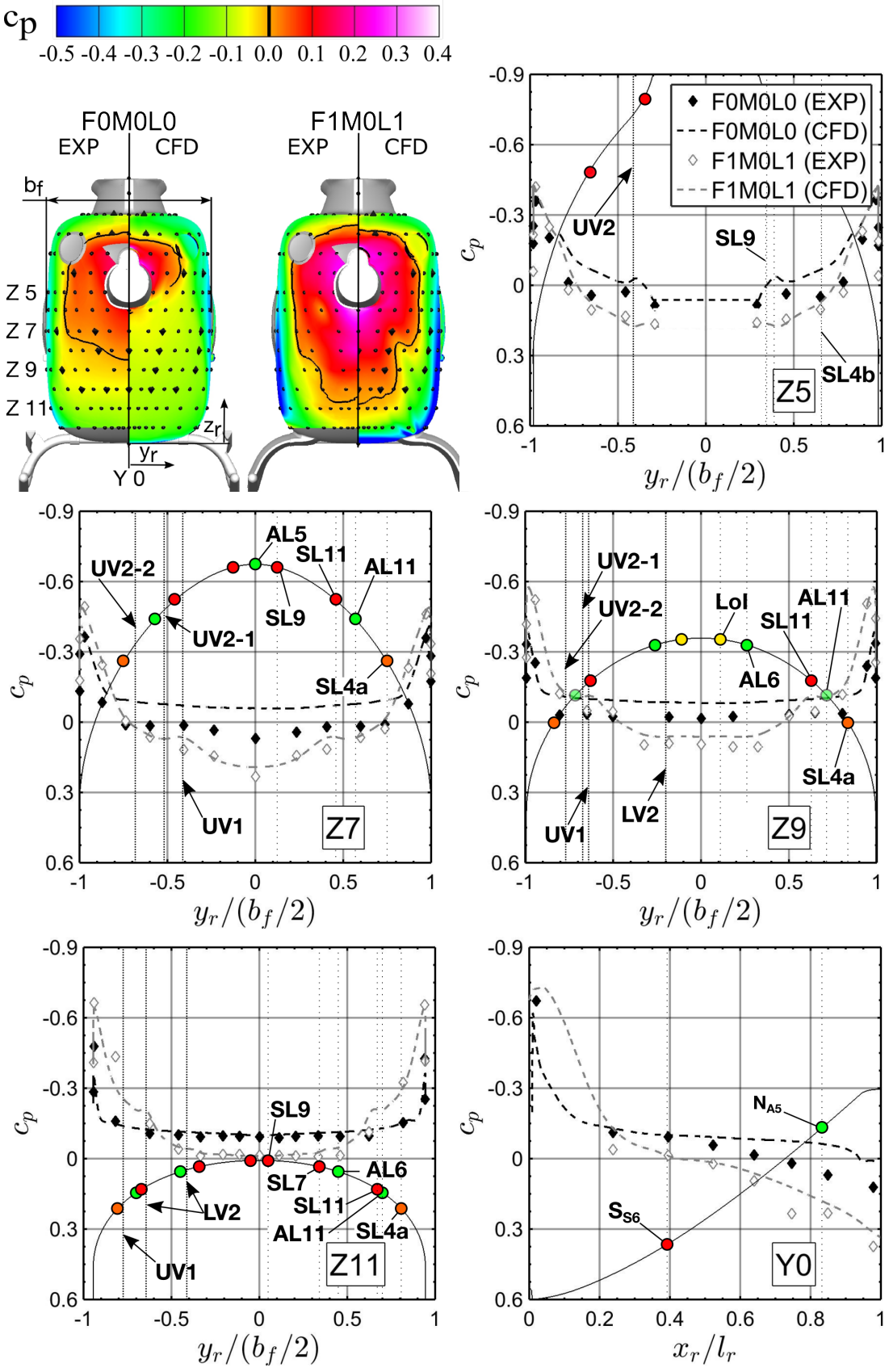

Figure 6.19: *c_p distribution at the rear fuselage for F0M0L0 and F1M0L1 (top left) and the associated slices Z5, Z7, Z9,Z11 and Y0. $Re_\infty \approx 0.95 \cdot 10^6$, $\alpha, \beta = 0$ deg.*

In Fig. 6.19, F0M0L0's and F1M0L1's c_p contours in the rear fuselage region are presented in analogy to Fig. 6.18 at $\alpha, \beta = 0\ deg$. The surface pressure data obtained by experiment and simulation are qualitatively and quantitatively in good to excellent agreement for F1M0L1 as well.
Comparing F0M0L0's and F1M0L1's c_p contours reveals that the base pressure is significantly increased by fairing the baseline skid-landing-gear over almost the entire rear fuselage. However, at the rear fuselage's lateral tapering the suction peaks due to the strong surface curvature are increased on F1M0L1. The reason for this increase is associated to the effective delay of the flow separation at the fuselage's rear upsweep; see section 6.1.4. Thus, the flow is accelerated around the lateral tapering more effectively and the suction peaks intensify. For F0M0L0 no upsweep vortex is formed due to the significant extension of the secondary separation. By fairing the skid-landing-gear and smoothing the fuselage's ventral side the extension of the recirculation zone is significantly reduced for F1M0L1 compared to F0M0L0. In consequence, the primary upsweep vortex UV1 is formed along the separation line SL4a. This leads to local surface pressure minima near UV1's trajectory, which are discernible at Z7 and Z9 for $y_r/(b_f/2) = \pm 0.4$ and $y_r/(b_f/2) = \pm 0.65$, respectively. Between AL11 and SL11 as well as between SL4a and AL11, respectively, the secondary upsweep vortex UV2-1 and UV2-2 is formed; see section 6.1.4. However, UV2-1's and UV2-2's vortex intensity is low and, thus, no local pressure minima are associated to these vortices. At L1's rear attachment fairing, the landing-gear vortex LV2 is formed due to a horseshoe type corner vortex. At Z11, LV2 are still in close proximity to the model's surface, which induces local pressure minima at $y_r/(b_f/2) = \pm 0.4$ and $y_r/(b_f/2) = \pm 0.65$. Downstream of the rear attachment fairing the flow attaches to F1M0L1's rear fuselage upsweep along AL6. In consequence, the pressure is increased for F1M0L1 compared to F0M0L0 at Z11 and Z9 close to the model's symmetry plane. At slice Z7 the same effect is observed. However, at Z7 the flow reattachment is associated to AL5. AL5 appears as the flow reattaches downstream of the recirculation zone at N_{A5}.
At Z5. F1M0L1's pressure level is also increased compared to F0M0L0's. This is associated to the suppression of flow entering the rear fuselage's upsweep along the fuselage dorsal side, which is observed for F0M0L0. Furthermore, the flow remains attached between SL4b and SL9 for F1M0L1 up to SL10, which further increases the pressure recovery.
In order to study the effect of the faired skid-landing-gear's aerodynamic interference on F1M0 in more detail, F1M0's and F1M0L1's c_p distributions in the rear fuselage region are compared; see Fig. 6.19 .Through this comparison it becomes clear, that the aerodynamic interference of L1 on F1M0 is considerably reduced compared to L0's aerodynamic interference on F0M0. Nevertheless, for c_p as a function of x_r/l_r along Y0 minor deviations can be observed.
At the beginning of the rear fuselage's upsweep, the presence of the faired skid-landing-gear leads to higher c_p levels. This is associated to the perturbation of the cross-beam elements which are not fully covered. In consequence, the suction peak at the beginning of the rear fuselage upsweep is attenuated. Further downstream along Y0 the faired skid-landing-gear reduces $\partial c_p/\partial(x_r/l_r)$ for $0.4 \leq x_r/l_r \leq 0.5$.

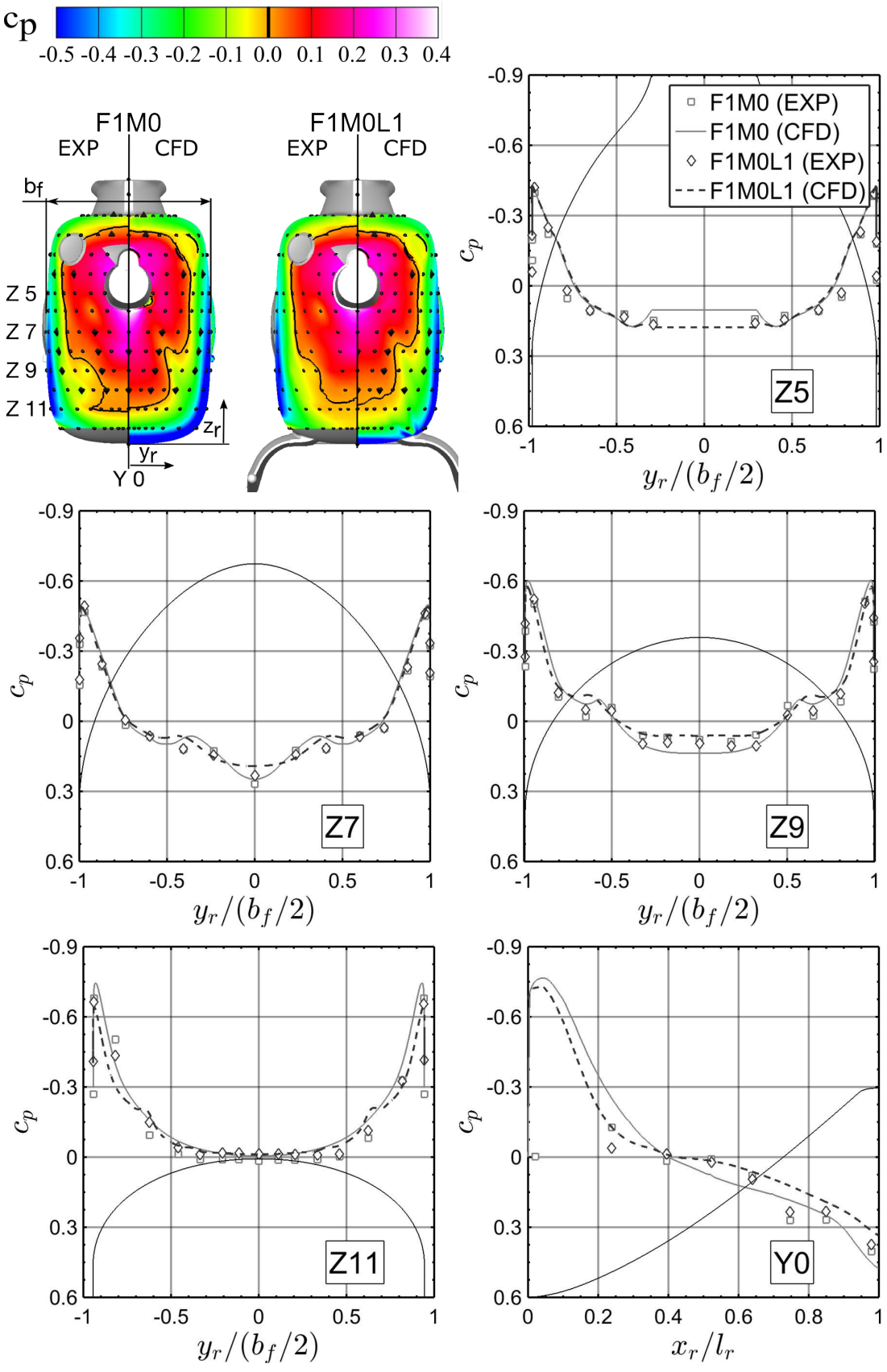

Figure 6.20: *c_p distribution at the rear fuselage for F1M0 and F1M0L1 (top left) and the associated slices Z5, Z7, Z9,Z11 and Y0. $Re_\infty \approx 0.95 \cdot 10^6$, $\alpha, \beta = 0$ deg.*

This deviation is associated to the more pronounced recirculation zone in the presence of L1; see section 6.1.4. Consequently, the total pressure recovery along slice Y0 is reduced and F1M0L1's c_p is lower compared to F1M0 for $0.4 \leq x_r/l_r \leq 1.0$. In consequence, of the attenuated pressure recovery in the presence of L1, also F1M0L1's c_p as a function of $y_r/(b_f/2)$ is reduced compared to F1M0 close to the model's symmetry plane. The affected region is associated to $-0.5 \leq y_r/(b_f/2) \leq 0.5$ and $-0.2 \leq y_r/(b_f/2) \leq 0.2$ at slices Z9 and Z7, respectively. Thus, further potential for parasite drag reduction is identified with respect to L1's aerodynamic interference on F1M0. The results of the associated optimisation are presented in section 6.2.

6.1.4 Flow Topology

In this section, the flow topologies of the optimised skid-landing-gear models F1M0 and F1M0L1 are analysed. This includes both the near-surface flow topology and the flow topology in the wake of these configurations. F1M0's and F1M0L1's near-surface topology is analysed first and relevant flow regions are identified; see section *Near-Surface Flow Topology*. This also includes a comparison of F1M0's and F1M0L1's near-surface flow topology against the corresponding topology of F0M0 and F0M0L0, respectively. In a second step, the resulting wake flow topologies of F1M0 and F1M0L1 are analysed in order to identify vortex structures and their trajectories, recirculation zones and the envelope of the wake regions. These results are presented in section *Wake Flow Topology*. Furthermore, the impact of the implemented modifications on the wake flow topology in comparison to the corresponding baseline configurations is presented.

Near-Surface Flow Topology

In Fig. 6.21 a) and b), the near surface flow topology is depicted for configuration F1M0 at $\alpha, \beta = 0\ deg$. This topology is derived from skin-friction-lines based on the performed numerical simulation; see section 4. In Fig. 6.21 a), the flow around the fuselage F1 is decomposed into relevant flow regions, whereas Fig. 6.21 b) depicts the identified structure of the near-surface flow topology.
The flow topology at F1M0's rear fuselage can be divided into four main flow regions (FR). Those four regions are found on both the starboard and port-side of the model, since the flow is symmetric with respect to the model's symmetry plane. FR1 covers the upper part of the fuselage; i.e. the engine cowling. It further divides into the sub-regions FR1a and FR1b. FR1a covers the engine cowling area close to the models symmetry plane. In the lateral direction, FR1a is limited by the symmetry plane and the characteristic streamline of the incoming flow $C1_i$. $C1_i$ connects the attachment nodus at the fuselage nose N_{A0} and the separation saddle point S_{S1}; see Fig. 6.21 b). At the downstream end, FR1a is limited by three separation lines (SL); i.e. SL1, SL2 and SL6. At S_{S1} the incoming flow separates and the separation SL1 originates. At the ends of SL1's inboard and outboard section, the limiting points are the separation foci F_{S1} and F_{S1-2}, respectively. Thus, a gap between F_{S1} and the symmetry plane remains. Through this gap the incoming flow within FR1a passes SL1. This includes the three characteristic streamlines of the back flow $C1_b$, $C2_b$ and $C6_b$. $C1_b$ and $C2_b$ are deflected back leading to the downstream side of S_{S1} and S_{S2} respectively. The inboard section of SL2 originating from S_{S2} ends in F_{S1-2}, which connects SL1 and SL2. The outboard section of SL2 ends in F_{S2-3-6}. $C6_b$ ends in S_{S6}, from which the characteristic streamline of the incoming flow $C6_i$ separates forming SL6. At the inboard and outboard limit of SL6, the foci F_{S5-6} and F_{S2-3-6} are located, respectively. F_{S2-3-6} connects SL2 and SL6, thus, completing the downstream end of FR1a. However, between the symmetry plane and F_{S5-6} the flow within FR1a exits towards the tailboom.

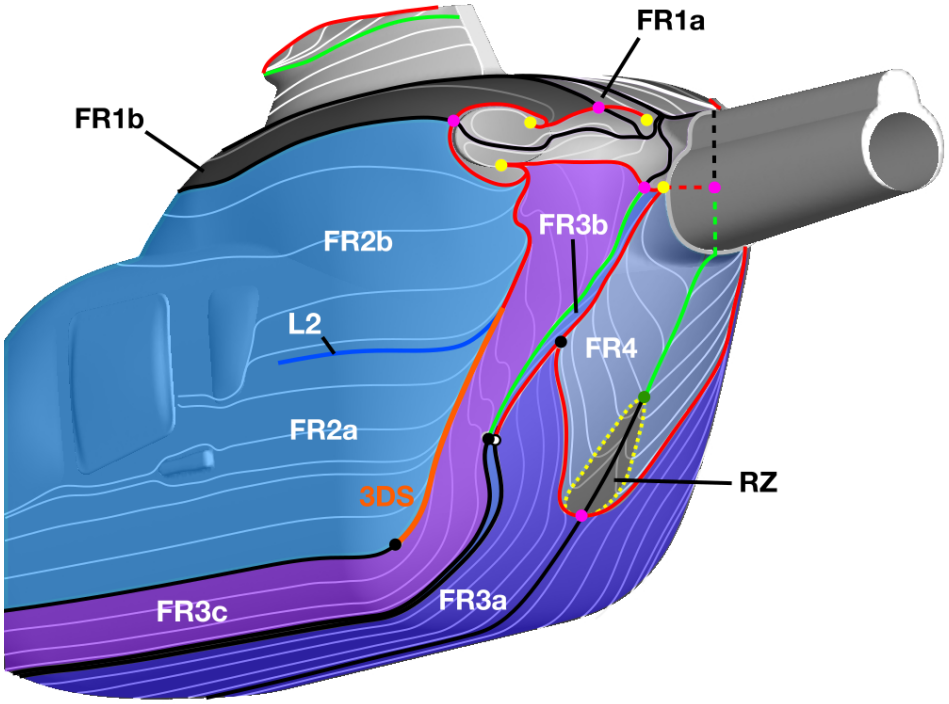

a)

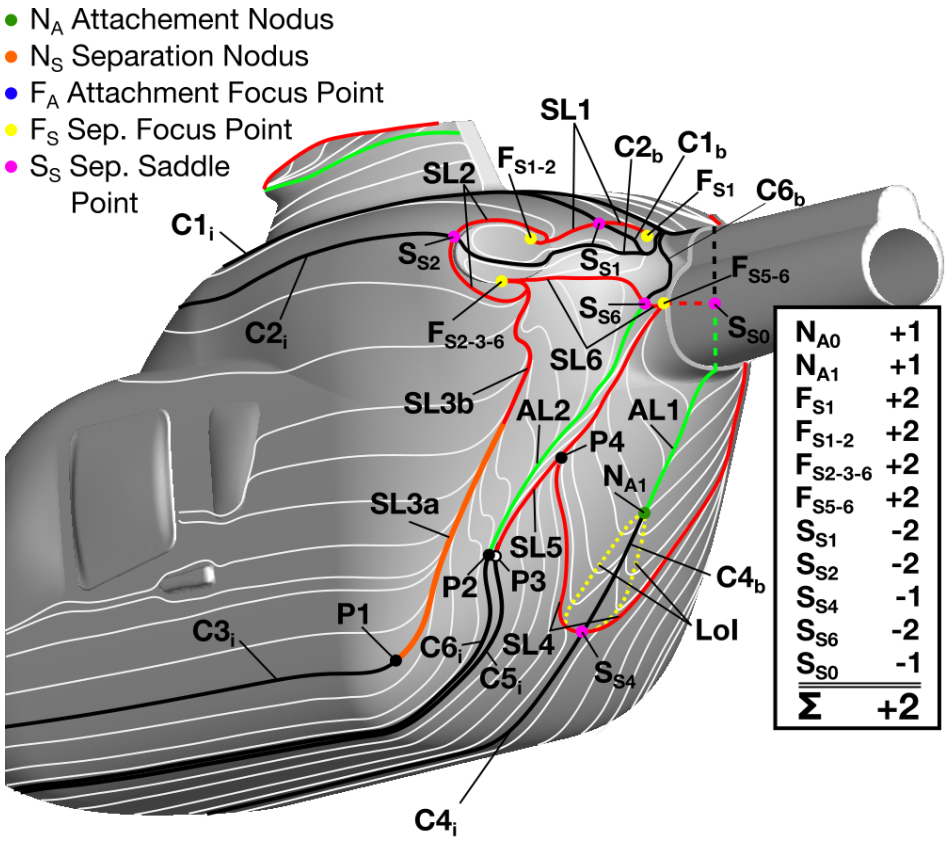

b)

Figure 6.21: *Schematic representation of the near-surface flow topology for F1M0; a) flow regions, b) flow topology.* $Re_\infty \approx 0.95 \cdot 10^6$, $\alpha, \beta = 0$ *deg.*

The near-surface flow topology along the tailboom is not considered in this analysis. Nevertheless, the topology can be closed by adding a fictional separation saddle point S_{S0} as outlined in section 5.4.1.
FR1b is located adjacent to the outboard limit $C1_i$ of FR1a, extending up to $C2_i$ in the lateral direction. $C2_i$ connects N_{A0} and S_{S2}. The limits at the downstream end of FR1b's longitudinal extension are the outboard section of SL1 and the inboard section of SL2.
At the fuselage's side the flow region FR2 is observed. In the vertical direction, FR2 is limited by the dorsal bounding streamline $C2_i$ and the ventral bounding streamline $C3_i$. $C3_i$ connects N_{A0} with the separation nodus F_{S2-3-6}. On $C3_i$ the point P1 is located, which marks the beginning of converging skin-friction-lines along $C3_i$. Downstream from this point, a three-dimensional free surface separation occurs. Thus, the section of $C3_i$ between P1 and F_{S2-3-6} constitutes SL3. F_{S2-3-6} connects SL3 with the outboard section of SL2. Hence, SL3 and the outboard section of SL2 define the downstream limit of FR2. However, SL3 is further divided into SL3a and SL3b. The distinction indicates the regions where the detaching shear-layer is fed into the primary upsweep vortex (SL3a) and where not (SL3b); see section 6.1.4. Consequently, it is distinguished between FR2a and FR2b at the downstream end of FR2. The boundary between those two regions in the vertical directions is defined by the incoming streamline L2, which converges towards SL3 at the interface between SL3a and SL3b.
At the fuselage's ventral side, the flow region FR3 is located. In the lateral direction FR3 is bounded by $C4_i$ and $C3_i$. This also includes the region of the three dimensional free surface separation along $C3_i$, i.e. SL3. $C4_i$ is congruent with the model's symmetry plane and connects N_{A0} with S_{S4}. The downstream end of FR3 constitute SL4, SL5 and SL6. SL4 originates at S_{S4} and separates from the surface as it encounters SL5 at P4. SL5 originates from the free-surface separation downstream of P3 along $C5_i$ and terminates in F_{S5-6}. Through F_{S5-6} SL5 is connected to SL6, thus closing FR3. Within FR3 the sub-regions FR3a, FR3b and FR3c are located.
FR3a is limited in the lateral direction by its inboard limits $C4_i$ and SL4 and its outboard limit $C5_i$. $C5_i$ connects N_{A0} with F_{S5-6}. The downstream end of FR3b is defined by SL5 between P3 and P4. FR3b is laterally bounded by $C5_i$ and $C6_i$. $C6_i$ connects N_{A0} with S_{S6}. On $C6_i$, P2 is located, which marks the beginning of diverging skin-friction lines along $C6_i$. At point P2, the fluid transported by the main upsweep vortex towards the surface starts to attach on the surface; see section 6.1.4. Thus, AL2 originates at P2 and terminates in S_{S6}. The inboard section of SL6 consequently constitutes the downstream end of FR3b. The region of FR3b between AL3 and SL5 defines the region where the secondary upsweep vortex UV2-1 is formed; see section 6.1.4.
The internal structure of FR3 is completed by FR3c. FR3c is closed at its downstream end by the outboard section of SL6, which is connected to FR3d's lateral bounds $C3_i$ and $C6_i$ through F_{S2-3-6} and S_{S6}, respectively.
The near-surface flow topology is completed by FR4. FR4 is limited laterally by SL4, SL5 downstream of P4, $C4_b$ and the attachment line AL1. Within FR4 the recirculation zone RZ is located. RZ is enclosed by the line of inflection (LoI) and $C4_b$. $C4_b$ connects the reattachment point N_{A1} with the downstream side of S_{S4}. AL1 is located at the symmetry plane and connects N_{A1} with the fictional

separation saddle S_{S0} introduced in order to close the topological field.
The box on the right of Fig. 6.21 b) summaries all identified characteristic points of the near-surface flow topology. All nodi, foci and saddle points which feature a symmetric counter-part are counted twice. As can be seen S_{S0} consistently closes the theorem, by returning a sum of 2 according to Eq. 5.4.
Comparing F1M0's near-surface flow topology against F0M0's reveals four main differences in consequence of smoothing the fuselage's ventral side. First of all the extension of the region where the primary upsweep vortex is generated increases by F1's smoothed shape. This is also associated to the second difference in F1M0's flow topology. Due to the reduced flow perturbation along F1's ventral side, the extension of the secondary separation (FR4) is significantly reduced. In consequence, the vortex formation along the three-dimensional free-surface is not disturbed by this secondary separation. Thus, the vortex formation is intensified along SL3a. The increased vortex strength of UV1 in turn amplifies the induced vertical velocity field near the model's symmetry plane. This leads to a reduced extension of the recirculation zone, since the flow reattaches to the surface at N_{A1} further upstream.
Fig. 6.22 a) and b) depict the near surface flow topology for configuration F1M0L1 at $\alpha, \beta = 0\ deg$. Adding the faired skid-landing-gear L1 to the isolated fuselage F1 significantly changes the near surface flow field. The interaction of the flow around L1's attachment fairings with the flow around the fuselage is responsible for this change. The main changes regarding F1's near surface flow field are associated to the flow past the fuselage's ventral side and the fuselage's rear upsweep. In consequence a fifth flow region FR5 emerges and the size of the recirculation zone RZ increases. Furthermore, RZ is now divided into two parts; i.e. RZa and RZb. The flow past the fuselage's dorsal side (engine cowling) within FR1a and FR1b is basically not affected by L1's presence.
FR1a still covers the engine cowling area close to the models symmetry plane and is limited in the lateral direction by the symmetry plane and the characteristic streamline of the incoming flow $C1_i$. FR1a's downstream end, as for F1M0, is defined by the three separation lines SL1, SL2 and SL10. SL10 corresponds to F1M0's SL6. This adaption in the nomenclature is associated to the increased number of characteristic points for F1M0L1's surface topology. In consequence, F1M0's S_{S6} becomes S_{S10} for F1M0L1 and the name of the separation line originating from this point is changed accordingly. At the inboard and outboard limit of SL10 the foci F_{S10} and $F_{S2-4-10}$ are located, respectively. $F_{S2-4-10}$ connects SL2 and SL10. As for F1M0's, F1M0L1's topology can be closed by adding a fictional separation saddle point S_{S0} at the downstream end of the observed flow topology.
The lateral and downstream limits of FR1b remain unchanged compared to F1M0. These limits are the characteristic streamlines of the incoming flow $C1_i$ and $C2_i$ and the outboard section of SL1 and the inboard section of SL2. The flow region at the fuselage's side still constitutes FR2, but the ventral limit of its associated sub-region FR2a is changed.
The flow topology at the fuselage's ventral side is dominated by the interference with the flow around the skid-landing-gears attachment fairings. For the following analysis the topological field is divided into two domains.

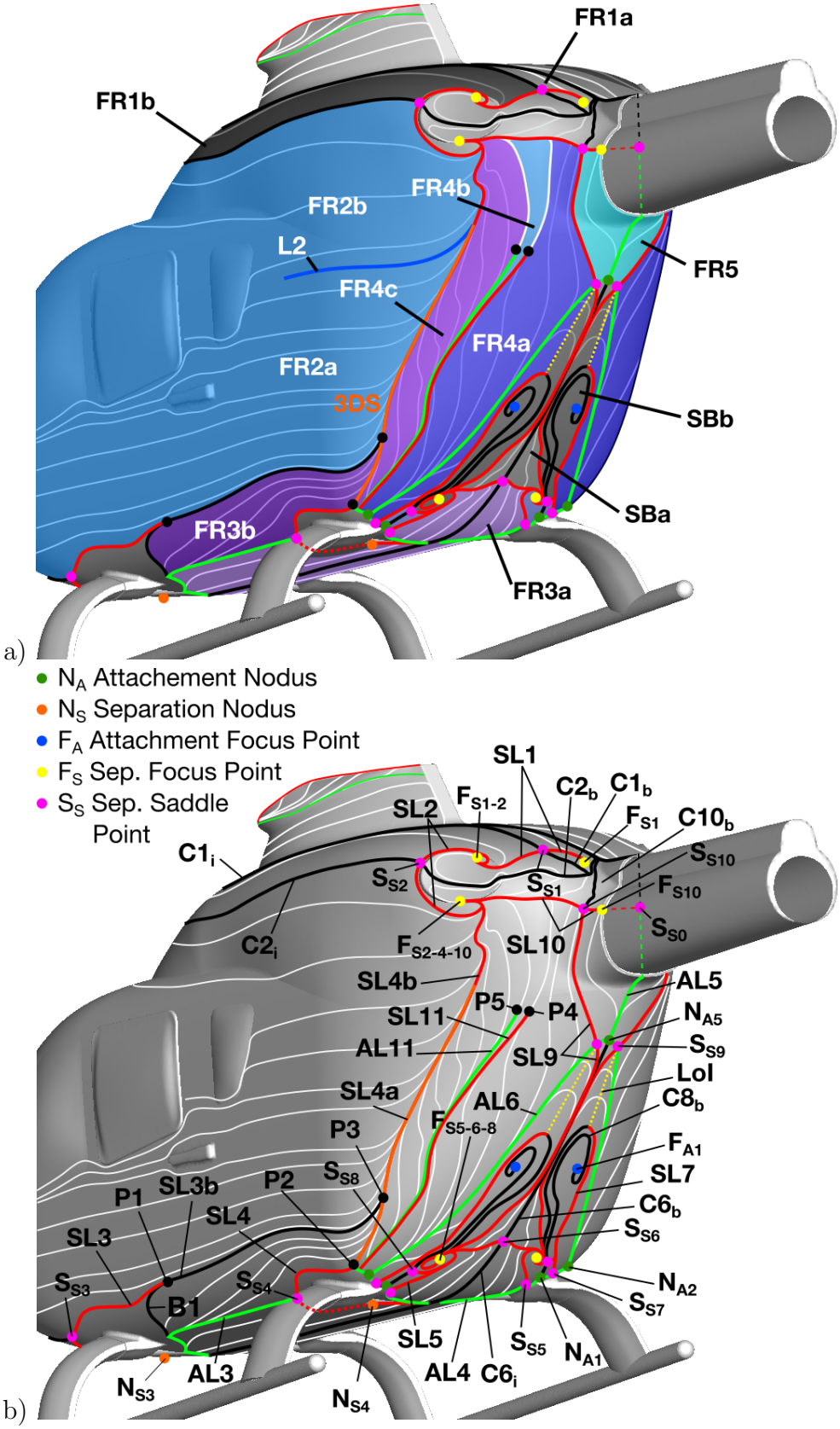

Figure 6.22: *Schematic representation of the near-surface flow topology for F1M0L1; a) flow regions, b) flow topology.* $Re_\infty \approx 0.95 \cdot 10^6$, $\alpha, \beta = 0$ *deg.*

The first domain is associated to the fuselage. The second domain is associated to the faired skid-landing-gear. The division of the topological field is performed such that the topological equation Eq. 5.4 for the fuselage domain still needs to return a sum of 2, whereas for the skid-landing-gear a sum of 0 is required. The flow topology within the skid-landing-gear domain is presented in detail in Appendix A.1.
For F1M0L1, the ventral limit of FR2b becomes SL3. SL3 originates at S_{S3} at the upstream end of the topological interface to the skid-landing-gear's front attachment fairing. S_{S3} is connected to N_{A0} by $C3_i$. At P3 SL3's separates from the surface as it encounters SL4a. The downstream end of FR2 is defined by SL4a, SL4b and the outboard section of SL2. The origin of SL4 is associated to the formation of the topological interface to the skid-landing-gear's rear attachment fairing.
The topological interface at the skid-landing-gear's front attachment fairing is defined by the separation lines SL3 and SL3c as well as the attachment line AL3 and the bounding streamline B1; see Fig. A.1. In consequence of the interaction of the flow with the front attachment fairing, the horse shoe vortex LV1 and the corner separation vortex CSV1 are generated. LV1 merges with CSV1 downstream of the front attachment fairing, such that only CSV1 is observed in the model's wake; see section 6.1.4. The topological interface at the rear attachment fairing is defined by SL4, SL4c, AL4, AL1 and AL2; see Fig. A.2. The interaction of the flow with the rear attachment fairing causes the formation of the horse shoe vortex LV2; see section 6.1.4.
At the fuselage's ventral side FR3 is located; see Fig. 6.22. FR3's lateral limits at the inboard and outboard end are $C6_i$ and SL3 together with SL3b and $C3_i$, respectively. $C6_i$ is congruent with the model's symmetry plane and connects N_{A0} with S_{S6}. FR3 encompasses the two topological interfaces with the skid-landing-gear's front and rear attachment fairing; see Fig. A.1 and Fig. A.2. Within FR3 the sub-regions FR3a and FR3b are located.
FR3a's inboard lateral limit is defined by $C6_i$. FR3a's outboard lateral limit constitute $C3_i$, SL3's inboard section, SL3b, AL3, SL4's inboard section, SL4c and AL4. The downstream end of SL3a is defined by SL5 and the separation line originating from S_{S6}; i.e. SL6. SL5 and SL6 are connected by F_{S5-6-8}.
FR3b's upstream limit is defined by the bounding line B1. B1 emerges from AL3 and separates from the surface by encountering SL3 at P1. B1 is located aside $C3_b^{LS}$ and the downstream section of $SL3^{LS}$; see Fig. 6.22 and Fig. A.1. B1 terminates in P1 on SL3b. The inboard and outboard lateral limits of FR3b are defined, respectively, by AL3 together with SL4's outboard section and SL3b. At FR3b's downstream end the section of SL4a between P2 and P3 is located.
Downstream of FR3a and the skid-landing-gear's rear attachment fairing a recirculation zone RZ is identified. RZ divides into two sub-regions; i.e. RZa and RZb. RZa is located downstream of FR3a, whereas RZb is located downstream of the rear attachment fairing. RZa's upstream limit is defined by SL6 originating from S_{S6}. S_{S6} results from the interaction of $C6_i$ and $C6_b$. $C6_b$ originates from the reattachment nodus N_{A5} at RZa's downstream end. RZa's downstream limit is defined by the lateral attachment lines originating from N_{A5}, which end at the downstream side of S_{S9}. The characteristic streamline of the incoming S_{S9} is defined by the attachment line originating from N_{A2}. In consequence, SL9 emerges

from S_{S9}. The upstream section of SL9 defines the lateral limit of RZa, which ends in F_{S5-6-8}.
RZb is limited at its upstream end by SL8. At S_{S8}, the characteristic streamline of the back flow originating from F_{A1} interacts with the characteristic streamline of the incoming flow originating from N_{A1}. In consequence SL8 emerges. SL8's inboard section separates from the surface as it encounters SL5, whereas its outboard section separates at SL7; also see Fig. A.2. RZb's inboard lateral limit is defined by SL9. The outboard lateral limit of SBb is defined by SL7 and the line of inflection LoI. SL7 emerges from S_{S7}. Further downstream the separation ends and continues as $C7_b$. In fact, $C7_b$ is bend back upstream by the presence of the attachment focus F_{A1}. Finally, $C7_b$ separates from the surface as it encounters SL9. LoI is defined by the apex of the near-surface streamlines originating from AL6, which are also bend upstream. RZb's downstream end represents S_{S9}.
Beside RZb the flow region FR4 is observed downstream of the skid-landing-gear's rear attachment fairing. FR4 is structured into the three sub-regions FR4a, FR4b and FR4c. FR4a is located adjacent to RZb outboard lateral limit. Consequently, FR4a inboard lateral limits constitutes SL7, LoI and the downstream section of SL9. The inboard and outboard section of AL2 defines FR4a's upstream limit. The outboard lateral limit of FR4a is defined by SL11 and the downstream characteristic streamline, which emerges from SL11's end at P4. This characteristic streamline separates from the surface at the outboard section of SL10. SL10 emerges from S_{S10} upon the interaction of SL9 with $C10_b$. SL10 also defines the downstream end of FR4a.
FR4b is laterally bound by SL11 and AL11. SL1 and AL11 diverge a short distance downstream of the outboard section of AL2. AL11 ends in P5 where the downstream characteristic streamline emerges, which separates from the surface at SL10. FR4b's downstream end is defined by SL10. Between the outboard lateral limit of FR4b and the downstream end of FR2 the last sub-region within FR4 is located; i.e. FR4c. Thus, FR4c's inboard lateral limit is defined by AL11 and the associated downstream characteristic streamline. The outboard lateral limit of FR4c constitute SL4a and SL4b. At FR4c downstream end SL10 is located, which is connected to SL4b by $F_{S2-4-10}$.
F1's near surface flow topology in the presence of L1 is completed by FR5. FR5 is located downstream of RZa. Thus, the lateral attachment lines originating from N_{A5} define the upstream end of FR5. The inboard lateral limit of FR5 is defined by AL5. AL5 is located at the symmetry plane and connects N_{A5} with the fictional separation saddle S_{S0}. The outboard lateral limit of FR5 constitutes the downstream section of SL9. FR5's downstream limit is represented by the inboard section of SL10 and the fictional separation line connecting S_{S0} with F_{S10}.
Table 6.1 summaries all identified characteristic points of F1's near-surface flow topology and their contribution to the topological equation Eq. 5.4. The topological interfaces to the skid-landing-gear L1 are defined such that all characteristic point associated to L1 return a sum of zero. Hence, a sum of two over all F1's characteristic points is required in order to close the topological field. As can be seen in table 6.1 this statement is true. Thus, a closed topological description of F1M0L1's near surface flow topology is obtained.

Comparing F1M0L1's near surface flow topology against F0M0L0's reveals that

N_{A0}	+1
N_{A1}	+2
N_{A2}	+2
N_{A5}	+1
F_{A1}	+2
F_{S1}	+2
F_{S1-2}	+2
$F_{S2-4-10}$	+2
F_{S5-6-8}	+2
F_{S10}	+2
N_{S3}	+2
F_{S4}	+2
S_{S1}	-2
S_{S2}	-2
S_{S3}	-2
S_{S4}	-2
S_{S5}	-2
S_{S6}	-1
S_{S7}	-2
S_{S8}	-2
S_{S9}	-2
S_{S10}	-2
S_{S0}	-1
Σ	+2

Table 6.1: *Topological equation for the characteristic points of F1's near surface flow topology in the presence of L1.*

fairing the skid-landing-gear effectively mitigates separation at the rear fuselage's upsweep. For F0M0L0 a large scale separation is observed around both the beginning of the lateral tapering and the rear fuselage upsweep. Furthermore, no upsweep vortex is formed at F0M0 in the presence of L0. By fairing the skid-landing-gear with design variant L1, the flow reattaches downstream of the rear attachment fairing and the separation is confined to the recirculation zone close to the model's symmetry plane. In consequence, also a upsweep vortex is generated along the three-dimensional free-surface separation at SL4a. Flow entering the rear fuselage upsweep along the fuselage dorsal side as on F0M0L0 is not observed for F1M0L1.

The aerodynamic interference of L1 on F1M0 is only affecting the recirculation zone. On F1M0 the extension of the recirculation zone is confined to a small region close to the model's symmetry plane. By adding L1 to F1M0 the recirculation

zone's extension increases. This explains the observed decrease in c_p for F1M0L1 compared to F1M0 at slices Z7 and Z9; see section 6.1.3.

Wake Flow Topology

In Fig. 6.23, the vortex formation at F1M0's rear fuselage is depicted for $\alpha, \beta = 0$ *deg*. The data arrangement in Fig. 6.23 corresponds to Fig. 5.14. At each side of the rear fuselage's upsweep a strong vortex is formed. These vortices are called the primary counter-rotating upsweep vortices UV1. The UV1 vortex roll-up begins as the shear-layer starts to separate along the three-dimensional separation at SL3a. UV1 are identified after the initial roll-up as two regions of $\omega_x \cdot l_{ref}/U_\infty = \pm 12$ at slice Z11. Up to slice Z7, the vortex core of UV1 is in close proximity to the surface. Thus, local pressure minima are observed at Z7 and Z9; see section 6.1.3. Furthermore, the UV1 induce a strong upward deflection of the flow past the rear fuselage's upsweep. Eventually, at point P2 the deflected fluid starts to attach to the surface along AL3; see section 6.1.4. This leads to the formation of the weak secondary upsweep vortices UV2-1 and UV2-2. Both these vortices feature an opposite sense of rotation compared to UV1 at each side of the fuselage. In consequence of the attaching fluid and the formation of UV2-1 and UV2-2, the trajectories of the primary vortices UV1 begin to deviate from the rear fuselage's upsweep. The interaction of UV1, UV2-1 and UV2-2 is discernible at slice Z7. UV2-1 deflects UV1 away from the surface. Similarly, UV2-2 deflects the shear-layer between AL3 and SL5 away from the surface. Thus, the roll-up of the shear-layer into UV1 begins to brake down in consequence of UV2-2. At Z9, the same vortex structures as in Z7 can be identified. However, UV2-1's cross-section is larger at Z9 than at Z7 and UV1 is shifted away from the surface. UV2-2 does not increase in size at Z9 compared to Z7, but the interaction with the shear-layer is more pronounced. At Z5, the roll-up of the shear-layer into UV1 is completely broke down. Therefore, the point where the shear-layer separates from the surface is now associated to SL3b; see section 6.1.4. The vortex cores of UV1 are not within the rear-fuselage region at Z5, because UV1 is shed into the wake at each side of the tailboom. At slice Z5, UV2-2 is located in close proximity to UV2-1. A short distance further downstream, AL3 ends in S_{S6} and UV2-1 detaches from the surface. At this point UV2-1 and UV2-2 merge into UV2 and shed into the wake.

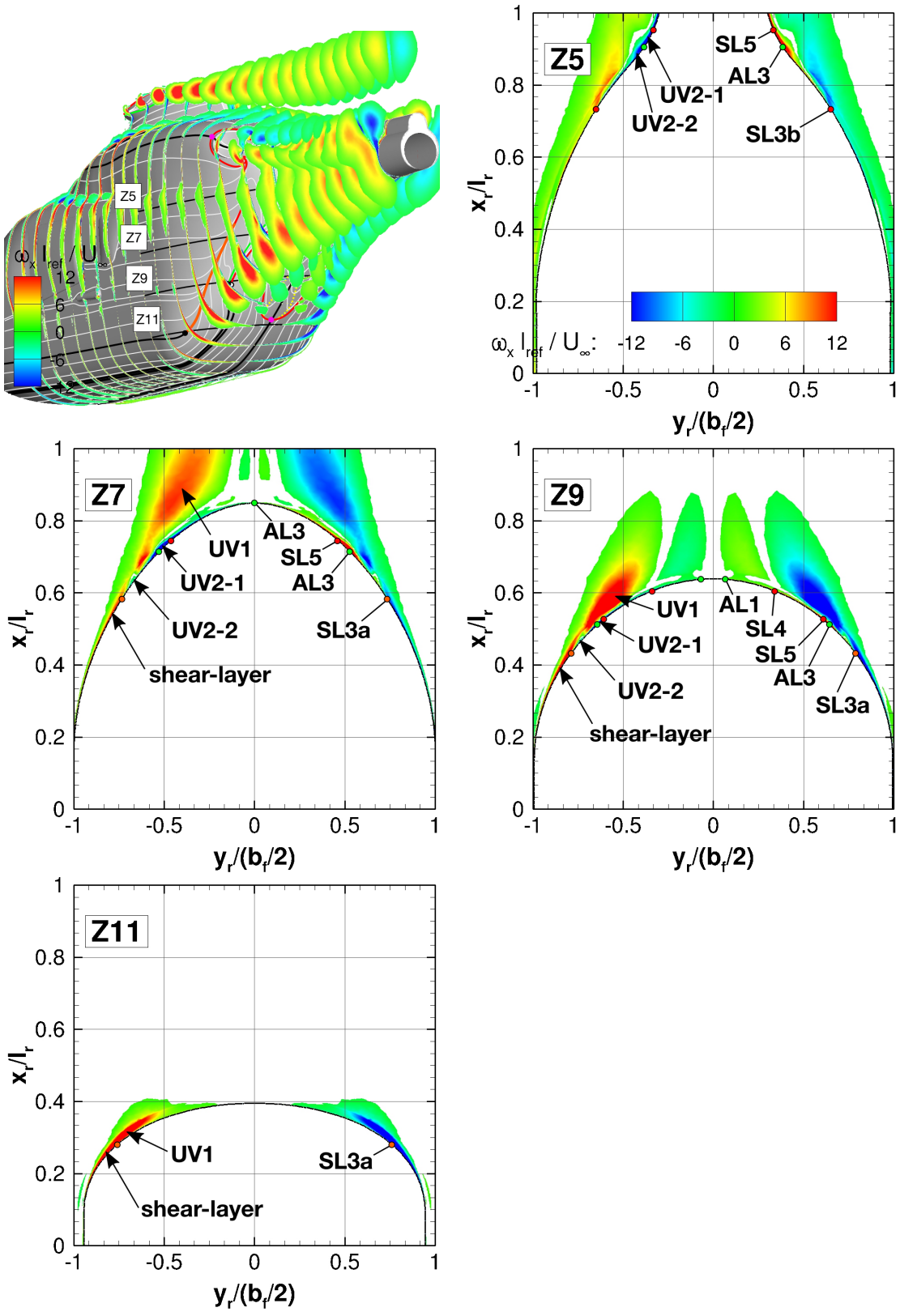

Figure 6.23: *Contours of $\omega_x l_{ref}/U_\infty$ in F1M0's wake at slices of constant x (isometric view) and constant z (2D view) at Z5, Z7, Z9 and Z11. $Re_\infty \approx 0.95{\cdot}10^6$, $\alpha, \beta = 0$ deg.*

In Fig. 6.24, the main flow features observed in F1M0's near wake are summarised. Besides the vortex systems which are generated at the rear fuselage's upsweep two more vortex systems are generated at F1M0. These vortex systems are the two pairs of counter-rotating exhaust vortices (EV) and the counter-rotating mast fairing vortex (MV). The EV are generated on both the closed exhaust pipes in consequence of a fixed surface separation. The fixed surface separation starts at SL2 originating from S_{S2}. The MV originate from the outer lip of the mast fairing top in consequence of a fixed surface separation as well. In Fig. 6.24, the fluid transport towards the surface is visualised as a green ribbon. The fluid transported to the surface passes along the fuselage's ventral side and then attaches along line AL3. In consequence of UV1's induced velocities, a significant upward deflection of the flow past the rear fuselage's upsweep is caused. This also pushes the separated flow back towards the surface. Thus, the recirculation zone RZ is generated.

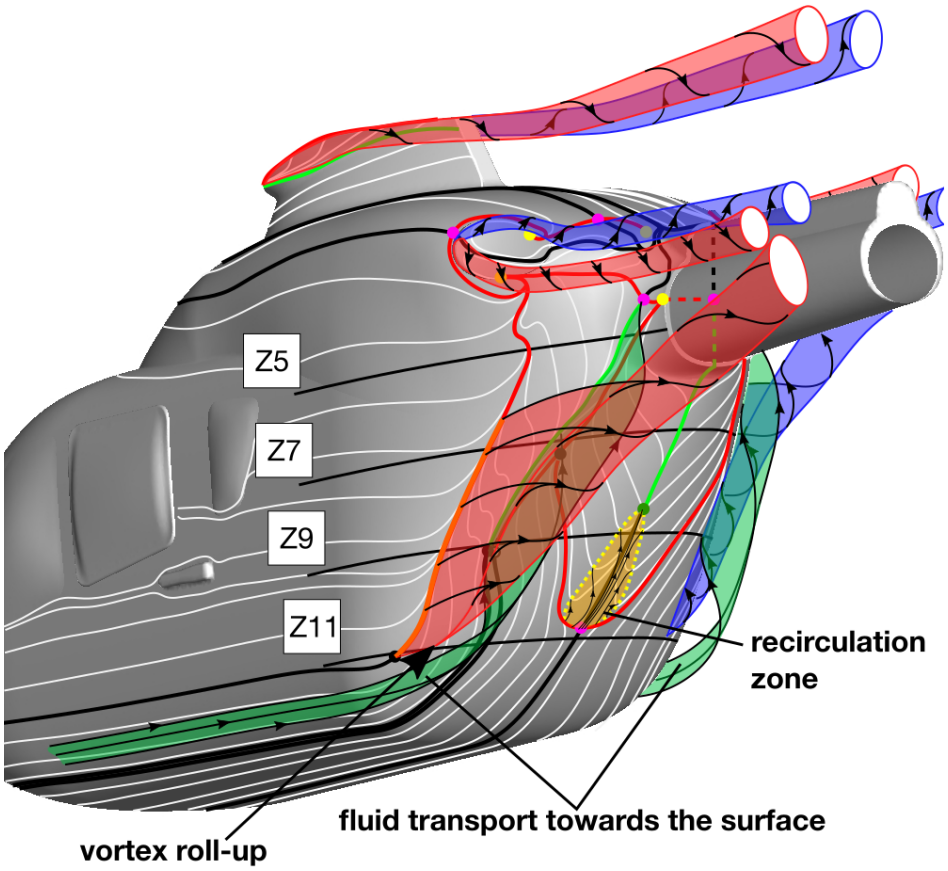

Figure 6.24: *Schematic representation of F1M0's vortex systems and recirculation zone.* $Re_\infty \approx 0.95 \cdot 10^6$, $\alpha, \beta = 0$ *deg.*

Fig. 6.25 visualises the formation of UV2-1 and UV2-2 and their trajectories towards the wake. In consequence of the attaching fluid along AL3, the secondary upsweep vortices are formed close to P2; i.e. the upstream end of AL3. UV2-1 and UV2-2 then progress along the rear fuselage's upsweep before they are shed into the wake upon the separation at SL6. In the wake UV2-1 and UV2-2 merge into UV2. UV2 is then convected downstream at each side of the tailboom.

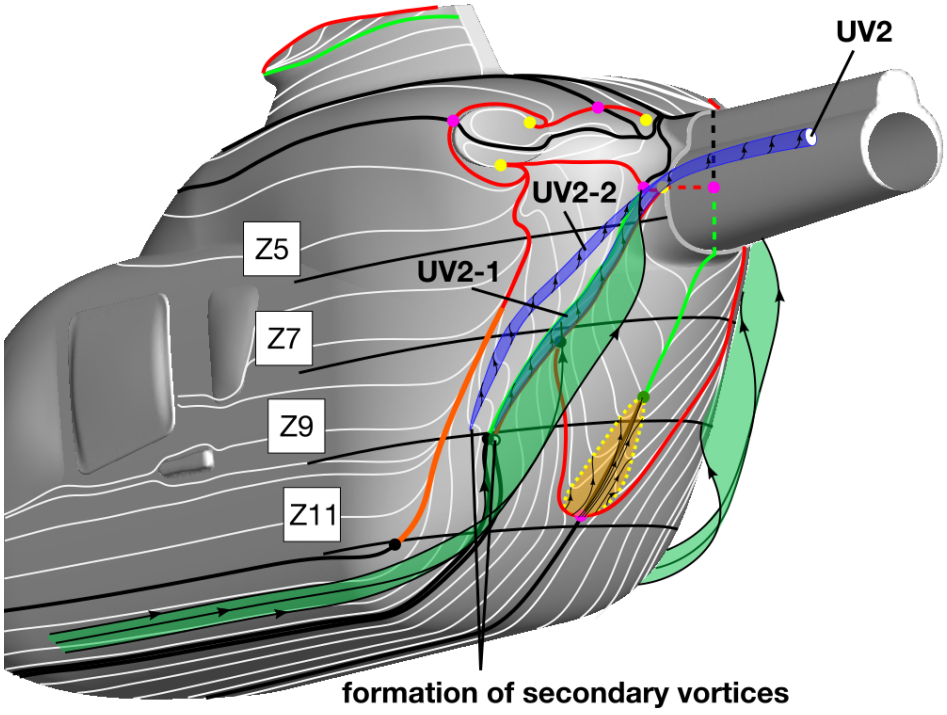

Figure 6.25: *Schematic representation of F1M0's secondary upsweep vortex systems.* $Re_\infty \approx 0.95 \cdot 10^6$, $\alpha, \beta = 0$ *deg.*

In Fig. 6.26, contours of the non-dimensional axial velocity u/U_∞ and $\omega_x \cdot l_{ref}/U_\infty$ are shown along the wake slice locations 'c','e' and 'f'. For u/U_∞ the experimental results obtained by PIV are compared to the CFD data. $\omega_x \cdot l_{ref}/U_\infty$ is only presented based on the CFD data. The identified wake regions are defined by iso-lines of $u/U_\infty = 0.8$.
The comparison of the PIV data with the CFD data does reveal a good to excellent agreement for u/U_∞ with respect to the absolute values and the extension of the wake region (WR). In particular, two wake regions can be distinguished. WR2 is located close to the models symmetry plane and below the fuselage's aft-body. WR2 is associated to the separation along SL4 and the formation of the recirculation zone RZ. WR1 extends to the side and the top of the fuselage's aft-body. This wake region originates from the separation along SL1, SL2 and SL3.
By superimposing the extension of the wake regions onto the contour plots of $\omega_x \cdot l_{ref}/U_\infty$ it becomes clear that WR1 defines the envelope for the observed vortex systems UV1, UV2 and EV within the wake. WR1 can be observed throughout the wake up to the tailboom's downstream end. However, WR2 is closing just upstream of wake slice 'e'. The significant upward deflection of the wake through UV1 and the associated mixing with high velocity fluid from further away from the wall cause WR2 to diminish earlier. This causes WR2 to dissolve just upstream of wake slice 'e'.

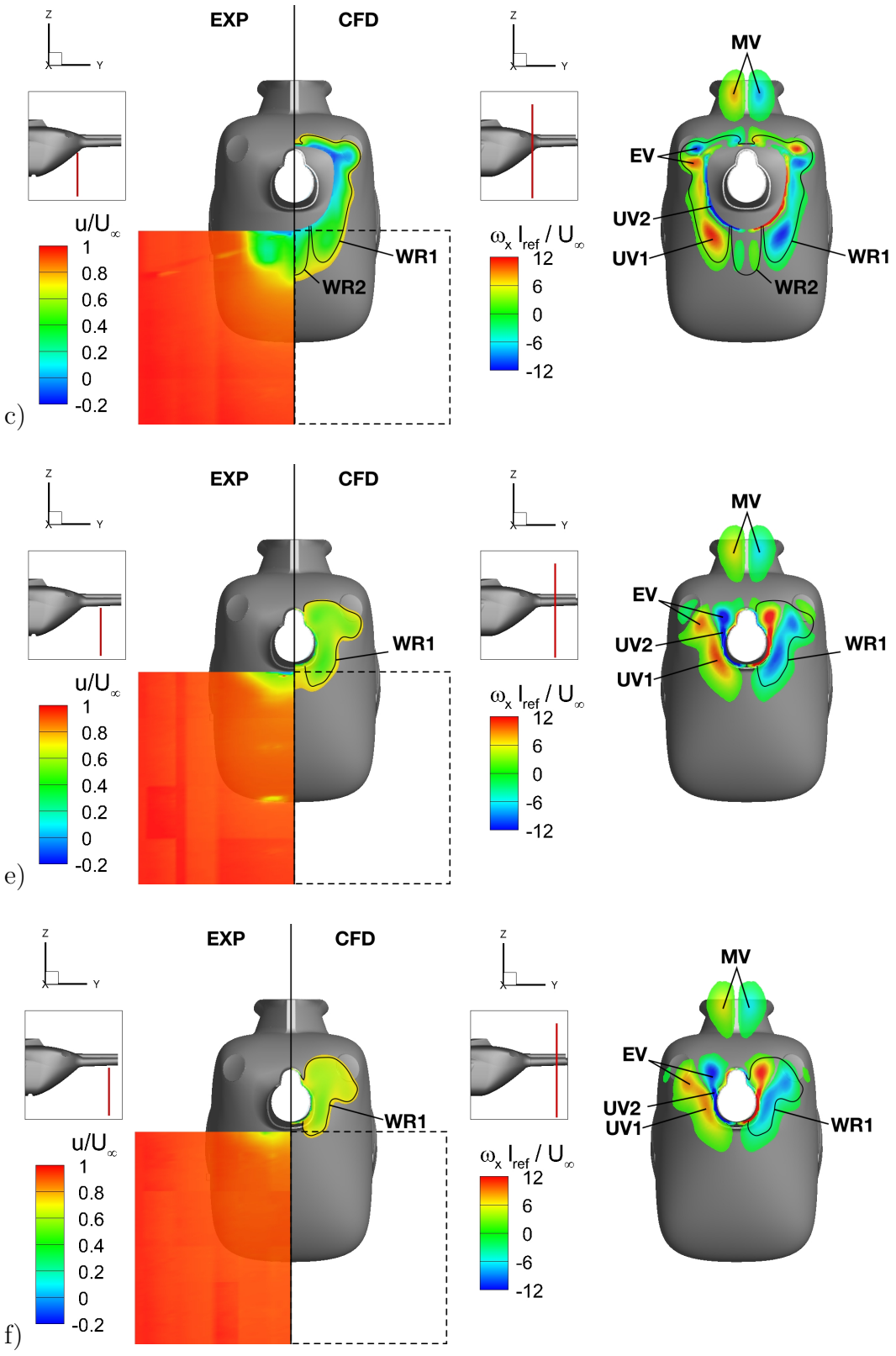

Figure 6.26: *Contours of u/U_∞ (Exp/CFD) and $\omega_x l_{ref}/U_\infty$ (CFD) in F1M0's wake at slice locations 'c','e' and 'f' for $Re_\infty \approx 0.95 \cdot 10^6$ at $\alpha, \beta = 0$ deg. Wake region boundaries correspond to $u/U_\infty = 0.8$.*

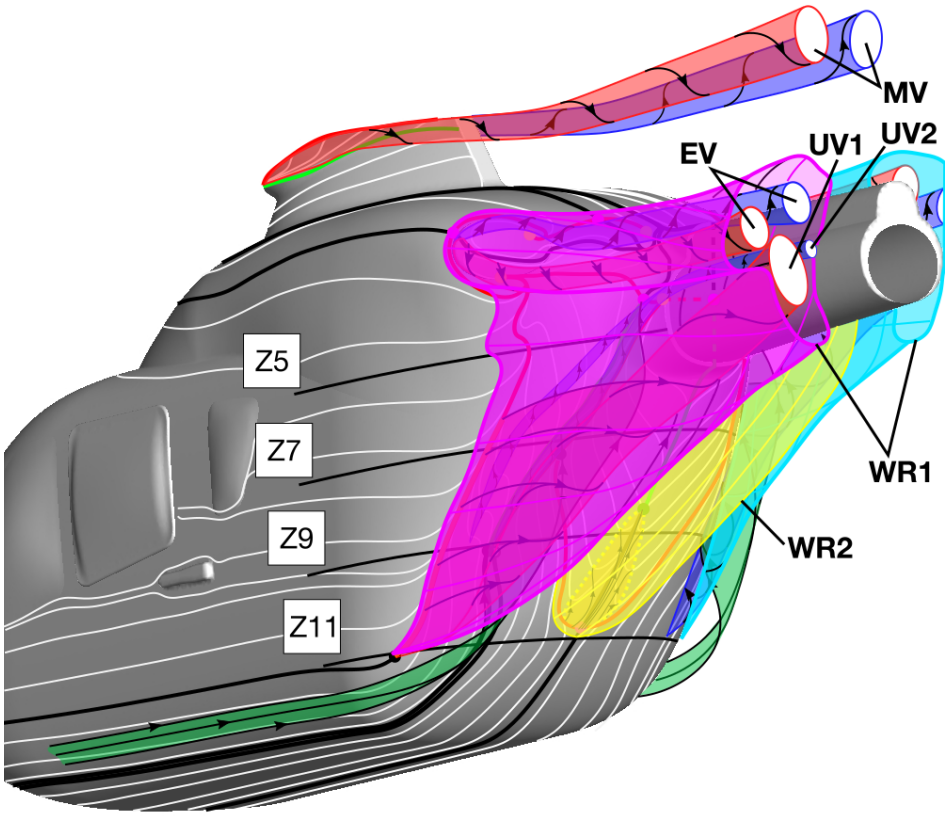

Figure 6.27: *Schematic representation of F1M0's wake including the vortex systems and the envelope of the wake regions.* $Re_\infty \approx 0.95 \cdot 10^6$, $\alpha, \beta = 0$ *deg.*

Fig. 6.27 depicts a synthetic three-dimensional view of F1M0's wake including the vortex systems, the recirculation zone RZ and the two wake regions WR1 and WR2. Comparing the wake flow topology of F1M0 with F0M0 reveals the positive impact of smoothing the ventral side on the fuselage's wake; see Fig. 6.27 and Fig. 5.17. Both the extension of the wake regions WR1 and WR2 are reduced for F1M0 compared to F0M0. For F0M0, WR1 extends below the tailboom. This is not the case for F1M0 since the increased vortex intensity of UV1 increases the vertical deflection of the wake flow. As described in section 6.1.4, this is associated to the reduced flow perturbation along F1M0's ventral side compared to F0M0. In consequence, the extension of the secondary separation reduces at F1M0 and UV1 vortex formation is not disturbed. As a result the extension of F1M0's WR2 is also further confined, such that it does not extend throughout the wake as it is observed for F0M0. Finally, UV1's increased vortex intensity at F1M0 leads to the flow reattachment along AL2. This leads to the formation of the secondary upsweep vortices UV2-1 and UV2-2, which are not observed for F0M0. In summary, those effects yield the observed drag reduction of 3% and the increase in downforce for F1M0 compared to F0M0.

In Fig. 6.28, the vortex formation at F1M0L1's rear fuselage is presented similar to F1M0's; see Fig. 6.23. In section 6.1.4, it is shown that adding L1 to F1M0 significantly changes the near-surface flow topology. In consequence, also the wake flow topology is significantly altered by the presence of L1. The most significant difference is that the vortex system already starts to emerge at the skid-landing-gear's front attachment fairing. By the interaction of the flow around the fuselage and the skid-landing-gear's front attachment fairing a horse shoe vortex system is formed. The dorsal side of this vortex system is more intense than its ventral side due to a more extensive roll-up process; see section 6.1.4.
Furthermore, a corner separation occurs at the front attachment fairing. In consequence, the corner separation vortex CSV1 is formed. Downstream of the front attachment fairing the dorsal side of the horse shoe vortex LV1 merges with the corner separation vortex CSV1. CSV1 then convects downstream near the surface associated to FR3b. CSV1's induced velocity transports fluid towards the fuselage's bottom, which causes the flow reattachment along AL3. Before being shed into the wake, CSV1 is attenuated as it interacts with the skid-landing-gear's rear attachment . CSV1 can be identified as two regions of $\omega_x \cdot l_{ref}/U_\infty = \pm 3$ on either side of the fuselage's rear upsweep at slice Z11. At the rear attachment fairing the second horse shoe vortex system LV2 forms. At slice Z11 LV2 can be identified as two contour-rotating vortex pairs downstream of the rear attachment fairings.
As for F1M0 the primary counter-rotating upsweep vortices UV1 are observed at F1M0L1's rear fuselage upsweep. For F1M0L1 UV1's vortex roll-up begins as the shear-layer starts to separate along the three-dimensional separation at SL4a. UV1 is identified after the initial roll-up as two regions of $\omega_x \cdot l_{ref}/U_\infty = \pm 12$ at slice Z11. At F1M0L1's rear fuselage upsweep, as for F1M0, UV1 remains in close proximity to the surface up to Z7. In consequence, the associated characteristic local pressure minima are observed at Z7 and Z9; see section 6.1.3. Furthermore, the outboard side of LV2 merges with UV1 at Z9. LV2's inboard side remains in close proximity to the surface. At Z9, the trajectory of LV2's inboard side begins deviate from the surface contour and sheds into the wake.
In addition to the primary upsweep vortex, the same secondary upsweep vortices UV2-1 and UV2-1 are observed for F1M0L1 as for F1M0. UV2-1 begins to roll up as SL11 and AL12 diverge. At P4 and P5 UV2-1's roll-up process ends. UV2-2 is formed in the same region for F1M0L1 as for F1M0 between SL4a and AL11. For F1M0L1, the interaction of UV1, UV2-1 and UV2-2 also leads to the deflection of UV1 away from the surface. At Z5, the roll-up of the shear-layer into UV1 is completely broke down. Thus, the point where the shear-layer separates from the surface is associated to SL4b at Z5. UV2-1 and UV2-2 remain in close proximity to the wall up to Z5 where they merge. This results in UV2, which then sheds into the wake along the tailboom.

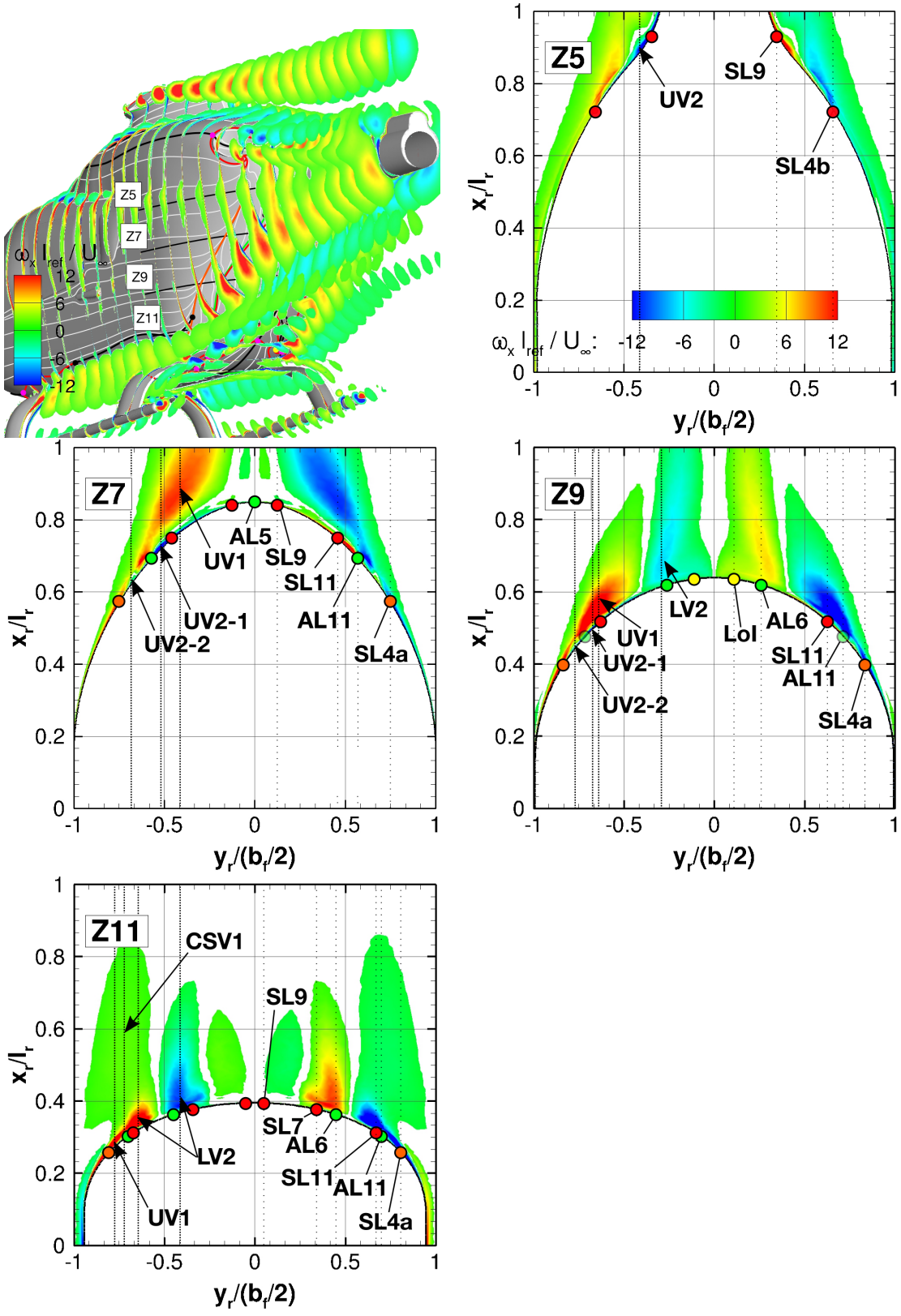

Figure 6.28: *Contours of u/U_∞ (Exp/CFD) and $\omega_x l_{ref}/U_\infty$ (CFD) in F1M0L1's wake at slice locations 'c','e' and 'f' for $Re_\infty \approx 0.95 \cdot 10^6$ at $\alpha, \beta = 0$ deg. Wake region boundaries correspond to $u/U_\infty = 0.8$.*

In Fig. 6.29, the trajectory of LV1's dorsal side and the corner separation vortex CSV1 are presented schematically. LV1 merges with CSV1 at P1. CSV1 is not significantly interacting with the flow past the fuselage's rear upsweep. This also becomes evident by the fact that the trajectory of CSV1 is not substantially deflected in the vertical direction at the rear fuselage.

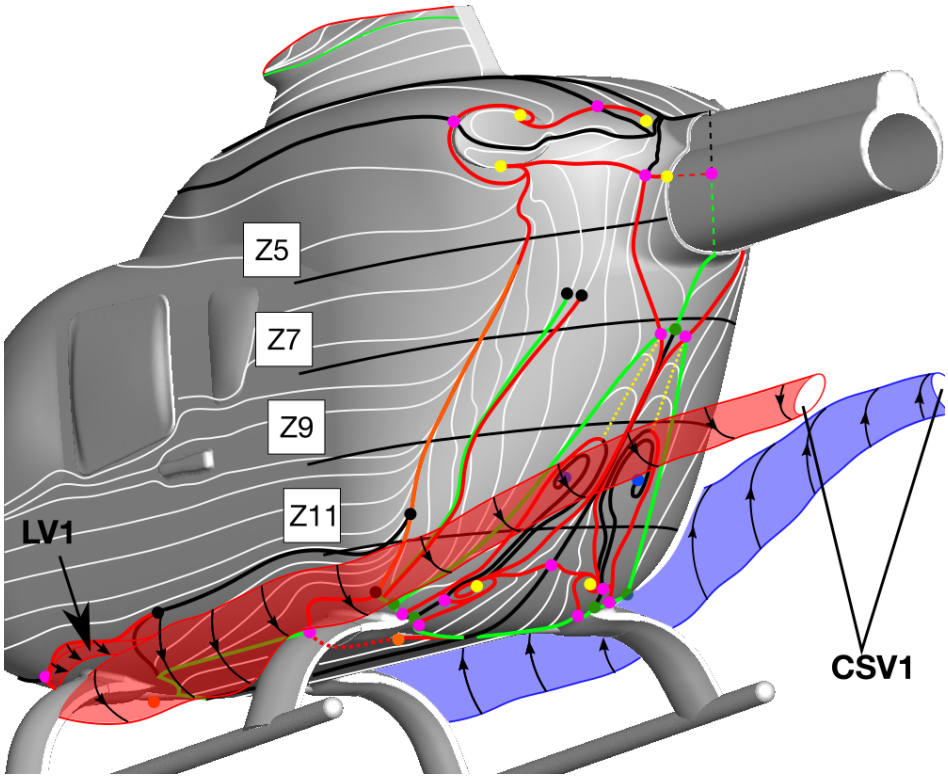

Figure 6.29: *Schematic representation of F1M0L1's wake including the landing-skid vortex LV1 and the corner vortex CSV1.* $Re_\infty \approx 0.95 \cdot 10^6$, $\alpha, \beta = 0$ *deg.*

In Fig. 6.30, the main flow features observed in F1M0L1's near wake are summarised. Except the horse shoe vortex LV2 originating from the skid-landing-gears rear attachment fairing; the same vortex systems as for F1M0 are observed for F1M0L1. This includes the primary upsweep vortex UV1, the exhaust vortex EV and the mast fairing vortex MV. As it can be seen by comparison with F1M0 (Fig. 6.24), the size of the recirculation zone is increased by the presence of L1. The fluid transport towards the surface is visualised as a green ribbon. The fluid transported to the surface passes below the skid-landing-gear's front cross-beam fairings. It enters the rear fuselage region along the dorsal side of the rear attachment fairing, where it attaches along line AL6. The flow attachment along AL6 is caused by LV2's induced velocities.

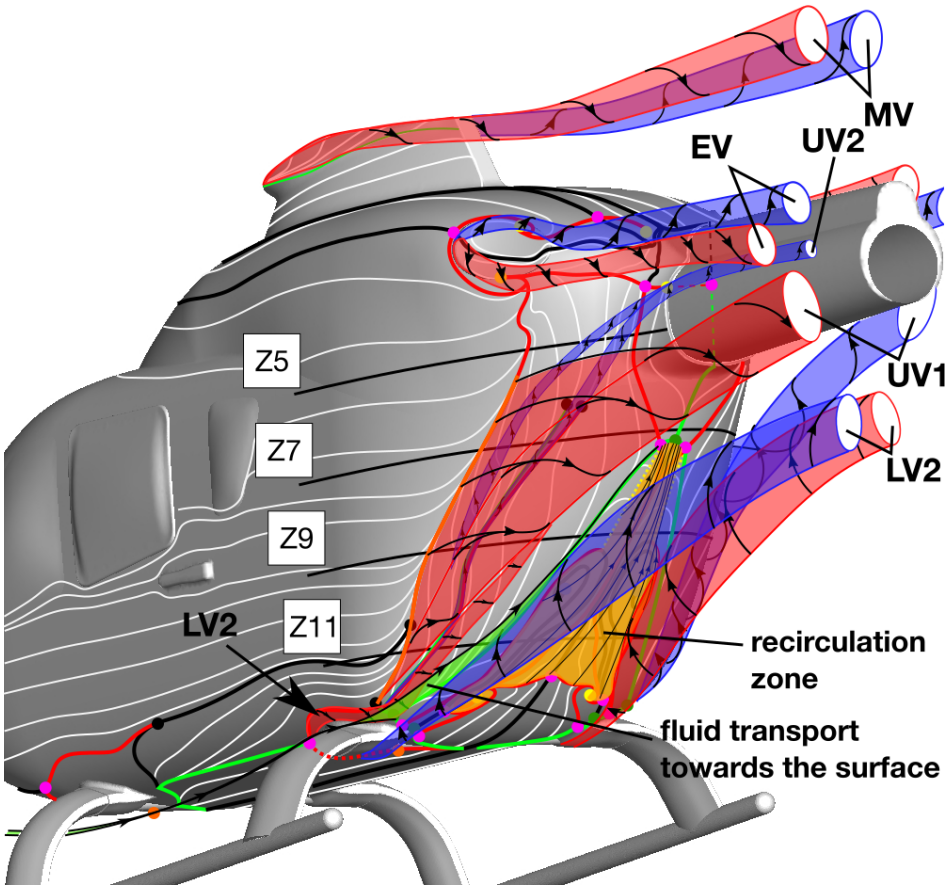

Figure 6.30: *Schematic representation of F1M0L1's main features within the near wake region of the rear fuselage.* $Re_\infty \approx 0.95 \cdot 10^6$, $\alpha, \beta = 0$ *deg.*

Fig. 6.31 visualises the formation of UV2-1 and UV2-2 and their trajectories towards the wake at F1M0L1's rear fuselage. The formation of UV2-2 is similar to the case without L1; i.e. F1M0. However, the formation of UV2-1 is located further upstream for F1M0L1 compared to F1M0. UV2-1 originates a short distance downstream of the rear attachment fairing. UV2-1 and UV2-2 progress along the rear fuselage's upsweep before they are shed into the wake where they merge to UV2. UV2 also convects downstream at each side of the tailboom for F1M0L1.

In Fig. 6.32, the non-dimensional axial velocity u/U_∞ and $\omega_x \cdot l_{ref}/U_\infty$ are shown along the wake slice locations 'c','e' and 'f'. The data arrangement follows Fig.6.26. As for F1M0, F1M0L1's comparison of the PIV data with the CFD data does reveal an excellent agreement for u/U_∞ with respect to the absolute values and the extension of the wake region (WR). For F1M0L1, also two wake regions can be distinguished. WR2 is located close to the models symmetry plane and below the fuselage's aft-body. However, for F1M0L1 WR2 is associated to the separation along SL6 and the separation at the skid-landing-gear's rear attachment fairing as well as the formation of the recirculation zone. The extension of F1M0L1's WR1 is almost identical as for F1M0. It also extends to the side and the top of the fuselage's aft-body and contains the same vortex systems as for F1M0. However, due to the increased near-surface flow topology's complexity, WR1's origin is associated to the separation along SL1, SL2 and SL4.

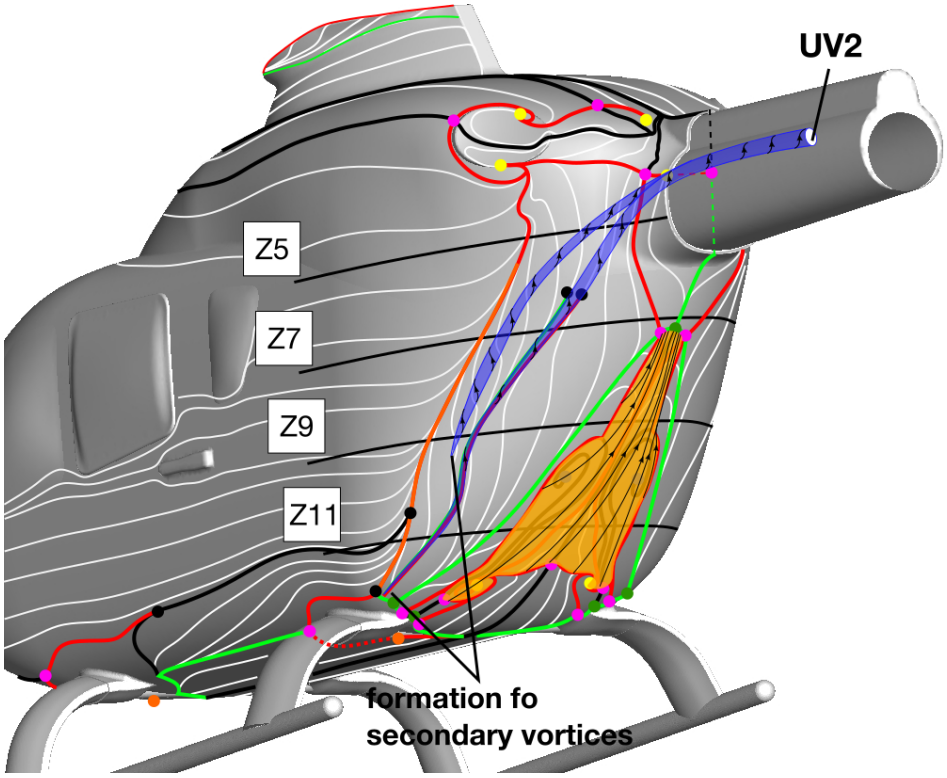

Figure 6.31: *Flow schematic for F1M0L1 presenting the formation of the secondary upsweep vortices within the near wake region of the rear fuselage.* $Re_\infty \approx 0.95 \cdot 10^6$, $\alpha, \beta = 0$ *deg.*

In consequence of the increased size of the recirculation zone RZ, WR2 extension is increased for F1M0L1 compared to F1M0. This is the case both for its lateral and vertical extension as well as for its longitudinal extension. Especially, WR2 is not closing upstream of the model's tailboom section end as for F1M0. Nevertheless, the lateral and vertical extension of WR2 significantly reduces as it is convected downstream along the tailboom section's ventral side. At the most downstream slice depicted in Fig. 6.32 (bottom row) WR2 has diminished to a confined tear drop like shape. Furthermore, WR2 encloses the trajectory of LV2.
Fig. 6.33 depicts a synthetic three-dimensional view of F1M0L1's wake including the vortex systems and the two wake regions WR1 and WR2. Comparing the wake flow topology of F1M0L1 with F0M0L0 shows the significant impact of fairing the skid-landing-gear on the extension of the wake; see Fig. 6.33 and Fig. 5.21. For F0M0L0, only one wake region (WR1) is observed which features a large extension in both the vertical and lateral direction. For F1M0L1, a significant reduction of the wake region's extension is observed. In consequence, also the structure of the wake region changes and two separated wake regions WR1 and WR2 are observed. The corner separation vortex CSV1 remains outside the wake region as it is observed for F0M0L0's landing-gear vortex LV1.

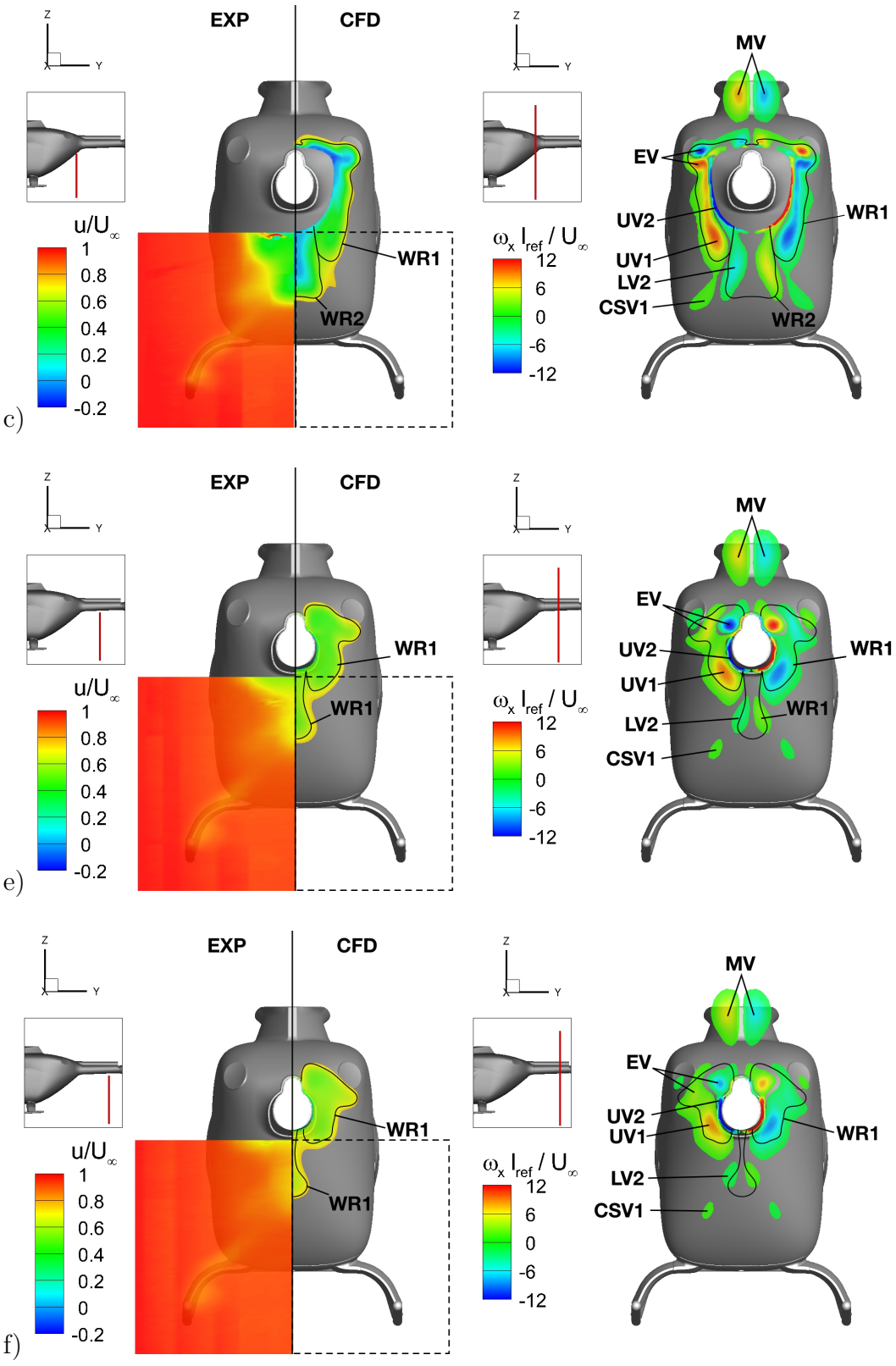

Figure 6.32: *Contours of u/U_∞ (Exp/CFD) and $\omega_x l_{ref}/U_\infty$ (CFD) in F1M0L1's wake at slice locations 'c','e' and 'f' for $Re_\infty \approx 0.95 \cdot 10^6$ at $\alpha, \beta = 0$ deg. Wake region boundaries correspond to $u/U_\infty = 0.8$.*

However, CSV1 is associated to corner separation at L1's front attachment fairing and not to the front outer cross-beam and skid as for LV1 on L0. In fact, F1M0L1's wake flow topology is similar to the wake flow field observed for F0M0. However, due to UV1's increased vortex intensity the wake region WR2 is shifted towards the ventral side of the fuselage. Since F0M0's open cavities at the fuselage's ventral side are faired for F1M0L1 no cavity vortex is immersed inside WR2, but the landing-gear vortex LV2. The extension of the wake region WR1 is also confined on F1M0L1 compared to F0M0. For F1M0L1's WR2 a similar extension is observed as on F1M0, which also encompasses the vortex systems UV1, UV2 and EV.

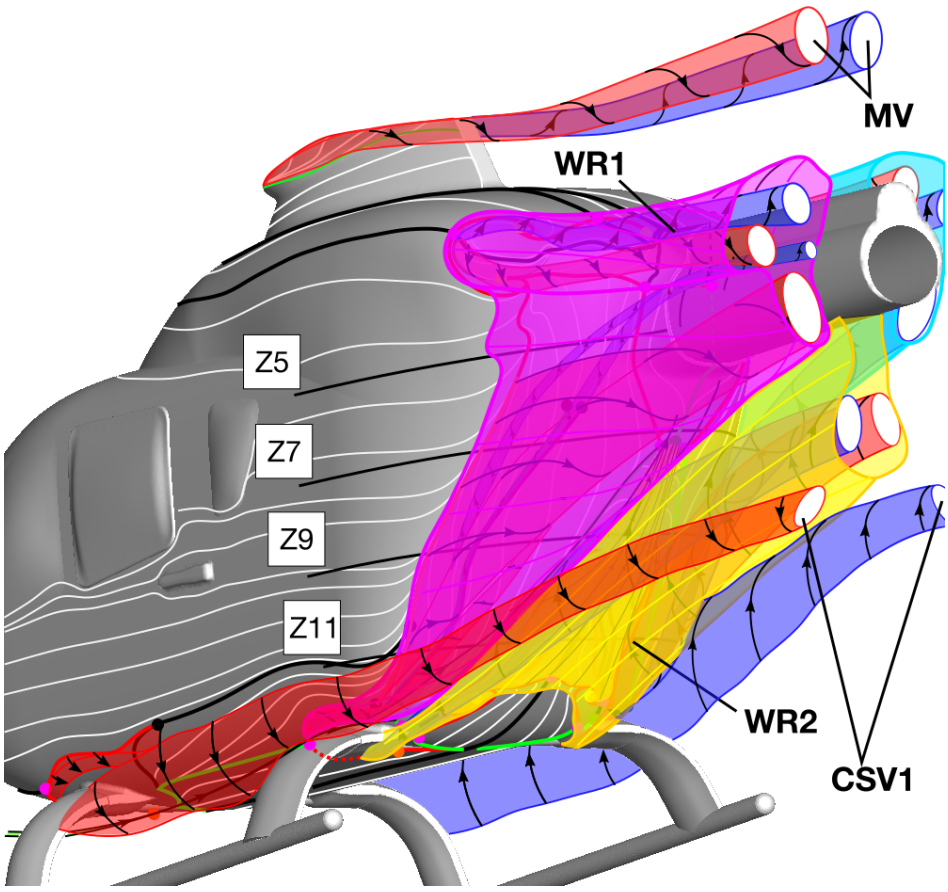

Figure 6.33: *Schematic representation of F1M0L1's wake including the vortex systems and the envelope of the wake regions.* $Re_\infty \approx 0.95 \cdot 10^6$, $\alpha, \beta = 0$ *deg.*

Comparing the wake flow topology of F1M0L1 with F0M0L0 shows the significant impact of fairing the skid-landing-gear on the extension of the wake; see Fig. 6.33 and Fig. 5.21. For F0M0L0, only one wake region (WR1) is observed which features a large extension in both the vertical and lateral direction. For F1M0L1, a significant reduction of the wake region's extension is observed. In consequence, also the structure of the wake region changes and two separated wake regions WR1 and WR2 are observed. The corner separation vortex CSV1 remains outside the wake region as it is observed for F0M0L0's landing-gear vortex LV1. However, CSV1 is associated to corner separation at L1's front attachment fairing and not to the front outer cross-beam and skid as for LV1 on L0. In fact F1M0L1's wake

flow topology is similar to the wake flow field observed for F0M0. However, due to UV1's increased vortex intensity the wake region WR2 is shifted towards the ventral side of the fuselage. Since F0M0's open cavities at the fuselage's ventral side are faired for F1M0L1 no cavity vortex is immersed inside WR2, but the landing-gear vortex LV2. The extension of the wake region WR1 is also confined on F1M0L1 compared to F0M0. For F1M0L1's WR2 a similar extension is observed as on F1M0, which also encompasses the vortex systems UV1, UV2 and EV.
The observed differences show that fairing the skid-landing-gear effectively mitigates the wake associated to L0 and minimizes L1's aerodynamic interference on F1M0. Nevertheless, L1's aerodynamic interference still affects the fuselage's wake. Thus, further modifications are considered to mitigate this effect; see section 6.2.

6.2 Application of Passive Flow Control Devices

Fairing the skid-landing-gear with aerodynamically optimised panels significantly increases the efficiency of twin-engine-light class helicopter; see 6.1. However, further drag reduction potential was identified for the rear fuselage upsweep region. Even though the aerodynamic interference of the faired skid-landing-gear L1 with the fuselage is reduced compared with L0, it is not entirely eliminated. The remaining separation at the fuselage's rear upsweep provides additional drag reduction potential. This also includes the separation at the fuselage's lateral tapering along the primary separation line. In section 5.3, it is shown that this separation is associated to the substantial positive pressure gradients downstream of the lateral suction peaks. Delaying this lateral separation, thus, also provides drag reduction potential.
Streamlining the aft-body region by implementing a "fish-tail" configuration would be the most effective solution for reducing the parasite drag in fast-forward level flight; see Leishman [26] pp.304. However, a "fish-tail" increases the projected surface in both the vertical and lateral direction. This can cause undesirable effects in off-design flight conditions. In particular, the increase in projected surface can affect hovering performance and longitudinal stability (pitch-up effect) during transitional flight. Furthermore, functional constraints for the requested rear loading capability of utility helicopter do not allow streamlining the aft-body region. Thus, the potential for achieving further efficiency gains by applying passive flow control devices is investigated.
The selected devices are counter-rotating vortex generators, contour modifications at the rear fuselage upsweep referred to as contoured strakes and simple plate-shaped strakes. In order to find a suitable arrangement of these devices and combination thereof, a large number of flow control configurations are tested on the wind tunnel model. In the following sections, the selection of efficient flow control configurations is presented and a detailed analysis is provided for the best candidate.

6.2.1 Configuration Study

In this section, the selection of the final flow control configuration is presented in detail; see also [19]. Firstly, the different flow control devices are presented. Secondly, the impact of the different flow control devices on the global characteristics is assessed. For this investigation 20 different flow control device geometries or positions are considered. Finally, based on this broad experimental investigation, the best candidate is selected for a detailed analysis of the global and local aerodynamic characteristics; i.e. the aerodynamic forces, surface pressure field, near-surface and wake flow topology.

Vortex Generator

Previous research on the effect of vortex generator conducted by Breitsamter [9] showed, that the counter-rotating vortex generator type is very efficient in delaying separation; see Fig. 6.34. Thus, this type of vortex generator is also applied in this work for the purpose of delaying flow separation. Counter-rotating vortex generators produce pairs of small scale counter rotating streamwise vortices. In consequence, higher momentum fluid from further away from the wall is mixed with the low momentum boundary layer flow. This increases the momentum in the boundary layer flow. Thus, the flow at the rear fuselage's upsweep can withstand a positive pressure gradient longer before separating from the surface.

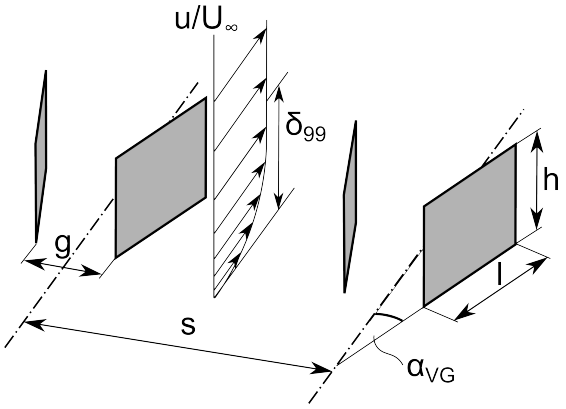

Figure 6.34: *Two pairs of counter-rotating vortex generators including the geometric parameter for the definition of the investigated configurations.*

The geometric details for the selected vortex generator configurations are based on studies performed by Boniface at ONERA [7]. This numerical study investigates the impact of flow control by vortex generators on heavy utility helicopter's rear loading ramp drag; i.e. the GOAHEAD configuration. The modified parameter include the location, pitch angle, arrangement (co- or counter-rotating) and the shape of the vortex generator elements. Based on Boniface's research two vortex generators are selected for the wind tunnel experiments.

l/δ_{99} [−]	h/δ_{99} [−]	α_{VG} [deg]	g/δ_{99} [−]	s/δ_{99} [−]
3.5	0.66 or 1	15	1.75	5.37

Table 6.2: *Vortex generator geometric parameter investigated through wind tunnel experiment; depending on the local boundary layer thickness* δ_{99}.

The selected vortex generators are scaled according to the local boundary layer thickness. The local boundary layer thickness $\delta_{99} = 6mm$ is extracted from numerical simulations for the configuration including the faired skid-landing-gear; i.e. F1M0L1. The two selected vortex generators only deviate in their non-dimensional

height h/δ_{99}, featuring values of 0.66 and 1. Thus, they are called sub-boundary-layer and boundary-layer scaled vortex generators, respectively. The full set of geometric parameters are presented in Tab. 6.2. For the definition of the vortex generator's length l , height h, angle of attack α, gap g and solidity s refer to Fig. 6.34.

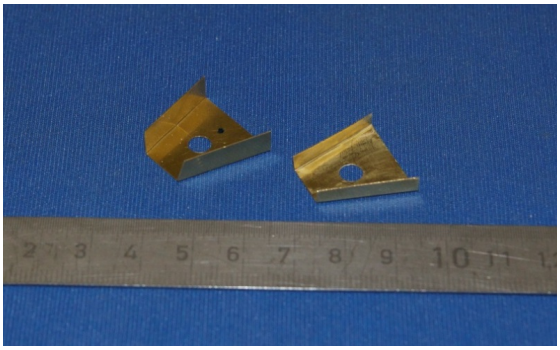

Figure 6.35: *Boundary-layer-scaled (left) and sub-boundary-layer (right) vortex generator wind tunnel models made from* 0.2*mm thick brass sheet metal.*

The vortex generator made from 0.2*mm* thick brass sheet metal are depicted in Fig. 6.35. For the wind tunnel experiments, the vortex generators are glued to the surface via the connecting base plate. Due to the minimal thickness of the sheet metal, the base plate should not interfere with the flow significantly. Two different streamwise positions are investigated. Following the suggestions made by Boniface, both streamwise positions are located around the onset of the rear fuselage's upsweep. The number of installed counter-rotating vortex generators is also varied; either 2, 4 or 6 vortex generator pairs are installed.

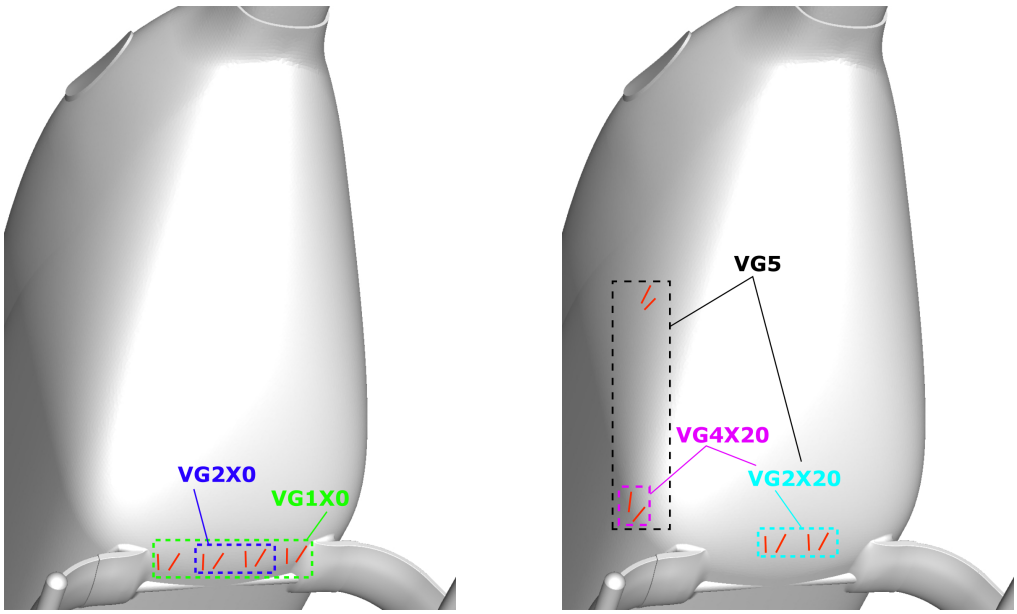

Figure 6.36: *Vortex generator positions indicated at F1M0L1's rear fuselage upsweep.*

Fig. 6.36 depicts the location of the different vortex generator configurations VG1X0, VG2X0, VG2X20, VG3X20, VG4X20 and VG5 at F1M0L1's rear fuselage

upsweep. Configuration VG1X0 includes 4 boundary-layer scaled vortex generator pairs, whereas configuration VG2X0 only includes 2 pairs. The suffix X20 of configuration VG2X20 reflects the fact that this configuration is located 20mm further downstream than configuration VG2X0. This corresponds to a vortex generator leading edge location x_r/l_r of 0.07 and 0.12, respectively, for X0 and X20. The vortex generator configuration VG3X20 is the only arrangement incorporating the sub-boundary-layer scaled vortex generator. Configurations VG4X20 and VG5 combine 2 vortex generators at the fuselage's ventral side, equivalent to VG2X20, and 2 or 4 vortex generator pairs at the lateral sides of the fuselage, respectively. These configurations are considered in order to investigate the potential of the vortex generators in suppressing separation at the fuselage's lateral tapering.

Contoured Strakes

The second investigated passive flow control device are the so-called "contoured strakes". As outlined at the beginning of this section, the contoured strakes are in fact a shape optimisation of the rear fuselage's upsweep geometry. However, the geometrical constraints for the automated optimisation are defined such that no inward deflection of the upsweep geometry is feasible. Thus, the obtained optimised shape can be easily retrofitted to existing vehicles. The automated optimisation has been conducted by Zhang et al. [49] at AHD.

Figure 6.37: *Contoured strakes as cast silicon parts (red) mounted on F1M0L1.*

The procedure employs a gradient decent approach. This optimisation logic is combined with the fluid dynamics solver TAU and the TAU mesh deformation module, which are developed by Deutsches Zentrum für Luft- und Raumfahrt (DLR). Both these modules are necessary in order to calculate the aerodynamics objective function and for adapting the surface geometry. In order to confine the computational effort, the gradients are solved with TAU's adjoint solver. This minimises the required number of functional evaluations. In Fig. 6.37 the resulting contoured strakes, further called S10, are shown as cast silicon parts mounted at F1M0L1's rear fuselage upsweep.

Plate-Shaped Strakes

For the plate-shaped strakes, 3 different planform geometries are considered for the wind tunnel experiments. The plate-shaped strakes are further referred to as "simple strakes". Those strakes are made from $1mm$ thick aluminium alloy sheet metal. The simple strakes are fitted with angle brackets at the strake's leeward side; see Fig. 6.38. When glueing the base of the angle brackets to the surface a small gap remains between the surface and the strakes. This gap is sealed with thin sticky tape.

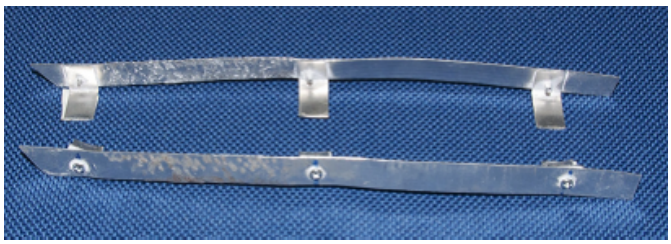

Figure 6.38: *Simple strakes fitted with angle brackets for attachment at the fuselage.*

The first planform geometry, planform 1, is derived from the shape of the contoured strakes S10. In order to obtain this shape the line of maximum height along the vertical position is extracted from the contoured strakes. Based on this geometrical information the planform 1 of the strake S1 is designed; see Fig. 6.39. For planform 1, the local height of the sheet metal element is defined similar to the contoured strake's height variation. Strake S1 is positioned near the separation line at the lateral sides of the fuselage. However, S1 is not mounted perpendicular to the surface but tangential to the lateral sides of the fuselage.

Figure 6.39: *Simple strakes S1 mounted on F1M0L1.*

The remaining two planform geometries 2 and 3 are shortened in the vertical direction compared to planform 1. Both planforms 2 and 3 feature a non-dimensional length $l/h_f \approx 0.46$; see Fig. 6.40. The planform 2 is identical to planform 1 except that the lower end is truncated. Plan form 3 only deviates from planform

2 in its height. The non-dimensional height h/δ_{99} of planform 2 is 4.2, but for planform 3 $h/\delta_{99} = 2$.

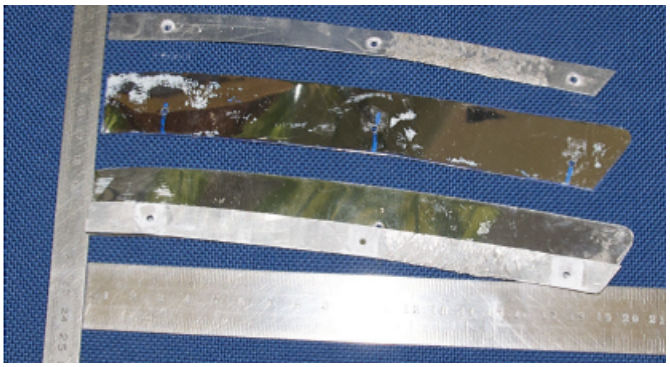

Figure 6.40: *Simple strakes plamforms 2 and 3. Top: planform 2, Center: planform 3, Bottom: Comparison planform 2 against planform 3.*

Planform 2 is employed for the configurations S2, S3, S4, S4b, S5, S5b, S6 and S6b at the indicated positions shown in Fig. 6.41. The configurations marked with suffix b are not aligned perpendicular to the surface but at an angle of approximately 45 degrees. For configurations S2L, S6L, S8L and S9L the planform geometry 3 is employed.

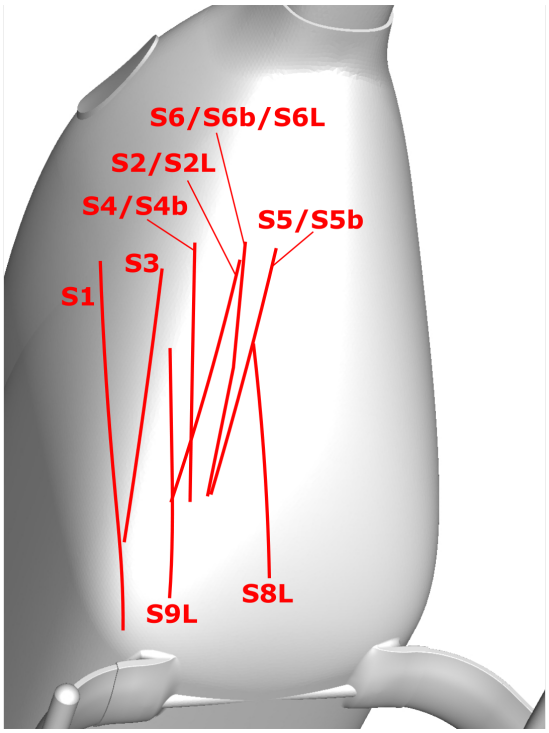

Figure 6.41: *Plate-shaped strake locations indicated at F1M0L1's rear fuselage upsweep.*

Selection of the Final Flow Control Configuration

Fig. 6.42 presents the drag reduction potential for all passive flow control configurations presented in the previous paragraphs. The reference for the stated percentages of drag reduction is F1M0L1 without flow control devices installed. This overview includes two fuselage attitudes α; i.e. $\alpha = 0$ *deg* and -1.5 *deg*. The nose down condition ($\alpha = -1.5$ *deg*) is included in this analysis in order to identify the specific configuration's sensitivity against variations in α. Results for configurations not yielding any benefit in parasite drag are blanked in Fig. 6.42. In this block chart the drag reduction against F1M0L1 is presented, from left to right, for the different strakes configurations, the different vortex generator configurations and for combinations thereof.
The best strake configurations with respect to drag reduction against F1M0L1 yield improvements in the order of 3 to 4%. Those strake configurations are S2L, S5 and S10. However, these configurations vary in their sensitivity against variations in the fuselage's pitch attitude. Configurations S2L and S10 are not very sensitive to changes in α; the variation is less then 0.5% of F1M0L1's drag level. When only $\alpha = 0$ *deg* is considered, S5 would also be a good candidate with about 3% drag reduction. But this gain is very sensitive to a variation in α. Thus, S5 is not considered any further. The best solution when only strakes are installed is apparently configuration S10; i.e. the contoured strakes. The configuration S2L is the best solution out of the plate-shaped strake configurations. Therefore, those two configurations will be considered for the analysis of the best combinations of strakes and vortex generator configurations.
Out of the vortex generator configurations the highest drag reduction against F1M0L1 with some 2% is achieved with configuration VG3X20. VG3X20 incorporates the sub-boundary-layer vortex generator. However, all the vortex generator configurations, except VG2X20, feature significant sensitivities against variations in α. Therefore, the configuration VG2X20 is selected for further analysis. With VG2X20 a drag reduction against F1M0L1 of about 1.6% can be achieved.

The combination of the selected vortex generator configuration and the two dif-

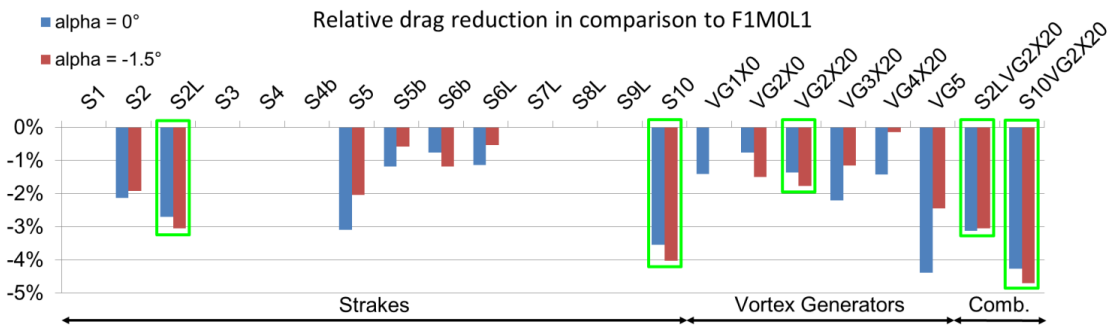

Figure 6.42: *Achieved relative drag reductions for the employed passive flow control devices in comparison to F1M0L1 without flow control. Results are shown for angles of attack equal* 0 *deg (blue) and* -1.5 *deg (red). Results for configurations with an increased drag level are blanked; e.g. S3.*

ferent considered strake configurations are called SL2VG2X20 and S10VG2X20. Adding VG2X20 to S2L levels out the observed variation in drag with respect to α for S2L. However, the assumption that the drag savings of the plate-shaped strakes and the vortex generator alone might add up is not confirmed. For the contoured strakes in combination with the selected vortex generator a different situation is observed. Not only the drag reduction sensitivity against variations in α is reduced further, but also the drag reduction increases at least by another 0.7%.

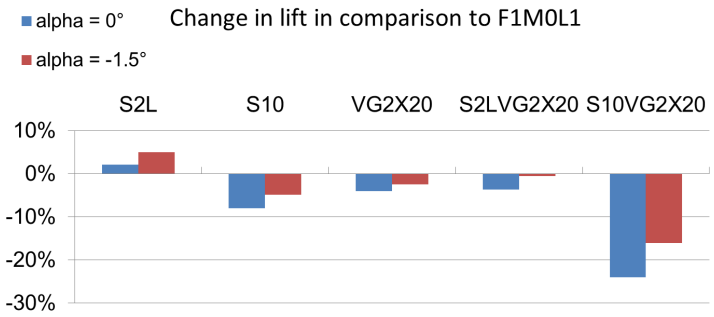

Figure 6.43: *Change in lift in comparison to F1M0L1 for $\alpha = 0$ deg (blue) and $\alpha = -1.5$ deg.*

Reducing the parasite drag is desirable in order to reduce the fuel consumption in fast-forward level flight. However, the second most important constraint is to increase the lift generated at the non-rotating components. Therefore, the selected configurations (S2L, S10, VG2X20, SL2VG2X20 and S10VG2X20) are also compared to F1M0L1 for their impact on lift. The reference configuration and all selected flow control configurations generate downforce in fact. Thus, a positive change in lift in comparison to F1M0L1 actually corresponds to a reduction in downforce. All selected configurations except S2L increase the downforce. Thus, the other configurations could deteriorate their positive impact on the power consumption obtained through drag reduction by imposing a penalty in downforce. However, for configurations S10, VG2X20 and S2LVG2X20 the penalty remains well below 10% of F1M0L1's downforce. Only configuration S10VG2X20 considerably impacts on the downforce. For $\alpha = 0$ *deg* and $\alpha = -1.5$ *deg* F1M0L1's downforce increases through S10VG2X20 by more than 20% and 15%, respectively.

As a result of the performed configuration study in order to identify the best possible solution for passive flow control at F1M0L1's rear fuselage two potential candidates are identified. The first candidate is the plate-shaped strakes with planform 3 installed at location S2 in combination with two boundary-layer scaled counter rotating vortex generator at location $x_r/l_r = 0.12$; i.e. S2LVG2X20. The second candidate is the automatically optimised upsweep region in combination with the two boundary-layer scaled counter rotating vortex generator at location $x_r/l_r = 0.12$; i.e. S10VG2X20. Regarding the drag reduction relative to F1M0L1's total parasite drag the obtained improvements are in the order of 3% and 4.5% for configuration S2LVG2X20 and S10VG2X20, respectively. With respect to the vertical force characteristics, both candidates further increase the downforce observed

for F1M0L1. However, S2LVG2X20 does not increase the downforce relative to F1M0L1 by more than 4%. In contrast, S10VG2X20 increases the downforce by at least 16% and as much as 24%. Since both these objectives need to be improved in order to achieve a sound aerodynamic design for increasing fuel flow efficiency, candidate S2LVG2X20 is selected for further analysis. In addition to the aerodynamic criteria for this selection, mechanical and operational advantages support this decision. As long as the contoured strakes S10 are not incorporated in the primary production parts their weight penalty is inferior compared to the plate-shaped strakes. On the other hand, incorporating the contoured strakes in the backdoor geometry might lead to heavier and more complex door hinges.
Fig. 6.44 presents the final configuration for a detailed analysis of passive flow control's impact on the global and local aerodynamic characteristics for configuration F1M0L1. Both the vortex generator VG2X20 and the strakes S2L are shown in orange.

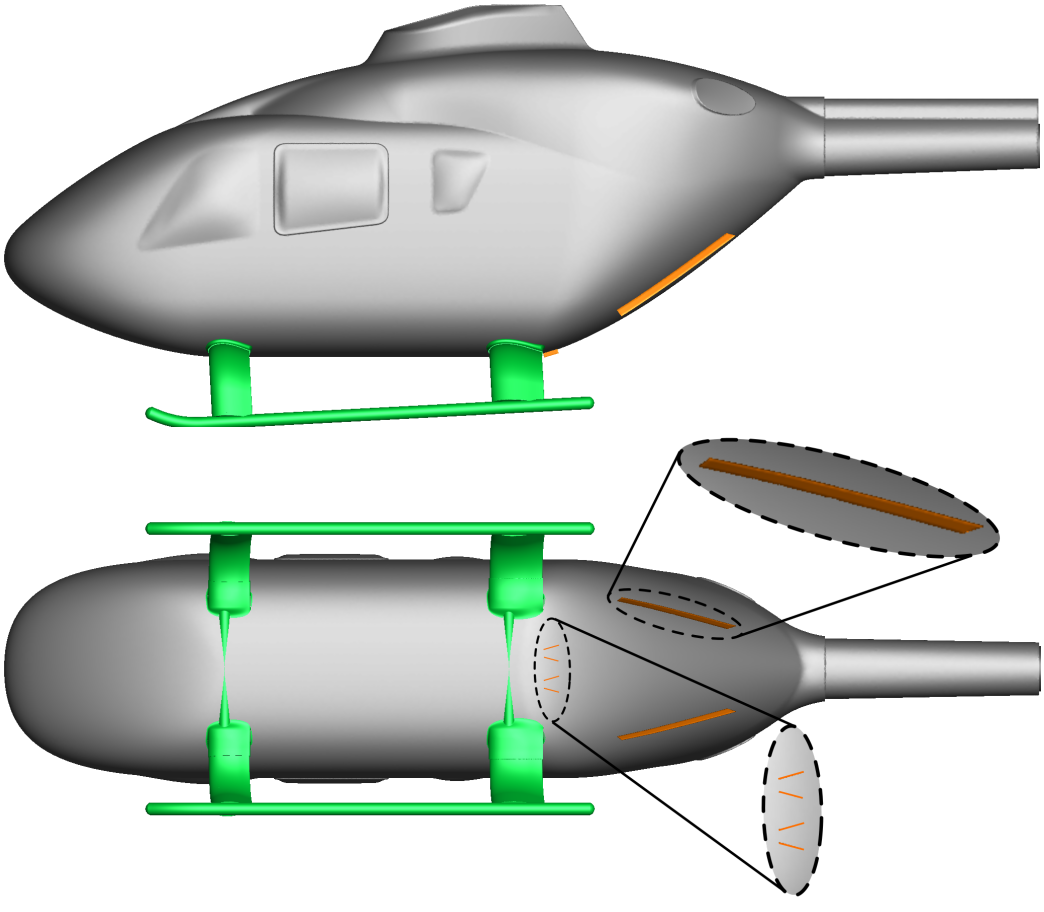

Figure 6.44: *Lateral and ventral views (CAD rendering) of the final flow control configuration installed on F1M0L1; i.e. F1M0L1S2LVG2X20.*

6.2.2 Aerodynamic Forces

For assessing the final aerodynamic characteristics when the plate-shaped strakes S2L are installed in combination with the vortex generator VG2X20 the global aerodynamic characteristics are investigated first. In Fig. 6.45, the contribution of each component to the total parasite drag is depicted and compared to the reference configuration at $\alpha, \beta = 0$ *deg*. For this purpose, all component drag coefficients C_D are set in relation to the global drag coefficient of the reference configuration $C_{D,ref}$. Thus, any change in the metric $C_D/C_{D,ref}$ allows to directly deduce the achieved reduction of the total parasite drag. As outlined in section 6.1.2, this means that any change in $C_D/C_{D,ref}$ weighted by a factor of 0.5 approximately corresponds to the achievable fuel flow reduction in fast-forward level flight.

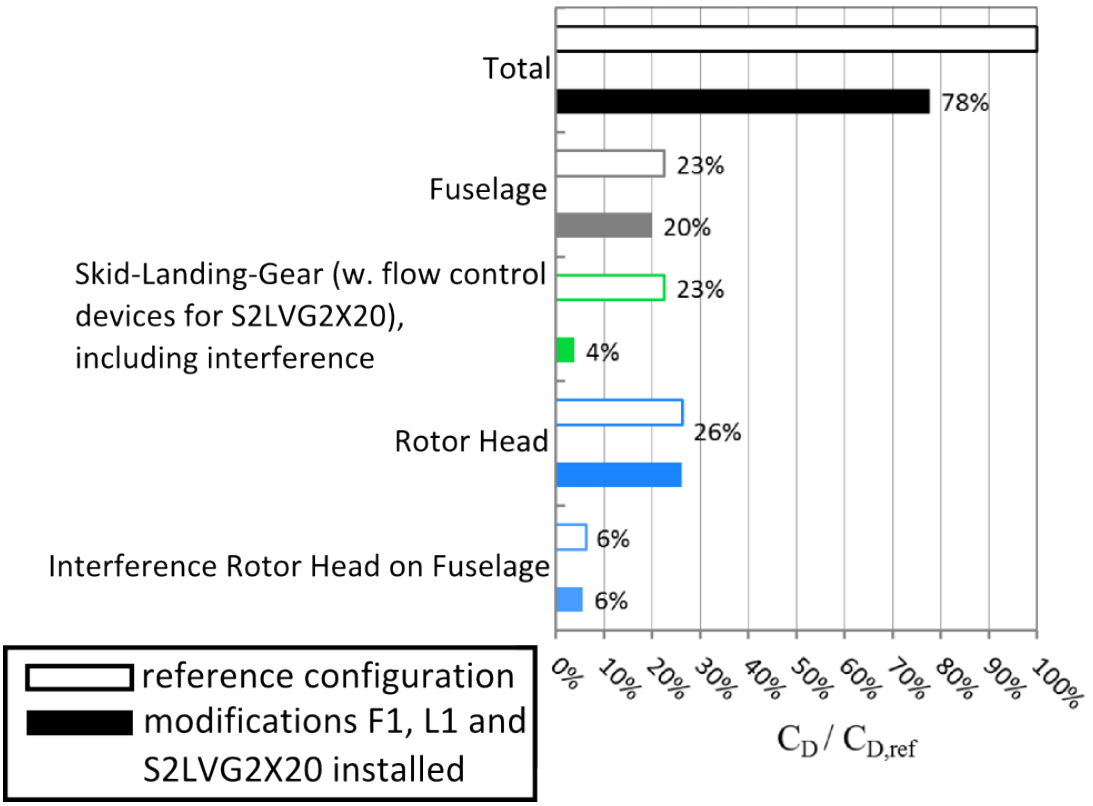

Figure 6.45: *Drag decomposition relative to the reference configuration's total parasite drag with and without modifications F1, L1 and S2LVG2X20 installed.* $Re_\infty \approx 0.95 \cdot 10^6$, $\alpha, \beta = 0$ *deg*.

In Fig. 6.45, $C_D/C_{D,ref}$ of the reference configuration is compared to the configuration featuring skid-landing-gear L1, fuselage F1 and the flow control device combination S2LVG2X20. This comparison reveals that the total parasite drag can be reduced by 22% with the retrofittable skid-landing-gear fairing, the smoothed fuselage's ventral side and the flow control devices installed on the reference configuration. The majority of this drag reduction is associated to the skid-landing-gear L1 and smoothed fuselage F1 (aggregate of 21% drag reduction); see section 6.1.2. The flow control devices drag fraction is included in the

skid-landing-gear's category in Fig. 6.45. The reason for this peculiarity is that it does not make sense to test the impact of the flow control devices without the skid-landing-gear installed. Adding the skid-landing-gear to the fuselage changes the flow topology considerably at the fuselage's rear upsweep; see section 6.1.4. However, the position of the flow control devices is adapted to this near-surface flow topology. Thus, it is only applicable to evaluate the impact of the faired skid-landing-gear L1 together with the selected flow control device combination S2LVG2X20. L1's drag fraction has been shown to aggregate to 5% $C_D/C_{D,ref}$. If also S2LVG2X20 is installed, this drag fraction reduces to 4%. Thus, the flow control device combination S2LVG2X20 yields another 1% in drag reduction. A deviation from the reference configuration for the direct rotor-head drag and its interference drag contribution is not observed for when F1, L1 and S2LVG2X20 are installed.
Based on the assumptions made, the total drag reduction achieved with the modifications L1, F1 and S2LVG2X20 of 22% could lead to a reduction of the total power requirements in fast-forward level flight of 11%. Thus, adding the flow control devices does reduce the fuel flow requirements further by a small margin. The near-surface and wake flow characteristics are improved when S2LVG2X20 is installed, see section 6.2.4. This means that the efficiency of the tail-surfaces could be improved by increasing the momentum of the incoming flow. In turn this might lead to a more compact design of the tail surfaces, which could provide potential for further efficiency gains. The impact of such a modification is not considered here though.

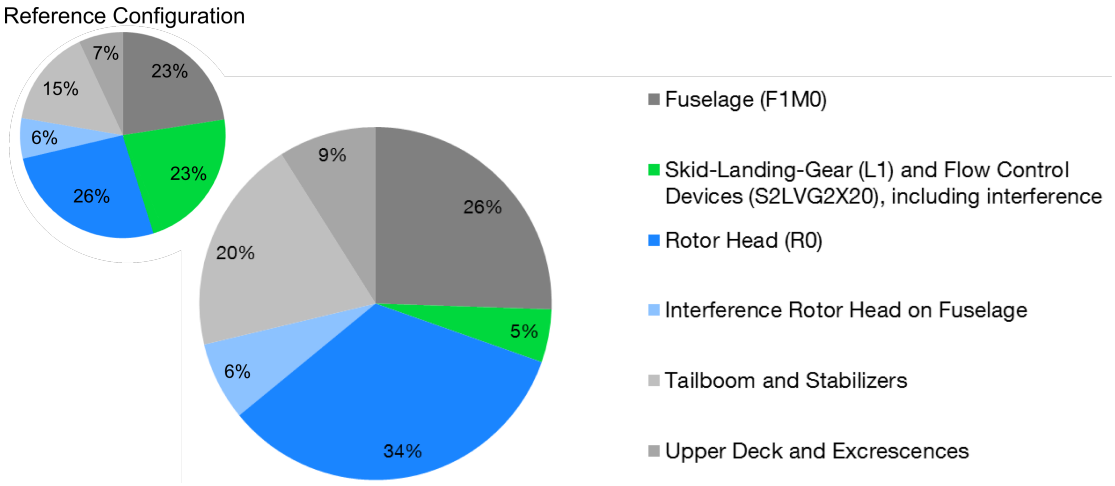

Figure 6.46: *Drag Decomposition for F1M0L1R0 fitted with S2LVG2X20. The drag contribution of the components not included on the ADHeRo W/T model are based on corporate data of Airbus Helicopters Deutschland.* $Re_\infty \approx 0.95 \cdot 10^6$, $\alpha, \beta = 0$ *deg.*

In Fig. 6.46, the resulting drag decomposition of the reference configuration fitted with F1, L1 and S2LVG2X20 is depicted. For the reference configuration fitted with F1, L1 and S2LVG2X20 the fuselage accounts for 26% of the configuration's total parasite drag; see Fig. 6.46. For the reference configuration the fuselage only contributed 23% to the reference total parasite drag. The skid-landing-gear (L1) drag contribution together with the flow control device com-

bination (S2LVG2X20), including interference, is reduced to 5%. Thus, adding S2LVG2X20 meets the expectation of reducing L1's interference on the fuselage. The rotor-head including interference effects is responsible for the largest single contribution (40%) to the total parasite drag of the reference configuration fitted with F1, L1 and S2LVG2X20. Hence, the relevance of the rotor-head's drag for further efficiency gains increases. For the reference configuration, the rotor head's drag only contributed 32% to the total parasite drag. The tailboom and stabilisers and the upper deck and excrescences add, respectively, another 20% and 9% to the total parasite drag. On the reference configuration those components only contributed 22% to the total parasite drag.
In Fig. 6.47, the lift decomposition of the baseline configuration is compared to the same configuration fitted with F1, L1 and S2LVG2X20. When the flow control device combination S2LVG2X20 is installed, L1's impact on lift is assessed together with the flow control devices. The contribution to the configurations total lift of the tailboom, the stabilisers, the flow through the upper deck and excrescences is not assessed.

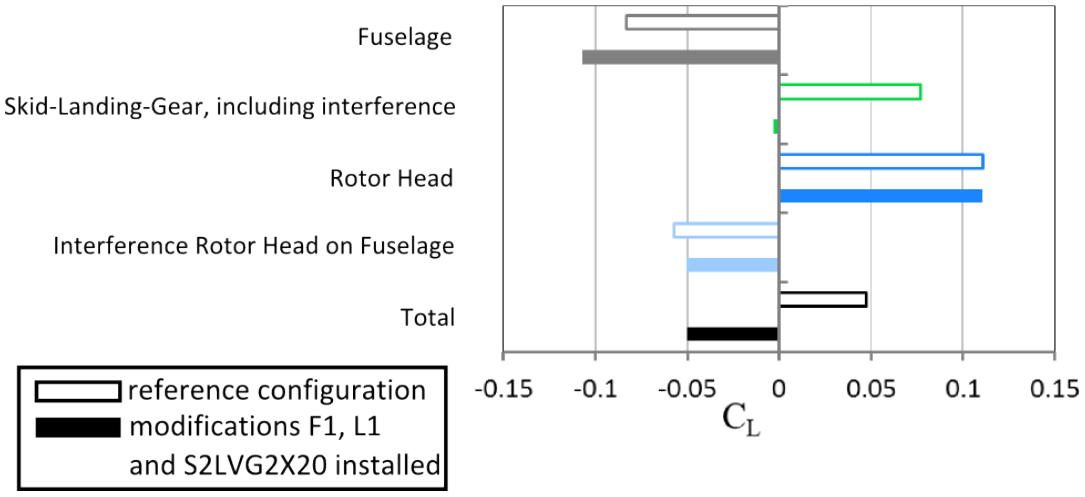

Figure 6.47: *Comparison of F1M0L1R0's lift decomposition against F0M0L0R0's.* $Re_\infty \approx 0.95 \cdot 10^6$, $\alpha, \beta = 0$ *deg.*

Adding S2LVG2X20 to the configuration F1M0L1R0 does not alter the downforce generated at the isolated fuselage F1M0. F1M0's C_L remains at -0.107. The skid-landing-gear L1 including its aerodynamic interference with the fuselage is basically neutral with respect to lift ($C_L = -0.0015$). When L1 and S2LVG2X20 are both installed this leads to an increment in C_L of -0.0028. Between configurations F0M0L0R0 and F1M0L1R0, a minor deviation between the rotor-head's contribution to lift is observed; see section 6.1.2. This deviation prevails in the presence of S2LVG2X20. In consequence of the discussed changes in the lift decomposition the total lift of configuration F1M0L1R0 with flow control deviates considerably from F0M0L0R0. Instead of a net lift equivalent to $C_L = 0.05$ for F0M0L0R0 a net downforce equivalent to $C_L = -0.05$ is obtained for F1M0L1R0 with flow control . However, the deviation of F1M0L1R0's C_L with flow control from F1M0L1R0's C_L without flow control s negligible.

6.2.3 Surface Pressure

In Fig. 6.48, F1M0L1's c_p contours in the rear fuselage's region with (S2LVG2X20) and without flow control, based both on experimental and numerical data, are depicted for $\alpha, \beta = 0\ deg$. The course of presentation is similar to Fig. 6.20.
The source of the observed drag reduction for F1M0L1 with flow control compared to F1M0L1 without flow control is associated to the suppression of the recirculation zone at the rear fuselage's upsweep. The impact of suppressing the flow separation causing this recirculation zone at the rear fuselage's upsweep on the surface pressure distribution can be assessed by comparing the contour plots for c_p; see top left image in Fig. 6.48. By applying the passive flow control device combination S2LVG2X20, the flow does not separate anymore at the rear fuselage's upsweep; see section 6.2.4. In consequence, the pressure recovery is improved especially at the ventral side of the rear fuselage's upsweep. The pressure recovery at the rear fuselage's lateral tapering is not affected by applying the passive flow control devices. This also becomes evident in c_p as a function of $y_r/(b_f/2)$ at Z5, Z7 and Z9. Compared to F1M0L1 the location and magnitude of the lateral suction peaks as well as the positive pressure gradient downstream of the suction peaks is not altered in the presence of S2LVG2X20 along these slices. Nevertheless, the combination S2LVG2X20 modifies the near-surface flow topology along the lateral tapering's ventral side; see section 6.2.4. This is also evident in c_p as a function of $y_r/(b_f/2)$ at Z11.
At the lateral sides, the presence of the flow control devices leads to an improved acceleration around the ventral side of the rear fuselage upsweep near Z11. In consequence, the primary separation is not associated to the separation line SL4 as on F1M0L1 anymore, but to the incoming streamline SL3; see section 6.2.4. This leads to lower c_p levels in the region between $y_r/(b_f/2) = \pm 0.7$ and $y_r/(b_f/2) = \pm 0.95$ along Z11. Furthermore, the onset of UV1's vortex formation is delayed in the presence of S2LVG2X20 and no three-dimensional free surface separation is identified at Z11. The separation line SL4 still originates from the separation saddle S_{S4} at the upstream end of the topological interface to the rear skid-landing-gear fairing. However, it is not deflected towards the lateral side of the fuselage as on F1M0L1. On F1M0L1 with flow control (S2LVG2X20), SL4 is located closer to the model's symmetry plane and passes along S2L's inboard intersection with the fuselage. In consequence of S2L, the flow reattaches again at S2L's outboard intersection with the fuselage along AL5. Z11 is intersecting with the rear fuselage in close proximity to S2L's leading edge, which leads to the observed substantial local pressure maximum and minimum near $y_r/(b_f/2) = \pm 0.6$ in between SL4 and AL5. Close to the models symmetry plane in between $y_r/(b_f/2) = \pm 0.2$ the c_p level is slightly increased for F1M0L1 with flow control compared to F1M0L1 without flow control.

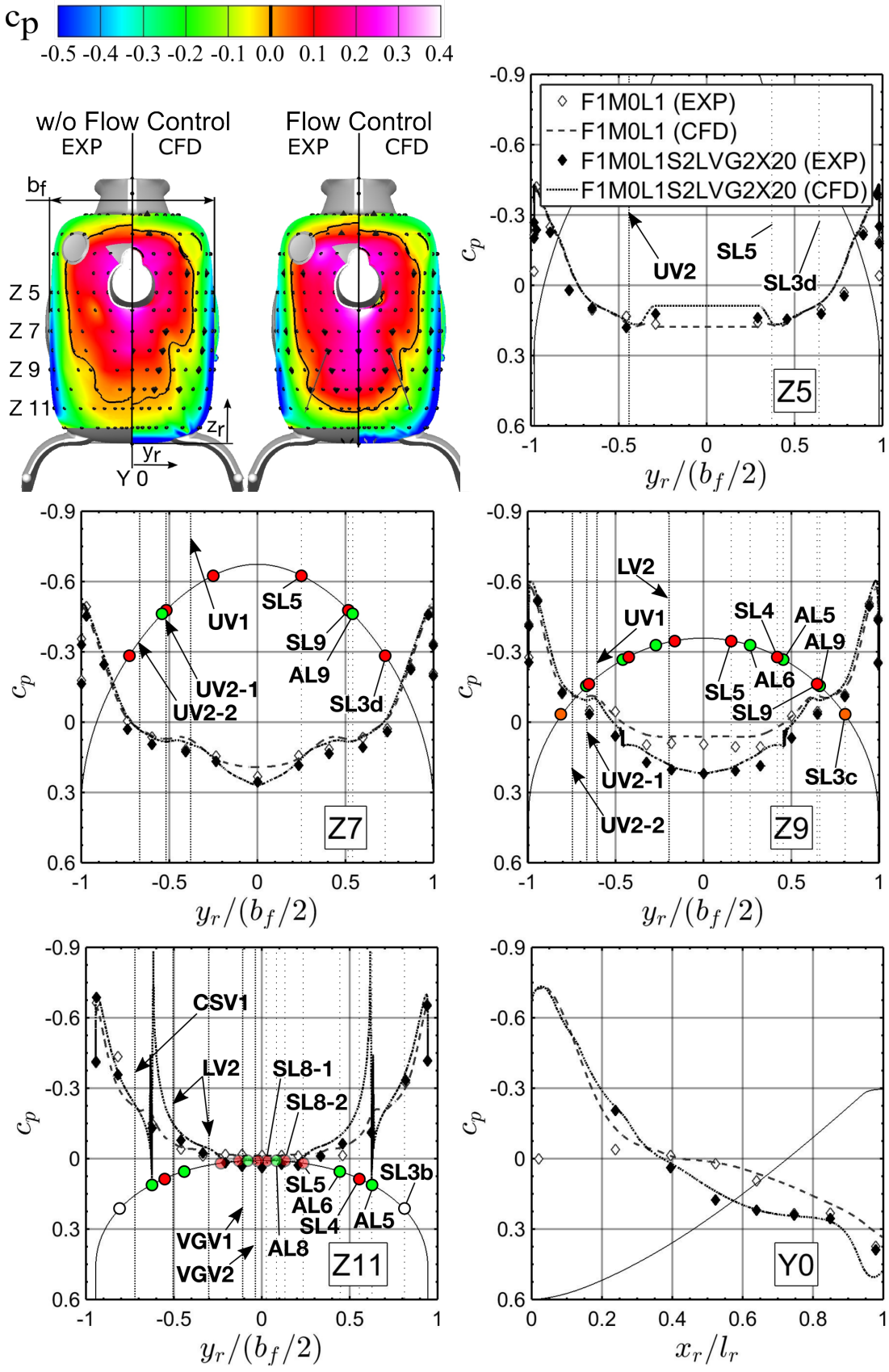

Figure 6.48: *c_p distribution at the rear fuselage for F1M0L1 (top left) and F1M0L1VG2X20 (top right) and the associated slices Z5, Z7, Z9,Z11 and Y0. $Re_\infty \approx 0.95 \cdot 10^6$, $\alpha, \beta = 0$ deg.*

These effects are associated to the formation of the counter-rotating vortex pairs VGV1 and VGV2 at the vortex generator VG2X20. In consequence, the boundary layer flow is reenergised with higher momentum fluid from further away from the wall and the flow remains attached instead of separating from the surface along SL6 as observed on F1M0L1.
At Z9, the impact of S2LVG2X20 on the local surface pressure is the most significant compared to the other horizontal slices. Especially in between the strakes, the pressure levels is increased significantly through S2LVG2X20; i.e. in between AL5 at $y_r/(b_f/2) = \pm 0.46$. The margin in c_p is in between $\Delta c_p = 0.1$ up to 0.15. As for F1M0L1, local pressure minima are observed at $y_r/(b_f/2) = \pm 0.6$ for F1M0L1 with flow control (S2LVG2X20) in consequence of UV1.
At Z7, the difference in c_p close to model's symmetry plane with or without S2LVG2X20 is below $\Delta c_p = 0.1$ in between $y_r/(b_f/2) = \pm 0.2$. For F1M0L1, the flow reattaches after the recirculation zone at N_{A5} upstream of Z7. Thus, Δc_p is not as significant as upstream of the reattachment when S2LVG2X20 is installed. At Z5, both F1M0L1's c_p with and without flow control as a function of $y_r/(b_f/2)$ are identical. This also reflects the fact that the flow topology along the dorsal side of the rear fuselage is not affected by S2LVG2X20; see 6.2.4.
The positive effect of S2LVG2X20 on the pressure recovery along the model's symmetry plane also becomes evident by comparing F1M0L1's c_p as a function of x_r/l_r at Y0 with F1M0L1 with flow control. By adding the passive flow control devices, c_p is increased throughout most of the rear fuselage's upsweep and no separation and reattachment occurs along Y0 as observed for F1M0L1. Only between $x_r/l_r = 0.15$ and 0.3, c_p is lower with flow control, because the vortex generators (VG2X20) enhance the vertical deflection of the flow at the beginning of the rear fuselage upsweep.
In order to investigate if the passive flow control device can suppress L1's aerodynamic interference on F1M0, F1M0's c_p contours and the c_p contours of F1M0L1 with flow control are compared for $\alpha, \beta = 0\ deg$ (top left); see Fig. 6.49 . Furthermore, c_p is depicted as a function of $y_r/(b_f/2)$ and x_r/l_r for selected horizontal slices $Z5, Z7, Z9, Z11$ and the vertical slice Y0, respectively.
By comparing c_p contours of F1M0 and F1M0L1 with flow control in the rear fuselage's region, it can be seen that the pressure level is increased compared with F1M0 throughout the rear fuselage region by adding S2LVG2X20. Thus, the aerodynamic interference of L1 on F1M0 is not only eliminated but even an additional improvement compared to F1M0 is achieved. However, the added form drag of the passive flow control devices still has to be taken into consideration.
Also at the selected slices Z5, Z7, Z9 and Y0 the passive flow control devices prove to be effective in increasing c_p as a function of $y_r/(b_f/2)$ and x_r/l_r, respectively. Only at Z11 the application of S2LVG2X20 leads to locally lower pressure levels compared to F1M0.

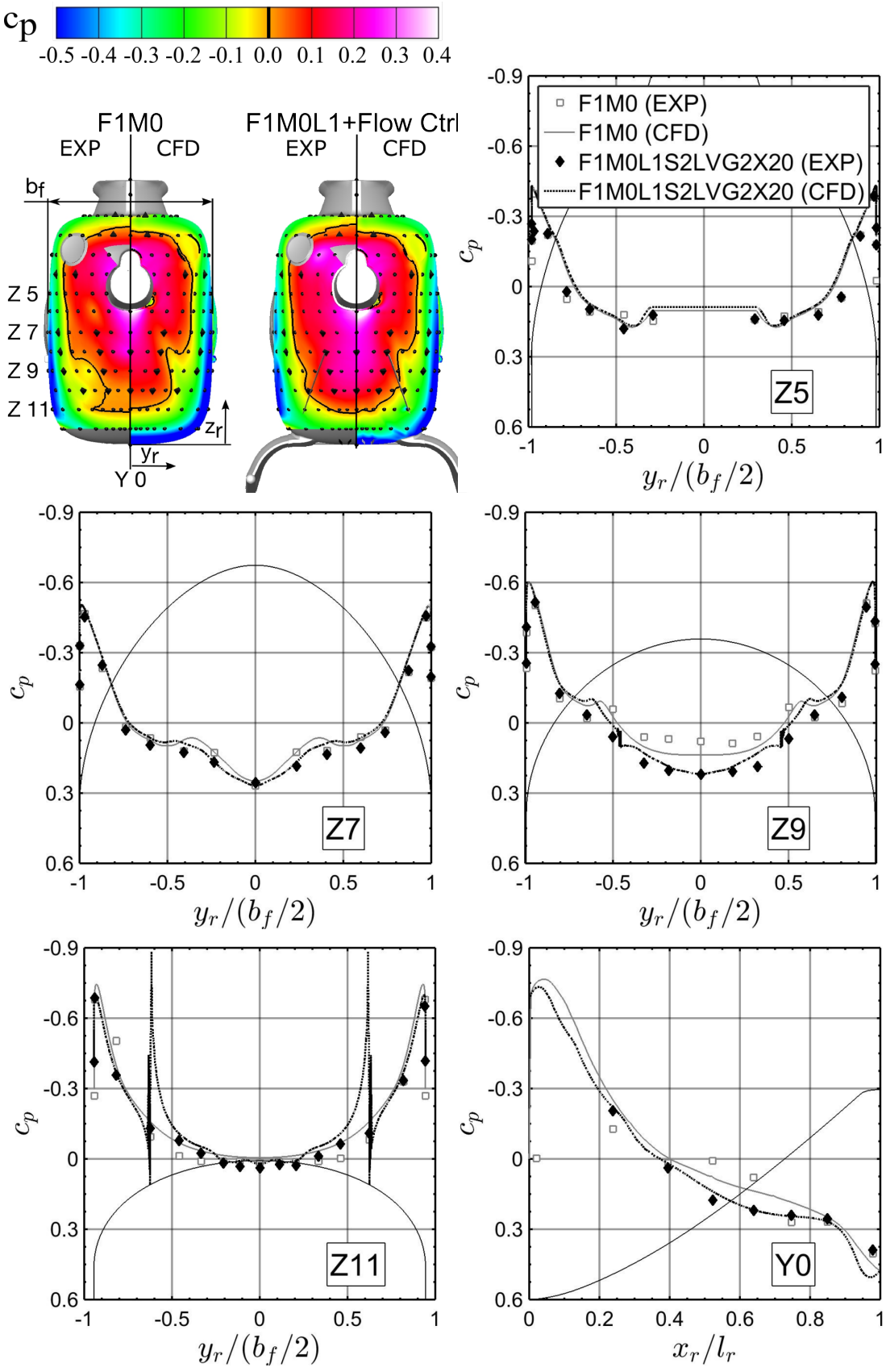

Figure 6.49: *c_p distribution at the rear fuselage for F1M0 (top left) and F1M0L1VG2X20 (top right) and the associated slices Z5, Z7, Z9,Z11 and Y0. $Re_\infty \approx 0.95 \cdot 10^6$, $\alpha, \beta = 0$ deg.*

6.2.4 Flow Topology

In this section, the flow topology of the configuration including the faired skid-landing-gear L1 and the passive flow control device combination S2LVG2X20 is analysed. As for the baseline model and the optimised skid-landing-gear design, both the near-surface flow topology and the flow topology in the wake of F1M0L1 fitted with S2LVG2X20 is presented. The near-surface topology is analysed first and relevant flow regions are identified; see section *Near-Surface Flow Topology*. This also includes a comparison of the near-surface flow topology of F1M0L1 with flow control to F1M0 and F1M0L0. Furthermore, the resulting wake flow topology of F1M0L1 with flow control is analysed in order to identify vortex structures and their trajectories and the envelope of the wake regions. These results are presented in the section *Wake Flow Topology*. This also includes a comparison with the wake flow topology of F1M0 and F1M0L1.

Near-Surface Flow Topology

In Fig. 6.50 a) and b), the near surface flow topology is depicted for configuration F1M0L1S2LVG2X20 at $\alpha, \beta = 0$ *deg*. This topology is derived from skin-friction-lines based on the performed URANS simulation; see chapter 4. In Fig. 6.50 a) the flow around the fuselage F1 is decomposed into relevant flow regions, whereas Fig. 6.50 b) depicts the identified structure of the near-surface flow topology.
Comparing F1M0L1's near-surface flow topology with and without flow control reveals some differences but also similarities; see Fig. 6.50 and Fig. 6.22. The near-surface flow topology of F1M0L1 with flow control can be divided into four flow regions; i.e. FR1, FR2, FR3 and FR4. The flow region FR5 and the recirculation zone RZ are not observed in the presence of S2LVG2X20 in contrast to F1M0L1.
Within FR1 and FR2 the same near-surface flow topology is observed on F1M0L1 with S2LVG2X20 as without. Only the nomenclature deviates to some extend due to the changed topology at the rear fuselage's upsweep in the presence of S2LVG2X20. F1M0L1's S_{S10}, $F_{S2-4-10}$ and F_{S10} are renamed in the presence of S2LVG2X20 to, respectively, S_{S7}, F_{S2-3-7} and F_{S7}. Consequently, F1M0L1's SL10 also becomes SL7 for F1M0L1 with flow control.
Furthermore, F1M0L1's downstream boundary of FR2 changes in the presence of S2LVG2X20. This is associated to the fact the near-surface flow within FR3 passes the rear attachment fairing's topological interface at the outboard side without separating along SL4. Thus, the primary separation at the lateral tapering of F1M0L1 with flow control is not associated to SL4 anymore. Instead the incoming streamline SL3, which originates at the topological interface to the front attachment fairing, becomes the primary separation line. Nevertheless, the primary separation's location along the lateral tapering is not affected by this modification. Along SL3 the point P3 is located, downstream of which the flow begins to separate along SL3 by a free-surface separation. Up to point P3, SL3 is divided into SL3a and SL3b; see section 6.1.4.

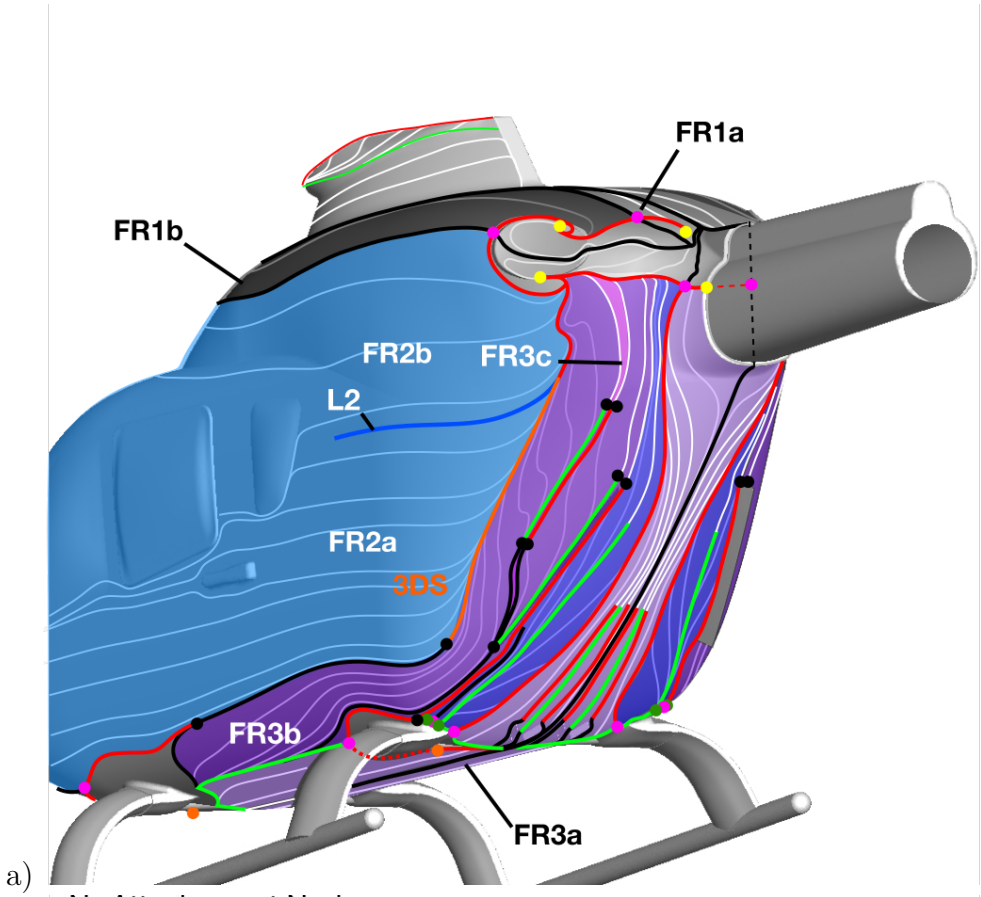

a)

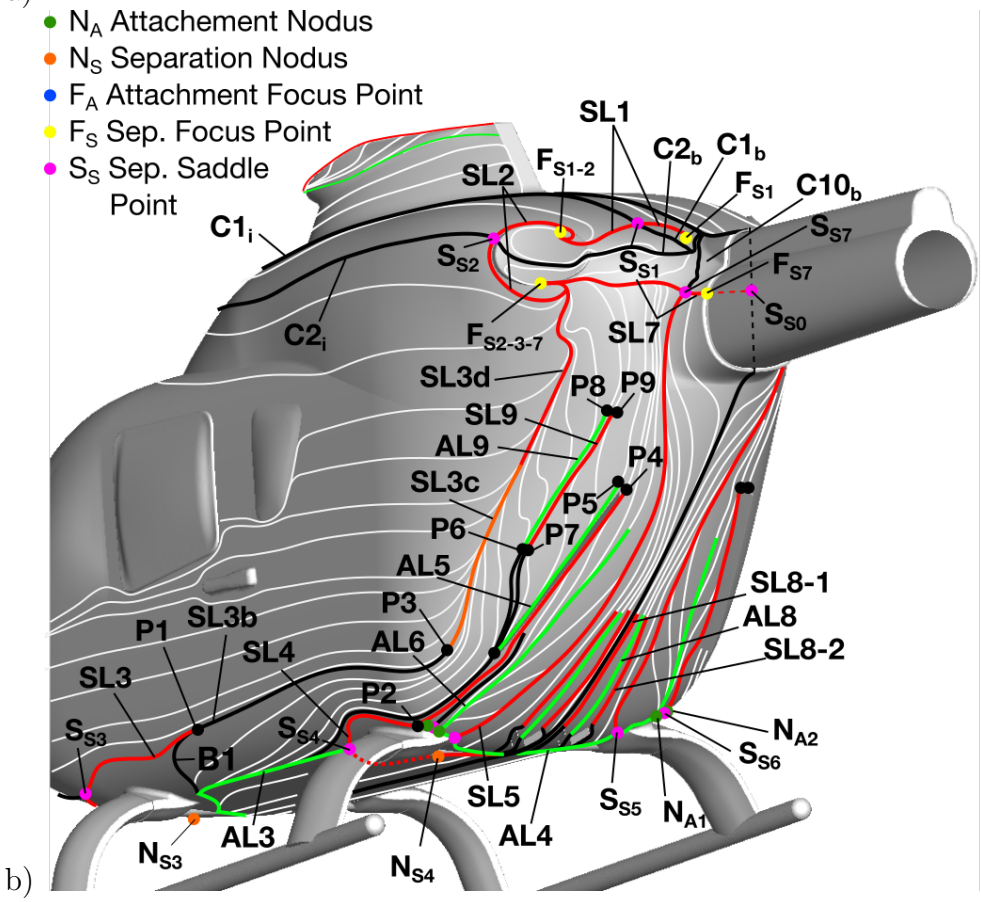

b)

Figure 6.50: *Schematic representation of the near-surface flow topology for F1M0L1S2LVG2X20; a) flow regions, b) flow topology.* $Re_\infty \approx 0.95 \cdot 10^6$, $\alpha, \beta = 0$ *deg.*

Downstream of P3 SL3 is divided into SL3c and SL3d. This distinguishes the region along SL3 where the formation of the primary upsweep vortex UV1 is effective and where not.
As for F1M0L1, FR3 is located at the fuselage's ventral side when S2LVG2X20 is installed. FR3's lateral limits remain unchanged on F1M0L1 with or without flow control, except that $C6_i$ is replaced by $C0_i$. $C0_i$ directly connects the attachment nodus at the nose N_{A0} with the fictional separation saddle S_{S0}, since no separation occurs at the models symmetry plane with flow control. On F1M0L1, the sub-regions FR3a and FR3b are located. On F1M0L1 with flow control, one additional sub-region is observed due to the changed near-surface flow topology at the rear fuselage's upsweep; i.e. FR3c.
For F1M0L1 without passive flow control, FR3a's downstream limit is defined by the separation lines SL5 and SL6. When the passive flow control device combination S2LVG2X20 is installed, this separation is suppressed by the generation of the vortex genetator vortices VGV1 and VGV2; see section 6.2.4. In consequence, SL3a extends across the rear fuselage's upsweep region. There FR3a is limited in the lateral direction by SL5. With S2LVG2X20 installed SL5 still originates at S_{S5} at the downstream end of the rear attachment fairing's topological interface. However, SL5 then separates from the surface as it encounters $C7_b$ at S_{S7}. S_{S7} of F1M0L1 with flow control corresponds to F1M0L1's S_{S10}. Consequently, FR3a's downstream end constitutes the inboard section of SL7, which originates at S_{S7}. Within FR3a the separation and attachment lines associated to VGV1's and VGV's induced flow field are located; i.e. SL8-1, SL8-2 and AL8.
FR3b's upstream limit and lateral limits up to points P2 and P3 remains unchanged when S2LVG2X20 is installed. But SL3b's downstream limit is not defined by SL4a between P2 and P3 anymore. This is the case since SL4 does not constitute the primary separation line as discussed above. In consequence, FR3b also extends into the rear fuselage's upsweep region. There FR3b's outboard lateral limit is defined by SL3c and SL3d. FR3b's inboard lateral limit downstream of P2 is defined by SL4 and its downstream characteristic streamline, which separates from the surface at the outboard section of SL7. Furthermore, SL7's outboard section defines FR3b's downstream boundary. Within FR3b, the attachment line AL5 is located at the outboard intersection of S2L and the fuselage. Additionally, FR3b encompasses FR3c.
FR3c is associated to the formation of the secondary upsweep vortex UV2-1. UV2-1 forms in between the separation and attachment line SL9 and AL9, respectively. The incoming characteristic streamlines originate at AL3. The vortex roll up begins along these characteristic streamlines downstream of points P6 and P7. The vortex roll up of UV2-1 ends at the points P8 and P9, downstream of which the characteristic streamlines continue before they separate from the surface at SL7. Thus, the lateral limits of FR3c are associated to the described characteristic streamlines and SL7 and SL9. Whereas, FR3c's downstream limit is also defined by SL7.
The near-surface flow topology if F1M0L1 with flow control is completed by FR4. FR4 is limited at its upstream side by AL1 and AL2. AL1 and AL2 are identical to the corresponding lines at F1M0L1 without passive flow control. They are located at the downstream side of the rear attachment fairing's topological interface; see section 6.1.4. FR4's inboard and outboard lateral limits are defined by SL5

and SL4, respectively. The outboard lateral limit also includes SL4's downstream characteristic streamline. The downstream boundary of FR4 constitutes SL7.
Table 6.3 summaries all identified characteristic points of F1's near-surface flow topology and their contribution to the topological equation after Chapman [11] in the presence of L1 and S2LVG2X20. As for F1M0L1, the topological interfaces to the skid-landing-gear L1 are defined such that all characteristic point associated to L1 return a sum of zero. Hence, a sum of two over all F1's characteristic points is required in order to close the topological field. As can be seen in table 6.3, this statement is true. Thus, a closed topological description of F1M0L1S2LVG2X20's near surface flow topology is obtained.

N_{A0}	+1
N_{A1}	+2
N_{A2}	+2
F_{S1}	+2
F_{S1-2}	+2
F_{S2-3-7}	+2
F_{S7}	+2
N_{S4}	+2
F_{S4}	+2
S_{S1}	-2
S_{S2}	-2
S_{S3}	-2
S_{S4}	-2
S_{S5}	-2
S_{S6}	-2
S_{S7}	-2
S_{S0}	-1
Σ	+2

Table 6.3: *Topological equation for the characteristic points of F1's near surface flow topology in the presence of L1 and S2LVG2X20.*

In order to identify the origin of the increased base pressure at F1M0L1's rear fuselage upsweep with flow control against F1M0's, their near-surface flow fields are compared with each other; see Fig. 6.21 and 6.50. At the lateral tampering the two near-surface topologies are very similar, except that the additional separation line and attachment line SL4 and AL5 are observed in the presence of S2LVG2X20. The increased pressure level and pressure recovery at F1M0L1's rear fuselage upsweep with flow control compared to F1M0's is associated to fully suppressing the separation and the corresponding recirculation zone near the model's symmetry plane. This is achieved by the generation of VGV1 and VGV2 at VG2X20 and the flow deflection along S2L; see section 6.2.4.

Wake Flow Topology

In Fig. 6.51, the vortex formation at F1M0L1's rear fuselage with flow control is depicted at $\alpha, \beta = 0\ deg$. The near-surface flow topology is only changed in the rear part of the fuselage by adding the passive flow control device combination S2LVG2X20 to F1M0L1. Consequently, the vortex formation around the front attachment fairing observed for F1M0L1 is also not altered when installing S2LVG2X20. Hence, the corner separation vortex CSV1 still emerges at F1M0L1's front attachment fairing and sheds into the wake when flow control is applied. CSV1 is identified on either side of the fuselage's rear upsweep at slice Z11.
In analogy to F1M0L1, the second horse shoe vortex system LV2 is formed at the rear attachment fairing of F1M0L1 with flow control. At Z11 and Z9, both the inboard and outboard part of the counter-rotating LV2 can be distinguished. Further downstream, the outboard part of LV2 merges with UV1 and, thus, is not discernible within Z7 and Z5. Without S2LVG2X20 LV2's outboard part already merges with UV1 in between Z11 and Z9.
In contrast to F1M0L1, UV1's vortex roll-up begins not at SL4 downstream of P2, but the onset of its formation is shifted more towards the fuselage's dorsal side. On F1M0L1 with flow control, UV1 begins to roll up along SL3 downstream of P3; i.e. along SL3c. At Z11, UV1 cannot yet be identified since Z11 intersects with the rear fuselage just upstream of SL3c. However, at Z9 and Z7 UV1 is clearly distinguished as two regions of $\omega_x \cdot l_{ref}/U_\infty = \pm 12$. At Z5, UV1's vortex formation is already broke down and UV1 is not discernible close to the model's surface anymore. Thus, the primary separation is defined by SL3d at Z5.
Even though the vortex roll-up of UV1 is modified in the presence of S2LVG2X20 compared to F1M0L1 the secondary upsweep vortices UV2-1 and UV2-1 are observed. In contrast to F1M0L1 without flow control, UV2-1's roll-up process is delayed in the presence of S2LVG2X20. At F1M0L1, UV2-1's begins to form just downstream of the rear attachment fairing along SL11 and AL11. When F1M0L1 is fitted with S2LVG2X20, UV2-1 begins to form downstream of point P6 and P7 at SL9 and AL9. The formation of UV2-2 is not affected considerably by S2LVG2X20 though. It still begins to form in between the attachment line associated to UV2-1 and the primary separation line. In contrast to F1M0L1, these lines are denoted as AL9 and SL3c on F1M0L1 with flow control. For F1M0L1 fitted with S2LVG2X20, the interaction of UV1, UV2-1 and UV2-2 leads to the deflection of UV1 away from the surface as it was observed for F1M0L1 as well. Furthermore, UV2-1 and UV2-2 still merge just upstream of Z5 into UV2.
In addition to the vortex systems already observed for F1M0L1, the vortex system associated to the vortex generators are identified for F1M0L1 fitted with S2LVG2X20. They are denoted as VGV1 and VGV2. VGV1 and VGV2 are generated along a fixed surface separation at, respectively, the outboard and inboard element of the vortex generator.

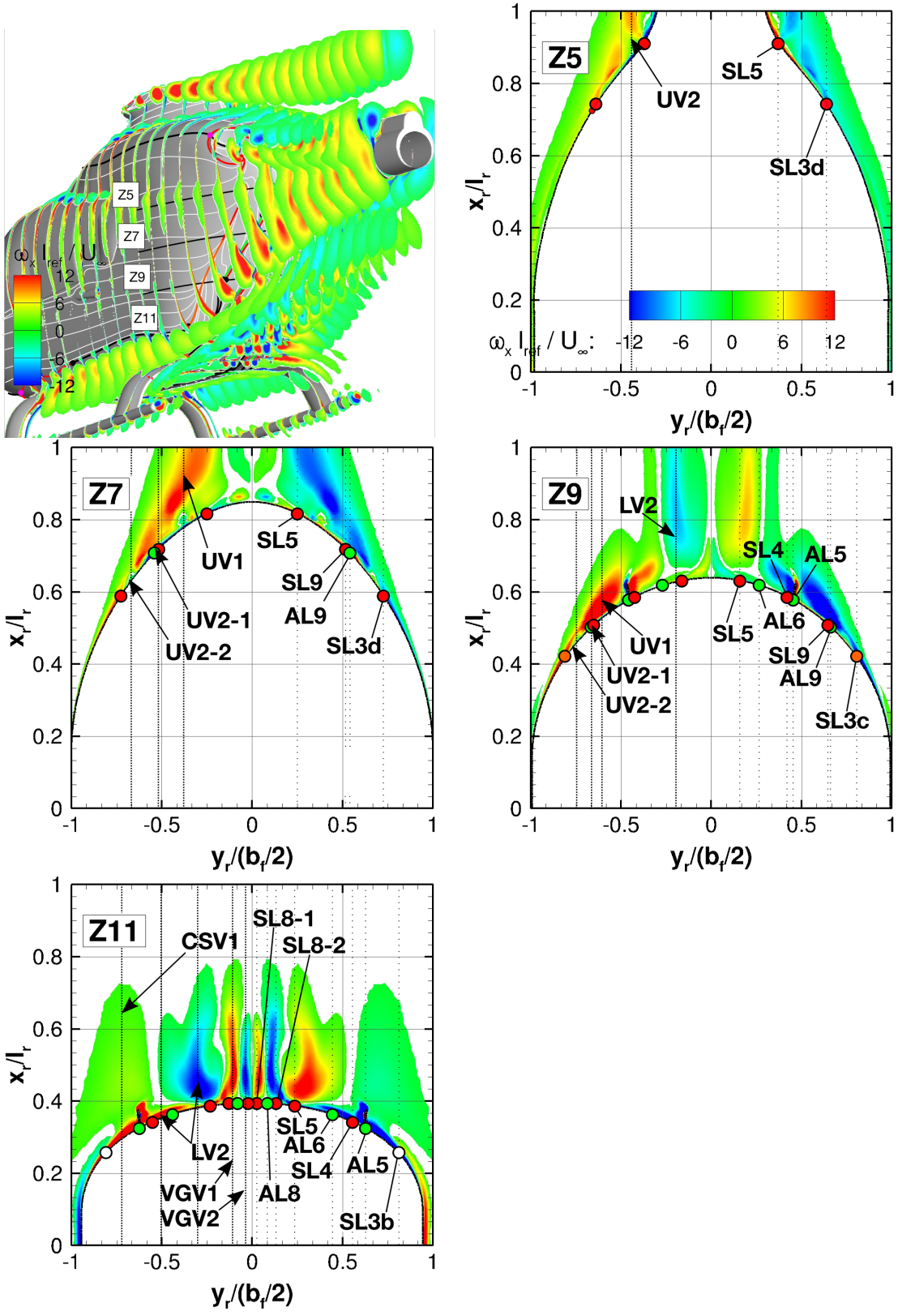

Figure 6.51: *Contours of u/U_∞ (Exp/CFD) and $\omega_x l_{ref}/U_\infty$ (CFD) in F1M0L1S2LVG2X20's wake at slice locations 'c','e' and 'f'. Wake region boundaries correspond to $u/U_\infty = 0.8$. $Re_\infty \approx 0.95 \cdot 10^6$, $\alpha, \beta = 0$ deg.*

VGV1 and VGV2 are only observed at Z11, because they only remain in close proximity to the wall at the ventral side of the rear fuselage upsweep. In the wake VGV2 merges with the inboard part of LV2 in between Z11 and Z9.
In Fig. 6.52, the main flow features observed in the near wake of F1M0L1 with flow control are summarised. The trajectory of CSV1 is not presented in detail here, since it is not altered compared to F1M0L1 without flow control; see Fig. 6.29.
The near wake of F1M0L1 with flow control contains the same vortex systems as observed for F1M0L1 without flow control. This includes the primary upsweep vortex UV1, the secondary upsweep vortex UV2, landing-gear vortex LV2, the exhaust vortex EV and the mast fairing vortex MV. Furthermore, the vortex generator vortices VGV1 and VGV2 can be identified. VGV2 is shedding into the wake just below the inboard part of LV2, whereas VGV2 is merging with the inboard part of LV2. The flow reattaching to the surface downstream of the rear attachment fairing along AL6 is following the same incipient path as observed without flow control; see green ribbon. However, the recirculation zone observed on F1M0L1 completely vanishes in the presence of S2LVG2X20.

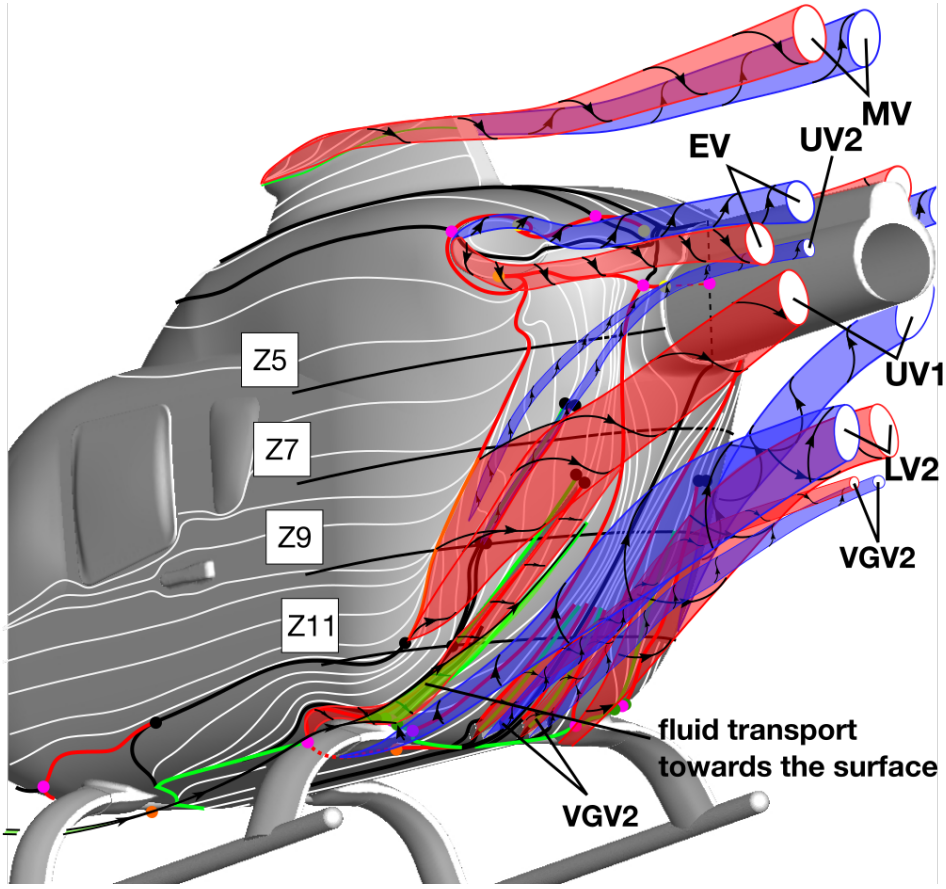

Figure 6.52: *Schematic representation of F1M0L1's main features within the near wake region of the rear fuselage.* $Re_\infty \approx 0.95 \cdot 10^6$, $\alpha, \beta = 0$ *deg.*

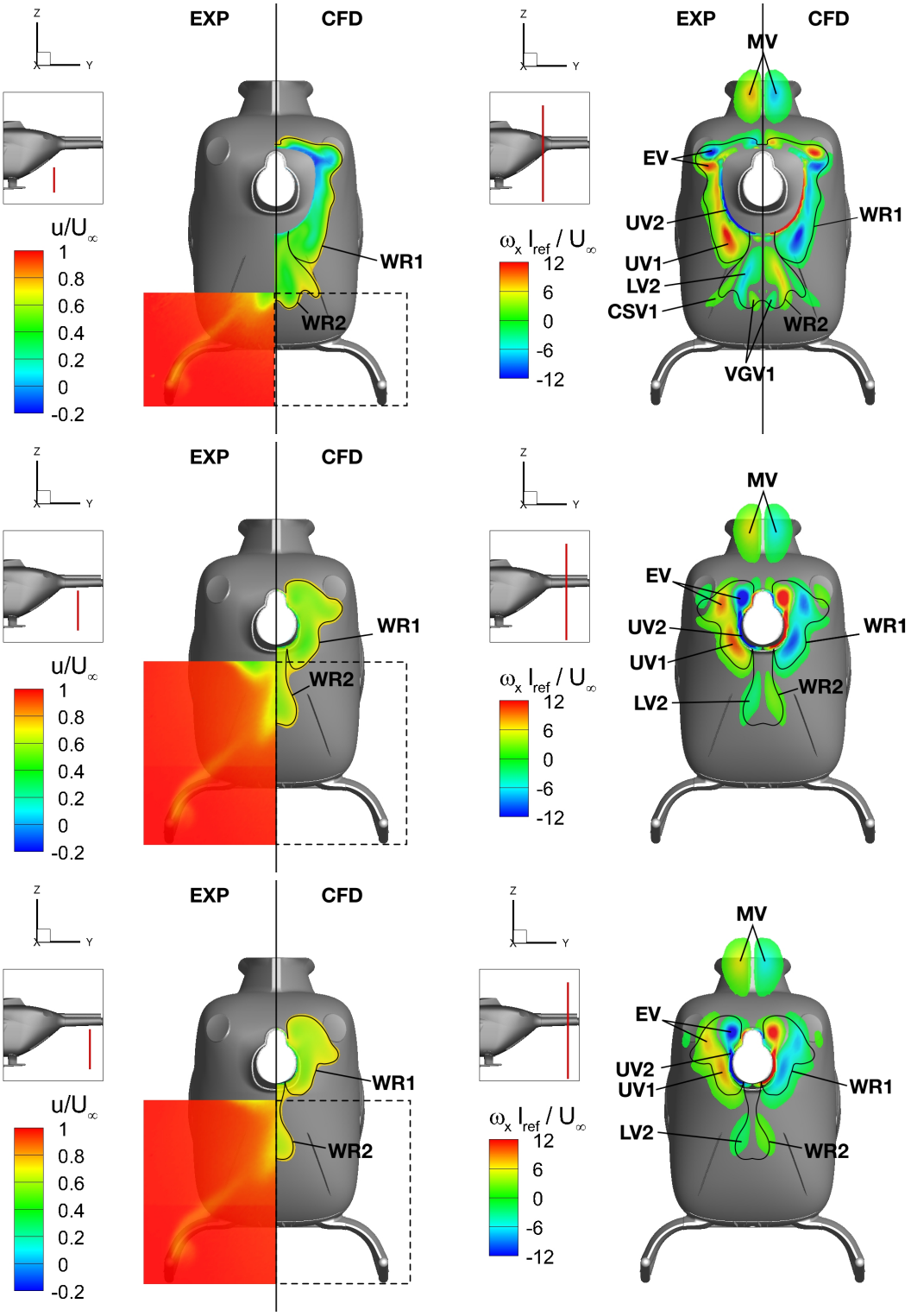

Figure 6.53: *Contours of u/U_∞ (Exp/CFD) and $\omega_x l_{ref}/U_\infty$ (CFD) in F1M0L1S2LVG2X20's wake at slice locations 'c','e' and 'f'. Wake region boundaries correspond to $u/U_\infty = 0.8$. $Re_\infty \approx 0.95 \cdot 10^6$, $\alpha, \beta = 0$ deg.*

In Fig. 6.53, contours of the non-dimensional axial velocity u/U_∞ and $\omega_x \cdot l_{ref}/U_\infty$ are shown along the wake slice locations 'c','e' and 'f'. As for all the other configurations, except F0M0L0, F1M0L1 with flow control does reveal an good to excellent agreement of the PIV data with the CFD data with respect to the absolute values and the extension of the wake region (WR). For F1M0L1 with flow control, also two wake regions can be distinguished. WR2 is still located close to the models symmetry plane and below the fuselage's aft-body. However, for F1M0L1 with flow control, WR2 is associated to the wake of the rear attachment fairing and the vortex generator. The extension of F1M0L1's WR1 is almost identical to F1M0L1's fitted with the passive flow control device combination S2LVG2X20. It inhibits also the same vortex systems UV1, UV2 and EV. Regarding the extension of WR2, the same statement is true as for WR1 in comparison between F1M0L1 with and without flow control. However, the velocity deficit within both wake regions is confined when the passive flow control devices are installed on F1M0L1. Thus, it is shown that the wake impinging on the empennage features more momentum. This could be exploited for future machines in order to achieve additional efficiency gains by the design of more compact tail surfaces.

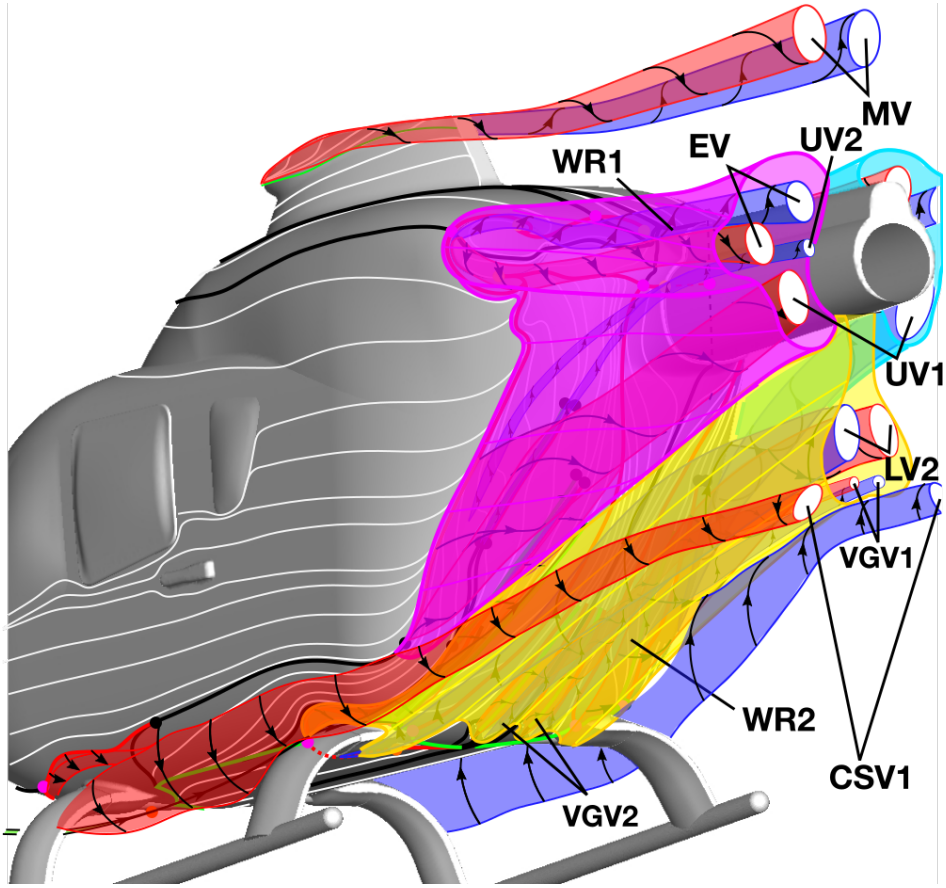

Figure 6.54: *Schematic representation of F1M0L1S2LVG2X20's wake including the vortex systems and the envelope of the wake regions.* $Re_\infty \approx 0.95 \cdot 10^6$, $\alpha, \beta = 0$ *deg.*

Comparing the wake flow of F1M0L1 with and without flow control (S2LVG2X20) shows that the general wake topology is not affected by passive flow control; see

Fig. 6.33 and Fig. 6.54. Nevertheless, the velocity deficit inside the wake can be further reduced by applying passive flow control.

7 Conclusions and Outlook

In order to achieve progress towards the design of next-generation helicopter, a state-of-the-art twin-engine-light (TEL) class utility helicopter was subject to aerodynamic design optimisation. The main objective for this optimisation was to increase the dynamic productivity for achieving high level goals such as reduced fuel consumption and emissions. The reference configuration for this optimisation constitutes a TEL-class utility helicopter featuring a blunt aft-body, skid-landing-gear and a five-bladed rotor head. The dominant flight condition for the missions performed by TEL-class helicopter is fast-forward level-flight at $1000m$ above Mean Sea Level (MSL) according to International Standard Atmosphere (ISA) conditions. Thus, the performed aerodynamic design optimisation aimed at improving the performance for this flight condition.

A detailed analysis of the reference configuration's aerodynamic characteristics revealed, that reducing parasite drag is an effective means for achieving the set objectives. Therefore, the optimisation task was to reduce the helicopter's parasite drag without significantly increasing its downforce. For this purpose, a large number of configurations has been studied by wind tunnel experiments and numerical flow simulations.

The design of the wind-tunnel model is based, on a newly developed methodology for achieving the maximum feasible model scale under consideration of aerodynamic, actuation and structural limits. An as large as possible model scale for a given wind tunnel test section is desirable for mitigating low Reynold's number effects. For the flow simulations, the Unsteady Reynolds Averaged Navier Stokes (URANS) equation model was used in combination with the Reynold's Stress turbulence Model (RSM). The combined experimental and numerical approach allowed for gaining a detailed understanding of TEL-class helicopter's aerodynamic characteristics and how to improve them.

The reference configuration's main parasite drag sources were identified to be the form drag of the fuselage (23%), the skid-landing-gear (21%) and the rotor head (26%). Improving the aerodynamic design of the skid-landing-gear and the fuselage is focused on in this work. In order to achieve a more efficient design, aerodynamic fairings for the skid-landing-gear and passive flow control devices at the rear fuselage's upsweep are considered. Initial investigations revealed, that analysing the impact of the design modifications on the aerodynamic characteristics at zero angle of attack and angle of sideslip is sufficient for the design evaluation. The main sources of downforce at the reference configuration were identified to be the fuselage itself and the interference of the rotor-head on the fuselage.

The isolated fuselage of the reference configuration (F0M0) features a hybrid flow topology. This flow topology combines features of both the eddy and the vortex flow topology observed at ramp-type aft-body geometries. The appearance of the

hybrid flow topology could be related to the smooth contour change at both the rear fuselage's lateral tapering and upsweep. The two main features of this flow topology are counter-rotating upsweep vortices on each side of the rear fuselage and a recirculation zone near the fuselage's symmetry plane. Furthermore, vortices are generated by the interaction of the flow past the fuselage lateral side with the open cavities for housing the skid-landing-gear's central cross beam elements. In consequence of the upsweep vortices, high-momentum fluid from further away from the wall is pushed towards the surface. This leads to flow reattachment at the rear fuselage upsweep, which confines the extension of the recirculation zone. Thus, explaining the observed downforce at the isolated fuselage. The downforce generated by aerodynamic interference of the rotor-head with the fuselage is apparently associated to the mast fairing cavity. Other indications for aerodynamic interference of the rotor head with the fuselage or even the skid-landing-gear were not observed.

Adding the skid-landing-gear to the fuselage (F0M0L0) significantly impacts on the flow topology. In consequence of the additional perturbances along the fuselage ventral side due to the wake of the circular cross-tubes, the upsweep vortices are no longer formed. Thus, the flow does not reattach to the fuselage's rear upsweep region and the flow separation spans over basically the entire aft-body. Furthermore, due to the lack of upward directed momentum the flow past the fuselage's dorsal side enters the upsweep region. This causes the formation of the separation vortices on either side of the rear fuselage. The modified near-surface and wake flow topology also explains the reduction in downforce by adding the skid-landing-gear, which is mainly associated to aerodynamic interference with the fuselage. In contrast to F0M0, only one instead of two wake regions can be observed for F0M0L0. F0M0L0's wake region features a significantly larger extension than the aggregate of F0M0's two wake regions.

Based on this insight the design of the landing-gear has been revised in order to identify potentials for drag reduction. Possible designs for helicopter's landing-gear include skid-landing-gear, fixed wheeled-landing-gears and retractable wheeled-landing-gear. A tradeoff analysis showed that a skid-landing-gear augmented with aerodynamically optimised fairings provides the best solution for TEL-class helicopter. Two different fairing types have been considered for this modification. The first type is characterised as a retrofittable solution, which can be mounted to the current production type skid-landing-gear. For the retrofittable faired skid-landing-gear, six design variants were evaluated in order to select the final design L1. Furthermore, the design of the fuselage has been revised at this stage. This led to a fuselage design featuring a smoothed ventral side, which is called F1. The second type is a more progressive design. It has been designed predominantly from an aerodynamic point of view. Thus, it allows to identify the full potential of faired skid-landing-gears. The progressive design variant L2 is more challenging to implement, because it requires a considerable amount of structural changes to the airframe.

The smoothed fuselage F1 yielded a drag benefit of 3% compared to the reference configuration's total parasite drag. Analysing the near-surface and wake flow topology of the isolated fuselage F1 reveals, that this drag reduction is mainly associated to the missing interaction of the flow past the fuselage's ventral side with the cavities housing the skid-landing-gear. In consequence, the stagnation

zone at the cavities vanishes and higher momentum fluid reaches the rear fuselage upsweep. This delays the separation upstream of the recirculation zone. Furthermore, the formation of the upsweep vortices is enhanced by this effect. In turn, also the extension of the recirculation zone is confined and secondary upsweep vortices could be identified. The extension of both the wake regions is also reduced compared against F0M0. Beside the impact on drag, smoothing the fuselage's ventral side increases the downforce by enhancing the vertical deflection of the flow at the rear fuselage.

Fairing the skid-landing-gear proofed to be very effective in reducing the parasite drag. With the retrofittable design variant L1 and the progressive design variant L2 the parasite drag could be reduced by, respectively, 18% and 19% compared against the reference configuration's total parasite drag. Regarding the downforce L1 is basically neutral. In consequence, the total lift of configuration F1M0L1R0 deviates considerably from F0M0L0R0. However, L1's equivalent weight penalty through aerodynamic downforce in cruise is less than 80 kg for the real helicopter. The faired skid-landing-gear L2 actually adds lift to the modified configuration including F1 and L2. The sources of this additional lift are L2's minimal aerodynamic interference with the fuselage, the fairing's applied twist variation and that the attachment fairings could be designed to avoid generating any downforce. The difference in generated down force between the configuration with L1 and L2 is equivalent to 30 kg weight penalty in cruise. However, this advantage of L2's design cannot outweigh the disadvantages due to the complexity of the required structural changes. Thus, the retrofittable faired skid-landing-gear variant L1 was selected for further analysis.

Fairing the skid-landing-gear (L1) effectively mitigates the separation at the rear fuselage upsweep observed in the presence of the baseline skid-landing-gear. Furthermore, upsweep vortices are generated when L1 is installed, which is not the case with L0. With L1 the separation is confined to the recirculation zone close to the model's symmetry plane just as on the isolated baseline fuselage F0M0. With L1 installed, in contrast to L0, no flow is entering the rear fuselage upsweep along the fuselage's dorsal side.

Those changes are also apparent in F1M0L1's structure and extension of the wake compared against F0M0L0. With L1 installed two separate wake regions can be distinguished and not only one as for F0M0L0. When L1 is installed the wake region's extension is significantly reduced . In fact, F1M0L1's wake flow topology is similar to the wake flow field observed for F0M0. However, due to the increased upsweep vortex intensity the associated wake region is shifted towards the ventral side of the fuselage. By fairing F0M0's open cavities at the fuselage's ventral side, no cavity vortices are observed in the wake, but the landing-gear vortex. It can be concluded that, fairing the skid-landing-gear effectively mitigates the wake associated to L0 and minimizes its aerodynamic interference on the fuselage. Nevertheless, L1's aerodynamic interference on the fuselage is not eliminated.

In order to further mitigate the drag associated to the rear fuselage's upsweep region and the skid-landing-gears aerodynamic interference with this region the application of passive flow control devices has been investigated. Out of a large number of passive flow control device combinations the most promising solution has been selected during a configuration study. This configuration study revealed, that the best combination includes two pairs of counter-rotating vortex generators

and sheet-metal type strakes. For the vortex generator it was found that, they should be located just upstream of the rear fuselage's upsweep. The strakes revealed the best impact when they are located just downstream of the region where the upsweep vortices are formed. This passive flow control device combination is called S2LVG2X20.
With S2LVG2X20 installed at F1M0L1 the total parasite drag is reduced by another 1% compared to the reference configuration's total parasite drag. An additional impact on lift is not observed by installing S2LVG2X20. The vortex generators shed two pairs of counter-rotating vortices into the wake. In consequence the boundary layer flow is reenergised along the fuselage's rear upsweep. By this added momentum, the flow remains attached and no recirculation zone is observed anymore in the presence of S2LVG2X20. In fact, F1M0L1's pressure level when fitted with S2LVG2X20 is even increased compared against F1M0 throughout the rear fuselage region. Thus, the aerodynamic interference of the faired skid-landing-gear L1 on the isolated fuselage is not only eliminated but even an additional improvement is achieved. However, this improvement is to a certain extent counter-balanced by the passive flow control devices form drag. The extension of the wake regions is not affected considerably by the presence of the selected passive flow control devices. Nevertheless, the velocity deficit inside the wake region is further reduced by the application of passive flow control.
In summary it can be concluded, that the developed design optimisations for TEL-class utility helicopter proofed to be very effective in improving their aerodynamic performance. On aggregate, the parasite drag could be reduced by 22% relative to the total parasite drag of current production type models. The parasite drag is responsible for about 50% of the total power requirements in cruise. Thus, the achieved drag reduction can reduce the required power in cruise by up to 11%. This also translates in a fuel flow reduction potential of similar magnitude. The results of the performed design optimisation have been incorporated in the design of Airbus Helicopters Bluecopter Demonstrator. During the performed flight tests of this demonstrator program, the fuel flow reduction through the suggested aerodynamic modifications was confirmed to be in the order of 10%.
For the reference configuration fitted with the faired skid-landing-gear and the passive flow control devices, the rotor head constitutes the largest single drag source. It contributes 40% to the total parasite drag. Thus, in order to achieve further drag savings, the design of the rotor-head needs to be revised. A first effort was contributed to this design task in the course of the Bluecopter Demonstrator program. The Bluecopter rotor head is fitted with a semi-watertight full fairing. However, the wind tunnel test performed at the Technical University of Munich's Institute of Aerodynamics and Fluid Mechanics and the flight test performed by Airbus helicopters only confirmed 2% additional drag savings. It was found that, most of the full fairings aerodynamic potential is lost due to the sealing concept. Thus, further improvements of the sealing concept need to be achieved for exploiting the full potential.

Bibliography

[1] d'Alascio, A.,Pahlke, K., Le Chuiton, F.: "Application of a structured and an unstructured CFD Method to the Fuselage Aerodynamics of the EC145 Helicopter. Prediction of the time averaged Influence of the Main Rotor." *European Congress on Computational Methods in Applied Sciences and Engineering*, ECCOMAS, Jyväskylä, Finland, 2004.

[2] Ansys Inc., "CFX-Solver Theory Guide", Release 14.5, 2012.

[3] Batrakov, A.S., Kusyumov, A.N., Mikhailov, S.A., Pakhov, V.V., Sungatullin, A.R., Zherekhov, V.V., Barakos, G.N.: "A Study in Helicopter Fuselage Drag.", *39th European Rotorcraft Forum*, pp. 25-1 – 25-14, Moscow, 2013.

[4] Batrakov, A.S., Garipova, L., Kusyumov, A.N., Mikhailov, S.A.: "Computational Fluid Dynamics Modeling of Helicoper Fuselage Drag.", *Journal of Aircraft*, Vo.52, No.5, pp. 1634 – 1643, 2015.

[5] Bebesel, M., Polz, G., Schšll, E.: "Aerodynamic and Aeroacoustic layout of the ATR." *55th Annual Forum*, American Helicopter Society, Montreal, Canada, 1999.

[6] Boelens, O. J., et al.: "The blind-test activity of the GOAHEAD project." *33rd European Rotorcraft Forum*, Kazan, 2007.

[7] Boniface, J.: "A Computational Framework for Helicopter Fuselage Drag Reduction Using Vortex Generators.", *70th Annual Forum*, American Helicopter Society, 2014.

[8] Breitsamter, C.: "Abnahmemessungen am Windkanal A", Lehrstuhl für Fluidmechanik, Technische Universität München, 1999.

[9] Breitsamter, C.: "Innovative high-lift concepts of the integrated research programs AWIATOR and IHK." *Luftfahrttechnisches Handbuch (LTH)*, AD-04-02-004, pp. 1-50, 2009.

[10] Breitsamter, C.B., Grawunder, M., Reß, R.: "Aerodynamic Design Optimisation for a Helicopter Configuration Including a Rotating Rotor Head.", *29th International Congress of the Aeronautical Sciences*, paper no. 686, St. Petersburg, Russia, 2014.

[11] Chapman, G.T.: "Topological Classification of Flow Separation on Three-Dimensional Bodies.", *24th Aerospace Sciences Meeting*, AIAA, 1986.

[12] Delaunay, B.N.: "Sur la Sphere Vide." *Bulletin of Academy of Sciences of the USSR*, Vol., Nr. 6, S. 793-800, 1934.

[13] Duhon, J. M.: "Cost Benefit Evaluation of Helicopter Parasite Drag Reductions.", *Symposium on Helicopter Aerodynamic Efficiency*, American Helicopter Society, 1975.

[14] Ewald, B.F.R.: "Wind Tunnel Wall Correction." *AGARDograph 336*, Advisory Group for Aerospace Research and Development, AGARD-AG-336, 1998.

[15] Freeman, C., Mineck, R. E.: "Fuselage Surface Pressure Measurements of a HelicopterWind-Tunnel Model with a 3.15-Meter Diameter Single Rotor.Ó NASA Langley Research Center Rept. TM- 80051, 1979.

[16] :Gormont, R.: "Some Important Practical Design Constraints Affecting Drag Reduction.", Rotorcraft Parasite Drag Special Report, presented at *31st Annual Forum*, American Helicopter Society, 1975.

[17] Grawunder, M., Reß, R., Breitsamter, C., Adams, N.A.: "Flow Characteristics of a Helicopter Fuselage Configuration Including a Rotating Rotor Head." *28th International Congress of the Aeronautical Sciences*, Brisbane, Australia, 2012.

[18] Grawunder, M., Reß, R., Breitsamter, C., Adams, N.A.: "Optimised Skid-Landing-Gear for Twin-Engine-Light Utility Helicopter." *39th European Rotorcraft Forum*, Moscow, Russia, 2013.

[19] Grawunder, M., Reß, R., Breitsamter, C.: "Helicopter aft-body drag reduction by passive flow control." *40th European Rotorcraft Forum*, Southampton, 2014.

[20] Grawunder, M., Reß, R., Breitsamter, C.: "Thermographic Transition Detection for Low-Speed Wind-Tunnel Experiments." *AIAA Journal*, Vol. 54, No. 6, pp. 2012-2016, 2016.

[21] Keys, C. N., Wiesner, R..: "Guidelines for reducing helicopter parasite drag". *Journal of the American Helicopter Society*, Vol. 20, No. 1, pp. 31Ð40, 1975.

[22] Khier, W.: "Navier-Stokes Prediction of the Effect of the Skids on the Aerodynamics of Helicopter Fuselage in Forward Flight.", *35th European Rotorcraft Forum*, 2006.

[23] Khier, W.: "Numerical Analysis of Hub and Fuselage Interference to Reduce Helicopter Drag.", *38th European Rotorcraft Forum*, pp. 48-1 – 48-12, Amsterdam, 2012.

[24] Kneisch, T., Krauss, R., d'Alascio, A., Schimke, D.; "Optimised rotor head design for an Economic Helicopter." *37th European Rotorcraft Forum*, Milan, 2011.

[25] Launder, B. E., Reece, G. J., Rodi, W.: "Progress in the development of a Reynolds-stress turbulence closure." *Journal of Fluid Mechanics*, Vol. 68, Nr. 03, pp. 537-566, 1975.

[26] Leishman, J.G.: "Principles of Helicopter Aerodynamics - Second Edition.", *Cambridge Aerospace Series*, ISBN 978-0-521-85860-1, 2006.

[27] Le Pape, A., Gatard, J., Monnier, J.C.: "Experimental Investigations of Rotor Ð Fuselage Aerodynamic Interactions." *Journal of the American Helicopter Society*, 52(2), pp. 99-109, 2006 .

[28] Lienard, C., Pape, A. Le, Verbeke, C.: "Numerical and Experimental Investigation of Helicopter Fuselage Drag Reduction Using Active Flow Control.", *68th Annual Forum*, American Helicopter Society, Chesterfield, MO, pp. 175-1 - 175-17, 2012.

[29] Menter, F. R.: "Two-equation eddy-viscosity turbulence models for engineering applications." *AIAA Journal*, Vol. 32, Nr. 8, pp. 1598Ð1605, 1994.

[30] Pape, A. Le, Lienard, C., Verbeke, C., Pruvost, M., De Coninck, J.-L.: "Helicopter Fuselage Drag Reduction Using Active Flow Control: A Comprehensive Experimental Investigation", *Journal of the American Helicopter Society*, Vol. 60, No. 3, 2015.

[31] Polz, G.: "Auswertung von Windkanalversuchen mit modifizierten BO 105-Rümpfen." MBB GmbH, TN-D127-2/72, 1972.

[32] Renaud, T., Brien, D. O., Smith M., Potsdam, M.: "Evaluation of Isolated Fuselage and Rotor - Fuselage Interaction Using Computational Fluid Dynamics." *Journal of the American Helicopter Society*, Vol. 53, (1), pp. 3-17., 2008.

[33] Renaud, T., LePape, A., Peron, S.: "Numerical Analysis of Hub and Fuselage Drag Breakdown of a Helicopter Configuration.", *38th European Rotorcraft Forum*, pp. 146-1 – 146-19, Amsterdam, 2012.

[34] Saporiti, P., Personal Communication, Courtesy of Clean Sky GRC2 partners, 2016.

[35] Seddon, J.: "Aerodynamics of the helicopter rear fuselage upsweep". *8th European Rotorcraft Forum*, Paper 2.12, Aix-en-Provence, 1982.

[36] Seddon, J., "Further Studies in Helicopter Body Aerodynamics.", *9th European Rotorcraft and Powered Lift Aircraft Forum*, Stresa, Italy, 1983.

[37] Shephard, M.S., Georges, M.K.: "Three-Dimensional Mesh Generation by Finite Octree Technique", *International Journal for Numerical Methods in Engineering*, vol 32, pp. 709-749, 1991.

[38] Spagl, M.: "Entwurf und Konstruktion von Landewerksverkleidungen für einen Transporthubschrauber", Diploma Thesis, Technische Universität München, Institute of Aerodynamics and Fluid Mechanics, 2012.

[39] Stroub, R. H., Rabbott, J. P. Jr.:"Wasted fuel - another reason for drag reduction." *31st Annual National Forum*, American Helicopter Society, Washington, D.C., 1975

[40] Venegoni, N.: "An industrial rationale for the aerodynamic design of the fuselage for a high performance light helicopter." *3rd European Rotorcraft and Powered Lift Aircraft Forum*, 1977.

[41] Vogel, F., Breitsamter, C., Adams, N.A.: "Aerodynamic Analysis of a Helicopter Fuselage." *New Results in Numerical and Experimental Fluid Mechanics VII*, Notes on Numerical Fluid Mechanics and Multidisciplinary Design, Vol. 112, pp 603610, 2010.

[42] Vogel, F., Breitsamter, C., Adams, N.A.: " Aerodynamic Investigations on a Helicopter Fuselage." *29th AIAA Applied Aerodynamics Conference*, Honolulu, Hawaii, 2011.

[43] Vogel, F.: "Aerodynamische Analysen an Helikopter Zellen-Ausleger Konfigurationen.", Dissertation, Technische Universität München, *Verlag Dr. Hut*, ISBN 978-3-8439-2696-6, 2016.

[44] Wagner, S.N.: "Problems of Estimating the Drag of a Helicopter." *AGARD Conference Proceedings No. 124*, 1973.

[45] Wentrup, M.: "An Adjoint Based Optimization Chain for Complex Helicopter Fuselage Parts Using a Free Form Deformation or CAD Based Parametrization Method.", *41st European Rotorcraft Forum*, Munich, Germany, 2015.

[46] Wilcox, D.C.: "Re-assessment of the scale-determining equation for advanced turbulence models.", *AIAA Journal*, Vol. 26, No. 11, pp. 1299-1310, 1988.

[47] Williams, R.M.: "A comprehensive plan for helicopter drag reduction.", *Symposium on Helicopter Aerodynamic Efficiency*, American Helicopter Society, 1975.

[48] Yerry, M.A., Shephard, M.S.: "Three-Dimensional Mesh Generation by Modified Octree Technique", *International Journal for Numerical Methods in Engineering*, vol 20, pp.1965-1990, 1984.

[49] Zhang, Q., Garavello, A., D'Alascio, A., Schimke, D.: "Advanced CFD-based optimization methods applied to the industrial design process of airframe components at Airbus Helicopters." *70th Annual Forum*, American Helicopter Society, Quebec, 2014.

[50] "Statistical Review of World Energy 2016", BP p.l.c., London, UK.

A Appendix

A.1 Flow topology at the faired skid-landing-gear L1

The flow topology at the fuselage's ventral side is dominated by the interference with the flow around the skid-landing-gears attachment fairings; see Fig. A.1 and Fig. A.2. The topological field is divided into two domains. The first domain is associated to the fuselage. The second domain is associated to the faired skid-landing-gear. All characteristic points and streamlines of the skid-landing-gear domain are denoted by the superscript LS. The division of the topological field is performed such that the topological equation for the fuselage domain still needs to return a sum of 2, whereas for the skid-landing-gear a sum of 0 is required. At the front attachment fairing's upstream side the flow reattaches at N_{A2}^{LS}; see Fig. A.1 a). Furthermore, a second attachment nodus is observed upstream of N_{A2}^{LS}; i.e. N_{A1}^{LS}. In consequence the separation saddle S_{S1}^{LS} appears between N_{A1}^{LS} and N_{A2}^{LS}. The backward flow characteristic streamline originating from N_{A1}^{LS} connects to the downstream end of S_{S3}. Thus, connecting the flow around the skid-landing-gears front attachment fairing to the topological interface with the flow around F1. This combination of two attachment nodi and two separation saddle is associated to the formation of a horse shoe vortex system at the upstream side of the front attachment fairing.

The primary horse shoe vortex LV1 is formed between the lateral attachment $AL2^{LS}$ and separation line $SL1^{LS}$ originating, respectively, from N_{A2}^{LS} and S_{S1}^{LS}. LV1 triggers the formation of a secondary (LV1-2) and tertiary (LV1-3) horse shoe vortex. LV1-2 is counter-rotating with respect to LV1, whereas LV1-3 is co-rotating. LV1-2 is formed between $AL1^{LS}$, originating from N_{A1}^{LS}, and $SL1^{LS}$. LV1-3 is formed between $AL1^{LS}$ and SL3. At the outboard side of the front attachment fairing LV1-2 quickly diminishes and LV1-3 merges with LV1. LV1 then convects further downstream and continues to intensify while the role up continues between $AL2^{LS}$ and SL3. The outboard side of $AL2^{LS}$ ends on the downstream side of the front attachment fairing in S_{S3}^{LS}. From S_{S3}^{LS} an upstream and downstream directed separation line emerges; i.e. $SL3^{LS}$. $SL3^{LS}$ separates from the surface by encountering SL3 a short distance further downstream. At $SL3^{LS}$ LV1's roll-up process ends.

Furthermore, a corner separation occurs on the dorsal side of the front attachment fairing. The corner separation commences at $SL2^{LS}$, which originates from S_{S2}^{LS}. The inboard and outboard side of $SL2^{LS}$ ends in F_{S2-3-7} and F_{S2-12}^{LS}, respectively. S_{S2}^{LS} is associated to the incoming flow characteristic streamline originating from

N_{A2}^{LS} and the back flow characteristic streamline originating from the reattachment point N_{A5}^{LS} at skid side of the front cross beam fairing's blunt trailing edge (not depicted). Through F_{S2-12}^{LS} the corner separation is connected to the dorsal separation at the cross beam fairing's blunt trailing edge; i.e. $SL12^{LS}$. $SL12^{LS}$ originates from the separation saddle S_{S12}^{LS}. S_{S12}^{LS} is located at the skid end of the trailing edge, but is not depicted in Fig. A.1.

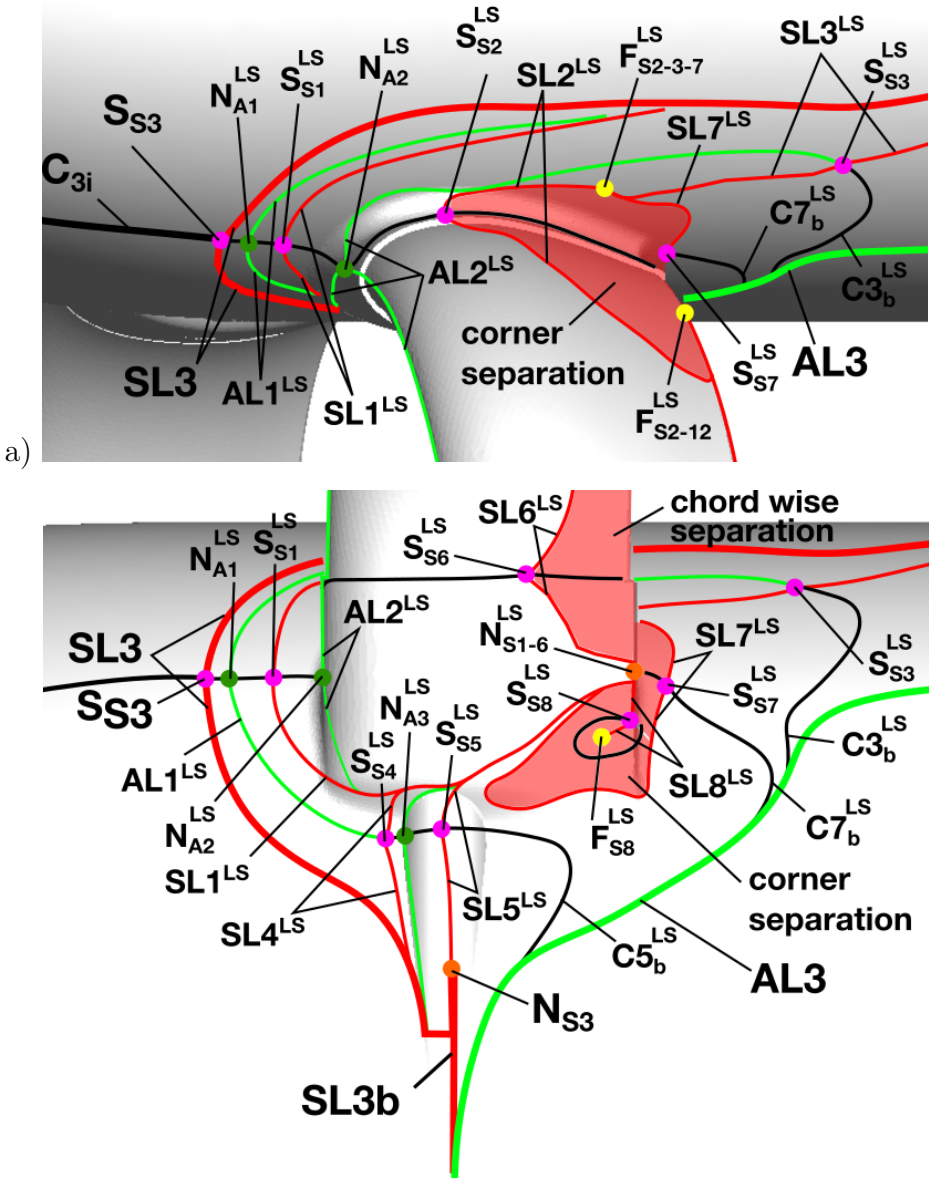

Figure A.1: *Schematic representation of F1M0L1's near-surface flow topology around the front skid-landing-gear's attachment fairing.* $Re_\infty \approx 0.95 \cdot 10^6$, $\alpha, \beta = 0$ *deg.*

At the ventral side of the front attachment fairing L1's roll-up is much more confined then on the dorsal side. This is the case because $SL2^{LS}$ already separates from the surface by encountering $SL1^{LS}$ at the attachment fairings leading edge; see Fig. A.1 b). The same situation is observed for the secondary and tertiary

horse shoe vortex. Due to the reattachment point N_{A3}^{LS} at the upstream face of the central cross-beam elements $AL1^{LS}$ ends in S_{S4}^{LS}. Thus, also L1-2 and L1-3 end to roll-up at $SL4^{LS}$ originating from S_{S4}^{LS}. The outboard section of $SL4^{LS}$ separates from the surface as it encounters $SL1^{LS}$, which then ends in N_{S1-6}^{LS}.
Near the models symmetry plane at the central cross beam elements the separation line SL3b and the attachment line AL3 diverge. SL3b separates from the surface at SL3, which ends in the separation nodus N_{S3}. AL3 is bend around the front attachment fairing and then convects downstream; see also Fig. 6.22. AL3 ends in S_{S4} upstream of the rear attachment fairing. Starting from AL3 the three backward flow characteristic streamlines $C3_b^{LS}$, $C5_b^{LS}$ and $C7_b^{LS}$ emerge which connect to the downstream side of, respectively, S_{S3}^{LS}, S_{S5}^{LS} and S_{S7}^{LS}.
$SL5^{LS}$ originates from S_{S5}^{LS} in consequence of the interaction with the incoming flow characteristic streamline originating from N_{A3}^{LS}. $SL5^{LS}$ ends at the inboard side in N_{S3} and separates from the surface by encountering $SL1^{LS}$ at the outboard side. S_{S7}^{LS} results from the interaction of the incoming flow characteristic streamline originating from N_{A5}^{LS} with $C7_b^{LS}$. From S_{S7}^{LS} the separation line $SL7^{LS}$ originates. The inboard side of $SL7^{LS}$ separates from the surface as it encounters $SL1^{LS}$. The outboard section of $SL7^{LS}$ ends in F_{S2-3-7}^{LS}. Thus, $SL7^{LS}$ closes the downstream end of the corner separation on the dorsal side of the front attachment fairing and defines the boundary for the corner separation on the ventral side. Within the corner separation at the ventral side F_{S8}^{LS} is located. Around F_{S8}^{LS} the flow characteristic streamline coming from the cross beams trailing edge is curled back and defines the incoming flow characteristic streamline for S_{S8}^{LS}. At S_{S8}^{LS} $SL8^{LS}$ originates, whose inboard and outboard side ends, respectively, in F_{S8}^{LS} and by separating from the surface at $SL1^{LS}$.
At the cross beam fairing's ventral side the flow separates at approximately 80% of the chord length. The origin of this separation is S_{S6}^{LS}. At S_{S6}^{LS} the incoming flow characteristic streamline originating form $AL2^{LS}$ interacts with another back flow characteristic streamline originating from N_{A5}^{LS}. In consequence $SL6^{LS}$ is formed. The inboard side of $SL6^{LS}$ ends in N_{S1-6}^{LS}, thus, defining the inboard end of the chord wise separation.
At the rear attachment fairing's upstream side the flow reattaches at N_{A6}^{LS}; see Fig. A.2 a). The back flow characteristic streamline originating from N_{A6}^{LS} connects to the downstream end of S_{S4}. AL3 defines the incoming flow characteristic streamline for S_{S4}. Thus, connecting the flow around the skid-landing-gears rear attachment fairing to the topological interface with the flow around F1.
N_{A6}^{LS} and S_{S4} are associated to the formation of a single horse shoe vortex LV2 at the upstream side of the rear attachment fairing.
The horse shoe vortex LV2 is formed between the lateral attachment line $AL6^{LS}$ and separation line $SL4$ originating, respectively, from N_{A6}^{LS} and S_{S4}. The outboard section of $AL6^{LS}$ ends on the downstream section of the rear attachment fairing in S_{S14}^{LS}. S_{S14}^{LS} appears in consequence of $AL6^{LS}$'s interaction with the back flow characteristic streamline originating from N_{A2}. From S_{S14}^{LS} an upstream and downstream directed separation line emerges; i.e. $SL14^{LS}$. The downstream section of $SL14^{LS}$ separates from the surface by encountering SL4 at P2; see also Fig. 6.22. At $SL14^{LS}$ LV2's roll-up process ends.

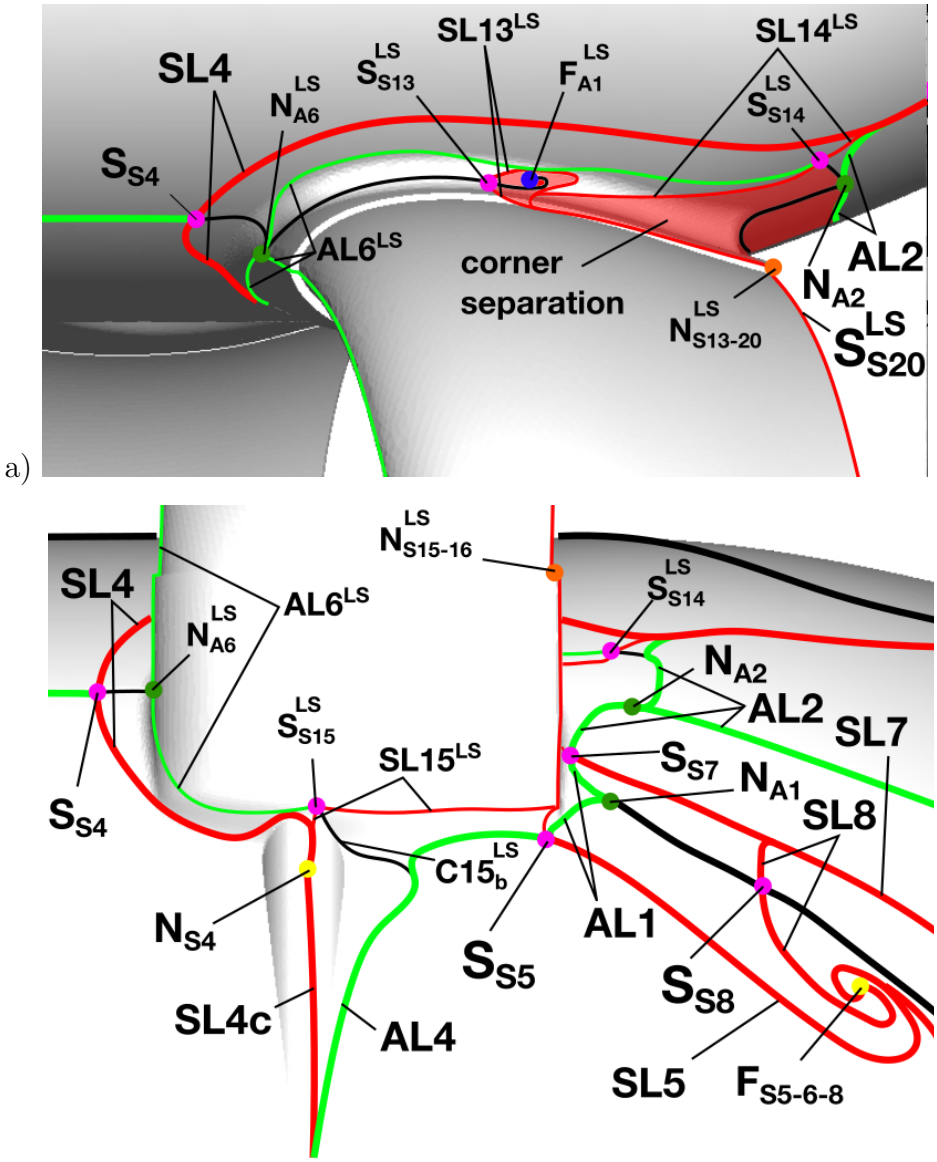

Figure A.2: *Schematic representation of F1M0L1's near-surface flow topology around the rear skid-landing-gear's attachment fairing.* $Re_\infty \approx 0.95 \cdot 10^6$, $\alpha, \beta = 0$ *deg.*

On the dorsal side of the rear attachment fairing a corner separation occurs as well. This corner separation commences at $SL13^{LS}$, which originates from S^{LS}_{S13}. The inboard and outboard section of $SL13^{LS}$ both end in N_{S13-20}. This peculiarity is associated to the presence of the attachment foci F^{LS}_{A1} directly downstream of the inboard section of $SL13^{LS}$. In consequence the inboard section of $SL13^{LS}$ is bend around F^{LS}_{A1} and separates from the surface at the outboard section of $SL13^{LS}$. S^{LS}_{S13} is associated to the incoming flow characteristic streamline originating from N_{A6} and the back flow characteristic streamline originating from F^{LS}_{A1}. $SL14^{LS}$'s upstream section separates from the surface at $SL13^{LS}$. Through F^{LS}_{S13-20} the corner separation is connected to the dorsal separation at the cross beam fairing's blunt trailing edge; i.e. $SL20^{LS}$. In analogy to the front cross beam fairing, $SL20^{LS}$ originates from the separation saddle at the skid end of the trailing edge;

i.e. S^{LS}_{S20} (not depicted).
L2's roll-up process at the ventral side of the rear attachment fairing is also more confined then on the dorsal side. For L2 this is the case because $AL6^{LS}$ ends in S^{LS}_{S15} by interaction with $C15^{LS}_{b}$. The backward flow characteristic streamline $C15^{LS}_{b}$ emerges from AL4; see Fig. A.2 b). The inboard section of $SL15^{LS}$ separates from the surface at $SL4$, which ends in N_{S4}. Near the models symmetry plane at the central cross beam elements, the separation line SL4c and the attachment line AL4 diverge. SL4c also ends in the separation nodus N_{S4}. Whereas, AL3 is bend around the front attachment fairing and ends in S_{S5} further downstream.
S_{S5} appears in consequence of AL3's interaction with the inboard section of AL1, which originates at N_{A1}. From S_{S5} the separation line SL5 originates. SL5 ends in F_{S5-6-7}. Furthermore, a separation line emerges at S_{S5} in the outboard direction. This separation line separates from the surface as it encouters the outboard section of $SL15^{LS}$. After emerging from S^{LS}_{S15}, $SL15^{LS}$ first convects downstream along the inboard edge of the rear attachment fairing. At the rear attachment fairing's trailing edge $SL15^{LS}$ is deflected along the trailing edge and ends in N^{LS}_{S15-16}. The deflection is associated to the interaction of $SL15^{LS}$ with the outboard section of the separation line originating from S_{S5}.
Through the presence of the two attachment nodi N_{A1} and N_{A2} downstream of the rear attachment fairing the separation saddle S_{S4} is formed between these nodi. From S_{S7} a back flow characteristic streamline emerges, which also separates at $SL15^{LS}$. The outboard section of AL2 separates from the surface as it encounters SL4 at P1. Thus, closing the topological interface between F1 and the skid-landing-gear's rear attachment. This interface is defined by SL4, SL4c, AL4, AL1 and AL2.